DISPERSION ANALYSIS OF NONLINEAR PERIODIC STRUCTURES

A Dissertation
Presented to
The Academic Faculty

by

Kevin L. Manktelow

In Partial Fulfillment
of the Requirements for the Degree
Doctor of Philosophy in the
George W. Woodruff School of Mechanical Engineering

Georgia Institute of Technology
May 2013

DISPERSION ANALYSIS OF NONLINEAR PERIODIC STRUCTURES

Approved by:

Dr. Michael J. Leamy, Advisor
School of Mechanical Engineering
Georgia Institute of Technology

Dr. Massimo Ruzzene, Co-Advisor
School of Aerospace Engineering
Georgia Institute of Technology

Dr. Aldo Ferri
School of Mechanical Engineering
Georgia Institute of Technology

Dr. Alper Erturk
School of Mechanical Engineering
Georgia Institute of Technology

Dr. Julian J. Rimoli
School of Aerospace Engineering
Georgia Institute of Technology

Date Approved: 03-March-2013

ACKNOWLEDGEMENTS

I followed a rather unorthodox path to graduate school when I decided to pursue a Ph.D. several years ago. I didn't go through the same 'meet-and-greet' avenue that many new graduate students go through to meet their future advisers. Instead, I traveled 800 miles from Chicago, IL to Atlanta, GA prior to the start of the Fall semester in hopes of finding a research adviser(s) whose personality and research interests aligned with my own. After several enlightening discussions, I met with Dr. Aldo Ferri. I am grateful and fortunate to have met Dr. Ferri at that time, because he directed me to Dr. Michael Leamy and Dr. Massimo Ruzzene – two incredibly talented faculty members who would become my graduate mentors and co-advisers.

I feel fortunate to have been advised by Dr. Michael Leamy and Dr. Massimo Ruzzene. They provided me with an interesting research area, invaluable guidance and instruction, motivation during hard times, boundaries to keep me on track, opportunities to present my research, time to prepare for qualifying examinations, and invaluable feedback on all of my papers and presentations. I would like to specifically thank Dr. Leamy for providing support from before I even set foot on campus, and for fostering an environment and research relationship conducive to personal growth and professional development. I am also grateful for the invaluable technical and personal insight that Dr. Ruzzene always offered. I am deeply appreciative of the uncountable hours they spent working with me. I can't possibly describe all of the ways that Dr. Leamy and Dr. Ruzzene have supported and helped me throughout my graduate career. So, I hope that a simple and humble *thank you* will suffice for now.

I would also like to thank the members of my reading committee, Dr. Aldo Ferri, Dr. Alper Erturk, and Dr. Julian Rimoli, for their invaluable time and feedback throughout

the dissertation process. I take pride in noting that my committee members' involvement extended beyond my dissertation proposal and defense. Their well-crafted classes, experimental expertise, literature recommendations, and general advice were immensely helpful in crafting a successful graduate career. I would also like to thank Dr. Karim Sabra and his graduate students for their supportive role in initial experiments and to Dr. Raj Narisetti for his role in developing part of the literature directly supporting this dissertation.

I am also thankful for the friendships I developed while at Georgia Tech with my labmates. Unique insight and perspective from Kyle Karlson, Jason Kulpe, and Dekun Pei often helped resolve technical or research-related problems. Beyond research, Kyle, Jason, Dekun, and my other labmates Maj. Elsa Johnson, Farzad Sadeghi, John Arata, Kamil Koçak and Dr. Farhad Farzbod provided relief from inevitable frustration and daily minutiae. I have sincerely enjoyed time spent with each of these people outside the university.

I would like to acknowledge the unwavering support from my family, friends, and beautiful fiancée, Leia Curry. I attribute my persistence, dedication, and technical aptitude to the way my mother, Sally Manktelow, and father, Peter Manktelow, raised me. Their continued support, prayers, and encouragement motivated me to complete my doctoral studies. My brother, Scott, and sisters, Rebecca and Melissa, have been incredibly supportive throughout the process. Lastly, I would like to thank my beautiful fiancée Leia for her loving support, delicious dinners, and general understanding when research and qualifying examinations required late nights of studying and unexpected long hours in the lab.

In short, my graduate career would not have been possible without an incredible group of individuals supporting me. For that, I am thankful.

TABLE OF CONTENTS

LIST OF TABLES

LIST OF FIGURES

SUMMARY

The present research is concerned with developing analysis methods for analyzing and exploring finite-amplitude elastic wave propagation through periodic media. Periodic arrangements of materials with high acoustic impedance contrasts can be employed to control wave propagation. These systems are often termed phononic crystals or metamaterials, depending on the specific design and purpose. Design of these systems usually relies on computation and analysis of dispersion band structures which contain information about wave propagation speed and direction. The location and influence of complete (and partial) band gaps is a particularly interesting characteristic. Wave propagation is prohibited for frequencies that correspond to band gaps; thus, periodic systems behave as filters, wave guides, and lenses at certain frequencies. Controlling these behaviors has typically been limited to the manufacturing stage or the application of external stimuli to distort material configurations. The inclusion of nonlinear elements in periodic unit cells offers an option for passive tuning of the dispersion band structure through amplitude-dependence. Hence, dispersion analysis methods which may be utilized in the design of nonlinear phononic crystals and metamaterials are required. The approach taken herein utilizes Bloch wave-based perturbation analysis methods for obtaining closed-form expressions for dispersion amplitude-dependence. The influence of material and geometric nonlinearities on the dispersion relationship is investigated. It is shown that dispersion shifts result from both self-action (monochromatic excitation) and wave-interaction (multi-frequency excitation), the latter enabling dynamic anisotropy in periodic media. A particularly novel aspect of this work is the ease with which band structures of discretized systems may be analyzed. This connection enables topology optimization of unit cells with nonlinear elements. Several important periodic systems are considered including monoatomic lattices, multilayer materials, and plane stress matrix-inclusion configurations. The analysis methods are further developed into a procedure which can be implemented numerically with existing finite-element analysis software for analyzing geometrically-complex materials.

CHAPTER I

INTRODUCTION

1.1 Overview

This dissertation is concerned with developing analysis methods for analyzing and exploring small but finite-amplitude elastic wave propagation through periodic media. Perturbation analysis of dispersion relationships for periodic media serve as a vehicle for assessing wave propagation traits in materials exhibiting strain and displacement-dependent nonlinearities. These materials generally exhibit amplitude-dependent wave propagation characteristics which provides a broad range of opportunities for designing and analyzing acoustic signal processing equipment (filters, diodes, frequency de-multiplexers), vibration isolators, wave-based imaging, and energy harvesting. Mechanical energy transport by elastic waves through periodic material/systems particularly interests researchers because of innate filtering properties.

A dispersion relation describes the frequency-dependent propagation characteristics of periodic systems and is sometimes regarded as the DNA or signature of a periodic system. An overwhelming majority of wave propagation research and design efforts focus on low energy applications where system dynamics (and hence dispersion relations) are independent of amplitude. Dispersion analysis methods purposed for linear systems break down for finite-amplitude wave propagation where well-known frequency-amplitude dependencies arise.

The primary question addressed herein is how mechanical systems with nonlinearity can be effectively tailored so that their unique dynamics enable and enhance design, rather than hinder and suppress it. The present research addresses nonlinearities and their effect on dispersion in a positive light by providing dispersion analysis tools and validation studies with the intention of designing materials, systems, and devices which advantageously utilize nonlinear system dynamics. The specific nonlinearities considered involve displacement- or strain-dependencies in the governing equations. These situations arise commonly in structural systems which often exhibit geometrical nonlinearity (linear elasticity, but nonlinear strain-displacement), as well as in material systems whereby a nonlinear stress-strain constitutive relationship enters the governing equation. Because the geometry and particular nonlinearities considered take a variety of forms, a focus of this work is to present general analysis methods and tools which can be implemented computationally.

The reminder of this chapter provides an introduction to periodic systems and the characteristics of researchers (Sec. 1.2). Specific interest is given to two special classes of periodic materials which are termed *metamaterials* and *phononic crystals*. Dispersive properties are highlighted to motivate a detailed study of nonlinear analysis methods and design strategies for periodic systems. The link between dispersion and nonlinearity arising from high-intensity wave propagation is identified with examples from literature that serve as a basis for the contained work (Sec. 1.3.2). Some unique characteristics of nonlinear structures that motivate dispersion analysis are presented in Sec. 1.3. Section 1.4 summarizes the main results. Finally, Sec. 1.5 outlines the material contained in subsequent chapters.

1.2 Periodic systems

A *periodic system* is composed entirely of a single, repeating unit. Their appearance in nature is almost as ubiquitous as their use in man-made structures. Figure 1.1 depicts several common periodic structures, in order of increasing length scale. Atomic crystal lattices are composed of one or more types of atoms which are arranged periodically. Ionic and covalent bonds between atoms result in periodic energy potentials which are responsible for the propagation of heat through lattice vibrations (phonons) [4]. In nature, some insect shells (e.g. the jewel beetle [5]) evolved with layers of biological material with alternating refractive indices. The absorption of some frequencies of light and the reflection of others produces a unique color pattern (Fig. 1.1b). Another naturally-occurring periodic system is the hexagonal honeycomb structure constructed by various bee species. While elastic wave propagation in actual honeycombs is not necessarily of great concern, it is one of the most important structures in periodic composites for its ability to form complete band gaps and other unique traits (chirality, beaming, etc.) [6, 7, 8]. At larger length scales yet,

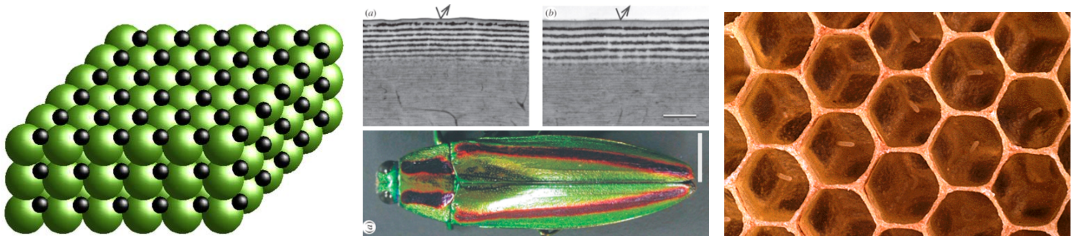

(a) Atomic lattices (b) Insect shell (c) Honeycomb

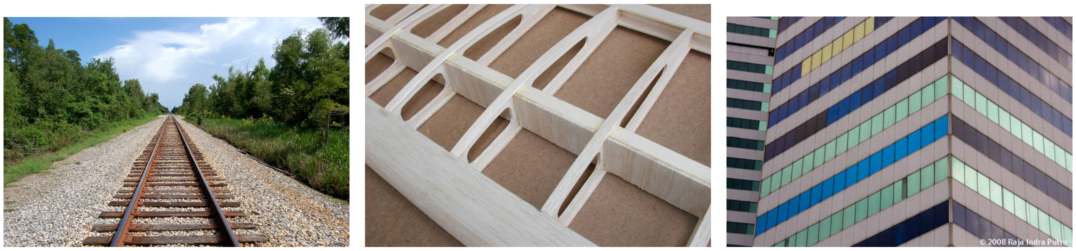

(d) Railroads (e) Aircraft ribs (f) Buildings

Figure 1.1: Periodic structure occurring in nature, in order of increasing length scale: atomic lattices, insect shells, and honeycomb. Man-made periodic structures employing periodicity include railroads, aircraft ribs, and multi-story buildings.

periodic systems that respond to entirely different frequency ranges appear in railroads, aircraft structures, and city structures such as sky-scrapers and bridges (Figs. 1.1d – 1.1f). Despite their ubiquity, only recently – within the last forty years – have researchers began to explore the unique system dynamics of these materials in depth [9, 10, 11].

It turns out that the ability to completely reflect impinging waves at some frequencies (band gaps) while allowing others to propagate (pass bands) is a universal trait among periodic materials. Frequency pass and stop bands are formed through the coherent and incoherent reflections inside a unit cell, respectively, as depicted in Fig. 1.2 for a layered material. An incident wave is partially reflected and partially transmitted at an interface;

each of the reflected and transmitted waves undergoes the same process *ad-infinitum* until a Bloch wave is formed. Bloch waves formed through constructive interference reside in the pass band frequency ranges. Evanescent waves, on the other hand, result from the destructive interference and thus exist in the stop band frequency ranges. Nevertheless, despite the fact that evanescent waves cannot carry energy deep into a material they have been purposed for ultra high-resolution imaging beyond the diffraction limit [12].

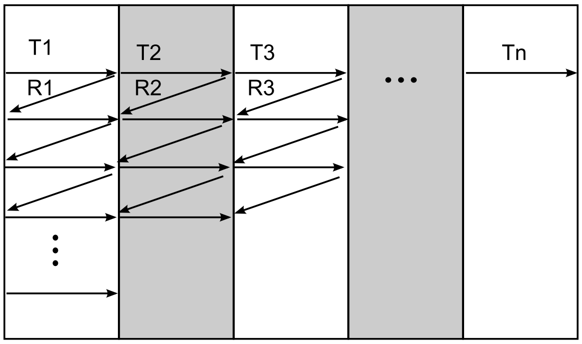

Figure 1.2: Reflections in periodic materials occur due to impedance contrasts. Interference among transmitted and reflected (assuming linearity) waves results in band gaps.

Dispersive materials are, by definition, characterized by a frequency-dependent wave speed. The dispersion relation contains a wealth of information pertaining to the wave propagation characteristics of a periodic material including the speed and direction of energy propagation, band gap locations, and resonant frequencies. In two- and three-dimensional systems, knowledge of this information can be used for a variety of purposes such as directing energy along pre-defined paths (wave guides), isolating structures from vibration, or focusing energy. Man-made materials which exploit these traits to achieve unique functionality are often termed *metamaterials* and *phononic crystals*, depending on the specific design strategy.

1.3 Motivation

The research contained within is motivated by the possibility of designing entire classes of new devices from the synthesis of two main ingredients: (1) periodic materials and, and (2) nonlinear elements. Phononic crystals and metamaterials without specific nonlinearities exhibit unique dynamics worthy of entire volumes. In a completely different category, nonlinear mechanical systems exhibit a variety of rich dynamic properties such as frequency-conversion, bi-stability, and harmonic generation. A significant body of literature exists for each of these distinct topics, individually. However, the synthesis of phononic crystals and metamaterials *composed of nonlinear elements* is a largely unexplored topic. The possibility of marrying the unique traits found in nonlinear systems with those in periodic structures motivates a number of questions that need answers: what happens to dispersion in periodic systems with nonlinear elements? how can nonlinear elements be used advantageously in metamaterials and phononic crystals? These are the fundamental questions motivating analysis of nonlinear periodic systems. Each of these individual elements is discussed next, followed by a summary of answers to these questions.

1.3.1 Engineered materials: phononic crystals and metamaterials

Phononic crystals consist of a homogeneous host/matrix material with strategically placed scattering inclusions in order to manipulate the location of band gaps in the frequency response [1, 13]. The location and width of these band gaps is of primary concern in the design of band gap-based diodes [14], switches, and filters. A combination of geometry and impedance mismatch between the host material and scatterers can produce large band gaps due to the overlap of Bragg and Mie resonances. Until recently, physical realization of phononic crystals has been limited to macroscopic structures of beads and rods within an air, water, or epoxy host material which typically limits phononic band gaps to about 1 MHz [15, 16]. Recently, advances in micro-machining have enabled phononic crystals to operate at much higher frequency ranges. Figure 1.3 depicts a microfabricated phononic crystal in a substrate designed at Sandia National Laboratories. Excitation and subsequent measurement from adjacent interdigital transducers reveals frequency stop bands bands in

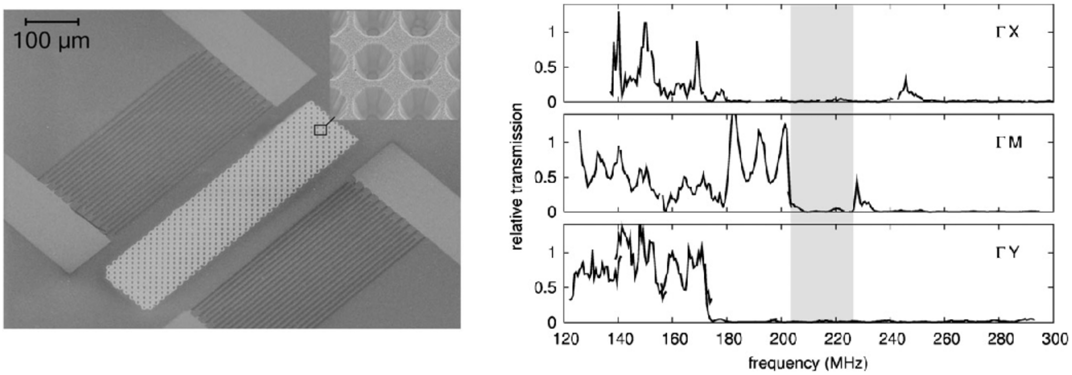

(a) SAW Phononic crystal

(b) Frequency response with band gaps

Figure 1.3: A surface acoustic wave (SAW) phononic crystal is formed form a lithium niobate substrate with low-impedance air inclusions. The transmission spectra depicts a complete band gap (colored gray) where propagation is prohibited in all directions [1].

the neighborhood of 210 MHz which block acoustic energy transmission. However, strategic removal of inclusions can produce high-Q resonators, notch filters, and waveguides that operate in this frequency range which may be useful in ultrasound imaging and other signal processing applications.

Acoustic metamaterials are designed to manipulate the propagation of acoustic waves in an entirely different manner in order to achieve desirable properties such as negative refractive indices, one-way transmission (i.e. diodes), and sub-diffraction resolution imaging (i.e. superlens) [17]. Metamaterials typically utilize effective material properties to tailor behavior. By including resonant elements that respond strongly at a particular frequency, metamaterials achieve behaviors not known to occur in natural materials. Of course, this usually limits the range of application to a small frequency band and so an on-going research topic seeks to broaden their range of application.

The acoustic cloak[1] depicted in Fig. 1.4 is the flag-ship metamaterial. It operates by redirecting wave energy around a cylindrical region through the use of a radially-periodic arrangement of resonators tuned to a particular frequency [2].

---

[1] An electromagnetic/optical analogue exists, an in fact served as the inspiration for the acoustic cloak

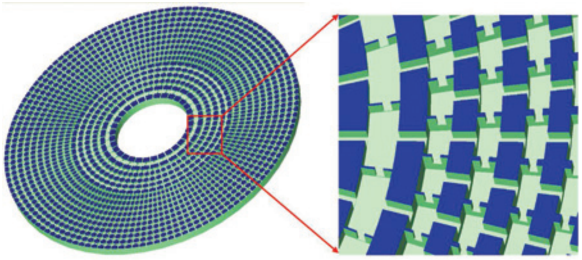

Figure 1.4: Acoustic cloak design which utilizes sub-wavelength resonators to redirect acoustic rays around a central cavity without distortion [2].

A primary difference between phononic crystals and acoustic metamaterials is the wavelength each operates at. Phononic crystals rely on band gaps and defect modes to control wave propagation; in contrast, acoustic metamaterials usually operate at longer wavelengths (and thus lower frequencies) where unit cell homogenization is valid. Because phononic crystals and acoustic metamaterials typically operate within fixed frequency limits, tunable frequency response is of primary concern. Adjustable (tunable) dispersion relations may be useful in engineering applications such as waveguides [1, 16], acoustic filters [18, 19], diodes [20], acoustic mirrors, and transducers [21, 22]. However, tunable band structure may only be obtained in linear systems by altering the geometry or material arrangement, which typically limits tuning beyond the manufacturing stage [18]. One option that has shown great promise for adding tunability to these systems utilizes nonlinearities for achieving amplitude-dependent dispersion, and thus amplitude-dependent frequency response.

1.3.2 Nonlinearity in periodic systems

The desire to achieve a more dynamic range of responses from metamaterials and phononic crystals has inspired several investigations of nonlinear metamaterial properties and analysis methods [23, 24, 19, 25, 26]. The intimate connection between frequency response and amplitude in stand-alone nonlinear systems is well-known [27]. Still, understanding the complexities that arise in nonlinear dynamical systems remains an active area of research. For example, the interaction of two waves in a constitutively-nonlinear material results in energy transfer between two waves at commensurate frequencies [28, 29]. In the same vein, finite-amplitude waves propagation almost always results in harmonic generation – a phenomena which has been exploited for designing acoustic diodes [20].

Cubic nonlinearities which appear in force-displacement type relationships are a particularly important class of nonlinearity, often termed the *Duffing nonlinearity*. The Duffing nonlinearity is responsible for bi-stability, resonant amplitude-dependent frequency-shifting, and chaos as just a few examples [30]. Nonlinearities play an increasingly dominant role in the dynamics of small scale applications such as resonators and gyroscopes [31, 32, 33]. Precise design at these scales relies on a complete understanding of how nonlinearities affect operation and performance. Individual Duffing oscillators have been purposed for enhancing energy harvesting applications that utilize high-energy periodic orbits [34]. Moreover, broadening of the frequency response in the vicinity of linear natural frequencies enables energy harvesters to operate in wider frequency bands [35]. Forced and free vibration response of coupled-oscillators have received some attention, but have received less attention than single oscillators. Hence, a present goal of acoustic metamaterial and phononic crystal research is to understand how nonlinearities influence operation and how they may be used to enhance and control material properties.

Nonlinear phononic systems provide unique opportunities for tunable band gap engineering such as wave-wave interactions [36], amplitude-dependent band structures [37, 38, 3], and extra harmonic generation. The effect of a cubic Duffing-like nonlinearity in force-displacement type relationships is of particular interest as it leads to amplitude-dependent dispersion [39, 40, 41, 42, 43], which has implications for device design. However, analysis methods and literature specifically addressing nonlinear phononic crystals and metamaterials are sparse.

A fundamental system of considerable interest in this realm is the 1D monoatomic chain of nonlinear oscillators. The coupled oscillator system finds application in anharmonic atomic lattice analysis, finite-difference modeling for continuous materials, and nonlinear modal analysis as some examples. Wave propagation in various nonlinear Duffing oscillator chains have been the subject of recent review. The nonlinear dynamics and band gap behavior were investigated to determine approximate closed-form expressions for band gap shifting [24, 3]. Others have investigated wave propagation in similar systems or those with locally-attached oscillators which have shown chaotic responses [26, 44, 45]. Often, these analyses assume a weakly nonlinear constitutive force-displacement relation which enables analysis through perturbation methods.

A strongly nonlinear system, on the other hand, which has seen increased interest lately is granular media composed of spherical or cylindrical elements. Continuum solutions for Hertzian contact between individual elements allows for lumped-parameter approximate solution of such systems. Strongly nonlinear waves in a chain of Teflon beads were investigated in [37] where tunable band gaps were reported in response to pre-compression. One-dimensional beaded systems have been devised for use in energy trapping, shock disintegration, and diode devices [38, 46, 47, 48, 49]. Raj et. al have specifically investigated the dispersion relationship in both one- and two-dimensional granular-media and have shown the existence of frequency ranges that exhibit wave beaming [50].

Continuous periodic systems have received less attention because of the inherent complexities associated with nonlinear partial-differential equations and geometrically-complex material domains. The one-dimensional bi-material system was investigated to determine the response of the system to second harmonic generation in and outside of the acoustic band gaps [22] and subsequently demonstrated as a potential acoustic diode [20]. However, the use of more complex media or integration of nonlinear continuous elements into periodic systems is a largely unexplored research area. As such, analysis methods specifically applicable to nonlinear phononic crystals and metamaterials are sparse. A recent perturbation-based analysis method for phononic systems offers an alternative method for determining the amplitude-dependent band structure of discrete nonlinear systems [50]. One component of the research presented herein stems from this work in particular by extending this analysis to discretized representations of more general continuous systems.

1.4 Main results

This dissertation contributes several major results of importance in analyzing the dispersion band structure of nonlinear periodic structures. These results support design of state-of-the-art phononic crystals and metamaterials which utilize nonlinear elements to achieve amplitude-tunable propagation behavior. A summary of these results is as follows:

- Two perturbation-based analysis methods for analyzing wave propagation are developed in a general manner such that they may be applied to discrete or continuous systems (post-discretization). The first applies to monochromatic excitations, and has been used to demonstrated novel wave-beaming and applied later in topology-optimization studies. The latter is more general in that it may be applied to multifrequency excitations for analyzing wave-wave interactions.

- Wave interactions in multi-frequency excitation of nonlinear systems leads to tunable dispersion relationships. The dispersion relation for each primary frequency component follows a different dispersion curve. Through these dynamic interactions, temporary lattice anisotropy can be introduced to steer/guide wave beams and alter group velocity. An example application for tunable-focus imaging is proposed.

- Amplitude-tunable dispersion relations in finite systems are explored and experimentally demonstrated. Frequency shifts are related to dispersion curves and it is found that a Bloch wavenumber of $\pi/3$ in a chain of nonlinear oscillators corresponds, mathematically, to the exact frequency shift of a single nonlinear oscillator.

- Constitutive material nonlinearities in various continuous systems exhibit optimal configurations with regard to the magnitude of dispersion shifts. Optimal configurations result from Bloch wave modes which exhibit high-strain regions that are confined to thin nonlinear layers. An efficient amplitude-tunable filter constructed of layered materials is simulated and discussed.

- A general numerical framework for implementing nonlinear perturbation-based analysis in general continuous systems is presented. Integration with finite-element software enables evaluation of geometrically-complex unit cells.

An outline of the remaining chapters is presented next.

1.5 Organization of the Work

General analysis methods and procedures are detailed in Chapter 2. The Bloch theorem as applied in later analytical work is presented along with a description of dispersion in both linear and nonlinear systems. Two methods for obtaining dispersion relations in nonlinear periodic systems are presented: one previously developed method based on Lindstedt-Poincaré and a new, more general method based on multiple scales formalism. Chapter 3 describes the interaction of multiple plane waves in 1D and 2D nonlinear periodic lattices. Nonlinear dispersion shifts are experimentally observed and related to discrete models in Chapter 4. Nonlinear constitutive laws and their effect on dispersion is presented in Chapter 5 using both perturbation analysis and a transfer matrix method for nonlinear systems. Topology design and optimization for unit cells with nonlinearity is described in Chapter 6 with the goal of attaining large shift sensitivity. Chapter 7 describes a general method for analytically obtaining nonlinear dispersion relationships for continuous systems enables the possibility of analyzing complex materials and nonlinearities. Finally, Chapter 8 concludes with a summary and describes several areas with promising opportunities for follow-on work.

CHAPTER II

ANALYSIS METHODS

2.1 Overview

This chapter documents the analytical methods and tools necessary for describing dispersion relations. An overview of periodic system geometry and Bloch wave solutions starts the discussion. The dispersion relation associated with Bloch waves and several of its important properties are presented next. The influence of nonlinearities on amplitude are described generally and illustrated with a simple and well-known example. The more general systems examined in later chapters are presented in a general way that allows nonlinearity to enter the governing equations. Then, two important wave-based perturbation analysis methods are introduced. The first is limited to situations with monochromatic frequency content. The second provides a more general means for analyzing nonlinear dispersion in the event of multiharmonic frequency response. Finally, a note on the presentation of nonlinear dispersion relations is given.

2.2 Analysis of dispersion in periodic systems

2.2.1 Bloch theorem

Bloch wave analysis, in the most general scenario, addresses wave propagation in domains of infinite extent which are generally composed of spatially repeating *unit cells* as depicted in Fig. 2.1 for a two-dimensional scenario. Unit cells are defined mathematically by the extent of the spatial period over which periodic geometry or coefficients repeat. Bloch theory was first introduced by Felix Bloch as a means for identifying wave functions to periodic electron potentials [4]. Since then, researchers have applied and extended the linear solution technique to multiple physical domains including electromagnetics (photonics, optics, and plasmonics) and elasticity (including acoustics and phononics). Literature concerning wave propagation in elastic media often refers to this type of problem as the *Floquet-Bloch* problem in honor of Floquet who independently investigated the same type of solution. However, recent literature concerning photonic and phononic systems (the focus of this research) typically favor the term Bloch wave and so that language is adopted herein.

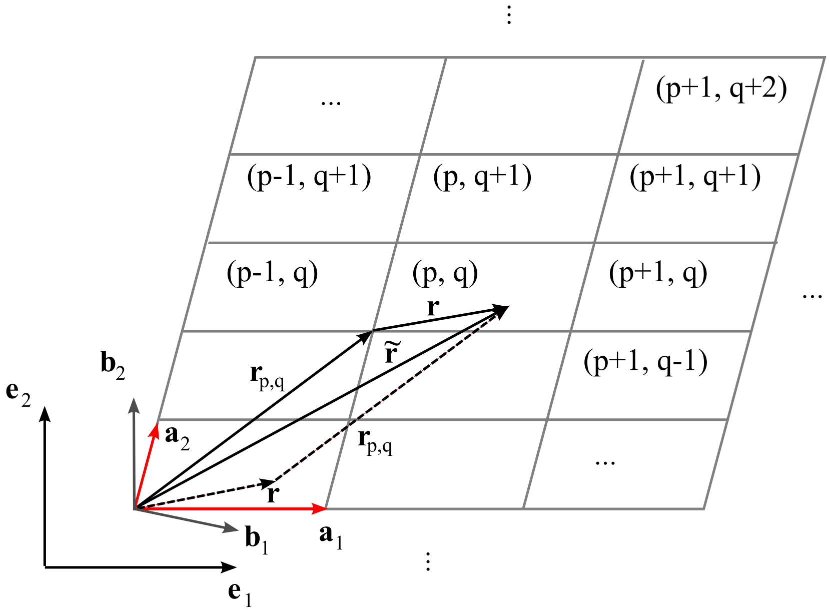

Figure 2.1: Generalized unit cell arrangement and notation for a 2D Bloch wave propagation scenario.

Figure 2.1 schematically depicts the geometry of a generalized periodic system in two dimensions. Individual unit cells are identified by by gray boundaries and referenced with indices p, q, and r (if a 3rd dimension is present). Unit cell boundaries are described using primitive lattice vectors $\mathbf{a}_i = d_i\mathbf{e}_i$, where d_i denotes the unit cell length in the ith dimension and $\mathbf{e}_i$ denote Cartesian coordinate system unit vectors. The definition of *reciprocal lattice vectors* $\mathbf{b}_i$ considerably simplifies analysis of Bloch wave propagation and their use in periodic system analysis is ubiquitous. These vectors are defined as [4]

$$\mathbf{b}_1 = \frac{\mathbf{a}_2 \times \mathbf{a}_3}{\mathbf{a}_1 \cdot \mathbf{a}_2 \times \mathbf{a}_3} \quad \text{and} \quad \mathbf{b}_2 = \frac{\mathbf{a}_3 \times \mathbf{a}_1}{\mathbf{a}_1 \cdot \mathbf{a}_2 \times \mathbf{a}_3}. \tag{2.1}$$

such that

$$\mathbf{a}_i \cdot \mathbf{b}_j = \delta_{ij}, \quad \delta_{ij} \equiv 1 \text{ if } i = j, \text{ and 0 otherwise.} \tag{2.2}$$

For rectangular unit cells, the reciprocal lattice vectors are simply $\mathbf{b}_i = (1/d_i)\mathbf{e}_\mathbf{i}$. The more general scenario commonly appears in hexagonal close-packed or body-centered cubic unit cells.

A state vector $\mathbf{u}(x, y, z, t) = \mathbf{u}(\tilde{\mathbf{r}}, t)$ describes field variables (e.g. displacement, pressure, etc.) at position $\tilde{\mathbf{r}} = x\mathbf{e}_1 + y\mathbf{e}_2 + z\mathbf{e}_3$ relative to an inertial coordinate system. The position vector is equivalently defined using a local coordinate system located at $\mathbf{r}$ such that

$$\tilde{\mathbf{r}} = \mathbf{r}_{p,q} + \mathbf{r}, \tag{2.3}$$

where the local position vector $\mathbf{r}$ describes position relative to the lower-left corner and the unit cell position vector $\mathbf{r}_{p,q} = p\mathbf{a}_1 + q\mathbf{a}_2 \ \forall \ (p,\ q) \in \mathbb{R}^2$.

The Bloch theorem postulates the existence of solutions in the form

$$\mathbf{u}(\tilde{\mathbf{r}}, t) = \boldsymbol{\psi}(\tilde{\mathbf{r}})e^{\mathrm{i}(\boldsymbol{\mu}\cdot\tilde{\mathbf{r}}-\omega t)} + c.c., \tag{2.4}$$

where $\boldsymbol{\mu} = \mu_1\mathbf{b}_1 + \mu_2\mathbf{b}_2$ denotes the *Bloch wave vector*, $\boldsymbol{\psi}(\mathbf{r})$ denotes the Bloch wave function, and *c.c.* denotes the complex conjugates of preceding terms. The Bloch wave function is spatially periodic such that $\boldsymbol{\psi}(\mathbf{r} + \mathbf{r}_{p,q}) = \boldsymbol{\psi}(\mathbf{r})$; thus, the Bloch relationship may be cast in the form

$$\mathbf{u}(\mathbf{r} + \mathbf{r}_{p,q}, t) = \boldsymbol{\psi}(\mathbf{r} + \mathbf{r}_{p,q})e^{\mathrm{i}(\boldsymbol{\mu}\cdot(\mathbf{r}+\mathbf{r}_{p,q})-\omega t)} + c.c. \tag{2.5}$$

$$\mathbf{u}(\mathbf{r} + \mathbf{r}_{p,q}, t) = \boldsymbol{\psi}(\mathbf{r})e^{\mathrm{i}\boldsymbol{\mu}\cdot\mathbf{r}_{p,q}}e^{\mathrm{i}(\boldsymbol{\mu}\cdot\mathbf{r}-\omega t)} + c.c.. \tag{2.6}$$

Comparing Eq. (2.6) to Eq. (2.4) with $\tilde{\mathbf{r}} \to \mathbf{r}$, we arrive at an alternative form of the Bloch theorem. Since Bloch wave propagation is time-harmonic with frequency ω by definition, the state vector $\mathbf{u}(\mathbf{r}, t)$ may be written with the aid of a *Bloch wave mode* $\boldsymbol{\phi}(\mathbf{r})$ such that $\mathbf{u}(\mathbf{r}, t) = \boldsymbol{\phi}(\mathbf{r}) \exp(-\mathrm{i}\omega t)$ and Eq. (2.6) reads

$$\mathbf{u}(\mathbf{r} + \mathbf{r}_{p,q}, t) = \boldsymbol{\phi}(\mathbf{r})e^{\mathrm{i}(\boldsymbol{\mu}\cdot\mathbf{r}_{p,q}-\omega t)} + c.c.. \tag{2.7}$$

Equation (2.7) states that response in any unit cell $(p,\ q)$ differs from the response in neighboring unit cells only by a phase change equal to $\boldsymbol{\mu} \cdot \mathbf{r}_{p,q}$. The latter form Eq. (2.7) considerably simplifies the analysis of discrete systems where the field vector $\mathbf{u}$ (and thus Bloch wave mode $\boldsymbol{\phi}$) is known only at discrete locations within each unit cell, as in the finite-element method or solid state physics [4, 11, 3, 36]. The former form Eq. (2.4) finds application in reflection and refraction analysis for periodic systems and is often associated with a solution technique known as the plane wave expansion [51, 52, 9]. This manuscript adopts the latter form Eq. (2.7) for its utility in conjunction with discretization schemes such as the finite-element and transfer matrix methods.

The governing equations[1] of the domain are responsible for coupling the oscillation frequency ω, Bloch wave vector $\boldsymbol{\mu}$, and either Bloch wave functions $\boldsymbol{\psi}(\boldsymbol{r})$ or Bloch wave modes $\boldsymbol{\phi}(\mathbf{r})$. Periodic system analysis is therefore typically defined as finding the nontrivial combinations of frequency, wave vector, and Bloch mode (or function) which solve the homogeneous governing equations. The elastodynamic systems considered herein require satisfaction of Newton's second law. After formulating the equations of motion, the problem reduces to a parametric eigenvalue problem which, ultimately, yields the dispersion relation $\omega = \omega(\boldsymbol{\mu})$ and the associated Bloch wave modes $\boldsymbol{\phi}(\mathbf{r}; \boldsymbol{\mu})$. The dispersion relationship governing a particular unit cell contains a wealth of information regarding the dynamic properties of both infinite and finite systems. These properties are the topic of Sec. 2.2.2. In closing this section, note that Bloch wave analysis *requires* linear system; however, by taking advantage of weak nonlinearity the analysis tools presented in the following section permit investigation of nonlinear system phenomena, which may enhance existing designs or suggest new device configurations.

2.2.2 Linear systems

The objectives of the following discussion are to introduce notation and describe relevant concepts for interpreting and assessing nonlinear dispersion as it pertains to periodic systems. For a more complete discussion on basic dispersive phenomena the reader is referred

---

[1] Partial differential equations in the case of continuous media, and difference equations in the case of discrete systems

to other comprehensive texts [4, 53, 54]. Dispersion describes a phenomena whereby the phase speed c of a propagating wave depends on frequency ω. The frequency and *material wave number*[2] k are related by the phase speed such that $\omega = ck$. The relationship between frequency and wavenumber, more generally described by $\omega(k)$, is termed the *dispersion relation*.

Periodic systems are dispersive by nature. *Bloch wave dispersion* refers to the *dispersion relation* $\omega(\mu)$ for linear systems. Figure 2.2 depicts a typical dispersion relation using a *dispersion diagram*. The original research contained in this manuscript makes liberal use of the dispersion diagram in presenting results because it graphically depicts a number of useful properties. Wave number is plotted along the abscissa, while the ordinate is reserved for frequency. The ranges of frequencies where propagating waves exist are termed *pass bands*. Evanescent Bloch wave solutions exist in regions with imaginary wave numbers; these frequency ranges are termed *stop bands* or *band gaps*.

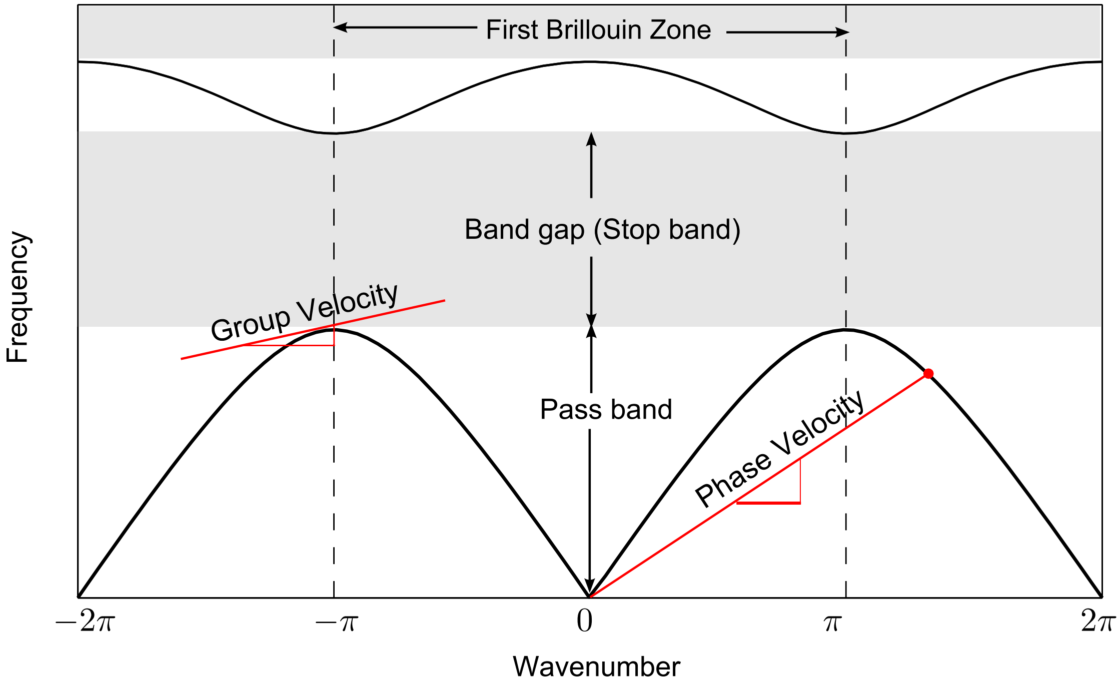

Figure 2.2: Schematic dispersion diagram illustrates multiple dispersion branches, band gaps, phase velocity, and group velocity.

---

[2] The deliberate use of k as a *material wave number* helps to distinguish it from the Bloch wave number μ

A unique feature of Bloch wave dispersion relationships is periodicity whereby $\omega(\mu) = \omega(\mu + 2\pi)$; this quality motivates the definition of a *first Brillouin zone* since periodic systems may be completely described by wave numbers or wave vectors within this region. The first Brillouin zone in one-dimensional systems is conventionally defined by the domain $\mu \in [-\pi, \pi]$ (as depicted); unit cells in higher dimensional space require more complex definitions. Moreover, as infinite domains do not distinguish "forward" from "backward" propagation the dispersion relationship also follows the symmetry relationship $\omega(-\mu) = \omega(\mu)$. These symmetries motivate the definition of an *irreducible Brillouin zone* which corresponds to $\mu \in [0, \pi]$ in Fig. 2.2.

Frequencies bounding pass and stop bands are particularly relevant for system design. These frequencies correspond to minima and maxima of each *dispersion branch* (black lines). Although unproven, these extrema appear at the edge of the first Brillouin zone in all but a few known cases [55]. Thus, in many cases (especially in two-dimensions where dispersion relations describe surfaces) the dispersion relation is evaluated only along the contour of the Brillouin zone.

Group velocity is an important concept in analyzing periodic structures because it describes the direction and speed of energy flow [56, 54, 57]. The general definition of group velocity $\mathbf{c}_g$ is obtained from the dispersion relation according to

$$\mathbf{c}_g \equiv \nabla_\mu \omega(\boldsymbol{\mu}) = \frac{\partial \omega}{\partial \mu_1}\mathbf{b}_1 + \frac{\partial \omega}{\partial \mu_2}\mathbf{b}_2 + \frac{\partial \omega}{\partial \mu_3}\mathbf{b}_3, \tag{2.8}$$

where $\mathbf{c}_g$ represents the group velocity in reciprocal space $\mathbf{b}_i$. In one dimension, group velocity is described simply by the slope of the dispersion curve as depicted in Fig. 2.2. Further inspection reveals zero group velocity at the edges of the Brillouin zone where band gaps begin. Group velocity finds particular utility in analyzing the response of a periodic structure to external excitation. Unlike phase velocity, group velocity is 2π-periodic in the wave vector space and also obeys the symmetry relation.

Generally, a Bloch wave travels with the group velocity $\mathbf{c}_g$. However, a Bloch wave can be expressed as a superposition of plane waves, each traveling at different phase speeds.

This Bloch analysis method is termed the *plane wave expansion method* or the *the method of space harmonics* [9, 11]. This method is not described in depth but it is mentioned for completeness. These space harmonic methods stem from Eq. (2.4) where the spatially periodic Bloch wave function $\boldsymbol{\psi}$ may be expressed using a Fourier series. Each of these individual space harmonics propagates and reflects on itself at each interface. Joannopoulos et al. refer to this phenomenon as coherent scattering [57]. The superposition of each space harmonic produces the overall Bloch wave described by $\boldsymbol{\phi}$. Application of Eq. (2.7) to discrete systems is a simple, exact, and effective approach for discrete systems; therefore this form of the Bloch theorem is preferred in the analyses to follow.

2.2.3 Nonlinear systems

Nonlinear dispersion analysis (NDA) is concerned with understanding the relationship between Bloch wave *amplitude* and dispersion in (usually weakly) nonlinear systems. The first appearance of NDA for weakly nonlinear one-dimensional systems demonstrated that a Lindstedt-Poincaré procedure applied in conjunction with the Bloch theorem could successfully identify frequency shifts in discrete chains [3]. Analytical expressions of the form

$$\omega(\mu; A) = \omega_0(\mu) + \varepsilon\omega_1(\mu; A) + O(\varepsilon^2) \tag{2.9}$$

were derived for both monoatomic and diatomic systems which identified the functional relationship between amplitude and frequency shifting. The expression for the monoatomic system was given (with some manipulation) as

$$\omega(\mu; A) = \sqrt{2 - 2\cos(\mu)} + \varepsilon\frac{3\Gamma A^2}{8}(2 - 2\cos(\mu))^{3/2} + O(\varepsilon^2) \tag{2.10}$$

where ε denotes a “small parameter”, Γ denotes a nonlinear stiffness coefficient, A is the Bloch wave amplitude, and μ is the Bloch wave number. A schematic of the system and the first-order corrected dispersion is presented in Fig. 2.3. This dispersion relation exhibits a very important feature: it is parametrized by the Bloch wave amplitude such that all of the properties germane to linear dispersion relations are now amplitude-tunable. For example, a the critical cutoff frequency for the linear monoatomic chain ($\Gamma = 0$) can be increased (tuned) with hardening springs ($\Gamma > 0$) or decreased with softening springs ($\Gamma < 0$).

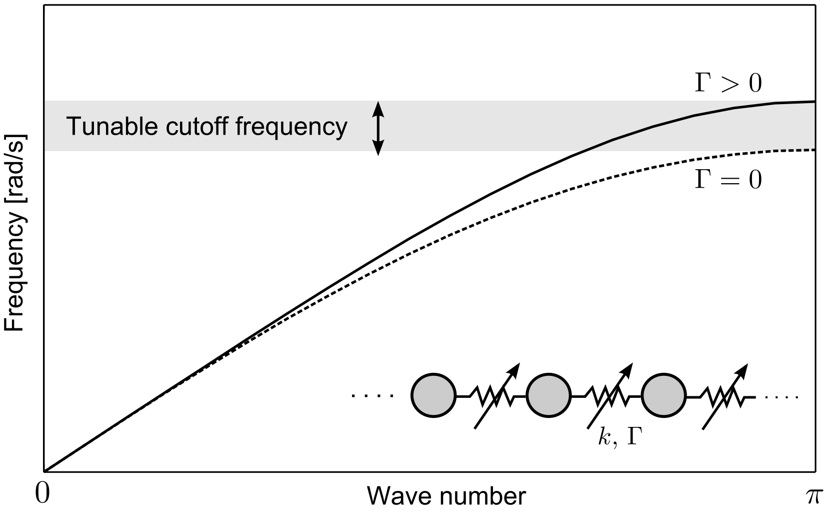

Figure 2.3: Dispersion relation for a hardening linear monoatomic chain with weakly nonlinear connecting springs as described in [3]

A related publication arrived at a similar conclusion using a similar perturbation analysis could identify amplitude-dependent wave numbers in both pass band and stop band regions, but could not be effectively implemented for complex systems [24]. In addition to tunable pass and stop bands, amplitude-dependent dispersion relations cause variation in group velocity and phase speed; two related concepts which find particular use in two-dimensional systems.

Significant strides have been made since the original appearance of NDA in literature. Many of these developments are cataloged in the dissertation by R. Narisetti [50], including the exact perturbation analysis of several discrete systems and the development of a similar harmonic balance approach for strongly nonlinear systems. The remainder of this document builds on his dissertation to analyze continuous systems, more general perturbation methods for analyzing nonlinear wave interactions, and identifying optimal system topologies.

2.3 Nonlinear equations of motion

The objectives of this section is to introduce and the general wave equation for elastodynamics, and to discuss the various simplified forms which are used in later chapters. Sources of nonlinearity are considered and discussed. When discretized, the nonlinear wave equation(s) reduces to a system of second-order differential equations describing motions at each node.

2.3.1 Governing equations for a unit cell

Elastodynamic wave propagation in nonlinear periodic systems is generally governed by a balance of linear momentum. The governing equation pertains to displacements belonging to the unit cell domain, denoted Ω, while Bloch boundary conditions discussed in 2.2.1 are applied to the domain boundary, denoted $\partial\Omega$. Many of the systems considered later derive from the elastic wave equation for isotropic solids. Equations of motion for those systems which are inherently discrete in nature, such as atomic systems, are derived and presented where necessary. The elastic wave equation for isotropic solids with negligible gravitational forces, in its most general form, is given by [58, 53] as

$$\nabla \cdot \boldsymbol{\sigma}(\mathbf{r}) = \rho_V \frac{\partial^2 \mathbf{u}(\mathbf{r})}{\partial t^2}, \quad \forall \mathbf{r} \in \Omega, \tag{2.11}$$

where ρ_V is the volume density, $\boldsymbol{\sigma}$ denotes the stress tensor, and $\mathbf{u} = [u(\mathbf{r}), v(\mathbf{r}), w(\mathbf{r})]^T$ denotes displacement from equilibrium at position $\mathbf{r} = x\mathbf{e}_1 + y\mathbf{e}_2 + z\mathbf{e}_3$ in the standard Cartesian basis. Equation (2.11), while general, is often more complex than necessary for assessing wave propagation in many geometries. Chapter 7 discusses a method for leveraging pre-existing finite-element software for directly attacking nonlinear implementations of Eq. (2.11).

The two-dimensional reduction of (2.11) explicitly considered in this manuscript are the plane stress elasticity equations. Plane stress describes a limiting conditions of 3D elasticity equations where a third dimension is considerably smaller than the other two.

The general form of these equations is obtained by assuming $\partial/\partial z = 0$ so that Eq. (2.11) reduces to

$$\frac{\partial \sigma_{xx}}{\partial x} + \frac{\partial \sigma_{xy}}{\partial y} = \rho_V \frac{\partial^2 u}{\partial t^2}, \quad \forall (x, y) \in \Omega, \tag{2.12a}$$

$$\frac{\partial \sigma_{xy}}{\partial x} + \frac{\partial \sigma_{yy}}{\partial y} = \rho_V \frac{\partial^2 v}{\partial t^2}, \quad \forall (x, y) \in \Omega, \tag{2.12b}$$

where σ_{ij} components relate to displacement components through a (generally) nonlinear constitutive law. Chapter 6 analyzes periodic systems with domains governed by Eqs. (2.12) using topology design and optimization methods.

One-dimensional bars and rods result from a further approximation of Eqs. (2.12) whereby displacements are constrained to a single direction (say $\mathbf{e}_1$) and spatial variation along the $\mathbf{e}_2$ is negligible. These approximations are valid for thin rods when characteristic wavelengths are much larger than the considered cross-sectional area. With these assumptions, Eq. (2.12) reduces to

$$\frac{\partial \sigma_{xx}}{\partial x} = \rho_V \frac{\partial^2 u(x,t)}{\partial t^2}, \quad \forall x \in \Omega, \tag{2.13}$$

where σ_{xx} may contain nonlinear terms due to stress-strain constitutive laws. Equation (2.13) is used in Chapter 5 and Chapter 6 for analyzing one-dimensional propagation, as well as in Chapter 7 as a validation case. Furthermore, a finite-element approximation of Eq. (2.13) reduces exactly to the open system of difference equations presented in Chapter 3. Next, we consider the mechanisms which introduce nonlinearity into these governing equations.

2.3.2 Sources of nonlinearity

Equations (2.11) – (2.13) are are completely general in the sense that they provide opportunity for nonlinear terms to enter through either a nonlinear constitutive law or nonlinear strains, for example. Figure 2.4 schematically depicts several typical nonlinearities considered herein. The types of nonlinearity considered generally take the form of displacement- or strain-dependent stiffness terms.

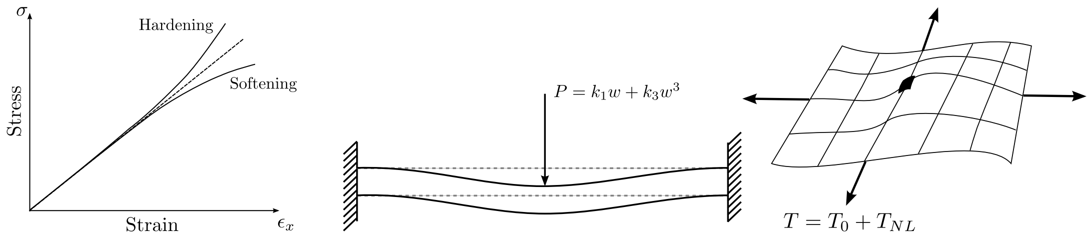

(a) Constitutive nonlinearity

(b) Geometric nonlinearity

(c) Geometric nonlinearity

Figure 2.4: Nonlinearities enter equations of motion through various avenues such as nonlinear constitutive laws or strain-energy relationships (a), or nonlinear geometry such as stretching in strings, membranes, beams, plates, and shells (b,c).

General hardening and softening nonlinearities may arise in a stress-strain constitutive relation when higher order terms are kept in a strain-energy potential. Linear stress-strain laws result when only quadratic strain-energy potential terms are retained; in contrast, retention of cubic and quartic strain-energy terms produces nonlinear elastic constitutive relations. Chapter 5, Chapter 6, and Chapter 7 discuss the influence of cubic stress-strain relations (resulting from quartic potential terms) on dispersion shifts. Chapter 3 similarly discusses nonlinear force-displacement relations encountered in lumped-parameter systems and atomic lattices.

Constitutive nonlinear nonlinearities enter Eqs. (2.13) or (2.12) directly through specification of a nonlinear stress-strain relation. In contrast, geometric nonlinearities depicted in Fig. 2.4b and Fig. 2.4c often arise in structural models such as the strings, membranes, beams, plates, and shells where various small-amplitude approximations are typically made in order to neglect such terms [59]. String and membrane structural models are considered in Ch. 4 and Ch. 7, respectively. In these models, an applied pretension load typically produces restoring forces; however, displacements dynamically increase the pre-tension and produce cubically nonlinear restoring forces that are a function of the specific geometry.

More specific nonlinearities such as Lennard-Jones potentials, pre-stressed Hertzian contact, and higher-order polynomial constitutive laws can be directly attacked by their specification in specialized finite-element software. Chapter 7 discusses a method for implementing the perturbation method in such cases.

2.3.3 Discretized and weakly nonlinear equations of motion

The equations of motion presented in the previous section are often too complex to solve when nonlinear terms are present. Even linear formulations of Eqs. (2.11) – (2.12) lead to difficulty where complex geometry is present. The standard method for solving such problems is the finite element method. A comprehensive discussion of finite-element discretization is well beyond the scope of this dissertation and the reader is referred to specific texts for complete details [60, 61]. In addition to local continuum-based equations of elasticity, many phononic systems of interest in vibration and thermal transport are inherently discrete in nature such as crystal lattice structures analyzed in solid-state physics.

In linear systems, one discretized unit cell and the associated internal forces from neighbor unit cells is sufficient for analyzing Bloch wave propagation. However, to obtain the equations of motion governing wave propagation through a single unit cell of an infinite nonlinear system it is necessary to analyze a unit cell and partial neighbors so that nonlinear forces on the unit cell boundary $\partial\Omega$ are left unexposed in a free body diagram [50]. Consider the slice of a continuous periodic 1D, 2D, or 3D elastic system governed shown

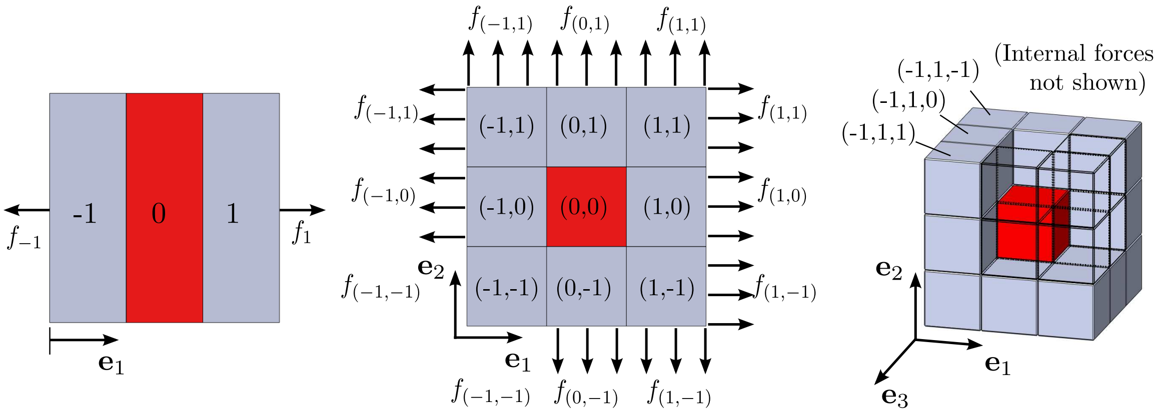

Figure 2.5: Central unit cell (colored red) surrounded by neighboring unit cells for 1D, 2D, and 3D periodic systems

in Fig. 2.5. The *global system* consists of a central unit cell (colored red) surrounded by identical neighboring unit cells and the associated internal forces $f_{(p,q,r)}$ on neighboring unit cells. All neighbor unit cells are included to avoid the appearance of internal forces for the central unit cell.

Each unit cell can be indexed as convenient; here the central unit cell is indexed as zero. Suppose that the continuous domain has been discretized so that $\mathbf{q}_i$ denotes the degrees of freedom (DOFs) for the ith node. Furthermore, let $\mathbf{u}_{(p,q,r)} = [\mathbf{q}_1, \mathbf{q}_2, \ldots \mathbf{q}_n]^{\mathrm{T}}$ denote the collection of DOFs within the unit cell indexed by p, q, and r (only p for a 1D system, or p and q for a 2D system). Then, the total collection of generalized coordinates for the discretized system is given by

$$\mathbf{u} = [\mathbf{u}_{(-1,-1,-1)}, \mathbf{u}_{(-1,-1,0)}, \ldots, \mathbf{u}_{(0,0,0)}, \ldots, \mathbf{u}_{(0,1,1)}, \mathbf{u}_{(1,1,1)}]^{\mathrm{T}}. \tag{2.14}$$

In order to apply the Bloch theorem, the meshes for each unit cell must be identical. Then, the sub-vectors $\mathbf{u}_{(p,q,r)}$ are the same length. Given this ordering scheme, the discretized equations of motion for the entire system are written in canonical form as

$$\mathbf{M}\ddot{\mathbf{u}} + \mathbf{K}\mathbf{u} + \mathbf{f}^{NL}(\mathbf{u}) = \mathbf{f}^{ext} + \mathbf{f}^{int}, \tag{2.15}$$

where $\mathbf{M}$ and $\mathbf{K}$ denote the mass and stiffness matrices for the central unit cell and its neighbors as shown in Fig. 2.5, $\mathbf{f}^{NL}(\mathbf{u})$ denotes a nonlinear force vector, $\mathbf{f}^{ext}$ denotes a vector of externally applied forces, and $\mathbf{f}^{int}$ denotes the internal forces acting on the neighbor unit cells. The mass and stiffness matrices arise from the linear and positive definite differential operators in the associated wave equation. The nonlinear force vector $\mathbf{f}^{NL}$ accounts for all other terms resulting from the discretization of nonlinear operators.

Nonlinear terms considered in Ch. 5–6 all arise from nonlinear force-deflection type relationships and so $\mathbf{f}^{NL}(\mathbf{u})$ depends only on $\mathbf{u}$. The following methods are, however, applicable to more complex nonlinear expressions which may take the form $\mathbf{f}^{NL}(\mathbf{u}, \dot{\mathbf{u}}, \ddot{\mathbf{u}})$ [62]. Moreover, only systems which are weakly nonlinear are amenable to the perturbation analyses presented herein. Thus, the nonlinear force vector is typically defined (or redefined) as $\mathbf{f}^{NL}(\mathbf{u}) \rightarrow \varepsilon\mathbf{f}^{NL}(\mathbf{u})$ in order to introduce a small perturbation parameter $|\varepsilon| \ll 1$ which controls where terms appear in an asymptotic perturbation expansion. Furthermore, free wave propagation is considered so that $\mathbf{f}^{ext} = \mathbf{0}$; then, Eq. (2.15) becomes

$$\mathbf{M}\ddot{\mathbf{u}} + \mathbf{K}\mathbf{u} + \varepsilon\mathbf{f}^{NL}(\mathbf{u}) = \mathbf{f}^{int}. \tag{2.16}$$

The specific origin of ε varies from case to case. It is generally possible to redefine some nonlinear coefficient (e.g. Γ) which is known to be small such that $\Gamma = \varepsilon\hat{\Gamma}$. In other situations, a small parameter may arise out of dimensional analysis of the governing equations.

The dynamic equations Eq. (2.16) resulting from a discretization of the central unit cell and its neighbors constitute an *open set* of nonlinear difference equations whose solution is dependent upon all $\mathbf{u}_{(p,q,r)}$ surrounding the central unit cell. Assuming a lumped mass matrix, the open set of difference equations for the *central unit cell only* are given by

$$\text{1D System:} \quad \mathbf{M}_0\ddot{\mathbf{u}}_0 + \sum_{p=-1}^{1} \mathbf{K}_p\mathbf{u}_p + \varepsilon\mathbf{f}_0^{NL} = \mathbf{0} \tag{2.17}$$

$$\text{2D System:} \quad \mathbf{M}_0\ddot{\mathbf{u}}_{(0,0)} + \sum_{p=-1}^{1}\sum_{q=-1}^{1} \mathbf{K}_{(p,q)}\mathbf{u}_{(p,q)} + \varepsilon\mathbf{f}_{(0,0)}^{NL} = \mathbf{0} \tag{2.18}$$

$$\text{3D System:} \quad \mathbf{M}_0\ddot{\mathbf{u}}_{(0,0,0)} + \sum_{p=-1}^{1}\sum_{q=-1}^{1}\sum_{r=-1}^{1} \mathbf{K}_{(p,q,r)}\mathbf{u}_{(p,q,r)} + \varepsilon\mathbf{f}_{(0,0,0)}^{NL} = \mathbf{0}, \tag{2.19}$$

where $\mathbf{M}_0$ denotes a partition of total mass matrix corresponding to the central unit cell, $\mathbf{K}_{(p,q,r)}$ denote partitions of $\mathbf{K}$ responsible for linear restoring forces on the central unit cell as a result of $\mathbf{u}_{(p,q,r)}$, $\mathbf{f}_{(p,q,r)}^{NL}$ denotes the partition of the nonlinear force vector, and it has been noted that internal forces on the central unit cell are identically zero[3]. A few notation simplifications permit the open set of difference equations (for a general 3D system) to be rewritten as

$$\mathbf{M}\ddot{\mathbf{u}} + \sum_{(p,q,r)} \mathbf{K}_{(p,q,r)}\mathbf{u}_{(p,q,r)} + \varepsilon\mathbf{f}^{NL}(\mathbf{u}_{(p,q,r)}) = \mathbf{0}, \tag{2.20}$$

---

[3] More specifically, the internal forces on the central unit cell are contained in the stiffness matrix such that $\mathbf{f}_0^{int} = -\mathbf{K}_{(p,q,r)}\mathbf{u}_{(p,q,r)}$.

where the simplified notation $\mathbf{f}^{NL}_{(0,0,0)} = \mathbf{f}^{NL}$ and $\sum_{p=-1}^{1}\sum_{q=-1}^{1}\sum_{r=-1}^{1} = \sum_{(p,q,r)}$ has been employed and zero subscripts have been dropped from $\mathbf{M}_0$ and $\mathbf{u}_0$. This form facilitates perturbation analysis and marks the point where the Lindstedt-Poincaré and multiple scales analysis methods presented next diverge.

2.4 Wave-based perturbation analysis

2.4.1 Lindstedt-Poincaré

Lindstedt-Poincaré perturbation analysis provides opportunity for amplitude-frequency interactions in nonlinear systems. The wave-based perturbation analysis as presented next was developed primarily by R. Narisetti et. al [3, 63] with some developments contributed by the author. This method is convenient to apply for monochromatic free wave propagation and has been validated extensively with numerics and by preliminary experimental results (Ch. 4). Full details of the perturbation approach to be presented next, as applied to discrete systems, are given in [50].

The small parameter ε appearing in Eq. (2.20) facilitates an asymptotic solution approach. We introduce a dimensionless time $\tau = \omega t$ and standard expansions

$$\begin{aligned} \omega &= \omega_0 + \varepsilon\omega_1 + O(\varepsilon^2) \\ \mathbf{u}_{(p,q,r)} &= \mathbf{u}^{(0)}_{(p,q,r)} + \varepsilon\mathbf{u}^{(1)}_{(p,q,r)} + O(\varepsilon^2). \end{aligned} \tag{2.21}$$

These expansions, when substituted into Eq. (2.20), yield ordered equations:

$$O(\varepsilon^0): \quad \omega_0^2\mathbf{M}\frac{\partial^2\mathbf{u}^{(0)}}{\partial\tau^2} + \sum_{(p,q,r)}\mathbf{K}_{(p,q,r)}\mathbf{u}^{(0)}_{(p,q,r)} = \mathbf{0} \tag{2.22}$$

$$O(\varepsilon^1): \quad \omega_0^2\mathbf{M}\frac{\partial^2\mathbf{u}^{(1)}}{\partial\tau^2} + \sum_{(p,q,r)}\mathbf{K}_{(p,q,r)}\mathbf{u}^{(1)}_{(p,q,r)} = -2\omega_0\omega_1\mathbf{M}\frac{\partial^2\mathbf{u}^{(0)}}{\partial\tau^2} - \mathbf{f}^{NL}\left(\mathbf{u}^{(0)}\right). \tag{2.23}$$

Since the discretized system at $O(\varepsilon^0)$ is periodic and linear, Bloch's theorem may be applied to Eq. (2.22) to produce a set of equations describing an infinite [linear] system. The Bloch wave takes the form of Eq. (2.7)

$$\mathbf{u}^{(0)}_{(p,q,r)} = \frac{A}{2}\boldsymbol{\phi}e^{\mathrm{i}(\boldsymbol{\mu}\cdot\mathbf{r}_{p,q,r}-\tau)} + c.c., \tag{2.24}$$

with $\boldsymbol{\phi}$ the Bloch mode[4] and A denoting the amplitude. Equation (2.22) reduces to

$$\omega_0^2 \mathbf{M} \frac{\partial^2 \mathbf{u}^{(0)}}{\partial \tau^2} + \mathbf{K}(\boldsymbol{\mu})\mathbf{u}^{(0)} = \mathbf{0}, \tag{2.25}$$

where $\mathbf{u}_{(0,0,0)} = \mathbf{u}$ are the DOFs in the central unit cell and the *wavenumber-reduced* stiffness matrix $\mathbf{K}(\boldsymbol{\mu})$ is

$$\mathbf{K}(\boldsymbol{\mu}) = \sum_{(p,q,r)} \mathbf{K}_{(p,q,r)} e^{\mathrm{i}(p\mu_1 + q\mu_2 + r\mu_3)}. \tag{2.26}$$

Equation (2.25) combined with Eq. (2.26) yields a standard eigenvalue problem for eigenfrequencies $\omega_j^{(0)}(\boldsymbol{\mu})$ and Bloch wave modes $\boldsymbol{\phi}_j(\boldsymbol{\mu})$, parametrized by the dimensionless Bloch wave vector

$$(\mathbf{K}(\boldsymbol{\mu}) - \omega_0^2 \mathbf{M})\boldsymbol{\phi}_j = \mathbf{0}. \tag{2.27}$$

The dispersion relation for the continuous system is approximated by $\omega_{0,j}(\boldsymbol{\mu})$, where the jth eigenvalue corresponds to the jth dispersion branch (or surface).

Secular terms identified in the $O(\varepsilon^1)$ Eq. (2.23) lead to a frequency correction to the eigenfrequency $\omega_j^{(0)}$. Equation (2.23) has the same linear kernel as Eq. (2.22), and thus the the same wave modes. Introduce the modal coordinates $\mathbf{z}^{(0)}(t)$ and $\mathbf{z}^{(1)}(t)$ according to

$$\mathbf{u}^{(0)} = \mathbf{\Phi}\mathbf{z}^{(0)}(t) \quad \text{and} \quad \mathbf{u}^{(1)} = \mathbf{\Phi}\mathbf{z}^{(1)}(t) \tag{2.28}$$

where $\mathbf{\Phi} = [\boldsymbol{\phi}_1, \boldsymbol{\phi}_2, \ldots, \boldsymbol{\phi}_N]$ is the square modal matrix and N denotes the number of DOFs per unit cell. Substituting Eq. (2.28) into Eq. (2.23) and subsequently pre-multiplying by $\mathbf{\Phi}^H$ yields

$$\omega_0^2 \mathbf{\Phi}^H \mathbf{M} \mathbf{\Phi} \frac{\partial^2 \mathbf{z}^{(1)}}{\partial \tau^2} + \mathbf{\Phi}^H \mathbf{K}(\boldsymbol{\mu}) \mathbf{\Phi} \mathbf{z}^{(1)} = -2\omega_0 \omega_1 \mathbf{\Phi}^H \mathbf{M} \mathbf{\Phi} \frac{\partial^2 \mathbf{z}^{(0)}}{\partial \tau^2} - \mathbf{\Phi}^H \mathbf{f}^{NL}\left(\mathbf{u}^{(0)}\right), \tag{2.29}$$

where again we note that $\mathbf{K}(\boldsymbol{\mu})$ denotes the reduced stiffness matrix as before. Having been obtained from a general eigenvalue problem, the modal matrix $\mathbf{\Phi}$ is orthogonal with respect to the mass and stiffness matrices such that

$$\boldsymbol{\phi}_i^H \mathbf{M} \boldsymbol{\phi}_j = m_{ij}\delta_{ij} \quad \boldsymbol{\phi}_j^H \mathbf{K}(\boldsymbol{\mu}) \boldsymbol{\phi}_j = k_{ij}(\boldsymbol{\mu})\delta_{ij} \tag{2.30}$$

---

[4] Normalized in some consistent manner

where m_{ij} and k_{ij} are modal mass and stiffness, and δ_{ij} denotes the Kronecker delta such that $\delta_{ij} = 1$ if $i = j$ and $\delta_{ij} = 0$ otherwise. It is important to note that Eq (2.29) can be interpreted as a system of real or complex equations. Complex equations are generally more amenable to solution via the Bloch theorem; however nonlinear terms in $\mathbf{f}^{NL}$ *must* be derived from purely real quantities. Equation (2.29) denotes a system of decoupled scalar equations. In particular, the jth equation takes the form

$$\omega_0^2 m_{jj} \frac{\partial^2 z_j^{(1)}}{\partial \tau^2} + k_{jj}(\boldsymbol{\mu}) z_j^{(1)} = \omega_0 \omega_1 A m_{jj} e^{-\mathrm{i}\tau} - \boldsymbol{\phi}_j^H \mathbf{f}^{NL}\left(\mathbf{u}^{(0)}\right) + c.c. \tag{2.31}$$

where $z_j^{(0)} = (A_j/2)\exp(-i\tau) + c.c.$ for modal amplitude A_j and repeated indices do not imply summation. The eigenfrequency is again $\omega_{0,j} = \sqrt{k_{jj}(\boldsymbol{\mu})/m_{jj}}$ and terms which appear on the R.H.S. of Eq. (2.31) with $\exp(-\mathrm{i}\omega_0 t) = \exp(-\mathrm{i}\tau)$ temporal-dependence produce resonant, and therefore secular, terms. Secular contributions from $\mathbf{f}^{NL}$ are identified by expanding the nonlinear vector $\mathbf{f}^{NL}(\mathbf{u}^{(0)})$ from Eq. (2.23) in a Fourier series

$$\mathbf{f}^{NL}\left(\mathbf{u}^{(0)}(\tau)\right) = \sum_{n=-\infty}^{+\infty} \mathbf{c}_n e^{-\mathrm{i}n\tau}. \tag{2.32}$$

Solutions which retain the coefficients $\mathbf{c}_1$ and $\mathbf{c}_{-1}$ (complex conjugates of one another) result in secular expansions due to resonance with the $O(\varepsilon^0)$ system of equations. Furthermore, any $\mathbf{c}_0$ terms are also secular because they require solutions $z_j \propto \tau^2$; this is not encountered with cubic nonlinearities. Equation (2.31) combined with Eq. (2.32) yields

$$\left(-\omega_0^2 m_{jj} + k_{jj}(\boldsymbol{\mu})\right) z_j^{(1)} = \left(\omega_0 \omega_1 A_j m_{jj} - \mathbf{c}_1\right) e^{-\mathrm{i}\tau} + \mathrm{O.H.T} + c.c. \tag{2.33}$$

where O.H.T. denotes other harmonic terms with $\exp(\mathrm{i}2\tau)$ and higher frequency association and $c.c.$ denotes the complex conjugate of the preceeding terms. The frequency expansion Eq. (2.21) for ω provides a degree of freedom in ω_1 which can be used to remove the secular term in Eq. (2.33). Specifically, for the jth scalar equation, we require the quantity in parenthesis to vanish identically

$$\omega_0 \omega_1 A_j m_{jj} - \mathbf{c}_1 = 0. \tag{2.34}$$

The $\omega_{1,j}$ which satisfies Eq. (2.34) yields a frequency correction for the jth dispersion branch (or surface) given by

$$\omega_{1,j}(\boldsymbol{\mu}) = \frac{\boldsymbol{\phi}_j^{\mathrm{H}} \mathbf{c}_1}{\omega_{0,j} A_j m_{jj}}. \tag{2.35}$$

Note that Eq. (2.35) can be expressed alternatively using the modal stiffness through the relationship $\omega_{0,j}^2 = k_{jj}/m_{jj}$. Multiply Eq. (2.35) by $\left(\omega_{0,j}/\omega_{0,j}\right)$ and recognize the modal stiffness $k_{jj} = \omega_0^2 m_{jj}$ in the denomonator; the result is

$$\omega_{1,j}(\boldsymbol{\mu}) = \frac{\omega_{0,j} \boldsymbol{\phi}_j^{\mathrm{H}} \mathbf{c}_1}{A_j k_{jj}}. \tag{2.36}$$

The updated dispersion relation is then given as

$$\omega_j(\boldsymbol{\mu}) = \omega_{0,j}(\boldsymbol{\mu}) + \frac{\varepsilon \omega_{0,j} \boldsymbol{\phi}_j^{\mathrm{H}} \mathbf{c}_1}{A_j k_{jj}} + O(\varepsilon^2), \tag{2.37}$$

which may be used to identify amplitude-dependent dispersion shifting. This form may be further simplified by factoring out $\omega_{0,j}$ from each term

$$\omega_j(\boldsymbol{\mu}) = \omega_{0,j}(\boldsymbol{\mu}) \left(1 + \varepsilon \frac{\boldsymbol{\phi}_j^{\mathrm{H}} \mathbf{c}_1}{A_j k_{jj}} \right) + O(\varepsilon^2), \tag{2.38}$$

which reveals a dimensionless frequency correction in terms of the ratio of the nonlinear force component described by $\boldsymbol{\phi}_j^{\mathrm{H}} \mathbf{c}_1$ to the linear force $A_j k_{jj}$.

2.4.2 Method of multiple scales

The method of multiple scales refers to a particular type of perturbation solution method which allows variables – usually amplitude and phase – to evolve on multiple time scales [64, 27, 65]. Therefore, like Lindstedt-Poincaré perturbation, the method of multiple scales provides for amplitude-frequency interaction that avoids secularity in perturbation solutions. The method of multiple scales, however, is more general than Lindstedt-Poincaré. Lindstedt-Poincaré perturbation specifies solutions with constant amplitude, and phases which are linearly proportional to time (i.e. constant frequency). The method of multiple scales, in contrast, does not require that the specific phase relationship be known and amplitude may not necessarily be constant. These are particularly desirable traits for dispersion analysis methods in nonlinear systems where multiple waves (frequencies) may be present in the lowest-order $O(\varepsilon^0)$ solution. Chapter 3 specifically employs this new analysis method for deriving dispersion shifts due to wave interactions.

The multiple scales analysis presented considers wave propagation in a unit cell where the governing equations have been discretized into the form of Eq. (2.20), repeated here

$$\mathbf{M}\ddot{\mathbf{u}} + \sum_{(p,q,r)} \mathbf{K}_{(p,q,r)}\mathbf{u}_{(p,q,r)} + \varepsilon \mathbf{f}^{NL}(\mathbf{u}_{(p,q,r)}) = \mathbf{0}. \tag{2.39}$$

The general postulation that variables evolve on multiple timescales is formally written as

$$\mathbf{u} = \mathbf{u}(t) = \mathbf{u}(T_0(t), T_1(t), ...T_n(t)) \quad \forall\, n \geq 0 \in \mathbb{Z}. \tag{2.40}$$

Individual timescales denoted by T_n are defined as $T_n = \varepsilon^n t$. For small ε that are valid in perturbation expansions (e.g. $\varepsilon = 0.01$), events occurring only on timescales T_1 are sufficient for describing long time-evolution. As an example, 1 s on a slow timescale T_1 with $\varepsilon = 0.01$ corresponds to 100 s on "fast" time $t = T_0$.

The derivatives in Eq. (2.20) transform accordingly. Assuming that only timescales up to T_1 are relevant, a first total derivative $d()/dt$ is expressed using the chain rule as

$$\frac{d(\,)}{dt} = \frac{dT_0}{dt}\frac{d(\,)}{dT_0} + \frac{dT_1}{dt}\frac{d(\,)}{dT_1} = D_0(\,) + \varepsilon D_1(\,), \tag{2.41}$$

where the specific timescale derivative operator notation $D_n = d(\,)/dT_n$ has been introduced. The second time derivative follows accordingly as

$$\begin{aligned} \frac{d}{dt}\left(\frac{d(\,)}{dt}\right) &= (D_0 + \varepsilon D_1)(D_0 + \varepsilon D_1) \\ &= D_0^2 + 2\varepsilon D_0 D_1 + \varepsilon^2 D_1^2, \end{aligned} \tag{2.42}$$

and D_n^p denotes the pth derivative with respect to time scale T_n. Note that in Eqs. (2.41) and (2.42) the equality does not strictly hold true in general because of the assumption that only timescales T_0 and T_1 are relevant. Using Eq. (2.42) with (2.20) produces

$$\mathbf{M}(D_0^2 + 2\varepsilon D_0 D_1 + \varepsilon^2 D_1^2)(\mathbf{u}) + \sum_{(p,q,r)} \mathbf{K}_{(p,q,r)}\mathbf{u}_{(p,q,r)} + \varepsilon \mathbf{f}^{NL} = \mathbf{0} \tag{2.43}$$

where the external force vector is ignored in anticipation of free wave propagation solutions.

Next, introduce a standard asymptotic expansion for $\mathbf{u}_{(p,q,r)}$ that allows the separation of individual solutions at each order of ε

$$\begin{aligned}\mathbf{u}_{(p,q,r)}(T_0, T_1) &= \mathbf{u}^{(0)}_{(p,q,r)}(T_0, T_1) + \varepsilon\mathbf{u}^{(1)}_{(p,q,r)}(T_0, T_1) + O(\varepsilon^2) \\ &= \sum_i \varepsilon^i \mathbf{u}^{(i)}_{(p,q,r)}(T_0, T_1).\end{aligned} \tag{2.44}$$

It is only necessary retain terms up to $O(\varepsilon)$ to solve for a first perturbation correction term at $\mathbf{u}^{(0)}_{(p,q,r)}$. Substitution of Eq. (2.44) into (2.43) gives

$$\mathbf{M}(D_0^2 + 2\varepsilon D_0 D_1 + \varepsilon^2 D_1^2)(\mathbf{u}^{(0)} + \varepsilon\mathbf{u}^{(1)}) + \sum_{(p,q,r)} \mathbf{K}_{(p,q,r)}(\mathbf{u}^{(0)}_{(p,q,r)} + \varepsilon\mathbf{u}^{(1)}_{(p,q,r)}) + \varepsilon\mathbf{f}^{NL} = \mathbf{0}. \tag{2.45}$$

After some rearranging, this equation becomes

$$\begin{aligned}D_0^2\mathbf{M}\mathbf{u}^{(0)} + \sum_{(p,q,r)} \mathbf{K}_{(p,q,r)}\mathbf{u}^{(0)}_{(p,q,r)} + \varepsilon\Big(D_0^2\mathbf{M}\mathbf{u}^{(1)} + 2D_0D_1\mathbf{M}\mathbf{u}^{(0)} \\ + \sum_{(p,q,r)} \mathbf{K}_{(p,q,r)}\mathbf{u}^{(0)}_{(p,q,r)} + \mathbf{f}^{NL}\Big) = \mathbf{0},\end{aligned} \tag{2.46}$$

where terms $O(\varepsilon^2)$ are neglected and the strict equality is no longer true. As ε is arbitrary, the coefficient multiplying each order of ε must vanish individually which produces the ordered system of equations

$$O(\varepsilon^0): \quad D_0^2\mathbf{M}\mathbf{u}^{(0)} + \sum_{(p,q,r)} \mathbf{K}_{(p,q,r)}\mathbf{u}^{(0)}_{(p,q,r)} = \mathbf{0} \tag{2.47}$$

$$O(\varepsilon^1): \quad D_0^2\mathbf{M}\mathbf{u}^{(1)} + \sum_{(p,q,r)} \mathbf{K}_{(p,q,r)}\mathbf{u}^{(1)}_{(p,q,r)} = -2D_0D_1\mathbf{M}\mathbf{u}^{(0)} - \mathbf{f}^{NL}\left(\mathbf{u}^{(0)}_{(p,q,r)}\right). \tag{2.48}$$

Hence, the nonlinear system of open difference equations reduces to a cascading set of linear problems. The ordered equations reduce further when the specific form of the Bloch wave is specified. Equation (2.47) admits a Bloch wave solution in the same form as Eq. (2.24). Moreover, a superposition of Bloch wave solutions is also a solution and may be used to assess nonlinear wave interactions

$$\mathbf{u}^{(0)}_{(p,q,r)} = \sum_i \frac{A_i(T_1)}{2}\boldsymbol{\phi}_i e^{\mathrm{i}(\boldsymbol{\mu}_i\cdot\mathbf{r}_{p,q,r} - \omega_{0,i}T_0)} + c.c., \tag{2.49}$$

where individual Bloch wave solutions $\mathbf{u}_i^{(0)}$ have wave mode $\boldsymbol{\phi}_i$, frequency $\omega_{0,i}$, and slowly varying complex amplitude $A_i(T_1)$.

Substituting Eq. (2.49) into the R.H.S of the $O(\varepsilon^1)$ Eq. (2.48) and evaluating the partial derivatives D_0 and D_1 yields

$$D_0^2\mathbf{M}\mathbf{u}^{(1)} + \mathbf{K}(\boldsymbol{\mu})\mathbf{u}^{(1)} = \mathrm{i}\mathbf{M}\sum_i \omega_{0,i}A_i'\boldsymbol{\phi}_i e^{-\mathrm{i}\omega_{0,i}T_0} - \mathbf{f}^{NL}\left(\mathbf{u}_{(p,q,r)}^{(0)}\right) + c.c., \tag{2.50}$$

where again $\mathbf{K}(\boldsymbol{\mu}_i)$ denotes the wavenumber-reduced stiffness matrix evaluated for the $\boldsymbol{\mu}_i$th wave vector and a prime denotes differentiation with respect to the argument. The R.H.S. of Eq. (2.50) expands with the introduction of a polar form for amplitudes $A_i(T_1)$ such that

$$A_i(T_1) = \alpha_i(T_1)e^{-\mathrm{i}\beta_i(T_1)}. \tag{2.51}$$

The amplitudes $\alpha_i(T_1) \in \mathbb{R}$ and phases $\beta_i(T_1) \in \mathbb{R}$ vary slowly with T_1 such that they are constant in the T_0 time scale. The R.H.S. of Eq. (2.50) evaluates to

$$(\dots) = \mathrm{i}\mathbf{M}\sum_i \omega_{0,i}\left(\alpha_i' - \mathrm{i}\alpha_i\beta_i'\right)\boldsymbol{\phi}_i e^{-\mathrm{i}\left(\omega_{0,i}T_0+\beta_i(T_1)\right)} - \mathbf{f}^{NL}\left(\mathbf{u}_{(p,q,r)}^{(0)}\right) + c.c.. \tag{2.52}$$

It is worth noting that at this point that Eq. (2.52) and (2.23) are exactly equivalent when the following conditions are true:

1. $\mathbf{u}^{(0)}$ is monochromatic (i.e. $i = 1$),
2. A constant amplitude is assumed such that $\alpha(T_1) = A =$ const, and,
3. Phase $\beta(T_1)$ varies linearly with slow time T_1 such that $\beta(T_1) = \omega_1 T_1 = \varepsilon\omega_1 t$.

Then, Eq. (2.52) reduces to

$$\begin{aligned} D_0^2\mathbf{M}\mathbf{u}^{(1)} + \mathbf{K}(\boldsymbol{\mu})\mathbf{u}^{(1)} &= \omega_0\omega_1\mathbf{M}A\boldsymbol{\phi}e^{-\mathrm{i}(\omega_0+\varepsilon\beta_1)T_0} - \mathbf{f}^{NL}\left(\mathbf{u}_{(p,q,r)}^{(0)}\right) + c.c.. \\ &= 2\omega_0\omega_1\mathbf{M}\mathbf{u}^{(0)} - \mathbf{f}^{NL}\left(\mathbf{u}_{(p,q,r)}^{(0)}\right) + c.c.. \end{aligned} \tag{2.53}$$

The ability of the multiple scales method to accommodate time varying, multi-harmonic, Bloch wave solutions in the form of (2.49), or simple monochromatic and constant amplitude solutions in the form (2.24) is very appealing. Indeed, for computing dispersion it may be necessary to make assumptions (2) and (3) to obtain tractable expressions for systems with many harmonics present.

Returning to Eq. (2.52), we note that the linear kernel is the same as the linear kernel of the $O(\varepsilon^0)$ equation Eq. (2.52). Therefore, the Bloch wave mode matrix $\mathbf{\Phi}$ decouples the linear kernel in the same manner as described previously for Lindstedt-Poincaré analysis. Introduce modal coordinates $\mathbf{u}^{(1)} = \mathbf{\Phi}\mathbf{z}^{(1)}(t)$ as before and pre-multiply by $\boldsymbol{\phi}_j^H$ to obtain

$$D_0^2 m_{jj} z_j^{(1)} + k_{jj} z_j^{(1)} = \boldsymbol{\phi}_j^H \mathrm{i}\mathbf{M} \sum_i \omega_{0,i} \left(\alpha_i' - \mathrm{i}\alpha_i\beta_i'\right) \boldsymbol{\phi}_i e^{-\mathrm{i}\left(\omega_{0,i}T_0 + \beta_i(T_1)\right)} - \boldsymbol{\phi}_j^H \mathbf{f}^{NL} + c.c.. \quad (2.54)$$

As before, terms proportional to $\exp(\pm \mathrm{i}\omega_{0,j}T_0)$ result in nonuniform perturbation expansions and must be removed. As the nonlinear force vector $\mathbf{f}^{NL}$ depends on $\mathbf{u}^{(0)}_{(p,q,r)}$, it must first be expanded to collect terms proportional to $\exp(\mathrm{i}\omega_{0,j}T_0)$. The discrete frequency combinations found in $\mathbf{f}^{NL}$ are amenable to a multi-dimensional Fourier series expansion as (in the case of two frequencies denoted by i and j)

$$\mathbf{f}^{NL}(T_0) = \sum_i \sum_j \mathbf{c}_{ij} e^{\mathrm{i}\omega_{0,i}T_0} e^{\mathrm{i}\omega_{0,j}T_0} + c.c., \quad (2.55)$$

where the Fourier coefficients are generally a function of all amplitudes and wave vectors $\mathbf{c}_{ij}(\cup A_k, \cup \boldsymbol{\mu}_k)$. This expansion specifically provides for the existence of higher generated harmonics as well as sum-and-difference frequency generations [66]. For simplicity, we denote the fundamental harmonic terms using a single index such that $\mathbf{c}_{i0} = \mathbf{c}_i$ and $\mathbf{c}_{0j} = \mathbf{c}_j$. The explicit dependence of $\mathbf{c}_i$ on the complex amplitude of each wave, as well as individual wave numbers has been noted. A special case arises when two frequencies $\omega_{0,m}$ and $\omega_{0,n}$ are commensurate with one another such that these extraneous harmonics occur at one of the input frequencies $\omega_{0,i}$. This case is treated analytically in Ch. 3 for third-harmonic interaction. Since cubic nonlinearities are considered herein, the coefficient vector $\mathbf{c}_i$ can be obtained symbolically (usually with the aid of symbolic manipulation software) or computationally with the aid of a Fourier transform.

Equations (2.54) and (2.55) combined facilitate the identification of secular terms

$$D_0^2 m_{jj} z_j^{(1)} + k_{jj} z_j^{(1)} = \boldsymbol{\phi}_j^H \sum_i \left[\left(\mathrm{i}\mathbf{M}\omega_{0,i}\boldsymbol{\phi}_i \left(\alpha_i' - \mathrm{i}\alpha_i\beta_i'\right) e^{-\mathrm{i}\beta_i(T_1)} - \mathbf{c}_i\right) e^{-\mathrm{i}\omega_{0,i}T_0}\right] + c.c., \quad (2.56)$$

where other harmonic terms (O.H.T.) exist but do not contribute to secularity and so have been omitted from the above expression. Terms on the R.H.S. of Eq. (2.56) with $\exp(\mathrm{i}\omega_{0,i}T_0)$ time-dependence result in secular expansions; therefore, we remove them by requiring they vanish identically. Factoring out the $i = j$ term from the summation provides the required condition

$$\mathrm{i}\omega_{0,j}m_{jj}\left(\alpha'_j - \mathrm{i}\alpha_j\beta'_j\right)e^{-\mathrm{i}\beta_j} - \boldsymbol{\phi}_j^H\mathbf{c}_j = 0, \tag{2.57}$$

where the orthogonality properties of the mass matrix have been enforced.

Incidentally, when the frequencies $\omega_{0,i}$ are incommensurate it is convenient to multiply Eq.(2.57) by $e^{\mathrm{i}\beta_j}$ to obtain for the jth equation

$$\mathrm{i}\omega_{0,j}m_{jj}\left(\alpha'_j - \mathrm{i}\alpha_j\beta'_j\right) - \boldsymbol{\phi}_j^H\mathbf{c}_j e^{\mathrm{i}\beta_j} = 0. \tag{2.58}$$

Equation (2.58) requires that real and imaginary components vanish individually such that

$$\omega_{0,j}m_{jj}\alpha_i\beta'_j - \mathfrak{R}\left(\boldsymbol{\phi}^H\mathbf{c}_j e^{\mathrm{i}\beta_j}\right) = 0 \tag{2.59}$$

$$\omega_{0,j}m_{jj}\alpha'_j - \mathfrak{I}\left(\boldsymbol{\phi}^H\mathbf{c}_j e^{\mathrm{i}\beta_j}\right) = 0. \tag{2.60}$$

where $\mathfrak{R}(\ )$ and $\mathfrak{I}(\ )$ return real and imaginary components of the included expression, respectively. Equations (2.59) and (2.60) are termed *evolution equations* because, when solved, they describe the slow-time evolution of the amplitude $\alpha_j(T_1)$ and phase $\beta_j(T_1)$.

In general, Eqs. (2.59) and (2.60) constitute a set of $2N$ nonlinear differential equations when a total of N Bloch wave modes are considered. The evolutions equations simplify considerably when the included frequencies are incommensurate. It happens that the coefficient $\mathbf{c}_j$ for the jth frequency always occurs, for cubic nonlinearities, in the fortuitous form $\mathbf{c}_j = \hat{\mathbf{c}}_j(\cup\,\alpha_k)\exp(-\mathrm{i}\beta_j)$. Moreover, the scalar product $\boldsymbol{\phi}^H\mathbf{c}_j$ results in a purely real expression quantity because $\boldsymbol{\phi}_j$ has been derived from a Hermitian eigenvalue problem. Then, the evolution equations are simply

$$\omega_{0,j}m_{jj}\alpha_j\beta'_j - \boldsymbol{\phi}^H\hat{\mathbf{c}}_j = 0 \tag{2.61}$$

$$\omega_{0,j}m_{jj}\alpha'_j = 0. \tag{2.62}$$

Equation (2.62) implies that $\alpha'_j = 0\,\forall\, j$ is constant with respect to slow time T_1. Moreover, Eq. (2.61) can be solved and directly integrated to obtain $\beta_j(T_1)$ since $\hat{\mathbf{c}}_j$ is independent of β_j

$$\beta_j = \frac{\boldsymbol{\phi}^H \hat{\mathbf{c}}_j}{\omega_{0,j}\alpha_j m_{jj}} T_1 \tag{2.63}$$

Thus, it is often of interest to specify the slow-time behavior of $A(T_1)$ *a priori* to reduce the complexity of the evolution equations. The nonlinear dispersion corrections produced, *for each Bloch wave*, using the method of multiple scales for the case of incommensurate frequencies read

$$\omega_j(\boldsymbol{\mu}) = \omega_{0,j}(\boldsymbol{\mu}) + \varepsilon \frac{\boldsymbol{\phi}^H \hat{\mathbf{c}}_j}{\omega_{0,j}\alpha_j m_{jj}} + O(\varepsilon^2). \tag{2.64}$$

Here again it is possible to manipulate the corrected frequency by introducing the modal stiffness according to $\omega_{0,j}^2 m_{jj} = k_{jj}$ so that the updated frequency is given as

$$\omega_j(\boldsymbol{\mu}) = \omega_{0,j}(\boldsymbol{\mu}) \left(1 + \varepsilon \frac{\omega_{0,j}\boldsymbol{\phi}^H \hat{\mathbf{c}}_j}{\alpha_j k_{jj}}\right) + O(\varepsilon^2). \tag{2.65}$$

In the more general case, the evolution equations (2.59) and (2.60) possess non-trivial solutions and must be solved as a coupled system of nonlinear differential equations for each $\alpha_j(T_1)$ and $\beta_j(T_1)$. Then, the instantaneous frequency correction yields frequency expansions in the form

$$\omega_j(\boldsymbol{\mu}) = \omega_{0,j}(\boldsymbol{\mu}) + \varepsilon\beta_j(T_1)/T_0 + O(\varepsilon^2) \tag{2.66}$$

such that the *i*th Bloch wave component is given by

$$\mathbf{u}_j^{(0)} = \frac{\alpha_i(T_1)}{2}\boldsymbol{\phi}_j e^{-\mathrm{i}\left[(\omega_{0,j}+\beta_j(\varepsilon t)/t)t\right]} + c.c. \tag{2.67}$$

This incommensurate case is generally more informative for assessing nonlinear dispersion. However, the incommensurate case is discussed in more detail in Chapter 3.

CHAPTER III

NONLINEAR WAVE-WAVE INTERACTIONS

3.1 Monoatomic chain

3.1.1 Overview

Acoustic devices may be subject to multi-harmonic excitations. In one-dimensional linear materials, the only wave-wave interactions expected are constructive and destructive interference. In nonlinear materials, additional wave-wave interactions take place such that the strength of the interaction causes dispersion to become both amplitude and frequency dependent. The interaction of harmonic waves that are commensurate[1] with frequency ratios close to 1:3 may be of particular concern for cubically nonlinear materials where super-harmonic generation may be present.

The propagation of multiple nonlinearly interacting waves has received considerably less attention than the propagation of a single wave. It is well-known that oscillations in nonlinear systems tend to generate super-harmonics and subharmonics [29]. This characteristic behavior of nonlinear systems motivates the investigation of wave-wave interactions. Nayfeh and Mook explored these interactions using the method of multiple scales for transverse waves along a beam on an elastic foundation [27]. Rushchitsky has been a primary investigator in the subject of wave-wave interaction and evolution in continuous solids [28, 29, 67]. Rushchitsky and Savel'eva also presented theoretical results on the interaction of harmonic elastic plane waves in a cubically nonlinear material using the method of multiple scales for a continuum model [29]. They derived a theoretical model governing the transfer of energy from a stronger primary wave to a nearly-commensurate super-harmonic.

---

[1] Two frequencies ω_A and ω_B where two integers n and m can be chosen to satisfy $n\omega_A + m\omega_B = 0$

Periodic materials are of particular interest in metamaterial research due to the presence of band gaps. Various types of periodic media have been studied in the past, including strongly nonlinear contact in beaded systems [37], kink dynamics [68], and weakly coupled layered systems [45, 44]. One of the most commonly studied systems in the last few decades is the one-dimensional, undamped spring-mass chain [3, 63, 69, 25]. Amplitude-dependent dispersion and band gap behavior has recently been explored in several discrete periodic systems characterized by cubic nonlinearities [3]. It is shown that the boundary of the dispersion curve may shift with amplitude in the presence of a single plane wave. Approximate closed-form solutions are obtained that allow the determination of the effects nonlinearities have on dispersion and group velocity.

In this work, the analysis presented in [3] is extended to include the propagation of multiple harmonic plane waves. It is shown that the method of multiple scales provides more generality than Lindstedt-Poincaré when wave-wave interactions occur due to commensurate or nearly-commensurate frequency ratios. The following development supports the interests being generated by the community by contributing a numerically verified theoretical framework in which the dispersion properties of discrete, periodic, cubically nonlinear systems undergoing harmonic wave-wave interactions may be determined.

The chapter is organized as follows. In Sec. 3.1.2 we describe the nonlinear model used for the perturbation analysis. For completeness, in Sec. 3.1.3.1 we briefly reconsider the case of a single harmonic wave present using Lindstedt-Poincaré perturbation and then recover the same result using MMS in Sec. 3.1.3.2. The method of multiple scales is applied to the same nonlinear spring-mass system under the influence of two waves to obtain theoretical dispersion relations and evolution equations in Sec. 3.1.4. Finally, the dispersion relations generated by the method of multiple scales are numerically verified in Sec. 3.1.5.

3.1.2 Model description and nonlinear governing equation

The monoatomic spring-mass chain with a cubic nonlinearity shown in Fig. 3.1 is considered. The equation of motion for the monoatomic chain considered is

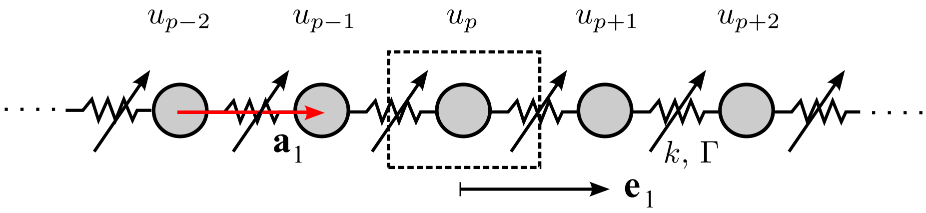

Figure 3.1: Monoatomic mass-spring chain with cubic stiffness and lattice vector $\mathbf{a}_1$.

$$m\ddot{\tilde{u}}_p + k(2\tilde{u}_p - \tilde{u}_{p-1} - \tilde{u}_{p+1}) + \varepsilon\Gamma(\tilde{u}_p - \tilde{u}_{p-1})^3 + \varepsilon\Gamma(\tilde{u}_p - \tilde{u}_{p+1})^3 = 0, \quad \forall p \in \mathbb{Z}, \tag{3.1}$$

where $\tilde{u}_p(t)$ is the displacement from equilibrium of the pth mass, ε is a small parameter, Γ characterizes the cubic nonlinearity, and m and k denote the mass and linear stiffness. We nondimensionalize the equation of motion (3.1) by first writing the equation of motion in canonical form, where $\omega_n^2 = k/m$

$$\ddot{\tilde{u}}_p + \omega_n^2(2\tilde{u}_p - \tilde{u}_{p-1} - \tilde{u}_{p+1}) + \frac{\varepsilon\Gamma}{m}(\tilde{u}_p - \tilde{u}_{p-1})^3 + \frac{\varepsilon\Gamma}{m}(\tilde{u}_p - \tilde{u}_{p+1})^3 = 0. \tag{3.2}$$

We represent space and time by introducing characteristic length and time parameters (d_c and t_c) and nondimensional variables for space and time (u_p and t) such that $\tilde{u}_p \equiv d_c\, u_p$ and $\tilde{t} \equiv t_c\, t$, where characteristic length is $d_c = \sqrt{k/\Gamma}$ and the characteristic time is $t_c = 1/\omega_n$. The equation of motion is then re-written using nondimensional variables as

$$\ddot{u}_p + (2u_p - u_{p-1} - u_{p+1}) + \varepsilon(u_p - u_{p-1})^3 + \varepsilon(u_p - u_{p+1})^3 = 0, \quad \forall p \in \mathbb{Z}. \tag{3.3}$$

Note that double dot corresponds to a second derivative with respect to nondimensional time t.

3.1.3 Single wave dispersion analysis

For the remainder of the chapter, a single-wave analysis refers to calculations presuming the presence of only one harmonic plane wave, whereas a multi-wave analysis refers to the presence of two or more dominant harmonics present such that wave-wave interactions take place.

3.1.3.1 Lindstedt-Poincaré analysis

It was shown in [3] that a correction to the linear dispersion relation for the mono-atomic chain could be obtained using Lindstedt-Poincaré perturbation as $\omega(\mu) = \omega_0(\mu) + \varepsilon\omega_1(\mu) + O(\varepsilon^2)$, where

$$\omega_0 = \sqrt{2 - 2\cos\mu} \tag{3.4a}$$

$$\omega_1 = \frac{3\alpha^2(\cos 2\mu - 4\cos\mu + 3)}{4\,\omega_0}, \tag{3.4b}$$

and α and μ denote the amplitude and nondimensional wavenumber, respectively. The dispersion relation $\omega(\mu)$ is periodic in wavenumber space such that only $0 < \mu \leq \pi$ is considered.

Equation (3.4b) provides a correction to the linear dispersion relation due to the presence of cubic nonlinearities. The same type of cubic nonlinearity in a spring mass chain was considered in [24], where a correction to the dispersion relations was also found. The approach presented in [24] consists in the application of Bloch Theorem directly to the nonlinear governing equations, while in [3] a perturbation method is applied to decouple linear and nonlinear terms. This leads to a set of linear equations for increasing order of the nonlinear parameter ε. Applying Bloch theorem to the lowest order equation, and imposing solvability conditions to the first order leads to the expressions presented in Eqs. (3.4a) and (3.4b).

We note that one simplification may be added to Eq. (3.4b) by substituting in the linear dispersion relation given by Eq. (3.4a). After some manipulation, Eq. (3.4b) can be rewritten as

$$\omega_1 = \frac{3\alpha^2}{8}\frac{\overbrace{(2 - 2\cos\mu)^2}^{\omega_0^4}}{\omega_0} = \frac{3}{8}\alpha^2\omega_0^3, \tag{3.5}$$

Given a point on the linear dispersion relation (μ, ω_0), a frequency correction may be calculated as a function of ω_0. The reconstituted dispersion relation is

$$\omega(\mu) = \sqrt{2 - 2\cos\mu} + \varepsilon\frac{3\alpha^2}{8}(2 - 2\cos\mu)^{3/2} + O(\varepsilon^2). \tag{3.6}$$

3.1.3.2 Dispersion Relation using the Method of multiple scales

We begin with the equation of motion (3.3) and seek expressions for time-varying amplitude and phase as described in Chapter 2. Slow time scales are introduced explicitly as $T_n = \varepsilon^n t$. As before, correction terms up to $O(\varepsilon^2)$ are sought so that the only time scales of interest are $T_0 = t$ and $T_1 = \varepsilon t$. An asymptotic expansion for the dependent variable $u_p(t)$ is expressed in multiple time scales as

$$u_p(t) = \sum_n \varepsilon^n u_p^{(n)}(T_0, T_1, \ldots T_n).$$

Keeping terms up to and including $O(\varepsilon^1)$ gives

$$u_p(\tau) = u_p^{(0)}(T_0, T_1) + \varepsilon u_p^{(1)}(T_0, T_1) + O(\varepsilon^2). \tag{3.7}$$

Substituting Eq. (3.7) into Eq. (3.3), and collecting terms in orders of ε, gives the first two ordered equations which may be written as

$$\varepsilon^0: \qquad D_0^2 u_p^{(0)} + (2u_p^{(0)} - u_{p-1}^{(0)} - u_{p+1}^{(0)}) = 0 \tag{3.8a}$$

$$\varepsilon^1: \qquad D_0^2 u_p^{(1)} + (2u_p^{(1)} - u_{p-1}^{(1)} - u_{p+1}^{(1)}) = -2D_0D_1u_p^{(0)} - f^{NL}(u_p^{(0)}, u_{p\pm1}^{(0)}), \tag{3.8b}$$

where

$$f^{NL} = (u_p^{(0)} - u_{p-1}^{(0)})^3 + (u_p^{(0)} - u_{p+1}^{(0)})^3. \tag{3.9}$$

Recall that D_0 and D_1 represent partial derivatives with respect to the time scales T_0 and T_1, respectively. In the presence of a single plane wave at frequency ω and wave number μ, the solution of (3.8a) is

$$u_p^{(0)}(T_0, T_1) = \frac{1}{2}A_0(T_1)e^{\mathrm{i}(\mu p - \omega_0 T_0)} + \frac{1}{2}\overline{A_0}(T_1)e^{-\mathrm{i}(\mu p - \omega_0 T_0)}, \tag{3.10}$$

where $A_0(T_1)$ is the complex quantity that permits slow time evolution of the amplitude and phase and an over-bar indicates a complex conjugate. The distinction may be made explicit by using polar form such that $A_0(T_1) = \alpha(T_1)e^{-i\beta(T_1)}$, where both $\alpha(T_1)$ and $\beta(T_1)$ are real-valued functions. Substituting Eq. (3.10) into Eq. (3.8a) and simplifying gives the linear dispersion relation that was previously given in Eq. (3.4a).

The linear kernel of the $O(\varepsilon^1)$ equation is identical to the linear kernel of the $O(\varepsilon^0)$ equation (3.8a), and thus the homogeneous solution has the same form as Eq. (3.10). Therefore, any terms appearing on the right hand side of Eq. (3.8b) with similar spatial and temporal forms result in a non-uniform expansion. Removal of these secular terms by setting them equal to zero results in a system of *evolution equations* for the functions $\alpha(T_1)$ and $\beta(T_1)$

$$\alpha' = 0 \tag{3.11a}$$

$$\beta' = \frac{3\alpha^2(\cos 2\mu - 4\cos\mu + 3)}{4\,\omega_0} = \frac{3}{8}\alpha^2\omega_0^3, \tag{3.11b}$$

where α' and β' denote the derivatives with respect to the slow time scale T_1. It is clear from Eq. (3.11a) that $\alpha(T_1) = \alpha_0$, and $\beta(T_1) = \beta_1 T_1 + \beta_0$, where α_0 and β_0 are arbitrary constants determined by imposing initial conditions on the plane wave given in Eq. (3.10). For the mass-spring chain in consideration, β_0 may be set to zero without loss of generality. Equation (3.10) may be expressed using trigonometric functions as

$$u_p^{(0)}(T_0, T_1) = \alpha_0 \cos\left(\mu p - (\omega_0 + \omega_1\varepsilon)T_0\right), \tag{3.12}$$

such that $\beta_1\varepsilon \equiv \omega_1\varepsilon$ may be regarded as a first order frequency correction which results in a shift of the linear dispersion curve. The reconstituted dispersion relation is identical to Eq. (3.6). Hence, the method of multiple scales recovers the same results as the Lindstedt-Poincaré procedure.

3.1.3.3 Multiple Scales vs. Lindstedt-Poincaré for Wave Interactions

It is well-known that super-harmonics are generated as a result of wave propagation in nonlinear media and that there exists nonlinear interaction between the waves [28, 27]. Therefore it is of interest to extend the problem to the propagation of multi-harmonic plane waves to obtain closed-form relationships capturing these interactions.

The Lindstedt-Poincaré method provides a tool to capture nonlinear amplitude-frequency interaction in systems with time-invariant amplitude and phase, but fails to capture time-variant behavior such as in the long wavelength limit where amplitude or frequency modulation may occur. The failure in the Lindstedt-Poincaré method results from the requirement that wave amplitudes remain constant such that a single secular term may be used to obtain a single frequency correction term. When there are multiple secular terms, additional degrees of freedom are necessary to obtain a perturbation solution. Allowing for multiple time-varying amplitudes and phases provides additional degrees of freedom to the problem.

The assumption implicit in the preceding single-wave analysis is that only a single harmonic plane wave exists for all time. However, when multiple waves are present with amplitudes that are the same order of magnitude, the single-wave analysis fails to accurately capture some nonlinear system behavior due to wave-wave interactions that are neglected.

3.1.4 Wave interaction analysis using multiple scales

Due to linearity of the $O(\varepsilon^0)$ expression Eq. (3.8a), a superposition of solutions in the form of Eq. (3.10) is also a solution, such that $u_p^{(0)} \Rightarrow \sum_n u_{p,n}^{(0)}$. When two waves are present, we superimpose two traveling wave solutions, labeled A and B, such that

$$u_p^{(0)}(T_0, T_1) = u_{p,A}^{(0)}(T_0, T_1) + u_{p,B}^{(0)}(T_0, T_1) + O(\varepsilon^2), \tag{3.13}$$

where

$$u_{p,A}^{(0)}(T_0, T_1) = \frac{1}{2} A_0(T_1) e^{\mathrm{i}(\mu_A p - \omega_{A0} T_0)} + c.c. = \frac{1}{2} \alpha_A(T_1) e^{\mathrm{i}\left(\mu_A p - \omega_{A0} T_0 - \beta_A(T_1)\right)} + c.c., \tag{3.14a}$$

$$u_{p,B}^{(0)}(T_0, T_1) = \frac{1}{2} B_0(T_1) e^{\mathrm{i}(\mu_B p - \omega_{B0} T_0)} + c.c. = \frac{1}{2} \alpha_B(T_1) e^{\mathrm{i}\left(\mu_B p - \omega_{B0} T_0 - \beta_B(T_1)\right)} + c.c., \tag{3.14b}$$

and *c.c.* represents the complex conjugates of the preceding terms. Here, α_A, α_B, β_A, and β_B are functions for the amplitude and phase of each wave, which will be determined by imposing uniform asymptotic expansion conditions.

Substituting Eqs. (3.13), (3.14a), and (3.14b) into Eq. (3.8b) and expanding the nonlinear terms denoted by f^{NL} allows for identification of secular terms. These terms are those which are proportional to $e^{\mathrm{i}\mu_A p} e^{\mathrm{i}\omega_{A0} T_0}$ and $e^{\mathrm{i}\mu_B p} e^{\mathrm{i}\omega_{B0} T_0}$, labeled S_A and S_B, respectively. Due to the arbitrary naming convention of the *A* and *B* waves, the secular terms arising from each wave are identical. For the *A* wave, secular terms are

$$\begin{aligned} S_A = e^{\mathrm{i}\mu_A p} e^{-\mathrm{i}\omega_{A0}\tau_0} \Big[& -\mathrm{i}A_0' \omega_{A0} + \frac{3}{4} A_0 |B_0|^2 e^{\mathrm{i}(\mu_A - \mu_B)} + \frac{3}{4} A_0 |B_0|^2 e^{\mathrm{i}(\mu_B - \mu_A)} \\ & + \frac{3}{8} A_0 |A_0|^2 e^{\mathrm{i}2\mu_A} + \frac{3}{8} A_0 |A_0|^2 e^{-\mathrm{i}2\mu_A} - \frac{3}{2} A_0 |B_0|^2 e^{\mathrm{i}\mu_A} - \frac{3}{2} A_0 |B_0|^2 e^{-\mathrm{i}\mu_A} \\ & - \frac{3}{2} A_0 |A_0|^2 e^{\mathrm{i}\mu_A} - \frac{3}{2} A_0 |A_0|^2 e^{-\mathrm{i}\mu_A} + \frac{3}{4} A_0 |B_0|^2 e^{\mathrm{i}(\mu_B + \mu_A)} + \frac{3}{4} A_0 |B_0|^2 e^{-\mathrm{i}(\mu_B + \mu_A)} \\ & - \frac{3}{2} A_0 |B_0|^2 e^{\mathrm{i}\mu_B} - \frac{3}{2} A_0 |B_0|^2 e^{\mathrm{i}\mu_B} + \frac{9}{4} A_0 |A_0|^2 + 3 A_0 |B_0|^2 \Big] + c.c.. \end{aligned} \tag{3.15}$$

Additional secular terms may arise if (μ_A, ω_{A0}) and (μ_B, ω_{B0}) are related such that their combination results in a secular term. When $\omega_{B0} \approx 3\omega_{A0}$ *and* $\mu_B \approx 3\mu_A$, these additional secular terms are

$$\begin{aligned}
&A_0^3 e^{\mathrm{i}3\mu_A p} e^{-\mathrm{i}3\omega_{A0}\tau_0}\left[-\frac{3}{8}\,e^{-\mathrm{i}\mu_A}+\frac{1}{3}-\frac{1}{8}\,e^{\mathrm{i}3\mu_A}+\frac{3}{8}\,e^{-\mathrm{i}2\mu_A}-\frac{3}{8}\,e^{\mathrm{i}\mu_A}-\frac{1}{8}\,e^{-\mathrm{i}3\mu_A}+\frac{3}{8}\,e^{\mathrm{i}2\mu_A}\right]\\
&\quad + {A_0}^2\overline{B_0}e^{\mathrm{i}(\mu_B-2\mu_A)p}e^{-\mathrm{i}(\omega_{B0}-2\omega_{A0})\tau_0}\Bigg[-\frac{3}{8}\,e^{-\mathrm{i}\mu_B}+\frac{3}{8}\,e^{2\mathrm{i}\mu_A}-\frac{3}{8}\,e^{\mathrm{i}\mu_B}-\frac{3}{4}\,e^{-\mathrm{i}\mu_A}\\
&\qquad -\frac{3}{8}\,e^{\mathrm{i}(\mu_B-2\mu_A)}-\frac{3}{4}\,e^{\mathrm{i}\mu_A}+\frac{3}{4}+\frac{3}{4}\,e^{\mathrm{i}(\mu_B-\mu_A)}\\
&\qquad -\frac{3}{8}\,e^{-\mathrm{i}(\mu_B+2\mu_A)}+\frac{3}{4}\,e^{-\mathrm{i}(\mu_B+\mu_A)}+\frac{3}{8}\,e^{-2\mathrm{i}\mu_A}\Bigg]+c.c.. \qquad (3.16)
\end{aligned}$$

The equivalent secular terms for the B wave may be obtained by letting $\mu_A \to \mu_B$, $\omega_{A0} \to \omega_{B0}$, and $A_0 \leftrightarrow B_0$. In light of Eqs. (3.15) and (3.16), there exist two possibilities for secularity when two harmonic plane waves are present:

Case 1. $\{(\mu_B, \omega_{B0}) \in \mathbb{R}^2 : (\mu_B, \omega_{B0}) \neq a \cdot (\mu_A, \omega_{A0})$ where $a = 1/3$ or $3\}$, such that wave-wave interactions are produced due to amplitude products (the most general case), and

Case 2. $\{(\mu_B, \omega_{B0}) \in \mathbb{R}^2 : (\mu_B, \omega_{B0}) = a \cdot (\mu_A, \omega_{A0})$ where $a = 1/3$ or $3\}$ such that wave-wave interactions are influenced by nonlinear frequency and wave number coupling, as in the long wavelength limit.

Case 1 is the most general case in which there are two waves present, and nonlinear coupling occurs only due to the products of amplitude coefficients A_0 and B_0. Case 2 produces secular terms due to amplitude products *and* nonlinear coupling of both the frequency and wave number. The super-harmonic ($a = 3$) and subharmonic cases ($a = 1/3$) are essentially the same due to the arbitrary choice in naming the A and B waves. Due to additional secular terms arising in the long wavelength limit for the super-harmonic (and subharmonic) case, a separate treatment is necessary.

3.1.4.1 Case 1. General wave-wave interactions

We suppose there are two waves A and B such that there is no wave-wave interaction due to special combinations of frequency and wave number ($a = 1/3$ or 3). Then, two independent, complex secular terms arise which lead to a nonuniform expansion at $O(\varepsilon^1)$ as in Eq. (3.15). Solvability conditions for a uniform expansion require these terms to vanish identically. Separating the real and imaginary components for each coefficient function and equating the resulting expressions to zero results in a set of four evolution equations

$$\begin{aligned} \alpha_A' &= 0 & \alpha_B' &= 0 \\ \beta_A' &= \frac{3}{8}\omega_{A0}^3\,\alpha_A^2 + \frac{3}{4}\omega_{A0}\omega_{B0}^2\,\alpha_B^2 & \beta_B' &= \frac{3}{4}\omega_{A0}^2\omega_{B0}\,\alpha_A^2 + \frac{3}{8}\omega_{B0}^3\,\alpha_B^2, \end{aligned} \tag{3.17}$$

Equations (3.17) lead to some interesting observations regarding the dispersion relationship when two waves interact. As with the single-wave case, the amplitudes α_A and α_B of both waves are constant at $O(\varepsilon^1)$. The separable equations β_A' and β_B', when integrated, yield linear phase corrections that can be interpreted as frequency (and thus dispersion) corrections similar to Eq. (3.12). After integration, the expressions in Eq. (3.17) become

$$\begin{aligned} \alpha_A &= \alpha_{A,0} & \alpha_B &= \alpha_{B,0} \\ \beta_A &= \beta_{A,1}T_1 + \beta_{A,0} & \beta_B &= \beta_{B,1}T_1 + \beta_{B,0}, \end{aligned} \tag{3.18}$$

where as before, one of the constants of integration $\beta_{A,0}$ or $\beta_{B,0}$ may be set to zero without any loss of generality, while the remaining constant controls the phase relationship between the two waves (but has no effect on dispersion). The slopes of β_A and β_B, given by $\beta_{A,1} = \beta_A'$ and $\beta_{B,1} = \beta_B'$ in Eqs. (3.18), determine the magnitude of the dispersion correction for each wave.

It is convenient to express the relationship between ω_{A0} and ω_{B0} by a single frequency on the linear dispersion curve $\omega_0 \equiv \omega_{A0}$ and a frequency ratio r so that both frequency corrections can be visualized on a single plot, and also so that $r = 3$ corresponds to Case 2 in the long wavelength limit

$$r \equiv \frac{\omega_{B0}}{\omega_{A0}} \longrightarrow \omega_{B0} = r\omega_0. \tag{3.19}$$

Furthermore, we assume without loss of generality, that $\omega_{A0} < \omega_{B0}$ so that a single frequency ω_0 and ratio $r > 1$ describe the dispersion corrections rather than two frequencies. The frequency correction terms become

$$\omega_{A1} \equiv \beta_{A,1} = \frac{3}{8}\omega_0^3\alpha_A^2 + \frac{3r^2}{4}\omega_0^3\alpha_B^2 \tag{3.20a}$$

$$\omega_{B1} \equiv \beta_{B,1} = \frac{3r}{4}\omega_0^3\alpha_A^2 + \frac{3r^3}{8}\omega_0^3\alpha_B^2. \tag{3.20b}$$

The reconstituted dispersion relations, corrected to $O(\varepsilon^1)$, are given by

$$\omega_A = \sqrt{2 - 2\cos\mu_A} + \varepsilon\Big(\frac{3}{8}\alpha_A^2 + \frac{3r^2}{4}\alpha_B^2\Big)(2 - 2\cos\mu_A)^{3/2} + O(\varepsilon^2) \tag{3.21a}$$

$$\omega_B = \sqrt{2 - 2\cos\mu_B} + \varepsilon\Big(\frac{3r}{4}\alpha_A^2 + \frac{3r^3}{8}\alpha_B^2\Big)(2 - 2\cos\mu_A)^{3/2} + O(\varepsilon^2) \tag{3.21b}$$

so that each wave follows its own dispersion curve for a given frequency ratio r and given amplitudes α_A and α_B. Thus, when two waves nonlinearly interact they form two amplitude and frequency dependent dispersion branches. In the absence of nonlinear wave-wave interaction, only a single dispersion curve exists.

Figure 3.2 shows two possible dispersion relation corrections for both hardening and softening chains. These dispersion curves were plotted using $\alpha_A = \alpha_B = 4$, $r = 2.7$ and $\varepsilon = \pm 0.01$ to produce hardening and softening curves. Note that the dotted section of the ω_A curve corresponds to values which would cause the super-harmonic $\omega_B = 3\,\omega_{A0} + \varepsilon\omega_{B1}$ to be in the band gap. This section of the curve is not explored here, but has been included as a visual aid to make the trends more apparent. At large amplitudes the single-wave corrected dispersion curve in Eq. (3.6), labeled ω in Fig. 3.2, underestimates the magnitude of the correction to both ω_A and ω_B. The failure is especially evident at the edge of the Brillouin Zone.

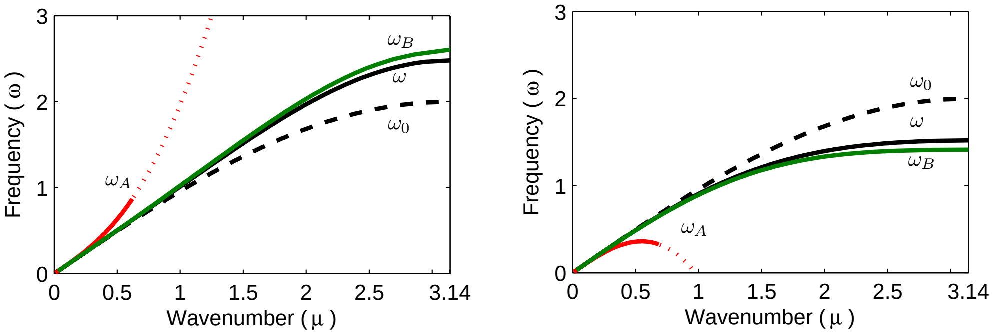

(a) Hardening Chain (b) Softening Chain

Figure 3.2: Multi-wave corrected dispersion curves compared with the linear curve ω_0 and the nonlinear single-wave corrected curve ω

If the frequency correction terms ω_{A1} and ω_{B1} in Eqs. (3.20a) and (3.20b) are interpreted as asymptotic frequency expansion terms as in the Lindstedt-Poincaré method, the ratios[2] of the $O(\varepsilon^1)$ correction terms to specified $O(\varepsilon^0)$ linear values $(\omega_{A0}, \omega_{B0})$ for each wave provide an estimate for the expansion uniformity and a normalized measure of the dispersion correction. These ratios are

$$\rho_A = \left|\frac{\varepsilon\omega_{A1}}{\omega_{A0}}\right| \Rightarrow \left|\frac{\varepsilon\omega_{A1}}{\omega_0}\right| = \frac{[(3/8)\omega_0^3\alpha_A^2 + (3r^2/4)\omega_0^3\alpha_B^2]|\varepsilon|}{\omega_0} = \left[\frac{3}{8}\alpha_A^2 + \frac{3r^2}{4}\alpha_B^2\right]|\varepsilon|\omega_0^2 \quad (3.22)$$

$$\rho_B = \left|\frac{\varepsilon\omega_{B1}}{\omega_{B0}}\right| \Rightarrow \left|\frac{\varepsilon\omega_{B1}}{r\omega_0}\right| = \frac{[(3r/4)\omega_0^3\alpha_A^2 + (3r^3/8)\omega_0^3\alpha_B^2]|\varepsilon|}{r\omega_0} = \left[\frac{3}{4}\alpha_A^2 + \frac{3r^2}{8}\alpha_B^2\right]|\varepsilon|\omega_0^2. \quad (3.23)$$

Hence, α_A, α_B, r, and the quantity $|\varepsilon|\omega_0^2$ determine the uniformity and magnitude of the correction terms. Uniform expansions correspond to when the ratios (3.22) and (3.23) are much less than one. Furthermore, since $\rho_{A,B}$ represent a percentage of the linear frequency at specified point on the dispersion curve, we can calculate parameters to obtain a specific dispersion shift. Numerical simulations, presented in Sec. 3.1.5, have shown good agreement for $\rho_{A,B}$ less than about 0.2.

---

[2] More specifically, the absolute value of the ratios in the event that $\varepsilon < 0$

3.1.4.2 Case 2. Long wavelength limit wave-wave interactions

We previously mentioned in Case 2 that additional wave-wave interactions may be produced due to nonlinear phase coupling when $\omega_{B0} \approx 3\,\omega_{A0}$ *and* $\mu_B \approx 3\mu_A$. This corresponds to when the phase velocities of each wave are approximately equal so that the waves travel together. The closeness of (μ_B, ω_{B0}) to $3(\mu_A, \omega_{A0})$ can be formally represented using detuning quantities $\bar{\sigma}_\omega$ and $\bar{\sigma}_\mu$, respectively, so that

$$\omega_{B0} = 3\omega_{A0} + \bar{\sigma}_\omega \text{ and } \mu_B = 3\mu_A + \bar{\sigma}_\mu \tag{3.24}$$

are exact relations. In the long wavelength limit, $\bar{\sigma}_\omega = \bar{\sigma}_\mu = \bar{\sigma} \equiv \sigma\varepsilon$ to $O(\varepsilon^3)$ where the detuning parameter σ is defined to be a real, positive number of order $O(\varepsilon^0)$. To show this, let $\mu_A \to \varepsilon\hat{\mu}_A$ and $\hat{\mu}_A \equiv O(\varepsilon^0)$, so that μ_A is in the long wavelength limit. Inverting the linear dispersion relation $\omega_{B0}(\mu_B)$ gives

$$\mu_B(\omega_{B0}) = cos^{-1}\left(1 - \frac{1}{2}\omega_{B0}^2\right).$$

Substituting $\omega_{B0} = 3\omega_{A0} + \sigma\varepsilon = 3\sqrt{2 - 2\cos(\varepsilon\hat{\mu}_A)} + \sigma\varepsilon$ in the previous expression and Taylor expanding $\mu_B(\hat{\mu}_A; \varepsilon, \sigma)$ in the small parameter ε gives

$$\mu_B(\hat{\mu}_A; \varepsilon, \sigma) = (3\hat{\mu}_A + \sigma)\varepsilon + O(\varepsilon^3).$$

Thus,

$$\mu_B \approx 3\mu_A + \bar{\sigma}. \tag{3.25}$$

Hence, Case 2 may be realized for small μ_A (and consequently small ω_{A0}) that are in the long wavelength limit. This one-to-one ratio of frequency to wave number is expected since the slope of the nondimensional linear dispersion relation is approximately 1 in the long wavelength limit where μ_A approaches zero.

One more implication of Eq. (3.25) arises when the substitutions (3.24) are made for ω_{B0} and μ_B in the $O(\varepsilon^0)$ solution (3.14b) – an additional *long spatial scale* $J_1 \equiv \varepsilon p$ arises.

Equation (3.14b) for Case 2, after substitutions, becomes

$$\begin{aligned} x_{p,B}^{(0)}(T_0, T_1, J_1) = \frac{B_0(T_1)}{2} e^{\mathrm{i}(\mu_B p - \omega_{B0} T_0)} + c.c. &= \frac{B_0(T_1)}{2} e^{\mathrm{i}(3\mu_A + \bar{\sigma})p} e^{-\mathrm{i}(3\omega_{A0} + \bar{\sigma})T_0} + c.c. \\ &= \frac{B_0(T_1)}{2} e^{\mathrm{i}(3\mu_A p + \sigma J_1)} e^{-\mathrm{i}(3\omega_{A0} T_0 + \sigma T_1)} + c.c.. \end{aligned} \tag{3.26}$$

From this point forward the procedure follows the development in Sec. 3.1.4.1. However, secular terms are instead proportional to $\exp(\mathrm{i}\mu_A p - \mathrm{i}\omega_{A0} T_0)$ as well as the third harmonic $\exp(\mathrm{i}3\mu_A p - \mathrm{i}3\omega_{A0} T_0)$ so that the secular terms arise from both Eq. (3.15) and Eq. (3.16). Separating the real and imaginary parts of the two solvability conditions yields a set of strongly coupled, nonlinear evolution equations with long spatial (J_1) and temporal dependence (T_1). It happens that the slow time variable T_1 exists in each evolution equation such that they may be written autonomously via substitution of a new variable $\gamma(T_1)$ and its slow time derivative

$$\gamma = -3\beta_A + \beta_B + \sigma T_1 - \sigma J_1 \tag{3.27a}$$

$$\gamma' = -3\beta_A' + \beta_B' + \sigma. \tag{3.27b}$$

Using this fact, the evolution equations may be written in a fashion similar to Eqs. (3.17) as

$$\alpha_A' = \frac{3}{2}\alpha_A^2 \alpha_B \xi \sin(\gamma) \tag{3.28a}$$

$$\alpha_B' = -\frac{1}{6}\alpha_A^3 \xi \sin(\gamma) \tag{3.28b}$$

$$\beta_A' = -\frac{3}{2}\alpha_A \alpha_B \xi \cos(\gamma) + a_1 \alpha_A^2 + a_2 \alpha_B^2 \tag{3.28c}$$

$$\beta_B' = -\frac{1}{6}\frac{\alpha_A^3}{\alpha_B} \xi \cos(\gamma) + b_1 \alpha_A^2 + b_2 \alpha_B^2 - \sigma, \tag{3.28d}$$

where the coefficients a_1, a_2, b_1, b_2 and ξ are most simply expressed as functions of $\omega_{A0} \equiv$

ω_0 given by

$$\begin{aligned}
a_1 &= \frac{3}{8}\omega_0^3 & b_1 &= \frac{1}{4}\omega_0^7 - \frac{3}{2}\omega_0^5 + \frac{9}{4}\omega_0^3 \\
a_2 &= \frac{3}{4}\omega_0^7 - \frac{9}{2}\omega_0^5 + \frac{27}{4}\omega_0^3 & b_2 &= \frac{1}{8}\omega_0^{11} - \frac{3}{2}\omega_0^9 + \frac{27}{4}\omega_0^7 - \frac{27}{2}\omega_0^5 + \frac{81}{8}\omega_0^3 \\
\xi &= -\frac{1}{4}\omega_0^5 + \frac{3}{4}\omega_0^3 & & \qquad (3.29)
\end{aligned}$$

The large state space of Eqs. (3.28) complicates the analysis. Some general observations can be made, though, about the character of the solution in certain limiting cases. The coefficients a_1, a_2, b_1, and b_2 occur in the general form $(a, b)_{1,2} = \sum_n c_n(-1)^{n+1}\omega_0^{2n+1}$, where $c_n > c_{n+1}$ by inspection. Thus, for low frequencies in the long wavelength limit the $c_1\omega_0^3$ terms dominate. Comparison of Eqs. (3.29) with Eqs. (3.20a) and (3.20b) shows that these leading order terms are identical for $r = 3$, and thus the primary difference in the resulting evolution equations of Case 1 and Case 2 is the existence of the $\xi\sin(\gamma)$ and $\xi\cos(\gamma)$ terms in Eqs. (3.28). These terms are responsible for coupling the α_A' and α_B' evolution equations with the β_A' and β_B' equations, and is *usually* negligible for small ω_0 (and hence small ξ).

Numerical integration of the evolution equations in Eq. (3.28) provides additional insight and verification to the previous assertions. The solutions of the differential equations depend on the initial values $\alpha_A(0) = \alpha_{A,0}$, $\alpha_B(0) = \alpha_{B,0}$, $\beta_A(0) = \beta_{A,0}$, and $\beta_B(0) = \beta_{B,0}$, and the parameters ω_0, σ, and ε. Some possible solutions for the evolution equations are illustrated in Fig. 3.3 for $\alpha_{A,0} = \alpha_{B,0} = \alpha_0 = [1, 2, 5]$, $\beta_{A,0} = \beta_{B,0} = 0$, and $\omega_0 = 0.5$, $\sigma = 0$, and $\varepsilon = 0.01$.

The frequency was chosen to illustrate the oscillations clearly; however, $\omega_0 = 0.5$ is at the edge of the long wavelength limit. The amplitudes α_A and α_B tend to oscillate periodically about some fixed point, while the phase corrections β_A and β_B tend to oscillate about some linear functions. Therefore, in the long wavelength limit the wave-wave interaction gives rise to amplitude and frequency modulation. Based on numerical observation, the modulations are negligible for small frequencies in the long wavelength limit so that

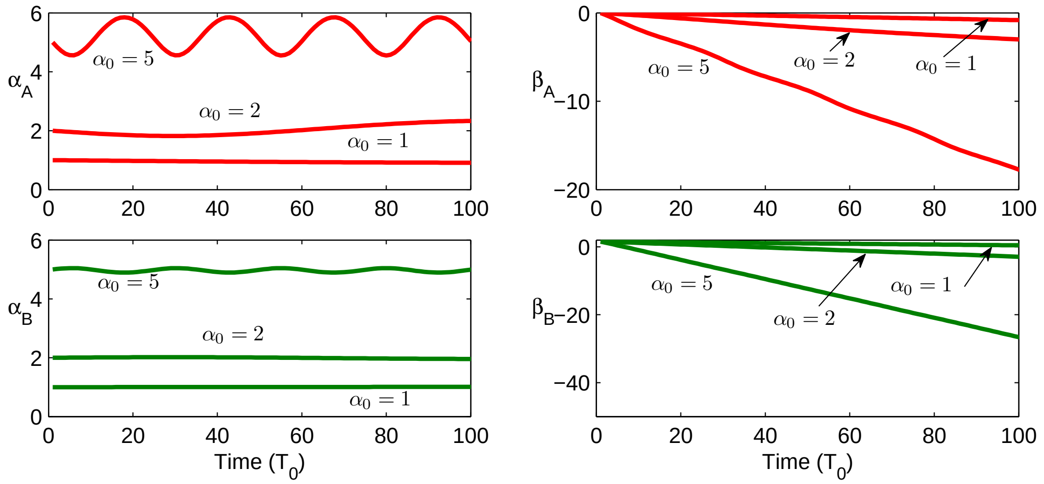

Figure 3.3: Typical solutions for α_A, α_B, β_A, and β_B

$\alpha'_A = 0$, $\alpha'_B = 0$, and β'_A and β'_B are both constant to $O(\varepsilon^1)$. Therefore, even when ω_{A0} and ω_{B0} are commensurate or nearly-commensurate, long wavelength limit wave-wave interactions may be negligible, and the corrected dispersion relations obtained for Case 1 provide a good (and potentially more useful) approximation.

3.1.5 Numerical verification and discussion

Numerical simulation of the mass-spring system depicted in Fig. 3.1 and governed by Eq. (3.3) verifies the presented asymptotic approach [3]. In deriving corrections to the linear dispersion curve, it was assumed that two interacting waves with $O(\varepsilon^0)$ amplitudes existed in a one-dimensional, nonlinear medium away from any forcing. By imposing plane-wave initial conditions and allowing a simulation to run for 100 – 200 nondimensional "seconds," a space-time matrix of displacements was produced. Points on the dispersion curve were located by performing a two-dimensional Fast Fourier Transform (2D FFT) on the displacement matrix.

Figure 3.4 illustrates how the frequency ratio r may be considered as a design parameter in addition to the wave amplitudes for tunable acoustic metamaterials. We seek to obtain a 10% ($\rho_B = 0.1$) frequency shift for a B wave with amplitude $\alpha_A = 2$ and frequency $\omega_{B0}(\mu_B) = r\omega_0 = 1.8$. Then, the parameters α_A and r may be chosen freely to obtain

$\rho_B = 0.1$ in Eq. (3.23) subject only to the restriction that $r > 1$ and $\alpha_A \in \mathbb{R}$ is order $O(\varepsilon^0)$. The parameter sets $[\alpha_A = 4.36, r = 3]$ and $[\alpha_A = 8, r = 5.5]$ were chosen such that these criteria were satisfied. The ratio $\rho_B = 0.1$ determines the dispersion curve of the B wave for *any* set of values α_A and r. However, the dispersion curve for the A wave varies depending on the choice of parameters according to Eq. (3.22). Several simulations were run and overlaid in Fig. 3.4a. The zoomed view in Fig. 3.4b plots the two different dispersion branches that the A wave follows for different choices of the parameters α_A and r.

The ratios ρ_A and ρ_B that were introduced earlier to estimate the uniformity of the expansion increase with ω_0^2. As the frequency $\omega_B = r\omega_0$ increases toward the cutoff frequency, the theoretical frequency corrections become less accurate. Numerical observation suggests that the propensity of the spring-mass chain to generate additional large-amplitude harmonics (comparable to the amplitude of the two injected waves) is responsible for this, owing to additional wave-wave interactions that are not accounted for herein.

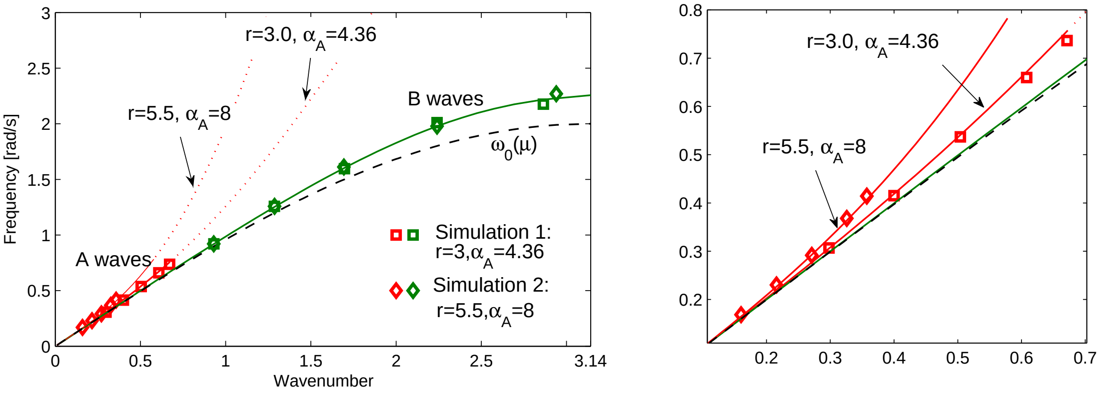

(a) Numerical simulation points

(b) Close-up of $\omega_A^{(1)}$ points

Figure 3.4: A 10% shift at $\omega_{B0} = 1.8$ can be achieved injecting high-amplitude, low frequency waves, or low-amplitude, high-frequency waves

3.1.6 Conclusion

A multiple time scales approach has been shown to yield accurate dispersion characteristics for wave-wave interactions in a discrete nonlinear medium with a cubic material nonlinearity. Evolution equations were derived for a monoatomic chain for both the single-wave and multi-wave scenarios.

The Lindstedt-Poincaré method and multiple time scales approach result in the same dispersion corrections when the resulting evolution equations are autonomous. However, the multiple time scales approach provides more generality than a Lindstedt-Poincaré method in dealing with time-varying amplitude and phase. In most cases, the two-wave interaction scenario results in a different time-invariant dispersion branch for each wave. These branches are parametrized by the wave amplitudes (α_A, α_B), the frequency ratio r, and the magnitude of the nonlinearity. Additional interactions may take place in the long wavelength limit due to frequency and wave number coupling between two waves. These interactions result in amplitude and frequency modulations, although transient effects such as super-harmonic generation may dominate such interactions.

Still, in the long wavelength limit and for small amplitudes, the single-wave dispersion correction in Eq. (3.12) provides a reasonable estimate for the dispersion behavior. Away from the long wavelength limit, such as near the edge of the Brillouin Zone and at larger amplitudes, the single-wave dispersion analysis fails to yield accurate frequency corrections. Hence, the wave-wave interaction analysis presented herein provides a more accurate and complete estimation of the monoatomic chain's dispersion in such cases.

3.2 Monoatomic lattice

3.2.1 Overview

Two-dimensional lattices and periodicity form the building blocks of many phononic crystals and metamaterials. Phononic crystal devices such as wave guides and resonators are formed from the strategic periodic arrangement of two-dimensional unit cells [16, 70, 71]. Crystal lattice planes and graphene sheets also exhibit 2D lattice periodicity where nonlinear restoring forces may arise from inter-atomic attraction and repulsion. For example, as early as 1973 dispersion relation and wave propagation in anharmonic atomic lattices were of interest to researchers [72]. The 2D anharmonic lattice considered herein is very similar to atomic systems and is one of the most fundamental and important systems for understanding and analyzing Bloch wave propagation in two-dimensional geometry. The monoatomic lattice is also unique in that in the long wavelength limit the lattice models wave propagation in membrane systems [73]. Membranes, like strings, exhibit cubic hardening nonlinearities as a result of stretch-induced tension so studying the cubic nonlinearity in the monoatomic system is particularly appropriate.

Wave propagation in two dimensional systems exhibit directionality in addition to other dispersion behaviors exhibited by one dimensional systems (1D). Directionality in 2D structures introduces conceptually new opportunities such as wave beaming, spatial filtering, and imaging. Wave beaming in the two-dimensional beam grillage considered by Langley et. al in [74], while Ruzzene et. al have considered wave beaming in two-dimensional cellular structures [75]. The cubically nonlinear lattice and some variations were studied extensively for single-wave propagation in [63]. They showed that the nonlinear monoatomic lattice exhibits tunable dispersion under the influence of self-action frequency shifts. Tunable parameters included the amplitude of the fundamental Bloch wave and its wave number.

Nonlinear wave interaction in two-dimensions offers a fundamentally different perspective for viewing tunability. The introduction of additional waves can predictably control or alter the behavior of the system, in addition to nonlinear self-action whereby a wave self-adjust its frequency according to local intensity. Wave interaction in two-dimensions provides three new tunable parameters[3]: two wave vector components and an additional wave amplitude (usually termed the *control wave* or *pump wave*). The idea that nonlinear wave interactions can enhance traits in two-dimensional periodic systems has been explored more recently in the photonic crystal community. Panoiu et. al. utilized the Kerr nonlinearity with a pump/control wave to enhance the "superprism" effect, whereby the direction of propagation in the photonic crystal is extremely sensitive to the wavelength and angle of incidence [76]. This chapter aims to continue the development of the multiple scales perturbation presented in Ch. 3 with the intent of realizing wave-tunable dispersion.

The following sections introduce the equation of motion for a single unit cell in the presence of nonlinear restoring springs. A multiple time scale perturbation analysis is applied to determine dispersion frequency shifts for a Bloch wave solution containing two dominant harmonic components. The resulting frequency shift expressions are analyzed and three distinct propagation cases are identified: collinear propagation, orthogonal propagation, and oblique propagation. Numerical simulations validate the expected dispersion shifts. Finally, negative group velocity corrections induced through a control wave are explored as a viable means for achieving amplitude-tunable focus and beam steering that may, ultimately, lead to a phononic superprism effect.

3.2.2 Model description and nonlinear governing equation

The monoatomic lattice equation of motion follows from Newton's second law derived for a unit cell at location indices (p, q). Each mass adjoins four neighbors (top, bottom, left, and right) via springs with nonlinear force-displacement relationships as shown in Fig. 3.5. Individual masses have only one degree of freedom in the out-of-plane direction $\mathbf{e}_3$. The out-of-plane displacements $u_{p,q}$ are described by the open set of nonlinear difference

---

[3] Assuming the presence of two waves

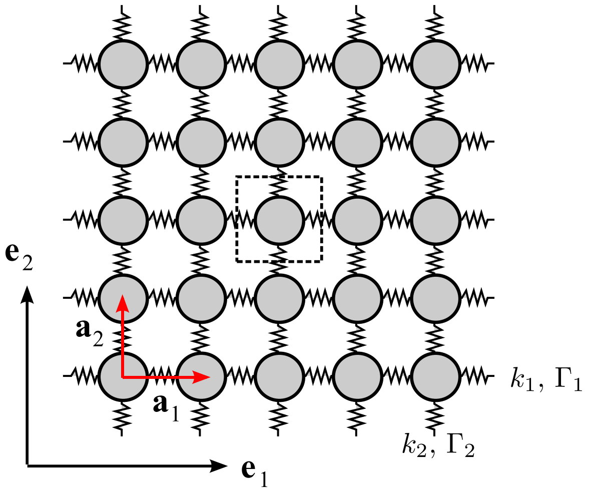

Figure 3.5: Monoatomic lattice configuration with lattice vectors $\mathbf{a}_1$ and $\mathbf{a}_2$. Dashed lines indicate boundaries for the unit cell.

equations

$$m\ddot{u}_{p,q} + k_1(2u_{p,q} - u_{p+1,q} - u_{p-1,q}) + k_2(2u_{p,q} - u_{p,q+1} - u_{p,q-1}) + f^{NL} = 0, \tag{3.30}$$

where m denotes mass, k_1 and k_2 denote linear stiffnesses in the $\mathbf{e}_1$ and $\mathbf{e}_2$ directions, and f^{NL} results from nonlinear stiffness contributions. The nonlinear force term f^{NL} that arises from cubically nonlinear inter-atomic springs is

$$f^{NL} = \Gamma_1(u_{p,q} - u_{p+1,q})^3 + \Gamma_1(u_{p,q} - u_{p-1,q})^3 + \Gamma_2(u_{p,q} - u_{p,q+1})^3 + \Gamma_2(u_{p,q} - u_{p,q-1})^3 \tag{3.31}$$

where Γ_1 and Γ_2 denote nonlinear stiffness coefficients along the $\mathbf{e}_1$ and $\mathbf{e}_2$ directions, respectively. Weak nonlinearity is enforced in the governing equation Eq. (3.30) by specifying nonlinear coefficients to appear at $O(\varepsilon^1)$ for small parameter $|\varepsilon| \ll 1$

$$\Gamma_1 \equiv \varepsilon\hat{\Gamma}_1, \quad \Gamma_2 \equiv \varepsilon\hat{\Gamma}_2, \tag{3.32}$$

and additionally specifying Γ_1 and $\Gamma_2 \approx O(\varepsilon^0)$. The resulting equation is amenable to perturbation analysis. Wave interactions are analyzed using the multiple scales perturbation analysis procedure outlined in Ch. 2.

3.2.3 Multiple scales perturbation analysis

Introduce an asymptotic expansion for the displacement in addition to multiple time scales

$$u_{p,q}(T_i) = u^{(0)}_{p,q}(T_i) + \varepsilon u^{(1)}_{p,q}(T_i) + O(\varepsilon^2) \tag{3.33}$$

where slow time scales are defined according to $T_i \equiv \varepsilon^i t$. Derivatives transform according to Eq. (2.42) where D_i denote derivatives with respect to the $T_i th$ time scale. Ordered perturbation equations result from substitution of Eq. (3.33) and slow time derivatives D_i into Eq. (3.30)

$$O(\varepsilon^0): \quad mD_0^2 u^{(0)}_{p,q} + k_1(2u^{(0)}_{p,q} - u^{(0)}_{p+1,q} - u^{(0)}_{p-1,q}) + k_2(2u^{(0)}_{p,q} - u^{(0)}_{p,q+1} - u^{(0)}_{p,q-1}) = 0 \tag{3.34}$$

$$O(\varepsilon^1): \quad mD_0^2 u^{(1)}_{p,q} + k_1(2u^{(1)}_{p,q} - u^{(1)}_{p+1,q} - u^{(1)}_{p-1,q}) + k_2(2u^{(1)}_{p,q} - u^{(1)}_{p,q+1} - u^{(1)}_{p,q-1}) = -2mD_0 D_1 u^{(0)}_{p,q} - f^{NL}\left(u^{(0)}_{p,q}, u^{(0)}_{p\pm1,q\pm1}\right) \tag{3.35}$$

where the nonlinear function f^{NL} depends only on the $O(\varepsilon^0)$ solution. The $O(\varepsilon^0)$ equation admits a Bloch wave solution

$$u^{(0)}_{p,q} = \frac{1}{2}A(T_1)e^{\mathrm{i}(\boldsymbol{\mu}\cdot\mathbf{r}_{(p,q)} - \omega T_0)} + c.c. \tag{3.36}$$

for Bloch wave numbers $\boldsymbol{\mu} = [\mu_1, \mu_2]$ and position vector $\mathbf{r}_{(p,q)} = [p, q]$. The complex amplitude $A(T_1)$ varies with slow time T_1 and is therefore considered constant at $O(\varepsilon^0)$. The zero-order equation, with application of the Bloch wave solution Eq. (3.36), reduces to

$$\left[-\omega^2 m + k_1(2 - e^{\mathrm{i}\mu_1} - e^{-\mathrm{i}\mu_1}) + k_2(2 - e^{\mathrm{i}\mu_2} - e^{-\mathrm{i}\mu_2})\right] u^{(0)}_{p,q} = 0, \tag{3.37}$$

Nontrivial solutions $u^{(0)}_{p,q} \neq 0$ exist when only when the dispersion relation is satisfied. Setting the expression in brackets equal to zero produces the linear dispersion relationship

$$\omega(\boldsymbol{\mu}) = \sqrt{\omega_{n1}^2(2 - 2\cos(\mu_1)) + \omega_{n2}^2(2 - 2\cos(\mu_2))} \tag{3.38}$$

where $\omega_{n1} \equiv \sqrt{k_1/m}$ and $\omega_{n2} \equiv \sqrt{k_2/m}$ denote characteristic frequencies. Next, corrections to this dispersion relationship due to weakly nonlinear wave interactions are considered.

As discussed in Ch. 2, dispersion shifts must be calculated for a specific frequency content and amplitude ordering. The input signal considered for wave interactions is composed of two Bloch waves at ω_{A0} and ω_{B0} and amplitudes ordered such that both signals are present in the $O(\varepsilon^0)$ equation

$$u_{p,q}^{(0)} = \frac{1}{2}A(T_1)\exp(\mathrm{i}\boldsymbol{\mu}_A \cdot \boldsymbol{r} - \mathrm{i}\omega_{A0}T_0) + \frac{1}{2}B(T_1)\exp(\mathrm{i}\boldsymbol{\mu}_B \cdot \boldsymbol{r} - \mathrm{i}\omega_{B0}T_0) + c.c. \tag{3.39}$$

The wave numbers $\boldsymbol{\mu}_A = [\mu_{A1}, \mu_{A2}]$ and $\boldsymbol{\mu}_B = [\mu_{B1}, \mu_{B2}]$ correspond to a primary wave at ω_{A0} and a control wave at ω_{B0} through the linear dispersion relationship Eq. (3.38), respectively. The frequencies ω_{A0} and ω_{B0} are incommensurate by definition. Indeed, the $O(\varepsilon^0)$ equation is identically satisfied for this multi-frequency Bloch wave solution.

A multiple time scales solution informed by a Lindstedt-Poincaré type phase expansion yields the resulting frequency corrections. The amplitude functions $A(T_1)$ and $B(T_1)$ take the form

$$A(T_1) = \alpha_A(T_1)e^{\mathrm{i}\beta_A(T_1)} \quad \text{and} \quad B(T_1) = \alpha_B(T_1)e^{\mathrm{i}\beta_B(T_1)} \tag{3.40}$$

for amplitudes α_A and α_B of $O(1)$. As per the discussion in 2.4.2, the amplitudes α_A and α_B will be constant with respect to T_1 time scales. The time-varying phase terms β_A and β_B result in instantaneous frequency shifts. Lindstedt-Poincaré type solutions correspond to the situation where the β_A and β_B depend linearly on T_1.

We can take, without loss of generality, the indices $p = 0$ and $q = 0$ for the central unit cell. Terms appearing on the right of the $O(\varepsilon^1)$ equation with $\exp(\mathrm{i}\omega_{A0}T_0)$ or $\exp(\mathrm{i}\omega_{B0}T_0)$ time-dependence result in primary resonances, and therefore secular expansions. Collecting these terms and setting the coefficients S_A and S_B to zero, respectively, produces two complex equations. The first of the secular equations is

$$
\begin{aligned}
S_A = {} & \frac{3}{2}\Gamma_1{\alpha_B}^2\alpha_A e^{\mathrm{i}\beta_A T_1} e^{\mathrm{i}\mu_{B1}} + \frac{3}{2}\Gamma_1{\alpha_B}^2\alpha_A e^{\mathrm{i}\mu_{A1}} e^{\mathrm{i}\beta_A T_1} + \frac{3}{2}\,\frac{\Gamma_1{\alpha_B}^2\alpha_A e^{\mathrm{i}\beta_A T_1}}{e^{\mathrm{i}\mu_{A1}}} \\
& + \frac{3}{2}\,\frac{\Gamma_1{\alpha_B}^2\alpha_A e^{\mathrm{i}\beta_A T_1}}{e^{\mathrm{i}\mu_{B1}}} + m_1\alpha_A\beta_A\omega_A e^{\mathrm{i}\beta_A T_1} - \frac{3}{4}\Gamma_2{\alpha_B}^2\alpha_A e^{\mathrm{i}\mu_{A_2}} e^{\mathrm{i}\beta_A T_1} e^{\mathrm{i}\mu_{B2}} \\
& - \frac{3}{4}\,\frac{\Gamma_2{\alpha_B}^2\alpha_A e^{\mathrm{i}\mu_{A2}} e^{\mathrm{i}\beta_A T_1}}{e^{\mathrm{i}\mu_{B2}}} - \frac{3}{4}\,\frac{\Gamma_2{\alpha_B}^2\alpha_A e^{\mathrm{i}\beta_A T_1} e^{\mathrm{i}\mu_{B2}}}{e^{\mathrm{i}\mu_{A2}}} - \frac{3}{4}\,\frac{\Gamma_2{\alpha_B}^2\alpha_A e^{\mathrm{i}\beta_A T_1}}{e^{\mathrm{i}\mu_{A2}} e^{\mathrm{i}\mu_{B2}}} \\
& - \frac{3}{4}\Gamma_1{\alpha_B}^2\alpha_A e^{\mathrm{i}\mu_{A1}} e^{\mathrm{i}\beta_A T_1} e^{\mathrm{i}\mu_{B1}} - \frac{3}{4}\,\frac{\Gamma_1{\alpha_B}^2\alpha_A e^{\mathrm{i}\beta_A T_1}}{e^{\mathrm{i}\mu_{A1}} e^{\mathrm{i}\mu_{B1}}} - \frac{3}{4}\,\frac{\Gamma_1{\alpha_B}^2\alpha_A e^{\mathrm{i}\beta_A T_1} e^{\mathrm{i}\mu_{B1}}}{e^{\mathrm{i}\mu_{A1}}} \\
& \qquad + \ldots \\
& - 9/4\,\Gamma_2{\alpha_A}^3 e^{\mathrm{i}\beta_A T_1} - 9/4\,\Gamma_1{\alpha_A}^3 e^{\mathrm{i}\beta_A T_1} = 0,
\end{aligned}
\tag{3.41}
$$

where some terms have been omitted for brevity; a similar equation results for ω_{B0} and has been omitted. The real and imaginary components of each of the two equations $S_A = 0$ and $S_B = 0$ must vanish independently such that

$$\Re(S_A) = \Re(S_B) = \Im(S_A) = \Im(S_B) = 0. \tag{3.42}$$

The resulting expressions, termed *solvability conditions* or *evolution equations*, describe the slow time evolution of the amplitude and phase. The imaginary equations reveal, as expected, that amplitudes α_A and α_B are constant with T_1 time scales. The other two evolution equations may be solved for the the instantaneous frequency corrections $\beta_A(T_1)$ and $\beta_B(T_1)$. The solution of the ordinary differential equations yields

$$
\begin{aligned}
\beta_A(T_1) = {} & \frac{3}{8}\frac{\hat{\Gamma}_1}{m\omega_{A0}}\Big[\alpha_A^2 f(\mu_{A1})^2 + 2\alpha_B^2 f(\mu_{A1}) f(\mu_{B1})\Big]T_1 \\
& + \frac{3}{8}\frac{\hat{\Gamma}_2}{m\omega_{A0}}\Big[\alpha_A^2 f(\mu_{A2})^2 + 2\alpha_B^2 f(\mu_{A2}) f(\mu_{B2})\Big]T_1
\end{aligned}
\tag{3.43}
$$

$$\text{and} \tag{3.44}$$

$$
\begin{aligned}
\beta_B(T_1) = {} & \frac{3}{8}\frac{\hat{\Gamma}_1}{m\omega_{B0}}\Big[\alpha_B^2 f(\mu_{B1})^2 + 2\alpha_A^2 f(\mu_{A1}) f(\mu_{B1})\Big]T_1 \\
& + \frac{3}{8}\frac{\hat{\Gamma}_2}{m\omega_{B0}}\Big[\alpha_B^2 f(\mu_{B2})^2 + 2\alpha_A^2 f(\mu_{A2}) f(\mu_{B2})\Big]T_1,
\end{aligned}
\tag{3.45}
$$

where the function $f(\theta)$ is defined as

$$f(\theta) \equiv 2 - 2\cos(\theta). \tag{3.46}$$

The function $f(\theta)$ is recognized as the squared dispersion relation for the 1D mono-atomic chain[4].

The linearity of $\beta_A(T_1)$ and $\beta_B(T_1)$ on slow time scale T_1 permits the definitions $\omega_{A1} \equiv \beta_A/T_1$ and $\omega_{B1} \equiv \beta_B/T_1$ such that a Lindstedt-Poincaré type asymptotic series in ε describes frequency corrections to ω_A and ω_B as

$$\omega_A(\boldsymbol{\mu_A}, \boldsymbol{\mu_B}) = \omega_{A0}(\boldsymbol{\mu_A}, \boldsymbol{\mu_B}) + \varepsilon\omega_{A1}(\boldsymbol{\mu_A}, \boldsymbol{\mu_B};\ \alpha_A, \alpha_B, \hat{\Gamma}_1, \hat{\Gamma}_2) \tag{3.47}$$

$$\text{and} \tag{3.48}$$

$$\omega_B(\boldsymbol{\mu_A}, \boldsymbol{\mu_B}) = \omega_{B0}(\boldsymbol{\mu_A}, \boldsymbol{\mu_B}) + \varepsilon\omega_{B1}(\boldsymbol{\mu_A}, \boldsymbol{\mu_B};\ \alpha_A, \alpha_B, \hat{\Gamma}_1, \hat{\Gamma}_2), \tag{3.49}$$

where the frequency corrections are given explicitly as

$$\begin{aligned} \omega_{A1} = {} & \frac{3}{8}\frac{\hat{\Gamma}_1}{m\sqrt{\omega_{n1}^2 f(\mu_{A1}) + \omega_{n2}^2 f(\mu_{A2})}}\Big[\alpha_A^2 f(\mu_{A1})^2 + 2\alpha_B^2 f(\mu_{A1})f(\mu_{B1})\Big] \\ & + \frac{3}{8}\frac{\hat{\Gamma}_2}{m\sqrt{\omega_{n1}^2 f(\mu_{A1}) + \omega_{n2}^2 f(\mu_{A2})}}\Big[\alpha_A^2 f(\mu_{A2})^2 + 2\alpha_B^2 f(\mu_{A2})f(\mu_{B2})\Big] \end{aligned} \tag{3.50}$$

$$\begin{aligned} \omega_{B1} = {} & \frac{3}{8}\frac{\hat{\Gamma}_1}{m\sqrt{\omega_{n1}^2 f(\mu_{B1}) + \omega_{n2}^2 f(\mu_{B2})}}\Big[\alpha_B^2 f(\mu_{B1})^2 + 2\alpha_A^2 f(\mu_{A1})f(\mu_{B1})\Big] \\ & + \frac{3}{8}\frac{\hat{\Gamma}_2}{m\sqrt{\omega_{n1}^2 f(\mu_{B1}) + \omega_{n2}^2 f(\mu_{B2})}}\Big[\alpha_B^2 f(\mu_{B2})^2 + 2\alpha_A^2 f(\mu_{A2})f(\mu_{B2})\Big] \end{aligned}. \tag{3.51}$$

3.2.4 Analysis of predicted dispersion shifts

Equations (3.50) and (3.51) depend on the input wave vectors $\boldsymbol{\mu}_A$ and $\boldsymbol{\mu}_B$ in a complicated manner. The qualitative nature of these dispersion shifts relies heavily on the behavior of $f(\theta)$. Several key results are evident with the observations $f(0) = 0$ and $f(-\theta) = f(\theta)$:

1. **Collinear wave vectors** Two waves which propagate collinearly along a lattice vector interact as if propagation were one-dimensional.

---

[4] With this definition, the dispersion relationship for the 2D monoatomic lattice may be written as $\omega = \sqrt{\omega_{n1}^2 f(\mu_1) + \omega_{n2}^2 f(\mu_2)}$.

2. **Orthogonal wave vectors** Two waves which propagate with orthogonal wave vectors aligned to the lattice vectors do not interact, and receive frequency shifts due only to self-action.

3. **Oblique wave vectors** Two waves propagating with oblique wave vectors do interact according to the derived relationship.

Figure 3.6 depicts each of these scenarios schematically. Case 1 describes the situation where $\boldsymbol{\mu}_A \cdot \mathbf{a}_2 = 0$ and $\boldsymbol{\mu}_B \cdot \mathbf{a}_2 = 0$, or alternatively $\boldsymbol{\mu}_A \cdot \mathbf{a}_1 = 0$ and $\boldsymbol{\mu}_B \cdot \mathbf{a}_1 = 0$. This case reduces to the 1D monoatomic array analyzed in Ch. 3. A special case of this occurs during resonant wave propagation whereby counter-propagating waves are described with $\boldsymbol{\mu}_B = -\boldsymbol{\mu}_A$. Case 2 describes orthogonal wave propagation only when wave numbers are aligned to lattice vectors; in this case, dispersion corrections to $O(\varepsilon^1)$ do not indicate any wave interaction. Case 3 depicts the most general situation where arbitrary wave vectors interact. Each of these three cases is validated numerically.

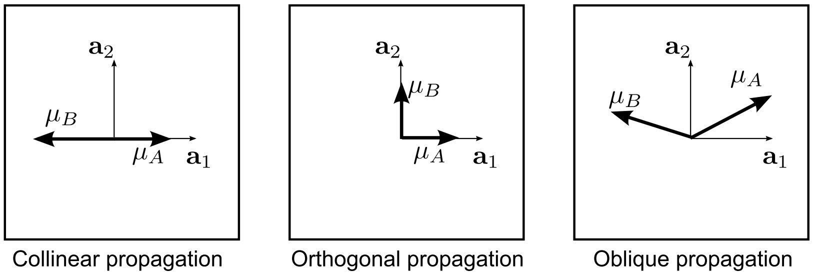

Figure 3.6: Three cases of wave-wave interaction in the monoatomic lattice.

There are additional important aspects of the predicted dispersion shifts which are subtle: Brillouin zone symmetry is retained, and group velocity remains zero along the Brillouin zone boundaries. Figure 3.7 depicts Brillouin zone symmetry in the linear dispersion relation $\omega_0(\boldsymbol{\mu})$ and the frequency correction $\omega_{A1}(\boldsymbol{\mu}_A, \boldsymbol{\mu}_B)$ evaluated with horizontal and oblique control waves $\boldsymbol{\mu_B}$ and $\boldsymbol{\mu_{B'}}$, respectively. The linear dispersion relationship in Fig. 3.7a depicts $\omega_0(\mu_1, \mu_2)$ and is symmetric with respect to both μ_1 and μ_2. Any reflection,

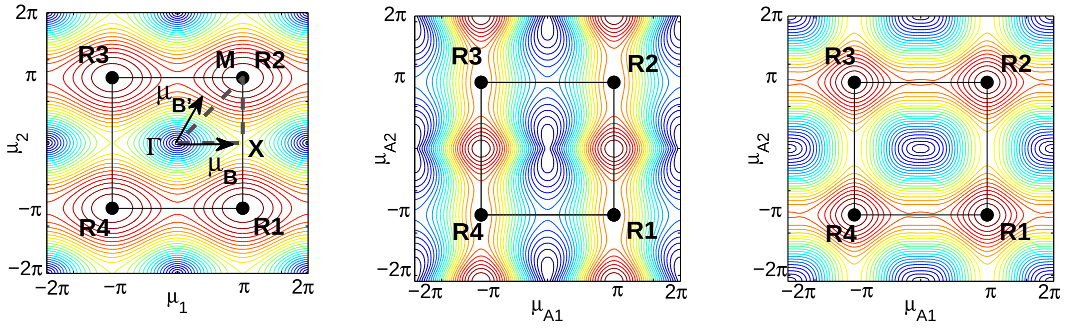

(a) ω_0 (b) $\omega_{A1}(\boldsymbol{\mu}_A, \boldsymbol{\mu}_B)$ (c) $\omega_{A1}(\boldsymbol{\mu}_A, \boldsymbol{\mu}_{B'})$

Figure 3.7: Brillouin zone symmetry is retained by dispersion shifts resulting from wave interactions. (a) Linear dispersion relationship with the FBZ identified by points R_i, $i = 1..4$. Wave vectors $\boldsymbol{\mu}_B = [3.0, 0.0]$ and $\boldsymbol{\mu}_{B'} = [1.0, 2.1]$ correspond to horizontal and oblique control waves used for frequency corrections plotted in (b) and (c), respectively.

or combination of reflections, of a wave vector $\boldsymbol{\mu}$ about axes μ_1 or μ_2 yields the same frequency. The same symmetry is retained by frequency corrections ω_{A1} and ω_{B1}. Figures 3.7b and 3.7c depict this symmetry for the ω_{A1} correction in Eq. (3.50) by evaluating the expression over the entire First Brillouin zone (FBZ), subject to a given control wave at wave number $\boldsymbol{\mu}_B$. It is easily verified that $\omega_{A1}(\boldsymbol{\mu}_A, \boldsymbol{\mu}_B)$ and $\omega_{B1}(\boldsymbol{\mu}_A, \boldsymbol{\mu}_B)$ are symmetric for all combinations of $\boldsymbol{\mu}_A$ and $\boldsymbol{\mu}_B$ since $f(-\theta) = f(\theta)$ and $f(\theta) \geq 0 \; \forall \; \theta \; \in \mathbb{R}$.

Less obvious is the fact that the group velocity of the corrected dispersion relationships ω_A and ω_B remains zero at the appropriate edges of the FBZ. Let $\mathbf{c}_{gA} = \mathbf{c}_{gA}^{(0)} + \mathbf{c}_{gA}^{(1)}$ and $\mathbf{c}_{gB} = \mathbf{c}_{gB}^{(0)} + \mathbf{c}_{gB}^{(1)}$, where $\mathbf{c}_{gA}^{(1)}$ and $\mathbf{c}_{gA}^{(1)}$ denote corrections to the linear group velocity from Eqs. (3.50) and (3.51), respectively. A group velocity calculation using the chain rule on the frequency correction Eq. (3.50) expresses this relationship as

$$\mathbf{c}_{gA}^{(1)} = \nabla_{\mu}\omega_{A1} = \frac{\partial \omega_{A1}}{\partial f(\mu_{A1})}\frac{\partial f(\mu_{A1})}{\partial \mu_{A1}}\mathbf{b}_1 + \frac{\partial \omega_{A2}}{\partial f(\mu_{A2})}\frac{\partial f(\mu_{A2})}{\partial \mu_{A2}}\mathbf{b}_2. \tag{3.52}$$

The function $f(\theta)$ has derivative $df/d\theta = 2\sin(\theta)$; therefore, along the FBZ edges where $\mu_{1,2} = \pm\pi$ the group velocity evaluates to zero along boundary normal directions.

The group velocity correction may be used to dynamically steer wave beams through the application of a control wave $\boldsymbol{\mu}_B$. The monoatomic lattice $k_1 = k_2$ exhibits a known singularity in the vicinity of $\boldsymbol{\mu}_A = [\pi/2, \pi/2]$ whereby wave beams form along diagonals

[63]. Express the group velocity correction $\mathbf{c}_{gA}^{(1)} = c_{gA}(\cos\theta_g \mathbf{b}_1 + \sin\theta_g \mathbf{b}_2)$ where c_{gA} denotes group velocity amplitude at an angle of θ_g. An interesting situation results when $\theta_g < 0$; group velocity corrections correspond to negative angles θ_g. Equation 3.52 evaluated in the vicinity of $\boldsymbol{\mu}_A = [\pi/2, \pi/2]$ yields an expression describing the control wave numbers which produce negative angled corrections[5]

$$\cos(\mu_{B2}) = \frac{1}{6}[6 - r_g r_A^2 + 7r_A^2 - 6r_g f(\mu_{B1})], \tag{3.53}$$

where $r_g \equiv \Gamma_1/\Gamma_2$ and $r_A \equiv \alpha_A/\alpha_B$ denote nonlinear stiffness and amplitude ratios, respectively. The solution of this equation yields two distinct solution regions: (I) $\theta_g < 0$ and (II) $\theta_g > 0$. Figure 3.8a depicts a wave beam of a linear system (black, dashed) and the corrected wave beam (black, solid) as a result of a negative group velocity correct (red vector). Figures 3.8b and 3.8c depict regions (I) and (II) where negative group velocity corrections exist for low and moderate amplitude ratios. This phenomena is unique to nonlinear lattices subject to wave-wave interactions; negative group velocity corrections, as depicted in Fig. 3.8, cannot be realized under nonlinear self-action corrections. This phenomena offers a unique opportunity for beam steering and tunable focusing; example applications

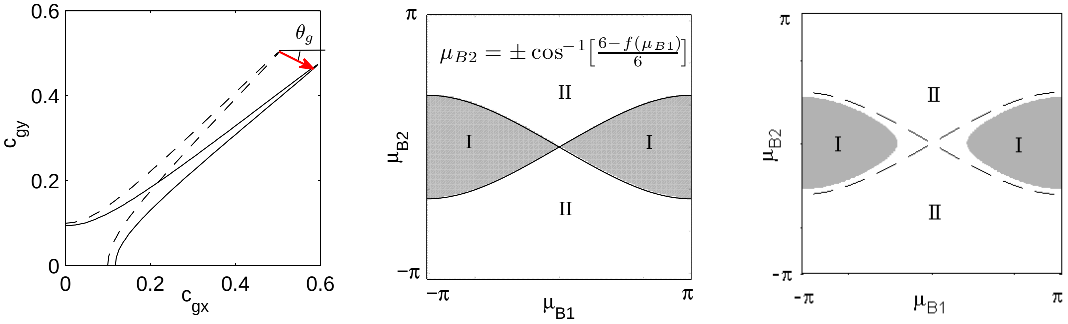

(a) Beam steering ($\omega_{A0} = 1.99$)

(b) $r_g = 1,\ r_A \ll 1$

(c) $r_g = 1,\ r_A = 1/3$

Figure 3.8: Negative group velocity corrections are a unique result of wave interaction. A linear wave beam (black, dashed) receives a negative group velocity correction (labeled red vector) to produce beam shifting (black, solid). Control waves which achieve $\theta_g < 0$ are found in region (I).

---

[5] Eq. (3.53) refers to the system described by $\omega_{n1} = \omega_{n2} = 1.0$

are presented later.

3.2.5 Numerical simulation validation cases

Time-domain finite-element simulations confirm the accuracy of analytical perturbation calculations. Simulations are constructed using a large array of masses and springs with unit parameters $m = 1\,\mathrm{kg}$ and $k_1 = k_2 = 1\,\mathrm{N\,m^{-1}}$ such that boundary reflections are not encountered. Bloch waves are introduced into the system by means of specifying initial conditions; numerical integration for a specified time interval of approximately 40 s results in space-time data for each mass. Each mass oscillates at a corrected frequency, depending on the initial amplitude, which is measurable from its time response signal.

3.2.5.1 Analysis method

A nonlinear least-squares model provides an accurate method of quantifying the frequency shift over short time periods. This method also provides quantified uncertainty levels for the determined parameter values, although in the cases presented the uncertainty is negligible. The nonlinear least-squares curve fit method attempts to minimize the sum of squared error between trial function $\mathcal{F}(\mathbf{x})$ and a provided signal $u(t)$. This analysis method is first analyzed without the influence of wave interactions, i.e. $\alpha_B = 0$. The left subfigure of figure 3.9 depicts the wave field corresponding to $\boldsymbol{\mu}_A = [1.8,\ 0]$ and amplitude $\alpha_A = 2$. The wave vector is aligned to the $\mathbf{a}_1$ lattice vector. The right subfigure shows the displacement field evaluated for $u_{p,q}(x, t)$ located centrally in the wave field such that boundary reflections have no influence for the times considered.

Figure 3.10 displays frequency shifts ω_{A1} as a function of the primary wave amplitude α_A. Frequency shifts obtained from numerical simulation (triangles) match the theoretical predictions almost exactly for amplitudes $\alpha_A < 2$. Simulation results for amplitudes $\alpha_A > 2$ diverge from theoretical perturbation calculations. This behavior is typical of asymptotic solutions where amplitude or frequency corrections exceed the $O(\varepsilon^0)$ values. Indeed, the frequency correction at $\alpha_A = 3$ results in a 7.2% to the linear frequency $\omega_{A0} = 1.567$. We

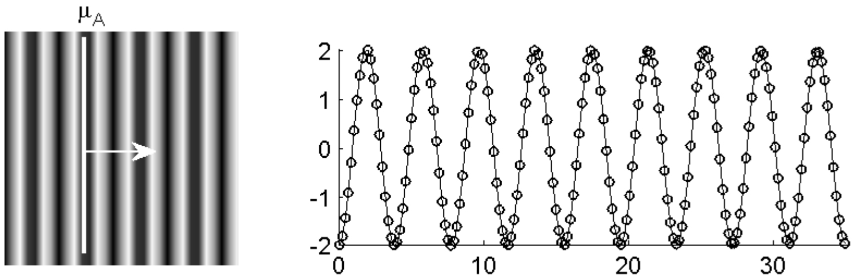

Figure 3.9: Initial wave field and corresponding displacement probe located centrally in the field ($p = 40$, $q = 40$). Markers denote a nonlinear least squares fit while solid lines indicate the numerical simulation time signal.

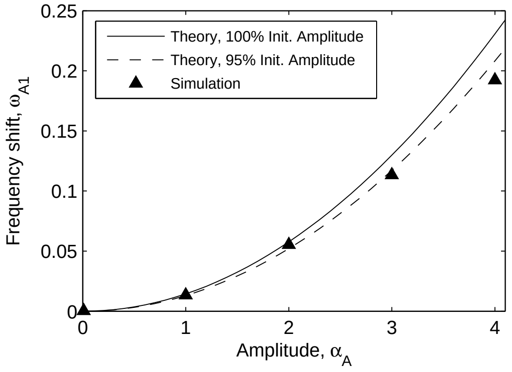

Figure 3.10: Numerical simulation results for frequency-amplitude relationship using a least-squares curve fit method

note that the theoretical frequency corrections tend to overestimate the resulting frequency shift due to energy transfer from a primary wave to sub- and super-harmonics. The dotted line in Fig. 3.10 represents theoretical frequency corrections evaluated for the same probe location with an amplitude $\alpha_A^* = 0.95\alpha_A$. This curve better fits data at higher amplitudes (e.g. $\alpha_A = 3$) where additional harmonic generation causes energy leakage from the primary harmonic. Thus, it is likely that frequency corrections will be less than predicted by a perturbation analysis when weakly nonlinear assumptions are no longer valid.

3.2.5.2 Orthogonal and oblique interaction

Numerical simulation of Case 2 (orthogonal interaction along a lattice vector) and Case 3 (general, oblique wave vectors) is presented next. Collinear propagation has been thoroughly addressed in Ch. 3. Recall that during the course of wave interaction, dynamic frequency shifts exist for both the primary wave ω_{A1} and the control wave ω_{B1}. In this section, emphasis is placed on validating ω_{A1}.

Figure 3.11 depicts initial wave fields for both orthogonal and oblique wave interaction. Each validation case considers a control wave a constant amplitude $\alpha_B = 2.0$ while the amplitude of the primary wave α_A varies from 0 to 2 (depicted in Fig. 3.12). Primary and control Bloch wave fields correspond to randomly generated wave vectors $\boldsymbol{\mu}_A = [1.811,\ 0.0]$ and $\boldsymbol{\mu}_B = [0.0,\ 1.043]$ for orthogonal propagation and $\boldsymbol{\mu}_A = [0.831,\ -2.528]$ and $\boldsymbol{\mu}_B = [-1.391,\ 0.294]$ for oblique propagation. Initial wave fields are depicted in the left graphics. Sub-plots on the right depict the multifrequency numerical time-domain responses (solid), along with least-squares data fits of the form $f(t) = \tilde{A}\cos(\tilde{\omega}_A t + \tilde{\theta}_A) + \tilde{B}\sin(\tilde{\omega}_B t + \tilde{\theta}_B)$ (markers). Least-squares data fit parameters are denoted by $(\tilde{\ })$. The frequencies associated with the fit agree well with the time-domain responses.

Amplitude-dependent frequency shifts ω_{A1} are plotted in Fig. 3.12. Solid lines denote theoretical frequency shifts, while markers indicate the frequencies extracted from simulation data. All simulation cases agree very well with perturbation theory. Figure 3.12a also overlays the result for no wave interaction presented previously in Fig. 3.10. As expected, two waves propagating along a lattice vector experience no additional frequency shift from the presence of control wave. In contrast, Fig. 3.12b depicts a nonzero frequency shift even for $\alpha_A \approx 0$ owing to dynamic lattice anisotropy introduced from the presence of $\boldsymbol{\mu}_B$. This result unique to wave-interaction has not been previously documented to the author's knowledge.

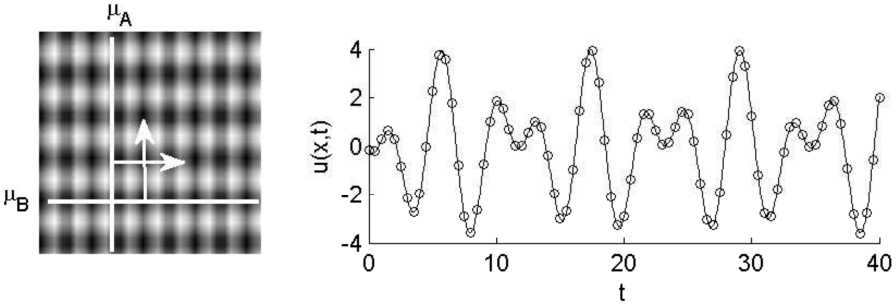

(a) Orthogonal propagation

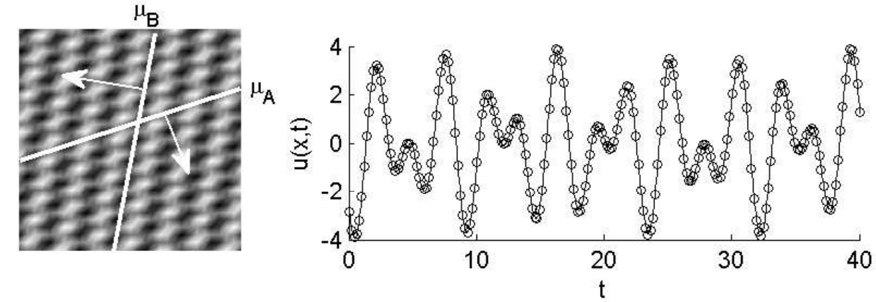

(b) Oblique propagation

Figure 3.11: Initial wave field for orthogonal and oblique wave interaction (for $\alpha_A = 2.0$) and corresponding displacement probe located centrally at $p = 40$, $q = 40$. Symbols demarcate the time series corresponding to the nonlinear least-squares curve fit for frequency, phase, and amplitude.

The idea that lattice anisotropy can be dynamically introduced through nonlinear control wave interaction is a powerful concept for nonlinear metamaterials and phononic devices. Dynamic anisotropy is explored next in an amplitude-tunable focus device which employs wave dynamic wave beaming.

3.2.6 Application: Amplitude-tunable focusing

The idea behind amplitude-tunable focusing was first explored in Sec. 3.2.4 where a group velocity analysis of dispersion frequencies exhibited possible negative group velocity corrections. Negative group velocity corrections offer the potential for tuning the direction of wave beams. Moreover, the constructive interference of two wave beams may be used to develop a metamaterial variation of the high-intensity focused ultrasound devices employed in medical procedures to locally heat or destroy tissue [77].

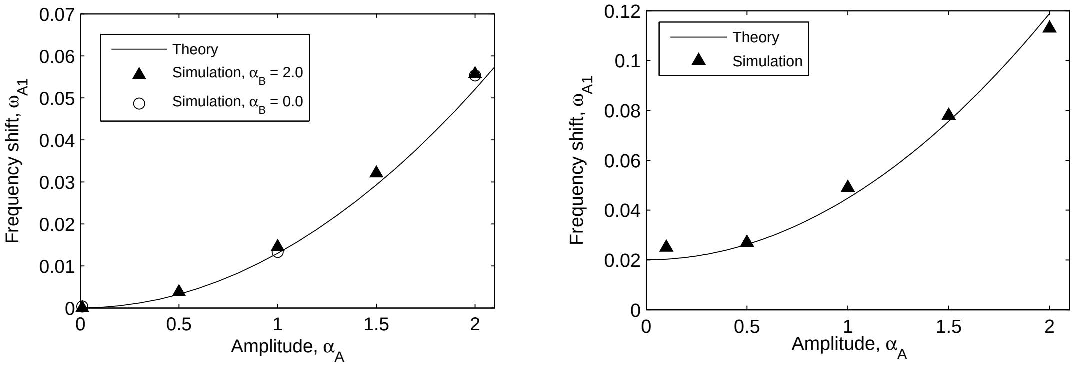

(a) Orthogonal propagation

(b) Oblique propagation

Figure 3.12: Numerical simulation results for orthogonal and oblique wave interaction. Theoretical results (line) are validated by numerical time-domain simulations (markers). Unlike orthogonal interaction (a), oblique interactions (b) result in nonzero frequency shifts for low-amplitude A waves.

Numerical validation of conjectures described in Sec. 3.2.4 are presented in Fig. 3.13. A control wave with wave number $\boldsymbol{\mu}_B = [3.0, 0.0]$ was injected into the nonlinear material ($r_g = 1$). At time $t = 0$, a centrally located point source forms wave beams along the diagonals. Solid black lines depict theoretical beam trajectories; dotted lines indicate low-amplitude (linear) trajectories for comparison. Root-mean-square displacements from numerical simulations are overlayed with theoretical beam trajectories. In order to visualize the primary wave field resulting from the point source, a notch filter was applied to the control wave frequency for each frame by transforming spatial data into the wave vector domain.

Increasing the control wave amplitude causes the beam to converge along the horizontal direction. At very high amplitudes $\alpha_B = 4.0$ as seen in Fig. 3.13c, the lattice response loses complete symmetry which may suggest more efficient transfer of energy in the direction of the control wave vector. Regardless of this, numerical simulations agree strongly with analytical group velocity calculations.

The same principle may be applied to an amplitude-tunable focus device (ATFD) as depicted schematically in Fig. 3.14. The ATFD operates on the principal of constructive

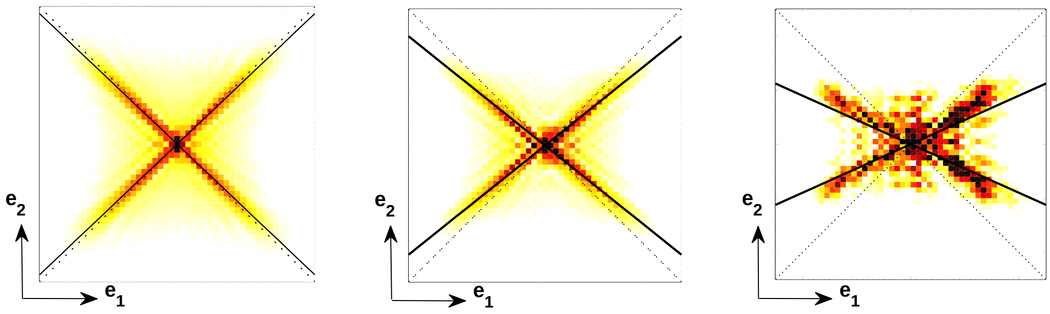

(a) $\alpha_B = 1.0$ (b) $\alpha_B = 2.0$ (c) $\alpha_B = 4.0$

Figure 3.13: Wave beam steering using a control wave with $\boldsymbol{\mu}_B = [3.0, 0.0]$ and a point source excitation at $\omega = 2.0$. Increasing levels of control wave amplitude α_B shown in (a) – (c) vary the beam angle. Solid lines indicate a theoretical beam path; dashed lines indicate the low-amplitude beam path for comparison.

interference. Two identical sources located at the edge of a nonlinear metamaterial provide tunable wave beams. At low amplitudes, the focal point (FP) lies on the mid-plane (focal plane) at a distance of half the source separation[6]. The presence of a control wave produces

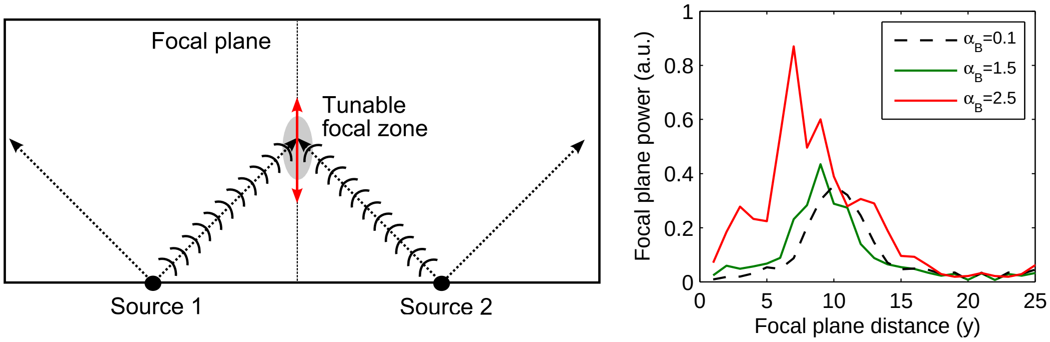

(a) Device schematic (b) Focal point

Figure 3.14: (a) Schematic of a tunable focus device which utilizes constructive interference on a central focal plane. (b) Power distributions calculated along the focal plane from numerical simulation results reveal a sharpening of the focal point (see Fig. 3.15 also) and tunable distance.

dynamic lattice anisotropy which adjusts the wave beam angle. By varying the intensity of the control wave, the FP moves toward or away from the sources. Numerical simulations of the ATFD at various amplitudes confirm the expected behavior as depicted in Figs. 3.14b

---

[6] This is because the wave beams form at 45 degree angles in the system considered

and 3.15. Figure 3.14b depicts the power distribution (a.u.) evaluated along the focal plane for three control wave amplitudes. An unexpected and positive consequence of the focusing mechanism is a distinct peak sharpening relative to the low-amplitude/linear scenario. The low-amplitude case (black dashed) exhibits a broader FP than do the cases with greater control wave amplitude (green and red). Figure 3.15 depicts a distinct change in the FP location. Indeed, the FP has shifted toward the sources from $y = 10.0$ to approximately $y = 6.0$, a 40% location change.

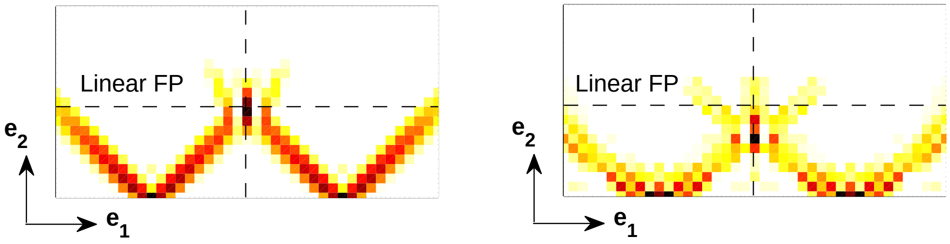

(a) $\alpha_B = 0.1$ (b) $\alpha_B = 2.5$

Figure 3.15: Time-domain simulation results for a tunable focus device. In the presence of a control wave field ($\boldsymbol{\mu}_B = [3.0, 0.0]$), dynamic anisotropy introduced into the alters the focal point (FP) distance and sharpness. Dashed lines indicate the focal plane.

3.2.7 Conclusions

Nonlinear wave interactions in the monoatomic lattice result in unique dispersion qualities that cannot be reproduced through simple self-action. In particular, a small but finite-amplitude control wave can modify the dispersion relation of a control wave through wave interaction. These wave interactions take place in all directions, with the exception of orthogonal propagation aligned to a lattice vector. Even infinitesimally small primary waves may experience dispersion frequency shifts as a result of other harmonic content present in the lattice.

Frequency shifts are intimately connected with group velocity and thus wave beaming directions. The possibility of negative group velocity corrections may result from the presence of control waves with properly selected wave vectors. Such wave vector combinations can be used to control wave beam directionality for use in devices such as the amplitude-tunable focus device presented.

3.3 Multi-DOF Systems: Diatomic chain

3.3.1 Overview

The diatomic chain offers a convenient model for assessing dispersion effects in bi-layered systems. The diatomic chain also exhibits all of the complexities required for extending the multiple scales analysis for wave interactions for continuous media: namely, the existence of non-trivial Bloch wave modes. The model and governing equations first presented. Then, the multiple scales dispersion analysis presented in Chapter 2 is applied to the system of weakly nonlinear equations. Frequency-corrections obtained for a primary wave under the influence of a control wave are evaluated. Finally, a first look at the variation of mass and stiffness ratios on wave interaction is considered.

3.3.2 Model description and nonlinear governing equations

The diatomic chain exhibits additional complexity as compared to a monoatomic system because nontrivial Bloch wave modes exist. The diatomic chain can be considered a first-order approximate model for a bi-layered system for wave lengths which are greater than the length of a unit cell. Figure 3.16 depicts a bi-layer unit cell with layer lengths denoted by L_i and density per unit length denoted by ρ_i. A lumped parameter model consists of two mass elements with mass $m_i = \rho_i L_i$ and linear stiffness $k_i = E_i A_c / L_i$ where E_i denote the linear elastic modulus of the ith layer and A_c denotes cross-sectional area (equal for both layers). A nonlinear constitutive law for stress and strain may exhibit cubic nonlinearities which are accounted for by the nonlinear stiffness coefficients Γ_i.

The pth unit cell contains two degrees of freedom u_1 and u_2 whose displacements are along the $\mathbf{e}_1$ direction. The equation of motion governing the infinite system derives from

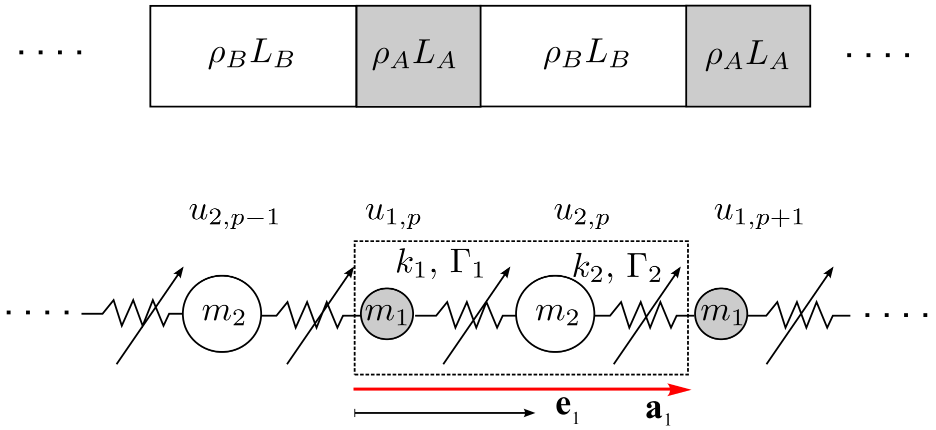

Figure 3.16: Monoatomic diatomic chain with cubic stiffness and lattice vector $\mathbf{a}_1$. Interatomic linear and nonlinear stiffness coefficients k and Γ are the same for each spring element.

a force balance on each degree of freedom:

$$\begin{bmatrix} m_1 & 0 \\ 0 & m_2 \end{bmatrix}\begin{bmatrix} \ddot{u}_{1,p} \\ \ddot{u}_{2,p} \end{bmatrix} + \begin{bmatrix} k_1 + k_2 & -k_1 \\ -k_1 & k_1 + k_2 \end{bmatrix}\begin{bmatrix} u_{1,p} \\ u_{2,p} \end{bmatrix} + \begin{bmatrix} 0 & -k_2 \\ 0 & 0 \end{bmatrix}\begin{bmatrix} u_{1,p-1} \\ u_{2,p-1} \end{bmatrix} + \dots$$
$$\begin{bmatrix} 0 & 0 \\ -k_2 & 0 \end{bmatrix}\begin{bmatrix} u_{1,p+1} \\ u_{2,p+1} \end{bmatrix} + \varepsilon \begin{bmatrix} \Gamma_1(u_{1,p} - u_{2,p})^3 + \Gamma_2(u_{1,p} - u_{2,p-1})^3 \\ \Gamma_1(u_{2,p} - u_{1,p})^3 + \Gamma_2(u_{2,p} - u_{1,p+1})^3 \end{bmatrix} = \begin{bmatrix} 0 \\ 0 \end{bmatrix}. \tag{3.54}$$

We note that Eq. (3.54) fits the general form of Eq. (2.20) outlined in Chapter 2, given by the compact expression

$$\mathbf{M}\ddot{\mathbf{u}} + \sum_{p=-1,0,1} \mathbf{K}_{(p)}\mathbf{u}_{(p)} + \varepsilon \mathbf{f}^{NL}\left(\mathbf{u}_{(p)}\right) = \mathbf{0}, \tag{3.55}$$

where $\mathbf{u}_{(p)} = \mathbf{u}$ and $\mathbf{u}_{(p\pm1)} = [u_{1,p\pm1},\ u_{2,p\pm1}]$ and stiffness matrices are given by

$$\mathbf{K}_{(p)} = \begin{bmatrix} k_1 + k_2 & -k_1 \\ -k_1 & k_1 + k_2 \end{bmatrix},\ \mathbf{K}_{(p-1)} = \begin{bmatrix} 0 & -k_2 \\ 0 & 0 \end{bmatrix},\ \text{and } \mathbf{K}_{(p+1)} = \begin{bmatrix} 0 & 0 \\ -k_2 & 0 \end{bmatrix}. \tag{3.56}$$

Next, the multiple scales perturbation analysis is applied to Eq. (3.55) as a demonstration of the procedure in a general multi-DOF system.

3.3.3 Multiple scales perturbation analysis

Multiple scales analysis begins with the postulation that the degrees of freedom (DOFs) for the unit cell evolve on multiple timescales according to

$$\mathbf{u} = \mathbf{u}(t) = \mathbf{u}(T_0(t), T_1(t)). \tag{3.57}$$

where we have retained only fast time $T_0 = t$ and one slow time scale $T_1 = \varepsilon t$. Time-derivatives transform with application of the chain rule as described in Sec. 2.4.2 such that

$$\frac{d}{dt}\left(\frac{d()}{dt}\right) = D_0^2 + 2\varepsilon D_0 D_1 + \varepsilon^2 D_1^2. \tag{3.58}$$

Next, introduce asymptotic perturbation expansions for the displacement as described by multiple time scales T_i. We consider only first-order approximations to establish corrections to the dispersion relation:

$$\mathbf{u}_{(p)}(T_0, T_1) = \mathbf{u}_{(p)}^{(0)}(T_0, T_1) + \varepsilon \mathbf{u}_{(p)}^{(1)}(T_0, T_1) + O(\varepsilon^2) \tag{3.59}$$

Substituting Eqs. (3.58) and (3.59) into the governing Eq. (3.55) produces, after some rearranging, a governing equation which accounts for interactions up to $O(\varepsilon)$

$$\begin{split} D_0^2\mathbf{M}\mathbf{u}^{(0)} + \sum_{p=-1,0,1} \mathbf{K}_{(p)}\mathbf{u}_{(p)}^{(0)} + \varepsilon(D_0^2\mathbf{M}\mathbf{u}^{(1)} + 2D_0D_1\mathbf{M}\mathbf{u}^{(0)} \\ + \sum_{p=-1,0,1} \mathbf{K}_{(p)}\mathbf{u}_{(p)}^{(0)} + \mathbf{f}^{NL}) = \mathbf{0}. \end{split} \tag{3.60}$$

As Eq. (3.59) must hold true for any and all ε, the coefficient of each ε must vanish identically. This statement leads to a system of ordered equations.

$$O(\varepsilon^0): \quad D_0^2\mathbf{M}\mathbf{u}^{(0)} + \sum_{p=-1,0,1} \mathbf{K}_{(p)}\mathbf{u}_{(p)}^{(0)} = \mathbf{0} \tag{3.61}$$

$$O(\varepsilon^1): \quad D_0^2\mathbf{M}\mathbf{u}^{(1)} + \sum_{p=-1,0,1} \mathbf{K}_{(p)}\mathbf{u}_{(p)}^{(1)} = -2D_0D_1\mathbf{M}\mathbf{u}^{(0)} - \mathbf{f}^{NL}. \tag{3.62}$$

Hence, the weakly nonlinear problem in Eq. (3.54) has been transformed to the solution of a cascading system of linear differential equations, whose solution at each order of ε is informed by previous orders. The $O(\varepsilon^0)$ equation admits a Bloch wave solution

$$\mathbf{u}^{(0)}_{(p)} = \frac{1}{2}A(T_1)\boldsymbol{\phi}e^{\mathrm{i}(\mu p-\omega T_0)} + c.c. \tag{3.63}$$

for Bloch wave numbers μ and position index p. The complex amplitude $A(T_1)$ varies with slow time T_1 and is therefore considered constant at $O(\varepsilon^0)$. The zero-order equation, with application of the Bloch wave solution Eq. (3.63), reduces to

$$-\omega^2\begin{bmatrix} m_1 & 0 \\ 0 & m_2 \end{bmatrix}\begin{bmatrix} u^{(0)}_{1,p} \\ u^{(0)}_{2,p} \end{bmatrix} + \begin{bmatrix} k_1+k_2 & -k_1-k_2e^{-\mathrm{i}\mu} \\ -k_1-k_2e^{\mathrm{i}\mu} & k_1+k_2 \end{bmatrix}\begin{bmatrix} u^{(0)}_{1,p} \\ u^{(0)}_{2,p} \end{bmatrix} = \begin{bmatrix} 0 \\ 0 \end{bmatrix}. \tag{3.64}$$

After collecting terms in $\mathbf{u}^{(0)}$, equation expressed (3.64) the wave-number reduced stiffness matrix $\mathbf{K}(\mu)$ reads

$$\left(-\omega^2\mathbf{M} + \mathbf{K}(\mu)\right)\boldsymbol{\phi} = \mathbf{0}, \tag{3.65}$$

where $\boldsymbol{\phi}$ denotes the degrees of freedom in the central unit cell, and $p = 0$ without any loss in generality. Equation (3.65) denotes an eigenvalue problem for Bloch wave modes $\boldsymbol{\phi}(\mu)$ and frequencies $\omega(\mu)$ that describe the dispersion relationship. The symbolic solution for $\omega(\mu)$ expressed with general stiffness coefficients k_1 and k_2 is a complicated expression. Thus, we present here the dispersion relation for a special case $k_1 = k_2 = k$

$$\omega = \sqrt{\frac{k(m_2+m_1)}{m_1m_2} \pm \frac{k}{2}\sqrt{\frac{4m_2^2+4m_1^2+8m_1m_2\cos(\mu)}{m_1^2m_2^2}}} \tag{3.66}$$

Equation (3.66) describes the acoustic branch $\omega_{ac}(\mu)$ when $-$ is taken under the radical and the optical dispersion branch ω_{opt} when the + sign is taken. Figure 3.17 depicts the acoustic and optical branch for the diatomic system. Similarly, the acoustic $\boldsymbol{\phi}_{ac}$ and optical $\boldsymbol{\phi}_{opt}$ Bloch wave modes are given, respectively, by

$$\boldsymbol{\phi}_{ac} = \begin{bmatrix} \dfrac{(1+e^{-\mathrm{i}\mu})m_2}{m_2-m_1+\sqrt{m_1^2+m_2^2+2m_1m_2\cos(\mu)}} \\ 1 \end{bmatrix} \tag{3.67a}$$

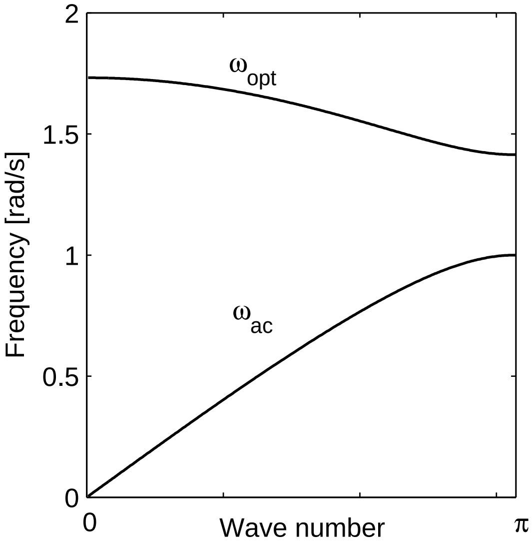

Figure 3.17: Dispersion relation evaluated for a diatomic chain where $m_1 = 1.0$ and $m_2 = 2.0$ and stiffness $k = 1.0$.

and

$$\boldsymbol{\phi}_{opt} = \begin{bmatrix} \dfrac{-(1 + e^{-i\mu})m_2}{m_1 - m_2 + \sqrt{m_1^2 + m_2^2 + 2m_1 m_2 \cos(\mu)}} \\ 1 \end{bmatrix}. \tag{3.67b}$$

The Bloch wave modes are unique only to a scalar multiple. Thus, the maximum component of each Bloch wave mode is normalized to unity according to $\boldsymbol{\phi}_j = \boldsymbol{\phi}_j / \max(\boldsymbol{\phi}_j)$ in all analysis that follows such that a scalar multiple specifies the amplitude.

The fact that there now multiple dispersion branches – optical and acoustic – leads to additional complexity in analyzing wave interactions. Specifically, *interacting waves are no longer completely characterized by specifying a wave number, a dispersion branch must also be specified.* As an example, in the monoatomic lattice of Chapter 3, the dispersion relation accounting for wave interactions required only the wave number of a B wave. Now, a specific wave number μ_B corresponds to *two* dispersion branches, and we must specify whether the B wave exists on the acoustic branch or the optical branch. The effect of a control wave B on the dispersion of a primary wave A is investigated next.

3.3.4 Wave-wave interaction effect on dispersion

Consider now the $O(\varepsilon^1)$ equation (3.62). The right hand side depends on the specific solution $\mathbf{u}^{(0)}$ at $O(\varepsilon^0)$. We study the effect of two interacting waves, labeled A and B, such that the solution to the zero-order problem is specified by

$$\mathbf{u}^{(0)} = \frac{A(T_1)}{2}\boldsymbol{\phi}_A e^{\mathrm{i}(\mu_A p-\omega_{A0}T_0)} + \frac{B(T_1)}{2}\boldsymbol{\phi}_B e^{\mathrm{i}(\mu_B p-\omega_{B0}T_0)} + c.c. = \mathbf{u}_A^{(0)} + \mathbf{u}_B^{(0)} + c.c. \tag{3.68}$$

where now Bloch wave modes $\boldsymbol{\phi}_A(\mu_A)$, $\omega_{A0}(\mu_A)$ and $\boldsymbol{\phi}_B(\mu_B)$, $\omega_{B0}(\mu_B)$ give the specific modal occupation of the A and B waves, respectively. We consider the case where ω_{A0} and ω_{B0} are incommensurate such that $\omega_{A0} \neq 3\omega_{A0}$. Amplitudes $A(T_1)$ and $B(T_1)$ are, in general, complex quantities that allow phase differences between the waves; however, the specific phase relationship of the A and B waves turns out to be irrelevant in a first-order perturbation analysis.

Substituting Eq. (3.68) into Eq. (3.62) and evaluating partial derivatives D_0 and D_1 yields the following inhomogeneous system of equations

$$\begin{aligned} D_0^2\mathbf{M}\mathbf{u}^{(1)} + \mathbf{K}\mathbf{u}^{(1)} = {} & \mathrm{i}\omega_{A0}A'\mathbf{M}\boldsymbol{\phi}_A e^{-\mathrm{i}\omega_{A0}T_0} \\ & +\mathrm{i}\omega_{B0}B'\mathbf{M}\boldsymbol{\phi}_B e^{-\mathrm{i}\omega_{B0}T_0} - \mathbf{f}^{NL}\left(\mathbf{u}^{(0)}_{(p,q,r)}\right) + c.c., \end{aligned} \tag{3.69}$$

where a prime denotes differentiation with respect to slow time T_1 and $c.c.$ denotes the complex conjugate of the preceding terms. Following the procedure in Sec. 2.4.2 and anticipating the appearance of secular terms in Eq. (3.69), we expand the nonlinear force vector $\mathbf{f}^{NL}$ into frequency components using a two-dimensional Fourier series and retain only primary frequency terms such that

$$\mathbf{f}^{NL}\left(\mathbf{u}^{(0)}_{(p,q,r)}\right) = \mathbf{c}_A e^{-\mathrm{i}\omega_{A0}T_0} + \mathbf{c}_B e^{-\mathrm{i}\omega_{B0}T_0} + O.H.T. + c.c. \tag{3.70}$$

where O.H.T. denotes other harmonic terms such as $3\omega_{A0}$, $2\omega_{A0} \pm \omega_{B0}$, etc. The nonlinear force vector, assuming $\Gamma_1 = \Gamma_2 = \Gamma$ can be expressed in the general form (due to a cubic nonlinearity)

$$\mathbf{f}^{NL} = \sum_{l,m,n} \mathcal{G}_{lmn}(\mathbf{u}_l^{(0)} \otimes \mathbf{u}_m^{(0)} \otimes \mathbf{u}_n^{(0)}) \quad (l,m,n) \in \left\{A,\ \bar{A},\ B,\ \bar{B}\right\}, \tag{3.71}$$

where $\otimes$ denotes the Hadamard product such that the ith element of the result is given by component-wise multiplication

$$(u_l \otimes u_m)_i = (\mathbf{u}_l)_i \otimes (\mathbf{u}_m)_i, \tag{3.72}$$

and the indices l, m, and n take either A, $\bar{A}$, B, or $\bar{B}$ where an overbar denotes complex conjugate. The specific terms which comprise the $\mathbf{c}_A$ coefficient are given by the sum of terms with the form

$$\mathbf{c}_A e^{-\mathrm{i}\omega_{A0}T_0} = \mathcal{G}_{AA\bar{A}}(\mathbf{u}_A^{(0)} \otimes \mathbf{u}_A^{(0)} \otimes \mathbf{u}_{\bar{A}}^{(0)}) + \mathcal{G}_{A\bar{B}B}(\mathbf{u}_A^{(0)} \otimes \mathbf{u}_B^{(0)} \otimes \mathbf{u}_{\bar{B}}^{(0)}), \tag{3.73}$$

because frequency terms from $\mathbf{u}_B^{(0)}$ exactly cancel one another since they are complex conjugates; the above expression expressed with Bloch wave modes explicitly is written

$$\begin{aligned} \mathbf{c}_A e^{-\mathrm{i}\omega_{A0}T_0} = &\frac{AA\bar{A}}{8}\left(\boldsymbol{\phi}_A e^{-\mathrm{i}\omega_{A0}T_0} \otimes \boldsymbol{\phi}_A e^{-\mathrm{i}\omega_{A0}T_0} \otimes \bar{\boldsymbol{\phi}}_B e^{\mathrm{i}\omega_{A0}T_0}\right) \\ &+ \frac{AB\bar{B}}{8}\left(\boldsymbol{\phi}_A e^{-\mathrm{i}\omega_{A0}T_0} \otimes \boldsymbol{\phi}_B e^{-\mathrm{i}\omega_{B0}T_0} \otimes \bar{\boldsymbol{\phi}}_B e^{\mathrm{i}\omega_{B0}T_0}\right). \end{aligned} \tag{3.74}$$

After appropriate cancellation and grouping of terms, this expression becomes

$$\mathbf{c}_A e^{-\mathrm{i}\omega_{A0}T_0} = \left[\frac{AA\bar{A}}{8}\left(\boldsymbol{\phi}_A \otimes \boldsymbol{\phi}_A \otimes \bar{\boldsymbol{\phi}}_A\right) + \frac{AB\bar{B}}{8}\left(\boldsymbol{\phi}_A \otimes \boldsymbol{\phi}_B \otimes \bar{\boldsymbol{\phi}}_B\right)\right] e^{-\mathrm{i}\omega_{A0}T_0}. \tag{3.75}$$

Note that wave number dependence is not explicitly included in the $\mathbf{c}_A$ coefficient; however, as the Bloch wave modes are a function of μ_A or μ_B this functional dependence enters through $\boldsymbol{\phi}_A(\mu_A)$ and $\boldsymbol{\phi}_B(\mu_B)$. Symbolic manipulation has been used here to expand the nonlinear force vector and obtain $\mathbf{c}_A$ and $\mathbf{c}_B$ coefficients. The specific expressions for these coefficients are complex and do not provide a great deal of insight into the phenomena of wave interactions beyond what has already been presented; therefore, they are not presented here in full.

Having defined the $\mathbf{c}_A$ and $\mathbf{c}_B$ coefficients, we rewrite Eq. (3.69) as

$$\begin{aligned} D_0^2\mathbf{M}\mathbf{u}^{(1)} + \mathbf{K}\mathbf{u}^{(1)} = &\left(\mathrm{i}\omega_{A0}(\alpha_A' - \mathrm{i}\alpha_A\beta_A')\mathbf{M}\boldsymbol{\phi}_A e^{-\mathrm{i}\beta_A} - \mathbf{c}_A\right) e^{-\mathrm{i}\omega_{A0}T_0} \\ &+ \left(\mathrm{i}\omega_{B0}(\alpha_B' - \mathrm{i}\alpha_A\beta_B')\mathbf{M}\boldsymbol{\phi}_B e^{-\mathrm{i}\beta_B} - \mathbf{c}_B\right) e^{-\mathrm{i}\omega_{B0}T_0} + c.c., \end{aligned} \tag{3.76}$$

where the polar form $A_i(T_1) = \alpha_i(T_1)\exp(-\mathrm{i}\beta_i(T_1))$ has been introduced. Secular terms are identified as described in Chapter 2 by pre-multiplying Eq. (3.76) with either $\boldsymbol{\phi}_A$ or $\boldsymbol{\phi}_B$. Following Eq. (2.58), secular terms are required to vanish for uniform expansions, leading to:

$$\mathrm{i}\omega_{A0}\boldsymbol{\phi}_A^H\mathbf{M}\boldsymbol{\phi}_A\left(\alpha_A' - \mathrm{i}\alpha_A\beta_A'\right) - \boldsymbol{\phi}_A^H\mathbf{c}_A e^{\mathrm{i}\beta_A} = 0 \tag{3.77a}$$

and

$$\mathrm{i}\omega_{B0}\boldsymbol{\phi}_B^H\mathbf{M}\boldsymbol{\phi}_B\left(\alpha_B' - \mathrm{i}\alpha_B\beta_B'\right) - \boldsymbol{\phi}_B^H\mathbf{c}_B e^{\mathrm{i}\beta_B} = 0. \tag{3.77b}$$

The real and imaginary components of Eqns. (3.77) must vanish separately, leading to a system of four differential equations for amplitudes and phases α_A, α_B, β_A, and β_B. These equations decouple (see Sec. 2.4.2 for details) when the frequencies are incommensurate such that first-order frequency corrections are given by

$$\omega_{A1} \equiv \frac{\beta_A}{T_1} = \frac{\boldsymbol{\phi}^H\hat{\mathbf{c}}_A}{\omega_{A0}\alpha_A\boldsymbol{\phi}_A^H\mathbf{M}\boldsymbol{\phi}_A} \quad \text{and} \quad \omega_{B1} \equiv \frac{\beta_B}{T_1} = \frac{\boldsymbol{\phi}^H\hat{\mathbf{c}}_B}{\omega_{B0}\alpha_B\boldsymbol{\phi}_B^H\mathbf{M}\boldsymbol{\phi}_B}. \tag{3.78}$$

where $\hat{\mathbf{c}}_A = \mathbf{c}_A\exp(\mathrm{i}\beta_A)$ and $\hat{\mathbf{c}}_B = \mathbf{c}_B\exp(\mathrm{i}\beta_B)$. Thus, the reconstituted expressions which account for wave interactions are given by

$$\omega_A = \omega_{A0}(\mu_A) + \varepsilon\left.\frac{\boldsymbol{\phi}^H\hat{\mathbf{c}}_A}{\omega_{A0}\alpha_A\boldsymbol{\phi}_A^H\mathbf{M}\boldsymbol{\phi}_A}\right|_{\mu_B} + O(\varepsilon^2) \tag{3.79a}$$

and

$$\omega_B = \omega_{B0}(\mu_B) + \varepsilon\left.\frac{\boldsymbol{\phi}^H\hat{\mathbf{c}}_B}{\omega_{B0}\alpha_B\boldsymbol{\phi}_B^H\mathbf{M}\boldsymbol{\phi}_B}\right|_{\mu_A} + O(\varepsilon^2), \tag{3.79b}$$

where we emphasize that each correction must be evaluated for a specific wave number and frequency pair that corresponds to a particular dispersion branch. Next, we will consider specifically corrections to a primary A wave in the presence of a control B wave by evaluating $\omega_A(\mu_A)$ subject to fixed μ_B and corresponding $\phi_B(\mu_B)$ on either the acoustic or optical dispersion branch.

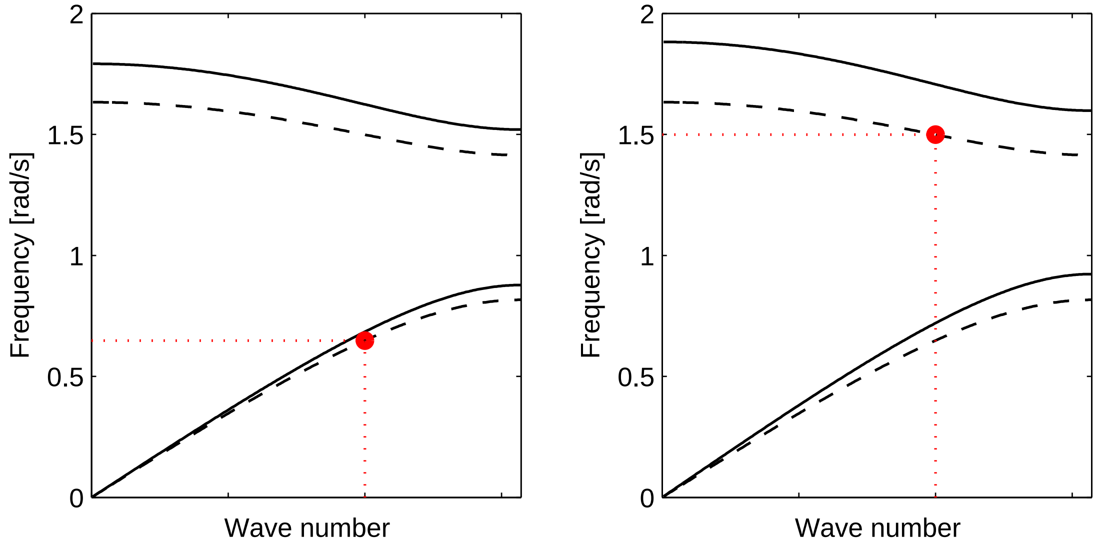

(a) Acoustic branch

(b) Optical branch

Figure 3.18: Dispersion shifts to the primary wave effected through the introduction of a control wave on (a) the acoustic branch, and (b) the optical branch. Red markers indicate the specific modal occupation of the B control wave. Dashed lines indicate the linear dispersion.

3.3.5 Analysis of predicted dispersion shifts

3.3.5.1 Acoustic vs. optical branch control wave

The dispersion relationship, hereby defined as $\omega_A(\mu)$, for the diatomic system depends on the specific modal occupation of the control B wave. The system parameters considered are $m_1 = 1.0$, $m_2 = 3.0$, $k_1 = k_2 = 1.0$, $\varepsilon\Gamma_1 = \varepsilon\Gamma_2 = 0.05$, and $\alpha_A = 1.0$. A control wave at $\mu_B = 2.0$ and amplitude $\alpha_B = 1.0$ is evaluated for modal occupation on the acoustic branch as well as the optical branch as shown in Fig. 3.18. We note that larger shifts are attained when the control wave occupies higher frequency modes. In fact, this is true in general for the diatomic system considered herein and it is likely to be true for more complex systems as well. Therefore, $\mu_B = 0$ on the optical branch produces greater frequency shifts than $\mu_B = \pi$ on the optical branch. An explanation for this may lie in the energy content of the mode.

3.3.5.2 Mass and stiffness ratio analysis

The diatomic system possesses a variety of parameters that offer avenues for tailoring dispersion shifts. We consider specifically the effect of varying the mass and stiffness ratio on dispersion. As the influence of dispersion near band gaps is often of interest, we specifically consider the acoustic branch shift evaluated at $\omega_{A1}(\mu = \pi)$. We fix the parameters $m_1 = 1.0$, $k_1 = 1.0$, and $\varepsilon\Gamma_1 = \varepsilon\Gamma_2 = 0.05$ and parametrically vary m_2 and k_2. Dispersion shifts are evaluated subject to a control wave at $\mu_B = \pi$ with amplitude $\alpha_B = 1.0$ on the optical branch. The amplitude primary amplitude $\alpha_A = 0.01$ such that dispersion shifts are entirely a result of wave interactions.

Figure 3.19 reveals that maximum dispersion branch shifts are achieved for high stiffness ratio contrasts. Optimal mass ratios for the specific configuration considered are approximately $m_2/m_1 = 0.6$. The major conclusions to be drawn here are that the nonlinear dispersion shifts exhibit complex functional-dependence on the specific system parameters. This dependence enters the nonlinear shift primarily through the Bloch wave modes. Specific system configurations which result in optimized dispersion shifts are considered later in Chapter 6.

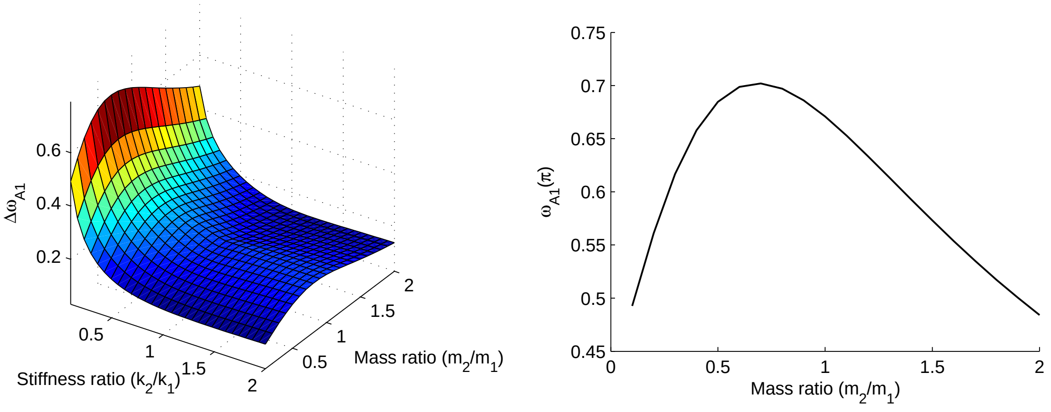

(a) (b)

Figure 3.19: (a) Parametric analysis of mass and stiffness ratios effects on the dispersion shift $\omega_{A1}(\pi)$. A specific slice at $k_2/k_1 = 0.1$ of the surface highlights the mass variation.

3.3.6 Conclusions

Wave interactions in complex systems with multiple degrees of freedom can be analyzed efficiently through the multiple scales analysis procedure presented in this chapter. Wave interactions in more complex materials require specification of which Bloch wave modes are interacting. As a consequence, the specific modal occupation of a control wave can have a significant influence on the dispersion shifts for a primary wave. Low-frequency modal occupation tends to produce smaller dispersion shifts than does high-frequency modal occupation (i.e. acoustic vs. optical branches). The diatomic chain exhibits all of the complexity needed to extend wave-wave interaction analysis into continuous media. Because the diatomic chain can be derived as a first-order approximation of a bi-layer system, it offers good perspective into wave interactions in layered materials. Dispersion shifts to a primary wave can be effected through the dynamic introduction of a control wave; thus, it may be possible to design phononic materials which exhibit band gaps only in the presence of a control wave. Further analysis should include numerical validation of the predicted dispersion. In closing, we note that the wave-interaction results presented herein degenerate exactly to those obtained for the monoatomic chain when $m_1 = m_2$ and $k_1 = k_2$.

CHAPTER IV

EXPERIMENTAL ESTIMATION OF NONLINEAR DISPERSION

4.1 Overview

Nonlinear amplitude-dependent dispersion relationships are experimentally investigated within the scope of a classical Duffing oscillator chain. The idea of amplitude-tunable dispersion relationships in nonlinear phononic systems has received relatively little attention on the experimental side. Moreover, to the author's knowledge no previous studies have attempted to link nonlinear dispersion frequency shifts to the backbone curves intrinsic to nonlinear frequency response functions. This work represents a critical step in moving towards nonlinear amplitude-tunable phononic devices.

Existing studies of nonlinear phononic systems focusing on dispersion typically fall into two categories: mass-loaded strings [78, 79, 80] and granular (spherical) beads [37, 81, 47]. Notable exceptions are some studies dealing with arrayed Helmholtz resonators [82, 83]. These types of systems are considered for two fundamental reasons: (1) they are readily fabricated in repeatable arrays, and (2) they exhibit nonlinear responses. However, many of these existing studies focus on other phenomena such as Anderson localization or tunable solitary wave propagation. The present study provides the theoretical background required to link backbone curves to nonlinear dispersion diagrams within the context of a chain of Duffing oscillators as well as experimental evidence to support these results.

Section 4.2 provides the requisite background on Duffing oscillator and reviews previous theoretical treatments of the nonlinear oscillator chain. A theoretical model for a nearly-discrete system of nonlinear oscillators is presented and used as the basis for designing a nonlinear test article in Sec. 4.3. Linear and nonlinear system responses are documented in Sec. 4.4 with specific attention called to the dispersive nature of the system.

Amplitude-dependent dispersion shifts are experimentally identified for the given system at the edge of the Brillouin zone where a tunable cutoff frequency could lead to initial devices such as amplitude-dependent filters [3]. Lastly, the theoretical model compared with the experimental results shows very good agreement.

4.2 Theoretical background

4.2.1 Nonlinear dispersion and the Duffing backbone

The frequency shifts arising in periodic systems can be connected with the classical duffing oscillator. The following analysis shows that an infinite chain of oscillators behaves similar to a single nonlinear oscillator (from a frequency shift viewpoint) when the wavenumber $\mu = \pi/3$. Moreover, a chain of nonlinear oscillators exhibits dispersion shifts due to the hardening or softening nature of the connecting springs. This behavior is intimately related to the Duffing backbone curve for the case of a single Oscillator. Consider the classical Duffing oscillator with forcing and cubic stiffness ordered at $O(\varepsilon)$

$$m\ddot{u} + k_1 u + \varepsilon k_3 u^3 = \varepsilon f(t), \tag{4.1}$$

$u(t)$ denotes displacement from equilibrium, m denotes mass, $f(t)$ denotes the forcing function, and k_1 and k_3 denote linear and nonlinear stiffness coefficients, respectively. Perturbation analysis of this system reveals that the resonant response of this system exhibits hardening or softening behavior according to

$$\sigma = \frac{3}{8}\frac{k_3 A^2}{m\omega_n} \pm \sqrt{\frac{f_0^2}{4\omega_n^2 A^2}}, \tag{4.2}$$

where $\omega_n = \sqrt{k/m}$, $f(t) = f_0 \cos(\omega t)$ and $\omega = \omega_n + \varepsilon\sigma$. The backbone curve of the duffing oscillator follow from setting $f_0 = 0$ and is given by $(3/8)(k_3/\omega_n)A^2$ [27]. This result is remarkably similar to the dispersion frequency correction terms in [3, 36], repeated here for convenience

$$\omega(\mu) = \omega_n\sqrt{2 - 2\cos(\mu)} + \varepsilon\frac{3}{8}\frac{k_3 A^2}{m\omega_n}(2 - 2\cos(\mu))^{3/2} + O(\varepsilon^2) \tag{4.3}$$

In fact, the backbone curve represents the natural frequency of oscillation for an unforced mass with initial amplitude A. This is quite similar to free wave propagation in an infinitely large system where boundary reflections do not exist.

Figure 4.1 graphically depicts this observation. The nonlinear dispersion relationship for coupled nonlinear oscillators Eq. (4.3) is plotted with wave amplitude A as a third dimension. Several dispersion curves are plotted with amplitude held constant as shown on the left subfigure. The locus of points in the amplitude-frequency plane (wavenumber held constant) is plotted with bold lines at various wave numbers. Specific attention is called to the red curve at $\mu = \pi/3$; this is exactly the Duffing backbone curve as shown in the right subfigure. Further analysis of this particular nonlinear dispersion relationship shows that for any given amplitude the largest frequency-shift occurs at $\mu = \pi$ (near the band edge/cutoff frequency). In this case, the $O(\varepsilon^1)$ frequency shift is given by $\omega_1 = 3k_3A^2/m\omega_n$ which amounts to an 8x increase in frequency shift sensitivity to amplitude.

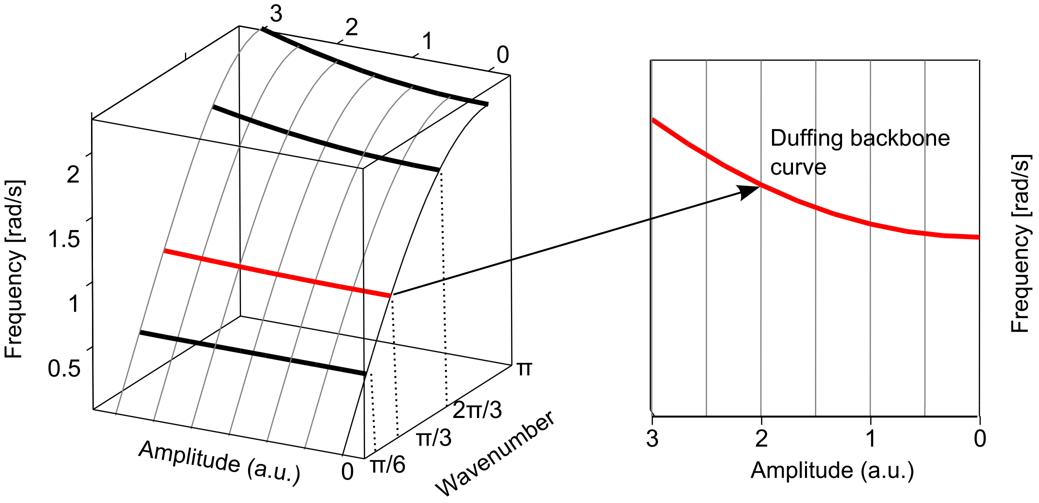

Figure 4.1: Amplitude-dependent dispersion in the monoatomic chain is strongly related to the Duffing backbone curve (red).

The notion that the Duffing backbone curve relates to nonlinear dispersion shifts in periodic media is of significant importance in experimentally observing nonlinear frequency shifts: the backbone curve corresponding to a given resonance frequency may be extracted and plotted as a nonlinear frequency shift on the dispersion relation. Next, a physical system which closely resembles the nonlinear spring-mass system is identified and discussed as a model for experimentally observing these shifts.

4.2.2 Nonlinear, periodic wire model

The ideal spring-mass system consists of infinitely small mass elements joined together along a common axis by infinitely light spring elements. A system that approaches this ideal model consists of lead weights joined with a segments of wire or string. A distinction between wire and string is made to emphasize the existence of bending rigidity at higher frequencies, particularly those with out-of-phase oscillations. However, the bending stiffness of the wire is negligible in cases where the wave mode exhibits low to moderate spatial oscillations [59, 73, 27]. The small-but-finite transverse displacement field $v(x,t)$ for a pretensioned wire undergoing without body forces and damping is modeled approximately by the nonlinear wave equation

$$\rho_V A_c \ddot{v} - T_0 \frac{\partial^2 v}{\partial x^2} = (EA_c - T_0)\frac{\partial}{\partial x}\left[\frac{1}{2}\frac{\partial v}{\partial x}\left(\frac{\partial v}{\partial x}\right)^2\right] \tag{4.4}$$

where T_0 denotes pretension, ρ_V denotes volume density, A_c denotes cross-sectional area, and E denotes Young's modulus [59, 27, 73] where in-plane motion transverse motion has been assumed. The term T_0 is typically neglected relative to the product EA_c so that the equation reads (after some rearranging)

$$\rho_V A_c \ddot{v} - T_0 \frac{\partial^2 v}{\partial x^2} - EA_c \frac{\partial}{\partial x}\left[\frac{1}{2}\left(\frac{\partial v}{\partial x}\right)^3\right] = 0. \tag{4.5}$$

The cubic nonlinearity in this expression arises from von Kármán strains which account for changes in tension induced by small-but-finite rotations and displacements in strings, beams, plates, and shells [59, 84, 85]. We suppose now that there are an infinite number of mass elements (termed *beads* herein) connected by wires segments of length a, and that the mass of the connecting wire is negligible compared to the beads. Then, Eq. (4.5) provides linear and nonlinear stiffness terms for the equation of motion governing the transverse displacement of a single bead. For short connecting lengths a, a finite-difference approximation for the wire displacement yields an open set of finite-difference equations in the form of coupled nonlinear oscillators

$$m\ddot{v}_p + \frac{T_0}{a}(v_p - v_{p+1}) + \frac{T_0}{a}(v_p - v_{p-1}) + \frac{EA_c}{2a^3}(v_p - v_{p+1})^3 + \frac{EA_c}{2a^3}(v_p - v_{p-1})^3 = 0, \qquad (4.6)$$

where m denotes the bead mass and v_p denotes the transverse displacement of the pth mass. The linear stiffness term is given by $k_1 = T_0/a$ and the nonlinear stiffness term is $\varepsilon k_3 = EA_c/(2a^3)$. According to the theory presented in Chapter 3, the nonlinear dispersion shift corresponding to a system of beads connected by pretensioned wires is given, *for a single propagating wave* by

$$\omega_1 = \frac{3}{16}\frac{EA_cA^2}{m\omega_n a^3}(2 - 2\cos(\mu))^{3/2} \quad \text{(single wave)}, \qquad (4.7)$$

accurate to a first-order approximation. However, a system in steady-state resonance with amplitude A is equivalent the summation of counter-propagating waves with equal amplitude $A^* = A/2$. Thus, the wave-wave interaction theory of Chapter 3 applies here with two waves with equal and opposite wave numbers $\pm\mu$. Following the wave-wave interaction theory, the zero-order displacement solution $v^{(0)}$ takes the form

$$v_p^{(0)} = \frac{A^*}{2}e^{\mathrm{i}(\mu p - \omega\tau_0)} + \frac{A^*}{2}e^{\mathrm{i}(-\mu p - \omega\tau_0)} + c.c., \qquad (4.8)$$

where τ_0 denotes the fast time scale (rather than T_0 in order to avoid confusion with the pretension notation). The nonlinear frequency shift in the case of resonance should consider counterpropagating Bloch waves according to Eq. (3.21a). Thus, the frequency shift for counterpropagating waves is

$$\omega_1 = \frac{3}{16}\frac{EA_c(A^*)^2}{m\omega_n a^3}(2 - 2\cos(\mu))^{3/2} + \frac{3}{8}\frac{EA_c(A^*)^2}{m\omega_n a^3}(2 - 2\cos(-\mu))^{3/2} \qquad (4.9)$$

where the first term is recognized as the self-action frequency shift and the second term results from nonlinear wave interaction. Since $\cos(-\mu) = \cos(\mu)$ and $A^* = A/2$, these terms combine to give

$$\omega_1 = \frac{9}{64}\frac{EA_cA^2}{m\omega_n a^3}(2 - 2\cos(\mu))^{3/2}. \qquad (4.10)$$

For experimental analysis and evaluation it will be convenient to introduce a shift percentage parameter η such that the frequency is given by

$$\omega = \omega_0(1+\eta), \tag{4.11}$$

where $\eta = \omega_1/\omega_0$ and $\omega_0 = \omega_n\sqrt{2-2\cos(\mu)}$. This arrangement allows one to arrive at an expression for the amplitude required in order to achieve a shift percentage η. Furthermore, we assume a circular cross-sectional area $A_c = \pi D^2/4$ for the wire where D denotes the diameter. The resulting expression for required amplitude, evaluated at the Brillouin zone edge[1], reads

$$A^2 = \frac{128}{9}\frac{\eta T_0 a^2}{\pi D^2 E\sqrt{2-2\cos(\mu)}}\Bigg|_{\mu=\pi} \rightarrow A^2(\eta) = \frac{64\eta}{9\pi}\left(\frac{T_0}{E}\right)\left(\frac{a}{D}\right)^2. \tag{4.12}$$

Equation (4.12) gives rise to several noteworthy points regarding the design of an experiment to observe frequency shifts. First, the required shift amplitude is independent of bead mass. Second, the required amplitude can be decreased by lowering the "stiffness" ratio T_0/E and geometry ratio a/D. An additional constraint on the bead mass is required to validate the model assumptions, namely that the bead mass is much greater than the wire mass for a given unit cell $m \gg \rho_V A_c a = \rho_V a(\pi D^2/4)$. A description of the test article, apparatus, and measurement system follows.

4.3 Experimental design and configuration

A test article closely following the system described in Sec. 4.2 consists of lead beads strung along a length of spring steel wire. The model outlined considers the wire mass negligible relative to the bead mass. In order to achieve this, 6.35mm diameter spherical lead beads were affixed to a 0.25mm diameter wire through high-precision holes bore through the center of the beads. Spherical beads and precisely located wire holes are necessary to obtain the in-plane motion assumed in the model. This configuration, pictured in Fig.

---

[1] We know *a priori* that the resulting frequency shift is greatest here for a given amplitude

4.2a realizes a 120:1 mass ratio between the bead and the wire (per unit cell); hence, the wire mass is negligible. Fourteen unit cells spaced by $a = 32.5mm$ comprise the test article. Table 1 summarizes the geometric and material properties of the system components. The test article is pretensioned between two upright I-beams designed to minimize flexure while a shaker excites the system in a horizontal plane (Fig. 4.2b). A scanning laser Doppler vibrometer (LDV) measures oscillation velocity (Fig. 4.2c).

(a) Mass element (b) Apparatus (c) Scanning head

Figure 4.2: Photographs of the experimental apparatus and scanning laser Doppler vibrometer head used to capture data. (a) Individual mass elements (dimensioned as shown) produce a mass-spring equivalent system. (b) The experimental apparatus is constructed of solid aluminum, with the test article tensioned between two I-Beams. (c) A scanning laser Doppler vibrometer measures individual masses to obtain data.

Table 1: Material and geometry properties for test article

Parameter	D [mm]	a [mm]	E [GPa]	m [g]	ρ_V [kg/m^3]	T_0 [N]
Value	0.254	32.5	205	1.57	7850	21.8

The schematic in Fig. 4.3 illustrates the major system components used to excite and measure the system. A B&K 4809 type modal vibration shaker, powered by a B&K 2718 amplifier, excites the system according. A Polytec PSV-400 scanning LDV head and an associated controller measure the system response at each bead site. Two primary modes of excitation are utilized: wide-band excitation at low excitation levels captures the linear system response, while slow, narrow-band frequency sweeps at high amplitude permit investigation of nonlinear system responses.

Low-amplitude system response is measured by exciting the system with a pseudo-random excitation signal. The internal function generator produces the pseudo-random

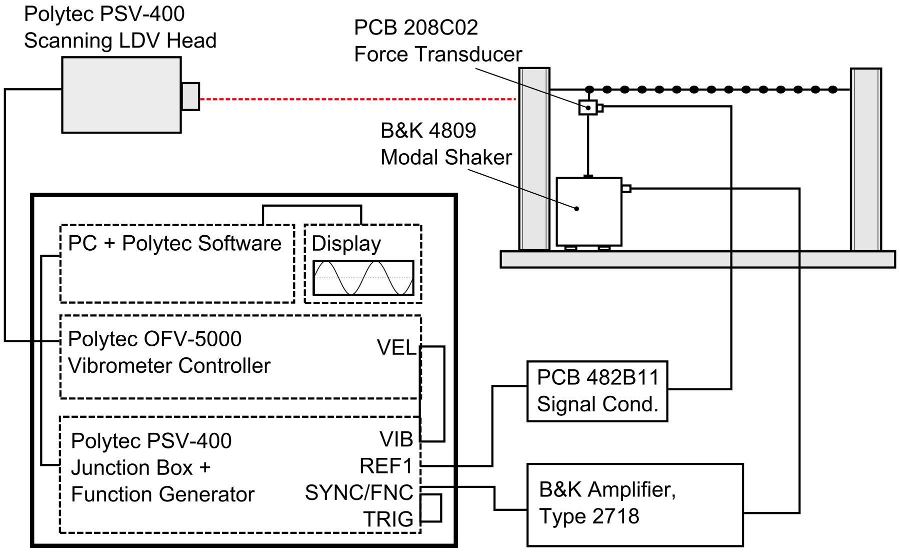

Figure 4.3: Test article and measurement hardware configuration

signal by inverting a uniform frequency distribution with randomly distributed phases. This periodic signal is supplied continuously to the system until a steady-state response is achieved[2]. The internal function generator is synchronized with the data acquisition trigger signal in order to accurately capture phase information. Moreover, automated complex-averaging techniques reduce random errors introduced into the measurements by noise.

The nonlinear system response desired cannot be achieved through a pseudo-random excitation signal since harmonic excitation has been assumed. Instead, slow frequency (0.2 Hz/sec) sweeps over a resonant frequency of the linear system identify steady-state response amplitude. In this configuration, an Agilent 33220A function generator is substituted for the internal function generator of the Polytec system. The Agilent 33220A is capable of producing sweeps which are initiated from a steady-state response at the starting frequency, thus eliminating data corruption from transient effects. The function generator sync port connects to the data acquisition system's trigger port to precisely initiate measurements.

---

[2] Less than 2-3 seconds

4.4 *Results and discussion*

4.4.1 Linear model validation

Characterizing the low-amplitude system response serves several important functions in nonlinear dispersion analysis. First, the resonant frequencies are identified and may be mapped to a Brillouin diagram to illustrate dispersion. Second, the pretension – a critical parameter in the frequency shift equation (4.12) – can be determined by fitting a linear model to the resulting frequency response function (FRF). Figure 4.4 depicts a typical FRF for the system. Low frequency resonant peaks (e.g. 1–8) occur at approximately equal intervals due to the linear relationship between wavelength and frequency in the long wavelength limit. Homogenization of the system unit cell at these frequencies produces a system model which accurately captures response characteristics [86]. Higher frequencies (e.g. peaks 9–14) associate with wavelengths approaching the unit cell dimension *a* and thus exhibit dispersive wave propagation where this approximation fails.

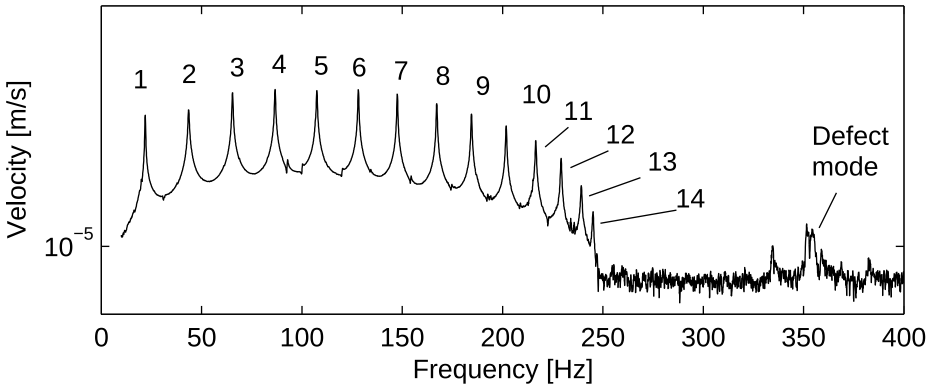

Figure 4.4: The frequency response reveals which Bloch wave numbers are excited

The Polytec software automatically records and processes the time-response at each mass location. The trigger signal is especially important to this process for ensuring accurate phase relationships between the excitation signal and individual masses. Figure 4.5a depicts the graphical user interface for data post-processing and viewing. The resulting forced response snapshots agree very well with what is expected; this is largely due to precise manufacturing and careful experiment design. Figure 4.5b also depicts the response at several other frequencies associated with the 2nd, 4th, 10th, and 14th resonant frequencies.

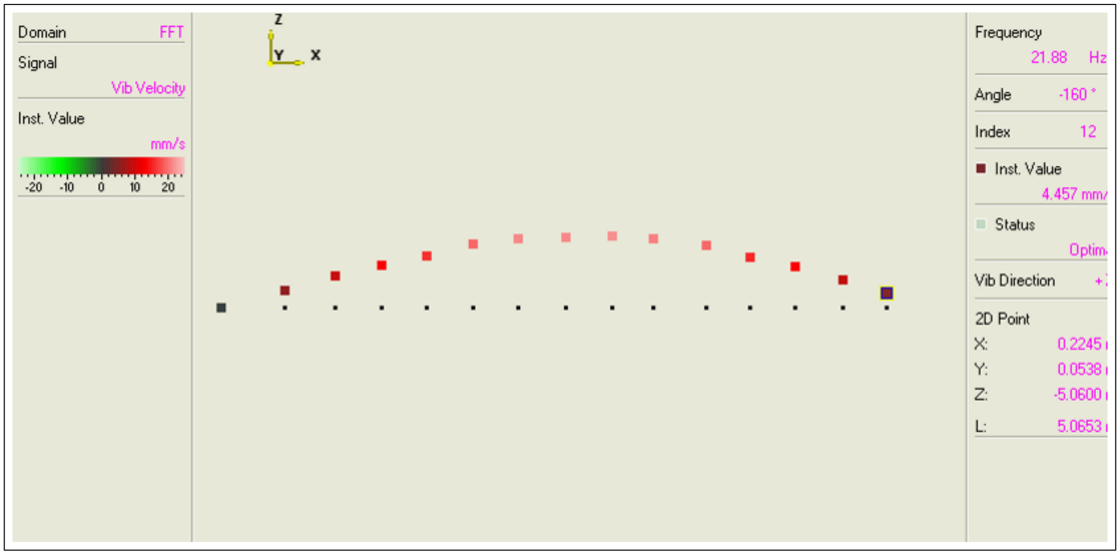

Domain FFT

Signal Vib Velocity

Inst. Value mm/s

Frequency 21.88 Hz

Angle -160 °

Index 12

Inst. Value 4.457 mm/

Status Optim

Vib Direction +

2D Point

X: 0.2245

Y: 0.0538

Z: -5.0600

L: 5.0653

(a) Polytec software output

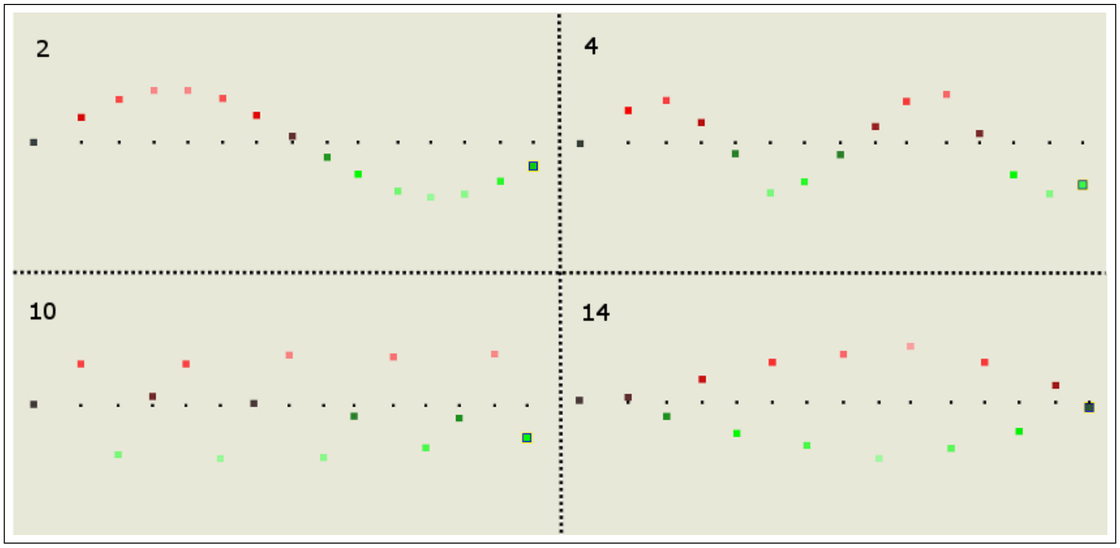

(b) Response snapshots near resonant frequencies

Figure 4.5: The Polytec software captures and automatically processes velocity data at each mass location using laser Doppler vibrometry. (a) A resonant frequency near 22 Hz and a portion of the user interface is depicted. (b) Several other snapshots near the 2nd, 4th, 10th, and 14th resonant frequencies.

Figure 4.6 contains snapshots of the forced steady-state motion near all the resonant frequency peaks of Fig. 4.4. All data has been directly imported from the Polytec software into MATLAB for visualization purposes only. Indeed, low frequency modes are reminiscent of a pinned-pinned string response $v(x,t) = \sin(n\pi x/L)$ for $n \in \mathbb{Z}$ and L denoting the system length. Neighboring beads increasingly oscillate out of phase as frequency increases. Moreover, by the 14th mode, neighboring bead modes are completely out-of-phase and thus natural frequencies are influenced by the bending rigidity of the wire. Not surprisingly, the out-of-phase motions in the 14th mode correspond to the edge of the Brillouin zone whereby group velocity reduces to zero. Figure 4.4 clearly shows the the first band gap frequency at around 250 Hz; beyond this frequency appears a resonant frequency associated with a defect mode at 350 Hz. This resonance appears only as a result of a lightweight copper connector used to secure a wire loop used for pretensioning the system. We note that although wave propagation initiates from the left side of the system, the highly evanescent mode reaches the right end and excites a localized resonance at the last bead.

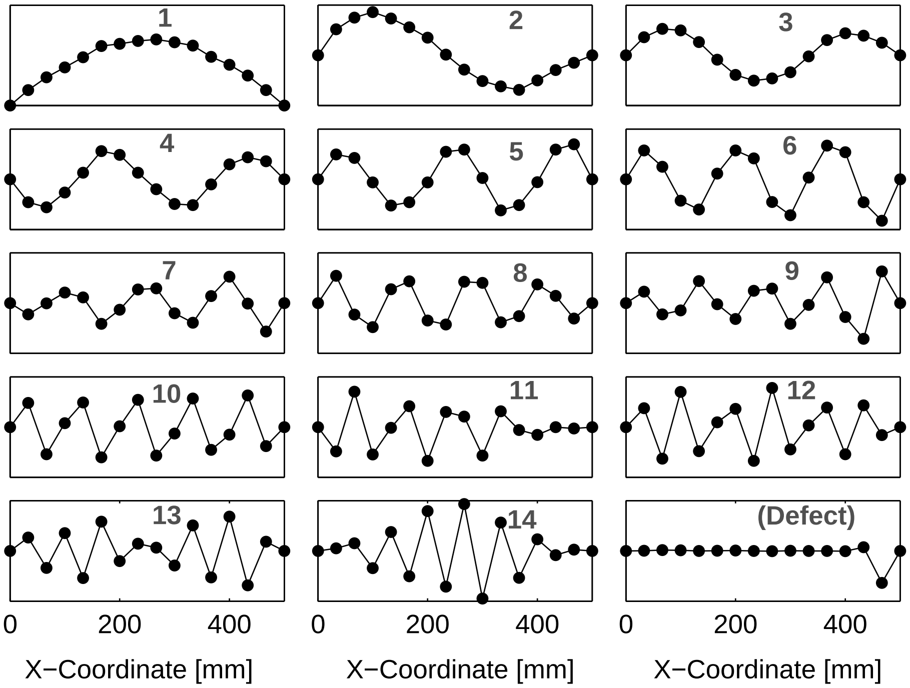

Figure 4.6: Snapshots of the forced steady-state motion near resonant frequencies (labeled 1–14) and near the defect mode (labeled accordingly). The 16 black markers indicate measurement points (14 masses and two endpoints).

The natural frequencies of periodic systems occur in tight groups [78, 79, 10]. These groups are located, with few exceptions, around pass band frequencies of the ideal infinite system. Figure 4.7 depicts the experimentally measured natural frequencies using a dispersion diagram; each resonant peak corresponds to a wavelength which achieves resonance in a finite system due to in-phase reflections from the boundaries. Although assumptions made previously dictate a spring-mass type model, we note that including bending rigidity provides an improved fit for the linear model. However, the nonlinear analysis of such a system is significantly more complex and provides less physical intuition and insight. The following sections describe the experimental measurement and analysis of nonlinear dispersion shifts.

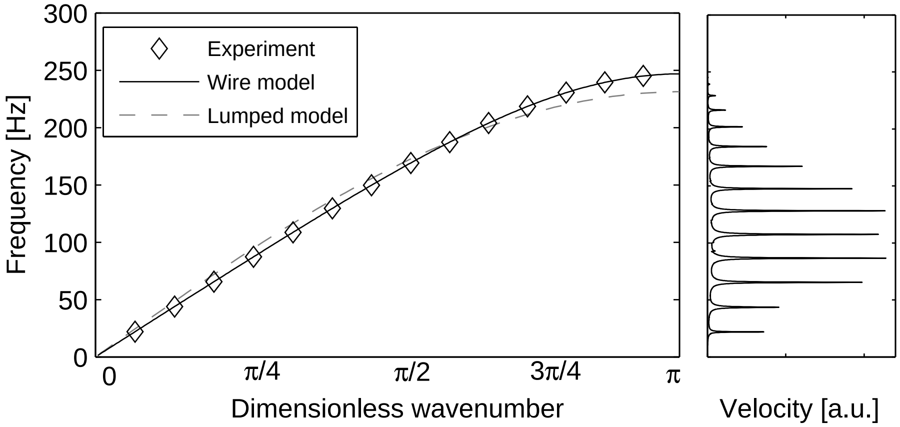

Figure 4.7: The analytical model accurately captures the expected Bloch-wave dispersion, revealing a band gap in the neighborhood of 250 Hz. Markers correspond to the experimentally measured natural frequencies of the system (pictured on the right subfigure). Dashed and solid lines indicate dispersion relationships for periodic string and wire models, respectively. The inclusion of bending stiffness (wire model) improves the fit at higher frequencies.

4.4.2 Measurement and analysis of nonlinear dispersion shifts

Measurement of nonlinear dispersion shifts is facilitated by the theoretical background provided in Sec. 4.2. As the Duffing backbone represents the frequency shift for wave propagation in an infinite system, it suffices to measure the forced response from which the backbone curve may be extracted and plotted as the amplitude-dependent dispersion curve (as in Fig. 4.1). Nonlinear frequency response measurements are made by initiating a slow frequency sweep of $\omega = \pm 2$ Hz around a measured natural frequency[3]. Slow frequency sweeps allow the system to achieve steady-state response amplitude at a single frequency. Unlike the broadband pseudo-random excitation used for low-amplitude measurements, single-frequency excitation is critical in nonlinear measurements to reduce wave-wave interaction effects [36].

Figure 4.8 shows the results of a typical frequency sweep. The response level increases as the sweep progresses over and beyond the natural frequency. A clear Duffing-like instability manifests around 15 seconds where the amplitude sharply declines. The oscillations following the instability result from transient signal response remaining from the previously high amplitudes. The red line denoting signal amplitude $A(t)$ represents the magnitude of the Hilbert transform $A(t) = |\mathcal{H}(v_p(t))|$, where $v_p(t)$ denotes the measured signal at the pth site. The Hilbert transform converts a real signal $v_p(t)$ into an *analytic* signal of the form $v_p(t) = A(t)\cos(\varphi(t))$, where $A(t)$ denotes the time-varying amplitude and and $\varphi(t)$ denotes the time-varying phase. Also implicit in the theoretical analysis presented previously is a monochromatic response. The right subfigure of Fig. 4.8 reveals an essentially sinusoidal

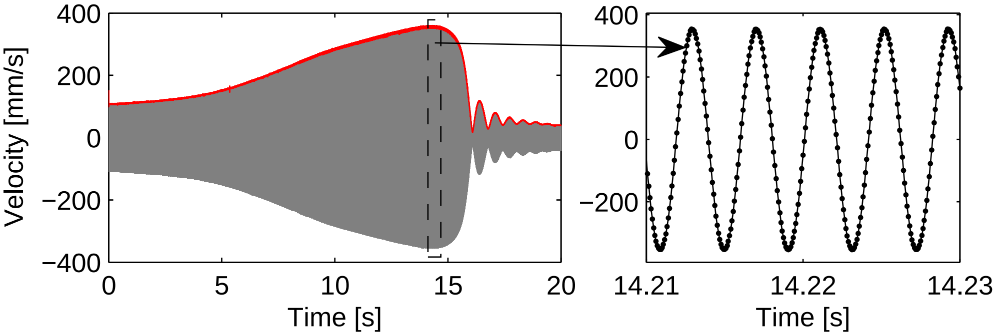

Figure 4.8: Example measurement at high excitation level shows clear Duffing instability post-resonance. The right subfigure reveals an essentially monochromatic response. Marker indicate sampled points.

---

[3] Natural frequencies refer to low-amplitude system response

response at the excitation frequency. As a result, velocity response measurements directly converted into amplitudes by dividing out the excitation frequency ω.

Figure 4.9 depicts the time-frequency response signal of Fig. 4.8 in the form of a spectrogram. The spectrogram combines time and frequency-domain data into a single figure by virtue of a sliding Fourier transform window. Higher frequency resolution is achieved by increasing the length of the window at the expense of temporal resolution, and vice-versa. The presence of super-harmonics at 2ω, 3ω and 4ω at -3 dB supports the monochromatic assumption since the amplitudes are several orders of magnitude less than the fundamental frequency. The existence of these harmonics is typical of nonlinear systems; the well-known third harmonic results directly from the cubic nonlinearity [28, 27], while wave-mixing produces sum and difference frequencies at $2\omega = 3\omega - \omega$ and $4\omega = 3\omega + \omega$ which are routinely analyzed in nonlinear optics literature [66, 39]. The right subfigure of Fig. 4.9 depicts a zoomed-in view around the fundamental frequency ω. The linearly-increasing frequency sweep is clearly visible here, as is the Duffing jump behavior around $t = 15$ seconds where stable motion is lost.

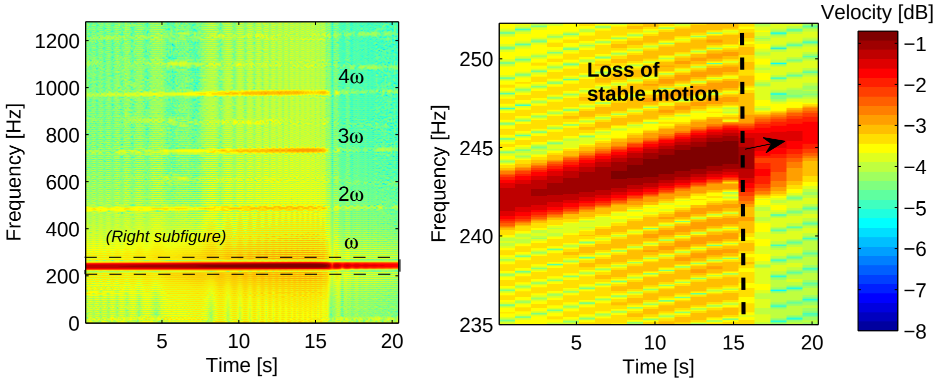

Figure 4.9: Spectrogram showing weak harmonic generation at high amplitudes. As the harmonics are approximately -3dB relative to the fundamental frequency, the signal is essentially monochromatic.

Several frequency sweeps at increasing amplitudes were conducted and analyzed with the aid of the Hilbert transform as previously described. High-amplitude excitations were limited by the ultimate tensile strength of the system as well as the propensity of the system

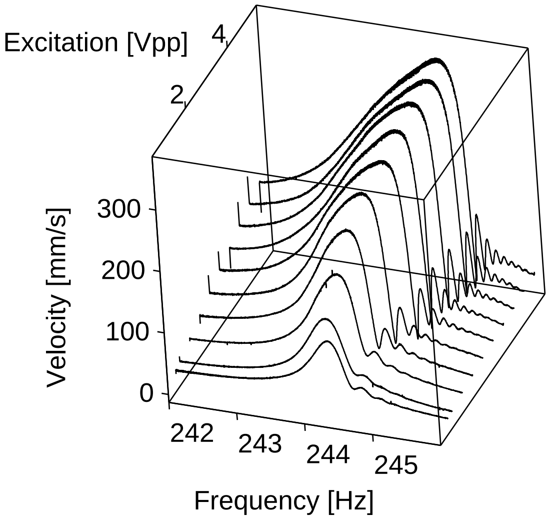

Figure 4.10: Several frequency up-sweeps performed from low (400 mVpp) to high (5 Vpp) excitation levels.

to whirl. Figure 4.10 depicts the amplitude function $A(t)$ for each sweep. Low-amplitude sweeps do not experience the jump-phenomena. The maximum amplitude of each frequency sweep traces out the backbone curve as can be seen from Eq. (4.1). Alternatively, the backbone curve may be extracted by performing both frequency up- and down-sweeps and extracting the mid-frequency. Figure 4.11 depicts the stable response points from both up and down-sweeps. Solid lines indicate stable response points, while the dashed black line indicates the jump phenomena. The backbone curve (solid gray) extracted from the experimental data describes change in dispersion frequencies with amplitude.

The backbone curve depicted in Fig. 4.11 depicts a nonlinear frequency shift percentage $\eta = \omega_1/\omega_0$ of approximately 0.6%. This shift occurs at a velocity amplitude of $360\,\mathrm{mm\,s^{-1}}$. As the signal is monochromatic, this translates into a displacement amplitude of A=0.23 mm. A computation using Eq. (4.12) and tension tuned to match the Brillouin zone edge results in a theoretical amplitude A=0.17 mm required to obtain the same shift.

The minor disparity between the theory and experiment can be attributed to several factors. The theoretical models assumes a truly infinite system with displacements occurring purely in the vertical direction. Additionally bending rigidity of the wire is not explicitly

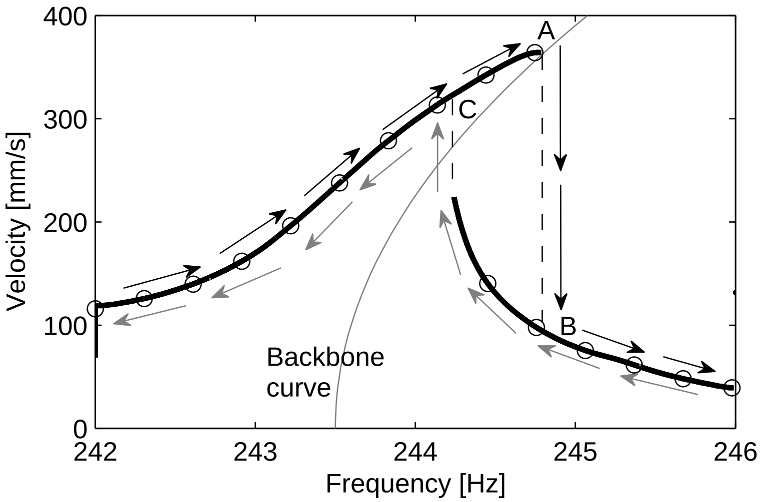

Figure 4.11: Jump phenomena and associated backbone curve

accounted taken into consideration, nor is rotary inertia from the beads. Despite this, the theoretical model used to design the experiment agrees well with experimental measurements as a first-order approximation.

4.5 Conclusions

Nonlinear dispersion in periodic systems was described within the context of backbone curves innate to nonlinear frequency response functions. A periodic wire-mass system, designed after a classical spring-mass system, exhibited amplitude-dependent wave propagation with good agreement to a theoretical model. The idea that amplitude-dependent dispersion relations are intimately related to backbone curves may have far-reaching consequences. At present, determining the hardening or softening behavior of periodic dynamic systems requires a full perturbation analysis. In contrast, nonlinear dispersion analysis of a single unit cell can provide complete hardening and softening behavior over a range of frequencies with a single comprehensive analysis. Further experimental analysis of nonlinear periodic systems should explore systems exhibiting stronger nonlinear response that allow for greater tunability.

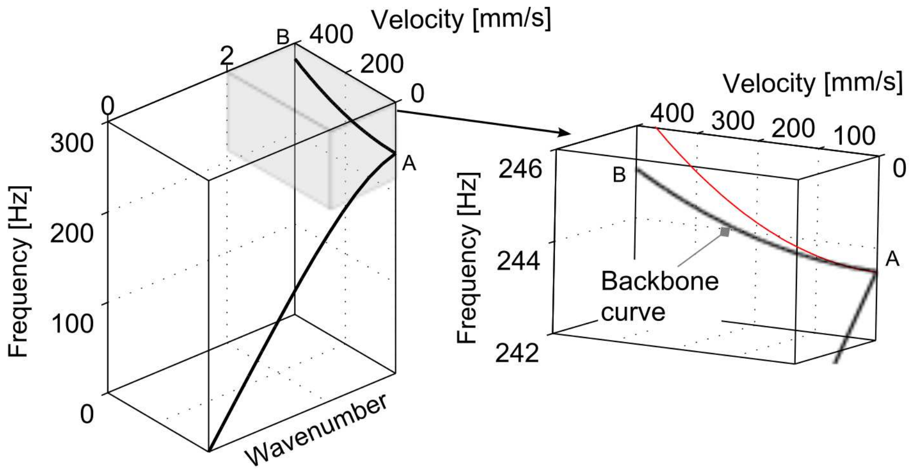

Figure 4.12: Dispersion diagram including amplitude dependence. The left subfigure depicts the typical Brillouin diagram with an additional 3rd axis denoting amplitude (shift not to scale on left subfigure). The right subfigure depicts a zoom of the experimental backbone curve *AB* (black) and theoretical backbone curve (red).

CHAPTER V

NONLINEAR DISPERSION IN LAYERED MATERIALS

5.1 Overview

This chapter analyzes intensity dependent dispersion of acoustic waves in nonlinear one-dimensional (1D) layered material characterized by constitutive laws with cubic strain nonlinearities. The analysis predicts amplitude-dependent dispersion leading to tunable bandgaps. These predictions are compared with those obtained from a simplified analysis conducted by linearizing the governing equations about an assigned field intensity followed by application of the transfer matrix method, as is commonly done in nonlinear photonic crystal studies. Comparison of the two methods generally shows good dispersion agreement; however, in phononic systems the transfer matrix analysis does not accurately capture high-strain behavior that occurs for some configurations, such as those with thin nonlinear layers, and may even predict erroneous bandgaps. Numerical predictions resulting from a finite-element analysis of the nonlinear media confirm the improved accuracy of the perturbation approach, suggesting its continued use for predicting intensity-dependent dispersion in 2D and 3D nonlinear phononic systems.

Nonlinear systems provide unique opportunities for bandgap engineering such as amplitude-dependent band structures [37, 38, 3], wave-wave interactions [36], and extra harmonic generation [87], but have received significantly less attention than linear systems. The nonlinearity often arises from an intensity-dependent constitutive law for stress. The effect of a cubic term, in either case, is of particular interest as it leads to amplitude-dependent dispersion [39, 40, 41, 42, 43, 3], which has implications for enhanced device design. For example, a wide variety of literature exists discussing the application of Kerr media to photonic systems such as left-handed metamaterials [88], light bullets [89], and optical switching [90]. Moreover, intensity-dependence induced by the Kerr nonlinearity is responsible for large phase shifts near the band edge, which may also be exploited to achieve slow group velocities of light for optical switching [91]. The nonlinear behavior of these systems is non-trivial and requires advanced analysis techniques.

Nonlinear periodic materials are commonly analyzed using finite-difference time-domain (FDTD) simulations [92, 11]. However, the computation and post-processing time involved reduces the appeal of FDTD simulations for nonlinear material optimization and design problems. A common theme in photonic crystal analysis literature is the approximation of a cubic polarization by a linearized relationship. In 1D analyses, this leads to a problem formulation which is amenable to analysis by the transfer matrix method. However, much of the influence from the nonlinear dynamics is ignored. A new method for calculating the band structure for nonlinear photonic crystals was proposed in [93], where a nonlinear dielectric coefficient in a layered material proportional to intensity is considered. By iteratively solving the field equations, a convergent solution for the bandgaps shifts was obtained. Two years later, the same system analyzed in [93] was addressed using a FDTD model of an oscillating dipole possessing a cubic Kerr nonlinearity [94]. In 2005, nonlinear bandgap tunability in a 2D photonic crystal with a Kerr nonlinearity was demonstrated experimentally and computationally [42]. The experimental results indicate that realistic bandgap shifting may be achieved in photonic microsystems doped with Kerr nonlinearities.

Analysis methods and literature specifically for nonlinear phononic crystals is more sparse than for photonic crystals. However, there are some notable contributions in the more general area of periodic composites. Mechanically triggered phononic bandgap shifts from external stimuli were investigated in 2008 [18]. The one-dimensional bimaterial system was investigated to determine the response of the system to second harmonic generation in and outside of the acoustic bandgaps [22]. This nonlinear one-dimensional layered system was demonstrated as a potential acoustic diode in 2009 [20]. The nonlinear dynamics and bandgap behavior of some discrete systems were investigated to determine closed-form expressions for the bandgap shifting [24]. Others have investigated wave propagation in several nonlinear periodic systems which have shown chaotic responses [26, 44, 45]. Strongly nonlinear waves in a chain of beads under Hertzian contact were investigated analytically using a harmonic balance method [95] as well as experimentally [37] where tunable bandgaps were reported in response to pre-compression.

A quasilinear material analysis employed with the transfer matrix method has not been applied to nonlinear phononic crystal design with regard to bandgap engineering. It is of interest to explore the application of the two techniques in both material systems, and to compare and contrast their findings. The present work addresses this by applying the existing photonic crystal analysis technique in the mechanical domain. The transfer matrix analysis method applies only to a continuous system whose constitutive law is first linearized. On the other hand, the perturbation-based analysis method presented herein is applicable only to discrete systems (finite-element discretized or lumped-parameter) and does not require *a priori* linearization of any constitutive laws. The applicability of each method in analyzing the behavior of bandgap size and location in response to finite-amplitude wave propagation is quantified and scrutinized.

One of the simplest phononic crystals that can be considered is a one-dimensional (1D) bilayered material, consisting of alternating material layers with contrasting properties. This type of structure exhibits many of the interesting properties of phononic crystals such as dispersion and bandgaps, while being sufficiently simple to analyze [96, 97]. Therefore, the bilayered material is our starting point for analyzing nonlinearities in continuous phononic, and for assessing the two techniques in regards to estimating the effects nonlinearities have on dispersion.

The work is structured as follows: first, the general nonlinear wave equation for 1D periodic layered systems is introduced. Then, a nonlinear constitutive relationship for stress introduces nonlinear terms into the wave equation which are later analyzed with two different nonlinear analysis techniques: (1) the quasi-linear analysis using transfer matrices, and (2) the perturbation-based approach. Dispersion curves are generated for a bilayered material using the two techniques. The results are compared to dispersion curves generated from finite element analysis simulations of the fully-nonlinear system. Finally, conclusions are drawn regarding the applicability of each technique to nonlinear systems together with the benefits and drawbacks of each.

5.2 Nonlinear model for layered media

The one-dimensional bi-layered material shown in Fig. 5.1 is governed by a nonlinear wave equation whose coefficients are piecewise functions of the material layer. The system considered is unbounded in directions transverse to material interfaces such that unidirectional plane wave propagation exists. Two layers per unit cell are considered in this analysis, although the method is generally applicable to any number of layers. The *p*th unit cell has layers with widths a and b such that the total unit cell length is $d = a + b$. The form of the nonlinear wave equation to be considered for a layer derives from Eq. (2.11) reduced to one-dimension and a nonlinear constitutive law. The one-dimensional wave equation takes the form

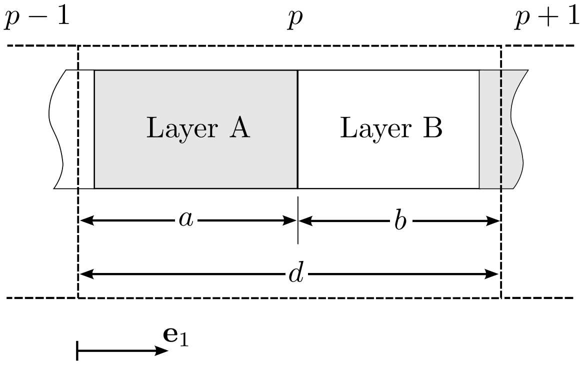

Figure 5.1: Bimaterial rod unit cell

$$\frac{\partial \sigma_{xx}}{\partial x} = \rho_V \frac{\partial^2 u(x,t)}{\partial t^2}, \quad \forall x \in \Omega, \tag{5.1}$$

where σ_{xx} denotes the $\mathbf{e}_1$ component of stress, $\rho_V(x)$ is the volume density, and $u(x, t)$ is the displacement field in the $\mathbf{e}_1$ direction. The nonlinear constitutive law considered is

$$\sigma_{xx} = E_1\epsilon_{xx} + \Gamma\epsilon_{xx}^3 + O(\epsilon_{xx}^5), \tag{5.2}$$

where $\epsilon_{xx} = u_{,x}$ is the strain component in the $\mathbf{e}_1$ direction, and $E_1(x)$ and $\Gamma(x)$ are the linear and nonlinear elastic moduli, respectively. Substituting Eq. (5.2) into Eq. (5.1) leads to a one-dimensional nonlinear wave equation

$$\frac{\partial}{\partial x}\left(E_1(x)\frac{\partial u(x,t)}{\partial x} + \Gamma(x)\left(\frac{\partial u}{\partial x}\right)^3\right) = \rho_V(x)\frac{\partial^2 u(x,t)}{\partial t^2}, \quad x \in \Omega. \tag{5.3}$$

The effect of the nonlinear stiffness term on dispersion is the focus of this work. The coefficient functions $E_1(x)$, $\Gamma(x)$, and $\rho(x)$ are defined in a piecewise fashion for the layered system considered

$$E_1(x) = \begin{cases} E_{1A} & \text{if } 0 \le x < a \\ E_{1B} & \text{if } a \le x < b \end{cases} \tag{5.4a}$$

$$\Gamma(x) = \begin{cases} \Gamma_A & \text{if } 0 \le x < a \\ \Gamma_B & \text{if } a \le x < b. \end{cases} \tag{5.4b}$$

$$\rho(x) = \begin{cases} \rho_A & \text{if } 0 \le x < a \\ \rho_B & \text{if } a \le x < b, \end{cases} \tag{5.4c}$$

where E_{1A}, E_{1B}, Γ_A, Γ_B, ρ_A, and ρ_B are constants. We assume only a single nonlinear layer such that $\Gamma_B = 0$.

The third order coefficient $\Gamma(x)$ is typically several orders of magnitude larger than the first order coefficient $E_1(x)$ [98]; thus, a weakly nonlinear system is obtained when the strain amplitude is small. The small parameter ε is quantified by a weakly nonlinear contribution in the stress-strain constitutive relation Eq. (5.2). Regrouping terms as $\sigma_{xx} = E_{1A}\epsilon_{xx}(1 + \Gamma_A\epsilon_{xx}^2/E_{1A})$ motivates the small parameter definition $\varepsilon = \Gamma_A\epsilon_0^2/E_{1A}$, where ϵ_0 denotes strain amplitude for a harmonic solution of the analagous linear problem where

$\Gamma_A = 0$. To this end, the small parameter ε is introduced through the expression $\Gamma_A = \varepsilon\hat{\Gamma}_A$ when perturbation calculations are performed. This form is not required in the transfer matrix analysis presented next.

5.3 *Transfer matrix analysis of linearized systems*

The transfer matrix analysis of cubically nonlinear layered materials with quasilinear material properties has been applied in nonlinear optics to deterimine dispersion properties [99]. This method is presented here as applied to phononic systems assess its utility and validity. The disperion relationship of a layered phononic system can be derived from a transfer matrix formulation when linear constitutive relationships are used [97, 100]. The appropriate interface matching conditions in conjunction with a Bloch periodicity statement result in a transfer matrix that relates values of the displacement field $u(x,t)$ and the strain $\epsilon_{xx}(x,t)$ at the beginning of a layer to the values at the end of a layer.

Repeated application of the transfer matrix for each layer results in an overall transfer matrix $\mathbf{T}$ for an entire unit cell. The field variables $u(x,t)$ and $\epsilon_{xx}(x,t)$ within the lth layer are contained in a state vector $\mathbf{u}^T = [u, \epsilon_{xx}]$ and related by a transfer matrix $\mathbf{T}_l$

$$\mathbf{T}_l = \begin{bmatrix} \cos(k_l d_l) & 1/Z_l \sin(k_l d_l) \\ -Z_l \sin(k_l d_l) & \cos(k_l d_l) \end{bmatrix}, \tag{5.5}$$

where $k_l = \omega/c_l$ is the material wave number, $c_l = \sqrt{E_{1l}/\rho_l}$ is the phase speed, and $Z_l = \rho_l c_l^2 k_l$ denotes an impedance. Each unit cell consists of two layers in the bimaterial system referenced by the subscript $l = A,\ B$. Application of the transfer matrix across a complete unit cell, together with Bloch boundary conditions, results in an eigenvalue problem whose solution yields the dispersion relationship and Bloch wave modes. For the two-layer periodic system considered, this is given as

$$\mathbf{u}(x+d,t) = \mathbf{T}_B\mathbf{T}_A\mathbf{u}(x,t) \longrightarrow \mathbf{u}(x,t)\exp(\mathrm{i}\mu) = \mathbf{T}\mathbf{u}(x,t), \quad \mathbf{T} = \mathbf{T}_B\mathbf{T}_A, \tag{5.6}$$

where $\mathbf{T}_{A,B}$ denote transfer matrices evaluated using properties for layers A and B, respectively, and $\mu = \hat{\mu}d$ relates the dimensionless Bloch wave number μ (normalized by unit cell length d) to its dimensional counterpart. We note that the particular eigenvalue problem here is linear in the Bloch wave number μ, but nonlinear in the frequency $\omega = c_l k_l$. Thus, it is more direct to solve for the inverted dispersion relation $\mu(\omega)$, rather than $\omega(\mu)$ as typical in discrete system analysis.

The transfer matrix analysis as stated above requires a linear system, although recent publications have appeared which combine a pertubation approach with a transfer matrix for nonlinear systems [101]. One common method of treating the cubic nonlinearity (i.e. the *Kerr nonlinearity*) in optics community involves linearizing the constitutive relationship for the nonlinear electric polarization field. The rationale behind the linearization process is that material properties are reasonably described by an intensity-dependent quantity for weak nonlinearities. This linearization can be applied more generally to any physical system where a constitutive relation can be approximated by a truncated Taylor series as in Eq. (5.2).

Consider the nonlinear *homogeneous* medium governed by Eq. (5.3) with $\Gamma_A \neq 0$. At a point x in space, the equivalent linear system ($\Gamma_A = 0$) exhibits time-harmonic behavior. We consider monochromatic wave propagation in the form $\epsilon_{xx}(x,t) = \epsilon_0 \cos(\omega t - kx)$ governing a wave of frequency ω, material wave number k, and strain amplitude ϵ_0 traveling in the $\mathbf{e}_1$ direction. Substituting the linear strain solution into the constitutive equation Eq. (5.2) truncated at the second term results in

$$\sigma(x,t) = E_1 \epsilon_0 \cos(\omega t - kx) + \Gamma \epsilon_0^3 \cos^3(\omega t - kx), \tag{5.7}$$

where E_1 and Γ denote linear and nonlinear elastic moduli of the homogeneous system under consideration. The average material property of the linearized system is obtained by expanding the cubic cosine term into individual frequency components and then collecting coefficients

$$\sigma(x,t) = E_1 \epsilon_0 \cos(\omega t - kx) + \Gamma \epsilon_0^3 \Big(\frac{3}{4} \cos(\omega t - kx) + \frac{1}{4} \cos(3(\omega t - kx)) \Big). \tag{5.8}$$

The third and higher harmonic terms are neglected on the basis that the nonlinearity is small, yielding a third harmonic amplitude of negligible order. This approximation is referred to as the rotating wave approximation (RWA) in some fields. The elastic modulus reduces to a linear relationship with effective linear material property $\bar{E} = (E_1 + 3\Gamma\epsilon_0^2/4)$

$$\sigma_{xx}(x,t) \approx \left(E_1 + \frac{3}{4}\Gamma\epsilon_0^2\right)\epsilon_0 \cos(\omega t - kx) = \bar{E}\epsilon_{xx}(x,t). \tag{5.9}$$

For harmonic plane waves, the power flux (intensity) is proportional to the strain amplitude squared. Thus, the effective material property at a point x in space is related to the time-averaged intensity of a propagating wave through Eq. (5.9). Heuristically, the derivation of Eq. (5.9) also shows that even-order nonlinearities do not contribute to the effective property $\bar{E}$ since even-ordered expansions of trigonometric functions do not contain terms of the fundamental frequency ω. Furthermore, Eq. (5.9) gives a condition for which a linearization may be practical. For weak nonlinearities, and thus negligible third harmonics, one expects only small deviations of the effective property $\bar{E}$ from the linear material property E_1. This condition is written in dimensionless form as

$$\left|\frac{\Gamma\epsilon_0^2}{E_1}\right| \ll 1, \tag{5.10}$$

which corresponds physically to small strains, or a small nonlinear modulus Γ relative to E_1.

This linearization process extends readily to layered periodic systems with coefficients $E_1 = E_1(x)$ and $\Gamma = \Gamma(x)$ that are piecewise functions in space. This quasi-linear description of the stress-strain relationship results in an amplitude-dependent phase speed $\bar{c} = \sqrt{\bar{E}(\epsilon_0)/\rho}$ since $\bar{E}$ is a function of the strain amplitude ϵ_0. Likewise, for periodic systems the phase speed in the lth layer is given by $\bar{c}_l(\epsilon_0) = \sqrt{\bar{E}_l/\rho_l}$ so that the effective impedance of the lth layer is $\bar{Z}_l(\epsilon_0) = \rho_l\bar{c}_l^2(\epsilon_0)k_l$. Thus, the effective quasilinear system is obtained when the Z_l coefficient in Eq. (5.5) is replaced by the effective $\bar{Z}_l$ (at a particular amplitude). Since the Z_l coefficient depends upon amplitude, it is no surprise that the dispersion relationship obtained from a transfer matrix analysis depends on the intensity of the propagating Bloch wave. This intensity-dependence gives rise to some interesting phenomena that are exploitable in the design of novel phononic systems such as tunable pass- and stop-bands. Obtaining the dispersion relationship from the transfer matrix at this point only requires the solution of an eigenvalue problem.

5.4 Perturbation analysis of nonlinear dispersion

A more consistent approximation of weakly nonlinear system may be obtained using perturbation methods where the nonlinearity is treated asymptotically. The governing wave equation for the nonlinear 1D layered material contains a linear kernel with associated wave modes. For weak nonlinearities, a perturbation method may yield corrections to the frequency of the linear system. However, the perturbed equations of the continuous system have a complex nature not amenable to solution. Thus, we choose to apply the perturbation scheme to a discretized system following Sec. 2.4.1 to obtain a first-order corrected dispersion band structure. The discretization and perturbation analysis as applied to the layered system are described next.

5.4.1 Discretization of the bilayer system

Consider the continuous layered system described by Eq. (5.3) with periodic coefficients $E_1(x)$ and $\rho_V(x)$ and a weakly nonlinear term given as $\Gamma_A = \varepsilon\hat{\Gamma}_A$ for $|\varepsilon| \ll 1$.

$$\frac{\partial}{\partial x}\left(E_1(x)\frac{\partial u(x,t)}{\partial x}\right) + \varepsilon\frac{\partial}{\partial x}\left(\hat{\Gamma}(x)\frac{\partial u}{\partial x}\right)^3 = \rho_V(x)\frac{\partial^2 u(x,t)}{\partial t^2}, \quad x \in \Omega, \tag{5.11}$$

This system is discretized using a Galerkin weighted residuals approach. The equation of the motion within a layer of the bimatieral rod is the same equation of motion that governs a single element (‘slice’) of the rod. Introduce comparison functions N_i as well as generalized coordinates $q_i(t)$ such that the displacement variable $u(x,t)$ can be approximated as a linear combination

$$u(x,t) = \sum_i N_i(x)q_i(t). \tag{5.12}$$

We use linear Lagrange such that only two comparison functions are necessary. The equation of motion no longer evaluates to zero, but to an error e

$$e(x,t) = E_1 \sum_{i=1}^{2} \left(\frac{\partial^2 N_i}{\partial x^2} q_i - \rho_V N_i \ddot{q} \right) + \varepsilon \hat{\Gamma} \frac{\partial}{\partial x} \left(q_1 \frac{\partial N_1}{\partial x} + q_2 \frac{\partial N_2}{\partial x} \right)^3 \tag{5.13}$$

Following the Galerkin method, we obtain two ordinary differential equations by seeking to minimize the error in the space spanned by N_1 and N_2. These equations are obtained by forming the inner product of the error with each comparison function and setting it equal to zero

$$\int_0^L e\, N_1 \,\mathrm{d}x = 0 \tag{5.14}$$

$$\int_0^L e\, N_2 \,\mathrm{d}x = 0. \tag{5.15}$$

Equation (5.14) integrates by parts to yield an equation of motion and boundary conditions

$$-\int_0^L \left(\rho_V N_1 N_2 \ddot{q}_2 + \rho_V N_1^2 \ddot{q}_1 + \sigma_{xx} \frac{\partial N_1}{\partial x} \right) \mathrm{d}x = 0 \tag{5.16}$$

$$\sigma(x,t) N_1(x) \Big|_{x=0}^{L} = 0, \tag{5.17}$$

while Eq. (5.15) yields a similar second equation of motion and boundary condition. The boundary condition derived at the left and right nodes are equal and opposite one another for any choice of N_i which verifies the necessary condition of equal internal forces. The specific comparison function used in this development are

$$N_1(x) = 1 - \frac{x}{L}, \quad N_2(x) = \frac{x}{L}. \tag{5.18}$$

The equations derived from Eqs. (5.14) and (5.15) yield nonlinear equations of motion. Linear mass and stiffness operators produce elemental mass and stiffness matrices ($\mathbf{M}_e$ and $\mathbf{K}_e$), while nonlinear terms produce the elemental nonlinear force vector $\mathbf{f}_e^{NL}$ given by

$$\begin{gathered} \mathbf{M}_e = \rho_V L \begin{bmatrix} 1/3 & 1/6 \\ 1/6 & 1/3 \end{bmatrix}, \quad \mathbf{K}_e = \frac{E_1}{L} \begin{bmatrix} 1 & 1 \\ -1 & -1 \end{bmatrix}, \quad \text{and} \\ \mathbf{f}_e^{NL} = \frac{\hat{\Gamma}}{L^3} \begin{bmatrix} (q_2 - q_1)^3 \\ -(q_2 - q_1)^3 \end{bmatrix}. \end{gathered} \tag{5.19}$$

The elemental matrices and nonlinear force vector for a nonlinear rod element may be assembled into global mass and stiffness matrices that may be used to describe the approximate dynamics of the continuous system. System mass and stiffness matrices are obtained by requiring continuity of displacements and internal force balance so that the equations of motion for the entire rod become

$$\mathbf{M}\ddot{\mathbf{u}} + \mathbf{K}\mathbf{u} + \varepsilon\mathbf{f}^{NL}(\mathbf{u}) = \mathbf{0}, \tag{5.20}$$

where the global mass and stiffness matrices take the form

$$\mathbf{M} = L\begin{bmatrix} \frac{1}{3}\rho_A & \frac{1}{6}\rho_A & 0 & \cdots & 0 \\ \frac{1}{6}\rho_A & \frac{2}{3}\rho_A & \frac{1}{6}\rho_A & \ddots & \vdots \\ 0 & \frac{1}{6}\rho_A & (\frac{1}{3}\rho_A + \frac{1}{3}\rho_B) & \frac{1}{6}\rho_B & 0 \\ \vdots & \ddots & \frac{1}{6}\rho_B & \frac{2}{3}\rho_A & \frac{1}{6}\rho_A \\ 0 & \cdots & 0 & \frac{1}{6}\rho_B & \frac{1}{3}\rho_B \end{bmatrix}_{n\times n} \tag{5.21}$$

and

$$\mathbf{K} = \frac{1}{L}\begin{bmatrix} E_{1A} & -E_{1A} & 0 & \cdots & \cdots & \cdots & 0 \\ -E_{1A} & 2E_{1A} & \ddots & & & & \vdots \\ 0 & \ddots & \ddots & -E_{1A} & & & \vdots \\ \vdots & & -E_{1A} & (E_{1A} + E_{1B}) & -E_{1B} & & \vdots \\ \vdots & & & -E_{1B} & \ddots & \ddots & 0 \\ \vdots & & & & \ddots & 2E_{1B} & -E_{1B} \\ 0 & \cdots & \cdots & \cdots & 0 & -E_{1B} & E_{1B} \end{bmatrix}_{n\times n}, \tag{5.22}$$

where n denotes the number of nodes and $\mathbf{u} \in \mathbb{R}^{n\times 1}$ denotes the nodal displacement vector.

Each jth term f_j^{NL} of the nonlinear force vector $\mathbf{f}^{NL}$ depends nonlinearly on the displacements u_j and $u_{j\pm 1}$, as well as the corresponding material properties. As a result, manual discretization of nonlinear terms is generally difficult and a method of automating the process is desirable. An efficient scheme for doing this is described in Chapter 7. As an example, a unit cell composed of four elements (u_1 through u_5) has a nonlinear force vector

$$\mathbf{f}^{NL} = \frac{1}{L^3}\begin{bmatrix} -\Gamma_A\left(u_1 - u_2\right)^3 \\ \Gamma_A\left(-2u_2 + u_3 + u_1\right)\left(u_2^2 - u_2u_3 - u_1u_2 + \cdots - u_3u_1\right) \\ -\Gamma_A u_2^3 + 3\Gamma_A + \cdots + 3\Gamma_B u_3 u_4^2 - \Gamma_B u_4^3 \\ \Gamma_B\left(-2u_4 + u_3 + u_5\right)\left(u_4^2 - u_4u_5 - u_3u_4 + \cdots - u_3u_5\right) \\ \Gamma_B\left(u_4 - u_5\right)^3 \end{bmatrix}, \tag{5.23}$$

where several terms have been excluded due to length. A unit cell with more nodes assembles similarly.

The global mass and stiffness matrices **M** and **K** are *consistent*. However, others have shown that a lumped mass matrix yields a more accurate approximation of the eigenvalues and eigenvectors associated with a system [60]. For this reason, a *proportional lumping* approach was used to diagonalize the mass matrix. The lumped mass matrix has an added benefit of inertially decoupling the equations of motion, thereby simplifying numerical calculations and perturbation analysis. The discretized system is depicted in Fig. 5.2. The end-to-end assembled elements produce a global system of equations describing any number of unit cells; however, 3 unit cells is sufficient for describing Bloch wave propagation in nonlinear systems as noted in Sec. 2.3.3. After the appropriate perturbation expansions,

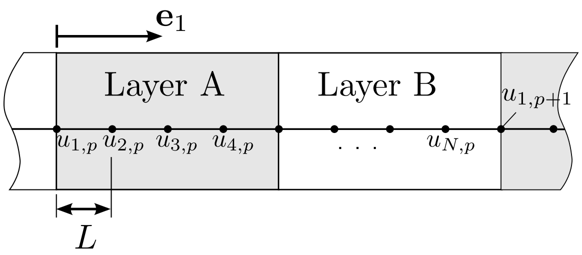

Figure 5.2: Discretized unit cell with N elements per unit cell, and N unique degrees of freedom. The $N + 1th$ DOF in a unit cell p lies on the boundary and therefore belongs to the next unit cell $p + 1$.

Bloch conditions applied at the zeroth order represent all other unit cell degrees of freedom in terms of the central unit cell degrees of freedom.

The matrices $\mathbf{M}_{(p)}$ and $\mathbf{K}_{(p)}$ for the pth unit cell and its two neighbors may be written as block matrices with submatrices $\mathbf{M}_{ij}$ and $\mathbf{K}_{ij}$. The equations of motion for a system of three unit cells neglecting outer neighbors are

$$\begin{bmatrix} \mathbf{M}_{11} & \mathbf{0} & \mathbf{0} \\ \mathbf{0} & \mathbf{M}_{22} & \mathbf{0} \\ \mathbf{0} & \mathbf{0} & \mathbf{M}_{33} \end{bmatrix} \begin{bmatrix} \ddot{\mathbf{u}}_1 \\ \ddot{\mathbf{u}}_2 \\ \ddot{\mathbf{u}}_3 \end{bmatrix} + \begin{bmatrix} \mathbf{K}_{11} & \mathbf{K}_{12} & \mathbf{K}_{13} \\ \mathbf{K}_{21} & \mathbf{K}_{22} & \mathbf{K}_{23} \\ \mathbf{K}_{31} & \mathbf{K}_{32} & \mathbf{K}_{33} \end{bmatrix} \begin{bmatrix} \mathbf{u}_1 \\ \mathbf{u}_2 \\ \mathbf{u}_3 \end{bmatrix} + \varepsilon \begin{bmatrix} \mathbf{f}_1^{NL} \\ \mathbf{f}_2^{NL} \\ \mathbf{f}_3^{NL} \end{bmatrix} = \begin{bmatrix} \mathbf{0} \\ \mathbf{0} \\ \mathbf{0} \end{bmatrix}, \tag{5.24}$$

where $\mathbf{u}_j$ is an $N \times 1$ vector holding the displacements of the pth unit cell, $\mathbf{f}_p^{NL}$ is an $N \times 1$ vector holding the nonlinear forces, and the submatrices $\mathbf{M}_{ij}$ and $\mathbf{K}_{ij}$ are each $N \times N$ matrices. For convenient matrix notation, the central unit cell p corresponds to an index $p = 2$ whereas its left and right neighbors are indexed with $p - 1 = 1$ and $p + 1 = 3$, respectively.

The exact subsystem governing the $p = 2$ unit cell's N DOFs are next obtained from the second row of Eq. (5.24). The internal interactions $\mathbf{f}_{p\pm1}^{int}$ (see Fig. 5.3) on unit cell p resulting from its neighbors are captured by the submatrices $\mathbf{K}_{21}$ and $\mathbf{K}_{23}$ as well as the first and last terms of $\mathbf{f}_2^{NL}$. The dynamic equations resulting from a discretization of the pth unit cell and its two neighbors constitute an *open set* of nonlinear difference equations whose solution is dependent upon $\mathbf{u}_{p+1}$ and $\mathbf{u}_{p-1}$

$$\mathbf{M}_{22}\ddot{\mathbf{u}}_2 + \sum_{p=1}^{3} \mathbf{K}_{2p}\mathbf{u}_p + \varepsilon \mathbf{f}_2^{NL}(\mathbf{u}_2, \mathbf{u}_{2\pm1}) = \mathbf{0}. \tag{5.25}$$

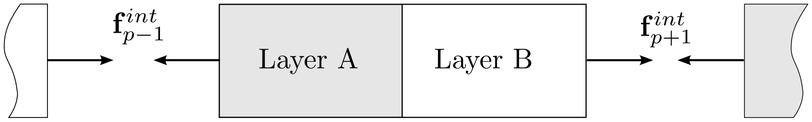

Figure 5.3: Interactions resulting from isolating unit cell p

5.4.2 Perturbation solution for an open set of difference equations

The small parameter ε appearing in Eq. (5.25) facilitates an asymptotic solution approach as described in Sec. 2.4.1. We introduce a dimensionless time $\tau = \omega t$ and standard expansions

$$\begin{aligned} \omega &= \omega_0 + \varepsilon\omega_1 + O(\varepsilon^2) \\ \mathbf{u}_p &= \mathbf{u}_p^{(0)} + \varepsilon\mathbf{u}_p^{(1)} + O(\varepsilon^2). \end{aligned} \tag{5.26}$$

These expansions are substituted into Eq. (5.25) to yield the ordered equations

$$O(\varepsilon^0): \quad \omega_0^2\mathbf{M}_{22}\frac{\partial^2\mathbf{u}_2^{(0)}}{\partial\tau^2} + \sum_{j=1}^{3}\mathbf{K}_{2j}\mathbf{u}_j^{(0)} = \mathbf{0} \tag{5.27}$$

$$O(\varepsilon^1): \quad \omega_0^2\mathbf{M}_{22}\frac{\partial^2\mathbf{u}_2^{(1)}}{\partial\tau^2} + \sum_{j=p}^{3}\mathbf{K}_{2p}\mathbf{u}_p^{(1)} = -2\omega_0\omega_1\mathbf{M}_{22}\frac{\partial^2\mathbf{u}_2^{(0)}}{\partial\tau^2} - \mathbf{f}_2^{NL}(\mathbf{u}_2^{(0)}). \tag{5.28}$$

Bloch's theorem may be applied to the $O(\varepsilon^0)$ equations (5.27) to produce a set of equations describing an infinite [linear] system that depends on the dimensionless Bloch wave number μ,

$$\omega_0{}^2\mathbf{M}\frac{\partial^2\mathbf{u}^{(0)}}{\partial\tau^2} + \mathbf{K}(\mu)\mathbf{u}^{(0)} = \mathbf{0}, \tag{5.29}$$

where the matrix $\mathbf{M} = \mathbf{M}_{22}$ and *reduced* matrix $\mathbf{K}(\mu) = \mathbf{K}_{21}\exp(-\mathrm{i}\mu) + \mathbf{K}_{22} + \mathbf{K}_{23}\exp(\mathrm{i}\mu)$ are both $N \times N$ matrices, and $\mathbf{u}^{(0)} = \mathbf{u}_2^{(0)}$ is an $N \times 1$ field displacement vector within the central unit cell at the ε^0 order. Seeking solutions that are time-harmonic with amplitude A

$$\mathbf{u}^{(0)} = \frac{A}{2}\boldsymbol{\phi}\exp(\mathrm{i}\tau) + c.c., \tag{5.30}$$

Eq. (5.29) yields a standard eigenvalue problem for eigenfrequencies $\omega_{0,j}(\mu)$ and Bloch wave modes $\boldsymbol{\phi}_j(\mu)$, parameterized by the dimensionless Bloch wave number μ

$$\left(\mathbf{K}(\mu) - \omega_0^2\mathbf{M}\right)\boldsymbol{\phi}_j = \mathbf{0}. \tag{5.31}$$

The dispersion relation for the continuous system is approximated by $\omega_{0,j}(\mu)$, where the jth eigenvalue corresponds to the jth dispersion branch. The approximate dispersion relations become more accurate as the number of mesh elements is increased; this is quantified in the results section. This is particularly important for comparing FEA-generated dispersion relations to the exact linear solution produced by the transfer matrix.

Expanding the nonlinear vector $\mathbf{f}_2^{NL}$ in a Fourier series and keeping only the $\mathbf{c}_1$ term, the $O(\varepsilon^1)$ system of equations may be reduced by assuming a "secular-Bloch" type solution. The eigenvectors (i.e. Bloch wave modes) for the reduced $O(\varepsilon^0)$ problem are the same as those for the reduced $O(\varepsilon^1)$ homogeneous system, and thus the matrix of wave modes $\mathbf{\Phi} = [\boldsymbol{\phi}_1 ... \boldsymbol{\phi}_N]$ decouples the system of equations in a similar manner. Removal of secular terms leads to an $O(\varepsilon^1)$ frequency correction term for the jth branch given by Eq. (2.36)

$$\omega_{1,j}(\mu) = \frac{\boldsymbol{\phi}_j^H \mathbf{c}_1}{\omega_{0,j} A \boldsymbol{\phi}_j^H \mathbf{M} \boldsymbol{\phi}_j},$$

where $\boldsymbol{\phi}_j^H$ denotes the Hermitian transpose of $\boldsymbol{\phi}_j$. However, when $\mathbf{f}_2^{NL}$ more-generally contains $\mathbf{u}_2^{(0)}$ *and* its time derivatives, such as in electromagnetics, the correction $\omega_{1,j}$ must be developed on an individual basis [62]. The updated dispersion relation for the jth branch is then given as

$$\omega_j(\mu) = \omega_{0,j}(\mu) + \varepsilon \omega_{1,j}(\mu) + O(\varepsilon^2), \tag{5.32}$$

which may be used to identify amplitude-depending shifting of dispersion bandgaps and variations in group velocity. Next, dispersion shifts computed using a quasilinear transfer matrix approach are compared and contrasted with those computed using this perturbation analysis.

5.5 Results

5.5.1 Linear system dispersion convergence analysis

Sufficient discretization of the domain is important in analyzing nonlinear dispersion using the perturbation method. The discretized systems at $O(\varepsilon^0)$ directly produce the dispersion relationship of the linear system following the procedure outlined in Sec. 5.4. The number and type of finite elements are important in obtaining accurate eigenvectors, particularly for higher frequencies. Figure 5.4 depicts the convergence of several dispersion branches for a phononic system as the number of finite elements is increased (parameters provided in Sec. 5.5.2). The solid branches $\omega_{\text{TMM}}(\mu)$ represent *theoretical* values for the linear system, obtained by solving the linear bilayered problem using the transfer matrix approach. Convergence is quantified as a percent difference from the theoretical values calculated using the transfer matrices. The point of measurement is $\mu = 0$ or $\mu = \pi$ where the largest deviation $\Delta\omega_{\text{FEA}}$ exists.

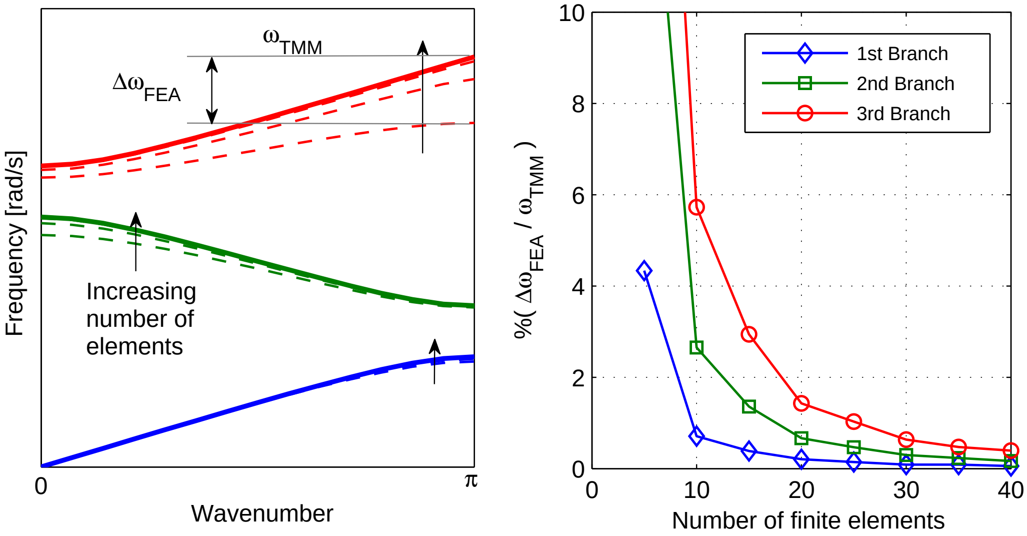

Figure 5.4: Dispersion branch convergence of the first 3 dispersion branches for a linear bilayered periodic system. Solid lines represent exact calculations using linear transfer matrix theory. Dashed lines indicate calculations performed using a discretized system. Arrows indicate the direction of convergence as the number of elements per unit cell increases $N = 5,\ 10,\ 20$.

$$\Delta\omega_{FEA} = \left.\frac{|\omega_{FEA} - \omega_{TM}|}{\omega_{TM}}\right|_{\mu=0,\pi}. \tag{5.33}$$

The first three branches of the discrete systems converge to the theoretical values (ω_{TMM}) within 0.5% or better when using 40 linear Lagrange elements to discretize a unit cell, as shown in Fig. 5.4

Caution must be taken near small bandgaps, because such bandgaps may erroneously arise from the discretization procedure. In such cases, these errors propagate through to the calculation of the eigenvectors. The result of an incorrect eigenvector calculation is manifested by anomalous dispersion characteristics such as branch crossings or non-smooth dispersion branches. This may be remedied by increasing the mesh resolution or using higher order elements, such as quadratic Lagrange elements. A few Bloch wavemodes are illustrated in Fig. 5.5 using both the transfer matrix method and the finite element method. The Bloch wavemodes are in good agreement with the theoretical mode shapes obtained using a transfer matrix analysis. In all nonlinear results presented next, the number of elements employed are chosen based on achieving modal convergence as explained above.

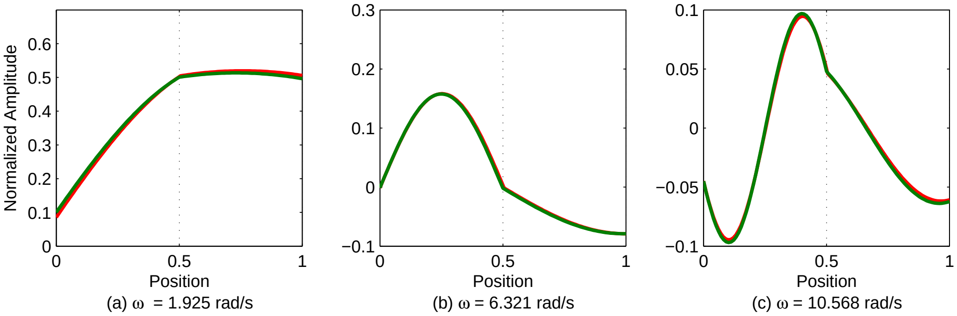

Figure 5.5: A few linear Bloch wave modes for (a) $\omega = 1.925$, (b) $\omega = 6.321$, and (c) $\omega = 10.568$ calculated using the transfer matrix method (solid green) and the finite element discretization (solid red). These Bloch wave modes correspond to points on the first three dispersion branches of the phononic system considered herein. The dashed line indicates the boundary between adjacent layers.

5.5.2 Dispersion for weakly nonlinear vs. linearized systems

After evaluating the eigenvalues and eigenvectors for the linear acoustic system (as a function of μ), the linearized transfer matrix analysis outlined in Sec. 5.3 and the perturbation procedure described in Sec. 5.4 quickly leads to the dispersion band structure for the nonlinear systems. The eigenvectors of the linear system are normalized such that each wave mode corresponds to a constant strain (and thus a constant ε value for any point on the dispersion curve). The dispersion band structure for the linear system is plotted with the dispersion relation for the weakly nonlinear system in Fig. 5.6a. The branches shift upward for hardening nonlinearities where $\Gamma_A > 0$ and downward for softening nonlinearities $\Gamma_A < 0$, which is consistent with past results [3].

The parameters used for the bimaterial rod model are $\rho_A = \rho_B = 1\,\mathrm{kg\,m^{-3}}$, $E_{1A} = 1\,\mathrm{Pa}$,

$E_{1B} = 4\,\mathrm{Pa}$, and $\Gamma_A = 1\,\mathrm{Pa}$ with a strain amplitude of $\epsilon_0 = 0.3$ such that $\varepsilon = 0.10$. These parameters are chosen to give an impedance mismatch of $Z_B/Z_A = 2$. This relatively low impedance mismatch illustrates how discretization and linearization affect the dispersion relation where a small bandgap may exist. The shifts calculated using quasilinear material properties in tandem with the transfer matrix method, also shown in Fig. 5.6, tend to overestimate the higher frequency wave modes slightly (relative to the perturbation results), while for acoustic wave modes and the first optical branch the differences are almost negligible. Figure 5.6 also contains data points obtained from time-dependent numerical simulations which are discussed shortly. Group velocity plots are presented in Fig. 5.7 to illustrate more explicitly the qualitative differences and similarities between each of the methods presented. The group velocity is defined as $c_g = \mathrm{d}\omega/\mathrm{d}\mu$ as described in Chapter 2. The existence of a new, and likely erroneous, bandgap in the quasilinear system is observed; a short discussion on this is presented in Sec. 5.5.4, where numerical comparisons are introduced.

5.5.3 Numerical validation

Time-dependent numerical simulations of the bimaterial rod were performed using the commercial finite element package Comsol. A large domain of 80 unit cells was constructed and simulated for times such that no reflections were produced, and such that spatial frequencies could be resolved using fast fourier transforms. A time-harmonic strain of the form

$$\epsilon_{xx}(0,t) = \epsilon_0 \sin(\omega t) \tag{5.34}$$

was applied at the left boundary, while the right boundary condition was fixed. Dispersion points were calculated by performing a two-dimensional fast fourier transform (2D-FFT) on the resulting time-space matrix of nodal displacement and then extracting peak values. Some error in the 2D-FFTs is introduced due to (small) extra-harmonic generation over the 80 unit cells considered.

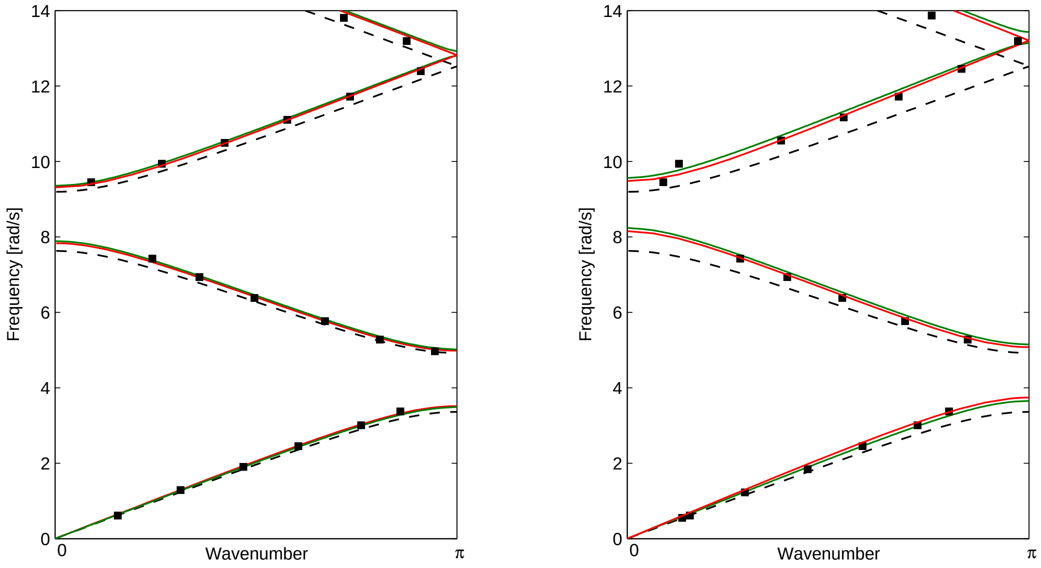

(a) $\varepsilon = 0.10$

(b) $\varepsilon = 0.25$

Figure 5.6: Dispersion points generated from numerical simulation of the bimaterial rod (black squares) for (a) $\varepsilon = 0.10$ and (b) $\varepsilon = 0.25$, compared to the analytical dispersion branches calculated using the transfer matrix method (solid green) and the proposed perturbation method (solid red). The linear dispersion relation (black dashed) is shown for comparison. Black markers denote data extracted from time-domain numerical simulation results.

Figure 5.6 documents very good agreement for both the transfer matrix and perturbation approaches. The nonlinear results for the bimaterial rod tend to agree quite well with the perturbation results for stronger nonlinearity ($\varepsilon = 0.25$) as well. The relatively good agreement between the perturbation approach and the transfer matrix approach shown in Figs. 5.6 and 5.6b does not hold true for all layered systems. The transfer matrix predicts almost no shift of the dispersion curve for *thin nonlinear layers*. The reason for this stems from the fact that large strains produced in certain wave modes are not captured in a constitutive law linearization. The transfer matrix (see Eq. (5.5)) corresponding to a thin nonlinear layer begins to look like an identity matrix as the layer thickness approaches zero. Since the off-diagonal terms contain the amplitude-dependent impedances multiplied by sine functions, the their relative contribution decreases with layer thickness as well. In contrast, perturbation approach captures fine details of the wave mode and their effect on

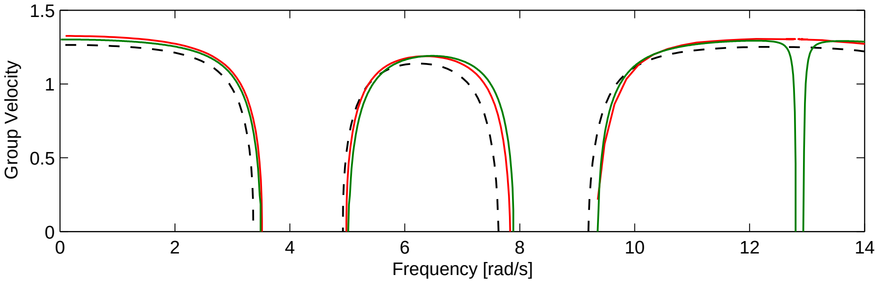

Figure 5.7: Group velocity plots for the first four branches of the bimaterial rod. The linear system (black dashed) has no bandgap between the third and fourth branches (around $\omega = 12.8\,\mathrm{rad\,s^{-1}}$), while the quasilinear system (green) exhibits a small bandgap. The nonlinear system (red) faithfully represents the dispersion qualities of the underlying linear system.

dispersion. An additional analysis case further highlights this behavior.

Time-domain simulation results are shown along-side perturbation and transfer-matrix calculations for a thin nonlinear layer ($a/d = 0.05$) in Fig. 5.8a. The time-domain simulation is performed using a higher impedance mismatch ($E_{1B} = 20\,\mathrm{Pa}$, $E_{1A} = 1\,\mathrm{Pa}$, $\rho_A = \rho_B = 1\,\mathrm{kg\,m^{-1}}$) and amplitude such that $\varepsilon = 0.10$. The Bloch wave modes are normalized in the same manner as those in Fig. 5.6a. The increased contrast in material properties results in a larger dispersion shift for the same amplitude. Unlike in Fig. 5.6a, the quasi-linear approach cannot capture the nonlinear shift. Analytical calculation of the dispersion curves using the transfer matrix approach is shown along-side results from a linear system (black dashed) and perturbation calculations (red). Markers are used to highlight the transfer-matrix calculations since the shift is nearly indiscernable from a linear system.

Figure 5.8b shows results from a time-domain simulation ($\omega = 11.0\,\mathrm{rad\,s^{-1}}$) that have been transformed in the frequency-wave number domain via 2D-FFT. This view of the time-domain results reveals that loss of energy to sub- and super-harmonics contributes to the small discrepency between predicted and realized dispersion relationships. Amplitudes greater those used for this simulation cannot be predicted using the perturbation approach as nonlinear interactions resulting from harmonic generation are not considered

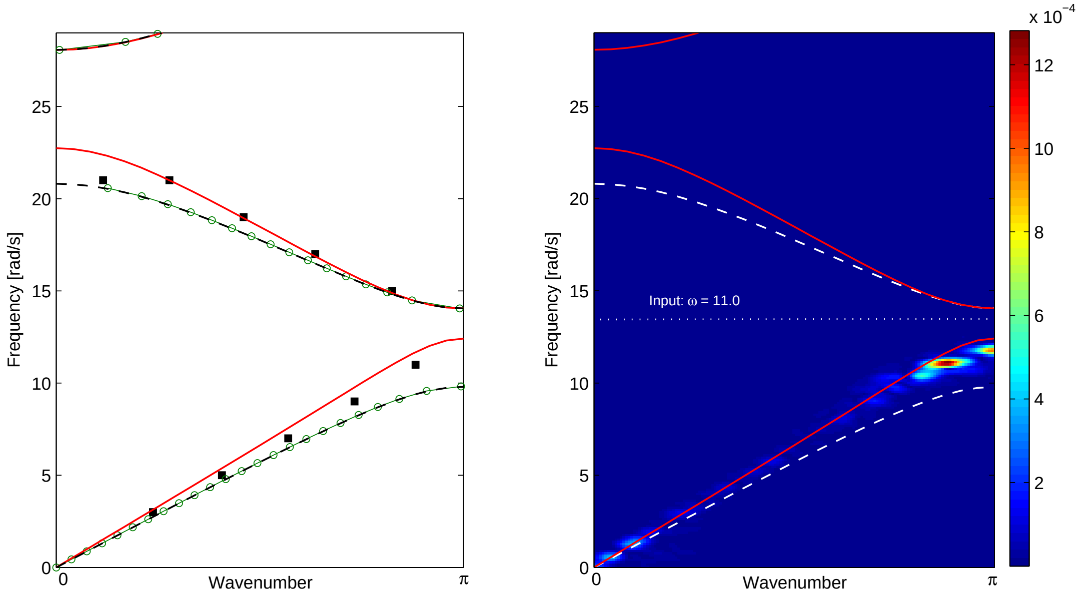

(a) Time-domain simulation results

(b) 2D-FFT Example

Figure 5.8: Nonlinear dispersion relation for a high-contrast thin nonlinear layer ($\varepsilon = 0.10$). The points generated from numerical simulation (black squares) are shown with analytical curves generated using the perturbation method on the nonlinear system (red) and the transfer matrix method on the quasi-linear system (green with markers). The linear curve (black dashed) is shown for comparison. Results are obtained from 2D-FFT transforms as depicted in Fig. 5.8b.

in the current analysis. Nevertheless, these generated harmonics tend to appear at wave number-frequency pairs which coincide with the predicted dispersion relationship.

5.5.4 Analysis of bandgaps

The choice of parameters for the bimaterial rod highlights an important difference between each nonlinear analysis method. A detailed analysis of Figs. 5.6a and 5.6b between the third and fourth dispersion branches ($\omega \approx 12.8\,\mathrm{rad\,s^{-1}}$) reveals no bandgap for a linear system. Linearizing system and applying the transfer matrix technique, however, results in a *new linear system* with *qualitatively different dispersion characteristics*. The quasilinear analysis predicts the existence of *new bandgaps*. The perturbation analysis predicts changes in only the size and location of existing bandgaps, while preserving the band structure qualities of the linear system. This qualitative disparity becomes more prominent as the nonlinearity increases.

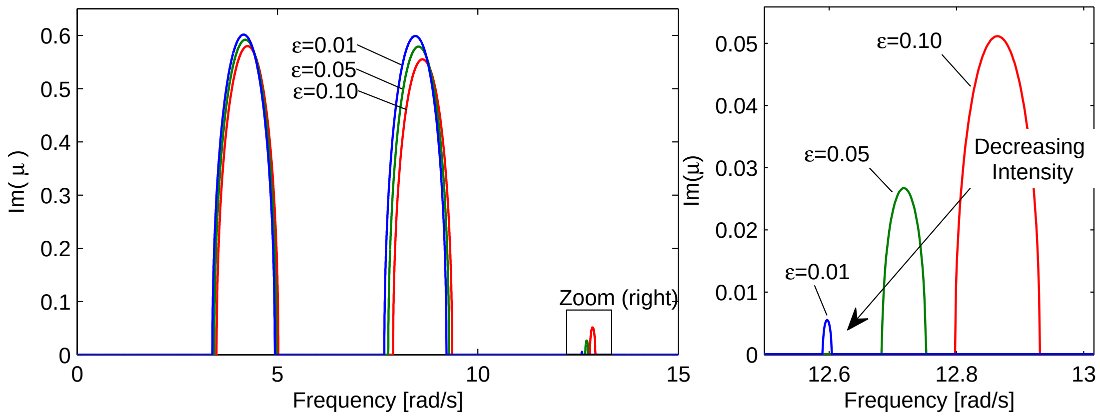

Figure 5.9: Attenuation coefficient for the quasilinear dispersion showing the existence of a small bandgap. The size and location of the bandgap changes with intensity.

The evanescent wave produced inside a bandgap is quantified by the magnitude of the imaginary component of μ, termed the attenuation coefficient. Larger attenuation coefficients cause exponential decay at a quicker per-unit-cell rate. Figure 5.9 shows the attenuation coefficient for several values of ε. The magnitude of the attenuation coefficient is such that many periods of a unit cell are required to observe any significant decay. Furthermore, any wave propagation of a given amplitude within this bandgap would undergo amplitude decay, which changes the location and size of the attenuation zone. Eventually, the wave reaches a point in space where there is no attenuation (a saturation behavior) as described in [24]. Because of this, it is difficult to show numerically that such a bandgap exists. However, since the linear system and the nonlinear system, as analyzed using a rigorous asymptotic technique (perturbation), do not exhibit these bandgaps, it is reasonable to expect that they are spurious.

5.6 Conclusions

Wave propagation through a bilayered material was investigated within the context of nonlinear phononic systems. The locations of bandgaps as a result of dispersive material behavior and amplitude-dependence were identified analytically using (1) a quasi-linear approach in conjunction with the transfer matrix method, and (2) a perturbation method whereby the continuous system is discretized. In applying the perturbation analysis, it is important to discretize the system finely-enough such that convergence is obtained in the dispersion relationship over the frequency range of interest.

For weakly nonlinear systems, the magnitude of the dispersion shifts predicted by both methods is comparable when the layer fraction of nonlinear material is large. For simple systems such as the bilayered material where the transfer matrix method may be used to obtain an analytical dispersion relationship, a quasi-linear analysis may be appropriate given the extra effort required to discretize the system. The transfer matrix method with quasi-linear material properties is less attractive when analyzing complex geometry in more than one dimension, or systems that support Bloch waves with localized regions of high-strain (thin layers), and so the proposed perturbation method may be more appropriate.

The quasi-linear analysis method of calculating dispersion shifts results in qualitatively different band structure than the linear system. In contrast, perturbation analysis of the weakly nonlinear system perserves and modifies the dispersion characteristics of the linear system such as the group velocity and the size, location, and number of bandgaps. Analysis of the attenuation coefficient for the weakly nonlinear systems shows that the differences are negligible for weak nonlinearities.

CHAPTER VI

TOPOLOGY DESIGN AND OPTIMIZATION

6.1 Overview

Topology designs which maximize dispersion shifts are explored through parametric optimization and an implementation of the genetic algorithm. The cubic nonlinearity commonly found in mechanical systems gives rise to frequency shifting and thus a shift in band gap location [102]. We consider two systems exhibiting this nonlinearity: (1) a continuous one-dimensional layered system, and (2) a binary plane-stress system composed of two materials. Each system contains one material governed by a nonlinear constitutive law.

The multilayer and plane stress systems provide convenient unit cells for exploring optimized topology configurations in the presence of nonlinearities. Layered systems often serve as fundamental building blocks in topology optimization studies [103, 104]. Compound layered systems (sometimes termed *sequentially ranked laminates*), for example, find use in topology optimization for microstructure distribution [86]. However, structures composed of sequentially ranked laminate microstructures derive their overall response from homogenized properties since wavelengths of concern in these problems are many orders greater than a unit cell length. In contrast, we focus on systems where these two length scales are similar.

The plane stress system provides a convenient entry point for analyzing the effects of topology on nonlinear periodic arrays in two dimensions where directionality, in addition to band gaps, may be tailored. Topology optimization of a *linear* binary inclusion system was considered in [104] with the goal of optimizing dispersion band structure and frequency response characteristics. The system considered in Sec. 6.4 resembles the system discussed in [104], but considers nonlinear stress-strain relationships that arise from large amplitude waves.

Genetic algorithms have been used extensively by the phononic/photonic crystal community for identifying configurations which achieve complete band gaps [105, 106, 107, 108, 109]. Genetic algorithms identify optimal solutions through iterative population generation, mutation, crossover, and selection processes. A fitness function ranks individual members of a population based on a specified criteria. Because these algorithms do not rely on knowledge of local gradients, there is a greater probability of finding a global maximum. Furthermore, the genetic algorithm handles binary material systems directly, whereas gradient-based optimization routines usually require continuous design variables and explicit gradient expressions. This partially explains why genetic algorithms have gained such popularity in phononic and photonic crystal analysis where it is known *a priori* that stark material contrasts are essential to producing the desired results.

This chapter is organized as follows. First, the equations of plane stress are introduced. A system of nonlinear coupled wave equations results from the introduction of a nonlinear constitutive perturbation term. A finite-element discretization of the governing equations for a single unit cell leads to computationally-intensive expressions for the nonlinear force vector when computing dispersion diagrams. A structured mesh and symbolic evaluation of the weak integral expedite computations. Moreover, an efficient algorithm for evaluating the nonlinear force vector is introduced. Application of nonlinear dispersion analysis to a simplified continous layered system yields configurations which are sensitive to stiffness nonlinearity (Sec. 6.3). The topology and material parameters of the layered system are varied systematically to identify configurations resulting in large dispersion relation shifts. Finally, we investigate topology variations which result in large band gaps for two-dimensional plane stress arrays in Sec. 6.4. A parametric study reveals that thin nonlinear layers (ligaments) produce large group-velocity and band gap variation with amplitude. A genetic algorithm implementation confirms that the intuitive designs examined in the parametric analysis are, indeed, near-optimal solutions for achieving nonlinear sensitivity. The results provide direction for designing unit cells optimized for dynamic tunability.

6.2 Theoretical background

6.2.1 System model

The developments that follow assume a periodic elastic structure whose dynamics are governed by the conservation of momentum in the absence of externally applied forces (Eq. (2.11)), repeated here

$$\nabla \cdot \boldsymbol{\sigma}(\mathbf{r}) = \rho_V \frac{\partial^2 \mathbf{u}(\mathbf{r})}{\partial t^2}, \quad \forall \mathbf{r} \in \Omega, \tag{6.1}$$

where $\boldsymbol{\sigma}$ denotes the elastic stress tensor, ρ_V is the material density, and $\mathbf{u}$ is the displacement field vector. We consider 1D and 2D computational domains. In the following, we report in detail the equations governing the 2D case, with the 1D case being omitted as a particular case for the sake of brevity.

In the 2D case, each material point with in-plane coordinates described by $\mathbf{r} = x\,\mathbf{e}_1 + y\,\mathbf{e}_2$ for $(x\,,y) \in \Omega$ undergoes in-plane motion. Then, the displacement vector $\mathbf{u} = [u(\mathbf{r}),\ v(\mathbf{r})]$ describes motion along the $\mathbf{e}_1$ and $\mathbf{e}_2$ directions, respectively. With these assumptions, Eqs. (6.1) are expressed as:

$$\frac{\partial \sigma_{xx}}{\partial x} + \frac{\partial \sigma_{xy}}{\partial y} = \rho_V \frac{\partial^2 u}{\partial t^2}, \quad \forall (x, y) \in \Omega, \tag{6.2a}$$

$$\frac{\partial \sigma_{xy}}{\partial x} + \frac{\partial \sigma_{yy}}{\partial y} = \rho_V \frac{\partial^2 v}{\partial t^2}, \quad \forall (x, y) \in \Omega, \tag{6.2b}$$

where σ_{ij} denotes the stress tensor, h denotes thickness in the $\mathbf{e}_3$ direction, and ρ_V denotes volume density. We adopt Voigt notation such that components of the stress tensor are given by $\sigma_i = [\sigma_{xx}, \sigma_{yy}, \sigma_{xy}]^T$. A nonlinear elastic constitutive law is considered

$$\begin{bmatrix} \sigma_{xx} \\ \sigma_{yy} \\ \sigma_{xy} \end{bmatrix} = \begin{bmatrix} c_{11}(\epsilon_{xx}) & c_{12} & 0 \\ c_{12} & c_{22}(\epsilon_{yy}) & 0 \\ 0 & 0 & c_{66}(\epsilon_{xy}) \end{bmatrix} \begin{bmatrix} \epsilon_{xx} \\ \epsilon_{yy} \\ 2\epsilon_{xy} \end{bmatrix}, \tag{6.3}$$

where small strain components are defined according to

$$\epsilon_{xx} = \frac{\partial u}{\partial x}, \quad \epsilon_{yy} = \frac{\partial v}{\partial x}, \text{ and } \epsilon_{xy} = \frac{1}{2}\left(\frac{\partial u}{\partial y} + \frac{\partial v}{\partial x}\right). \tag{6.4}$$

Strain dependence in off-diagonal terms c_{12} is neglected. The coefficient functions c_{11}, c_{22}, c_{12}, and c_{66} describe an isotropic material with cubic nonlinearities and are given by [58]

$$\begin{aligned} c_{11} &= \frac{E_1}{1-\nu^2} + \Gamma_x {\epsilon_{xx}}^2 && \text{(6.5a)} \\ c_{22} &= \frac{E_1}{1-\nu^2} + \Gamma_y {\epsilon_{yy}}^2 && \text{(6.5b)} \\ c_{66} &= \frac{E_1}{2(1+\nu)} + \Gamma_{xy} {\epsilon_{xy}}^2 && \text{(6.5c)} \\ c_{12} &= \frac{\nu E_1}{1-\nu^2}, && \text{(6.5d)} \end{aligned}$$

where E_1 and ν denote the linear modulus and Poisson ratio, respectively. The cubic nonlinearity coefficients Γ_x, Γ_y, and Γ_{xy} may be derived from experimental data, or from well-known nonlinear constitutive laws such as the Neo-Hookean, Mooney-Rivlin [110], or Murnaghan Potential models [28, 67].

Small strains and weak nonlinearity are enforced in the constitutive equations by introducing $\hat{\Gamma}_x$, $\hat{\Gamma}_y$, and $\hat{\Gamma}_{xy}$ according to $\Gamma_x = \epsilon\hat{\Gamma}_x$, $\Gamma_y = \epsilon\hat{\Gamma}_y$, and $\Gamma_{xy} = \epsilon\hat{\Gamma}_{xy}$. These terms result in a weakly nonlinear contribution when the stresses due to the nonlinear terms are much less than the stresses due to linear terms. The updated plane stress equations are

$$\frac{\partial}{\partial x}\left(c_{11}\frac{\partial u}{\partial x} + c_{12}\frac{\partial v}{\partial y}\right) + \frac{\partial}{\partial y}\left[c_{66}\left(\frac{\partial u}{\partial y} + \frac{\partial v}{\partial x}\right)\right] + \varepsilon f_x^{NL} = \rho\frac{\partial^2 u}{\partial t^2} \quad (x,y) \in \Omega \tag{6.6a}$$

$$\frac{\partial}{\partial x}\left[c_{66}\left(\frac{\partial u}{\partial y} + \frac{\partial v}{\partial x}\right)\right] + \frac{\partial}{\partial y}\left(c_{22}\frac{\partial u}{\partial x} + c_{12}\frac{\partial u}{\partial x}\right) + \varepsilon f_y^{NL} = \rho\frac{\partial^2 u}{\partial t^2} \quad (x,y) \in \Omega. \tag{6.6b}$$

and the nonlinear functions f_x^{NL} and f_y^{NL} are given by

$$\begin{aligned} f_x^{NL} &= \frac{\partial}{\partial x}\left[\hat{\Gamma}_x\left(\frac{\partial u}{\partial x}\right)^3\right] + \frac{\partial}{\partial y}\left[\hat{\Gamma}_{xy}\left(\frac{\partial u}{\partial y} + \frac{\partial v}{\partial x}\right)^3\right] \\ f_y^{NL} &= \frac{\partial}{\partial x}\left[\hat{\Gamma}_{xy}\left(\frac{\partial u}{\partial y} + \frac{\partial v}{\partial x}\right)^3\right] + \frac{\partial}{\partial y}\left[\hat{\Gamma}_y\left(\frac{\partial u}{\partial y}\right)^3\right]. \end{aligned} \tag{6.7}$$

6.2.2 Finite-element discretization

The nonlinear analysis of the *continuous* equations of motion is impractical for general periodic unit cells; therefore, discretized equations of motion as provided by the FE method will be employed herein. As the objective of the study is the dispersion analysis for periodic systems, the computational domain Ω of interest is a unit cell, which is discretized into a suitable number of elements $\Omega^{(e)}$, so that $\Omega = \bigcup_{(e)} \Omega^{(e)}$. Consider for a moment the plane stress equation (6.2) for an element domain $\Omega^{(e)}$. We choose to employ quadrilateral elements for several reasons:

1. Strain varies over the element, unlike triangular constant-strain elements,
2. Manual assembly is straight-forward and can produce a structured mesh, and,
3. A structured mesh improves evaluation speed of the nonlinear force vector, which is particularly beneficial in optimization routines (to be discussed later).

However, a weak formulation of the governing equations is next presented without bias towards any particular element type.

Each of the governing equations is multipled by an interpolation function $N_i(x, y)$ and integrated over the element domain to produce the weak form of the governing equations: (see [61] for complete details)

$$\begin{aligned} h \iint_{\Omega^{(e)}} \left[\frac{\partial N_i}{\partial x}\left(c_{11}\frac{\partial u}{\partial x} + c_{12}\frac{\partial v}{\partial y}\right) + \frac{\partial N_i}{\partial y} c_{66}\left(\frac{\partial u}{\partial y} + \frac{\partial v}{\partial x}\right) + \varepsilon f_{u_i}^{NL} + \rho N_i \ddot{u}\right] d\Omega^{(e)} \\ - h \int_{\partial\Omega^{(e)}} N_i \left[\left(c_{11}\frac{\partial u}{\partial x} + c_{12}\frac{\partial v}{\partial y}\right) n_x + c_{66}\left(\frac{\partial u}{\partial y} + \frac{\partial v}{\partial x}\right) n_y\right] ds = 0 \end{aligned} \tag{6.8a}$$

and, similarly for the second equation:

$$\begin{aligned} h \iint_{\Omega^{(e)}} \left[\frac{\partial N_i}{\partial x} c_{66}\left(\frac{\partial u}{\partial y} + \frac{\partial v}{\partial x}\right) + \frac{\partial N_i}{\partial y}\left(c_{12}\frac{\partial u}{\partial x} + c_{22}\frac{\partial v}{\partial y}\right) + \varepsilon f_{v_i}^{NL} + \rho N_i \ddot{v}\right] d\Omega^{(e)} \\ - h \int_{\partial\Omega^{(e)}} N_i \left[c_{66}\left(\frac{\partial u}{\partial y} + \frac{\partial v}{\partial x}\right) n_x + \left(c_{12}\frac{\partial u}{\partial x} + c_{22}\frac{\partial v}{\partial y}\right) n_y\right] ds. = 0 \end{aligned} \tag{6.8b}$$

Equations (6.8) represent the weak form of the plane stress equations. The first term in either equation is the field equation, while the latter term represents boundary conditions. Integration has been carried out over the entire domain, including the $\mathbf{e}_3$ direction, which is responsible for producing the thickness h in the expressions. The n_x and n_y terms denote components of the boundary normal in $\mathbf{e}_1$ and $\mathbf{e}_2$ directions, respectively. However, as the system considered is infinite in extent the latter term is not explicitely considered beyond this point.

The displacement fields $u(x, y, t)$ and $v(x, y, t)$ over the element domain $\Omega^{(e)}$ are represented with n interpolation functions N_i, $i = 1..n$ and nodal displacements $u_i(t)$ and $v_i(t)$ according to

$$u(x, y, t) = \sum_{i=1}^{n} N_i(x, y) u_i(t), \quad v(x, y, t) = \sum_{i=1}^{n} N_i(x, y) v_i(t). \tag{6.9}$$

Elemental mass, stiffness, and nonlinear force vectors are formed by introducing Eq. (6.9) into the weak form of the governing equations Eq (6.8), carrying out the integration, and collecting terms as appropriate. The discretized matrix form of the governing equations for an element can be expressed

$$\begin{bmatrix} \mathbf{M}_{(e)} & \mathbf{0} \\ \mathbf{0} & \mathbf{M}_{(e)} \end{bmatrix} \begin{bmatrix} \ddot{\mathbf{u}}_{(e)} \\ \ddot{\mathbf{v}}_{(e)} \end{bmatrix} + \begin{bmatrix} \mathbf{K}^{11}_{(e)} & \mathbf{K}^{12}_{(e)} \\ \mathbf{K}^{21}_{(e)} & \mathbf{K}^{22}_{(e)} \end{bmatrix} \begin{bmatrix} \mathbf{u}_{(e)} \\ \mathbf{v}_{(e)} \end{bmatrix} + \varepsilon \begin{bmatrix} \mathbf{f}^{NL}_{u} \\ \mathbf{f}^{NL}_{v} \end{bmatrix} = \begin{bmatrix} \mathbf{0} \\ \mathbf{0} \end{bmatrix}, \tag{6.10}$$

where $\mathbf{M}_{(e)}$, $\mathbf{K}^{mn}_{(e)}$, $\mathbf{f}^{NL}_{u,v}$, $\mathbf{u}_{(e)}$ and $\mathbf{v}_{(e)}$ denote element mass mass and stiffness matrices, elemental nonlinear force vectors, and displacement components. Exact expressions for the mass and stiffness matrix terms are given by

$$\begin{aligned} M_{ij} &= h \int_{\Omega^{(e)}} \rho N_i N_j d\Omega^{(e)} \\ K^{11}_{ij} &= h \int_{\Omega^{(e)}} \left(c_{11} \frac{\partial N_i}{\partial x} \frac{\partial N_j}{\partial x} + c_{66} \frac{\partial N_i}{\partial y} \frac{\partial N_j}{\partial y} \right) d\Omega^{(e)} \\ K^{12}_{ij} &= K^{21}_{ji} h \int_{\Omega^{(e)}} \left(c_{12} \frac{\partial N_i}{\partial x} \frac{\partial N_j}{\partial x} + c_{66} \frac{\partial N_i}{\partial y} \frac{\partial N_j}{\partial x} \right) d\Omega^{(e)} \\ K^{22}_{ij} &= h \int_{\Omega^{(e)}} \left(c_{66} \frac{\partial N_i}{\partial x} \frac{\partial N_j}{\partial x} + c_{22} \frac{\partial N_i}{\partial y} \frac{\partial N_j}{\partial y} \right) d\Omega^{(e)}. \end{aligned} \tag{6.11}$$

Each of Eqs. (6.8) contains a nonlinear force term that arises from nonlinearities in the constitutive law. These terms are derived exactly as in Eq. (6.8) but are retained as separate terms. Their contribution to the elemental nonlinear force vectors $\mathbf{f}_u^{NL}$ and $\mathbf{f}_v^{NL}$ are given by

$$\begin{aligned} f_{u_i}^{NL} &= h \iint_{\Omega^{(e)}} \frac{\partial N_i}{\partial x}\left[\hat{\Gamma}_x\left(\frac{\partial u}{\partial x}\right)^3 + \hat{\Gamma}_y\left(\frac{\partial u}{\partial y} + \frac{\partial v}{\partial x}\right)^3\right]\mathrm{d}\Omega^{(e)} \\ f_{v_i}^{NL} &= h \iint_{\Omega^{(e)}} \frac{\partial N_i}{\partial y}\left[\hat{\Gamma}_x\left(\frac{\partial u}{\partial y} + \frac{\partial v}{\partial x}\right)^3 + \hat{\Gamma}_y\left(\frac{\partial u}{\partial y}\right)^3\right]\mathrm{d}\Omega^{(e)}, \end{aligned} \tag{6.12}$$

where $f_{u_i}^{NL}$ and $f_{v_i}^{NL}$ denote nonlinear restoring forces applied to the ith node in the $\mathbf{e}_1$ and $\mathbf{e}_2$ directions, respectively. An assembly of nonlinear elastic plane stress elements of the form given in Eq. (6.11) produces a system of weakly nonlinear governing equations which fits the general form required for the perturbation analysis

$$\mathbf{M}\ddot{\mathbf{u}} + \mathbf{K}\mathbf{u} + \varepsilon\mathbf{f}^{NL}(\mathbf{u}) = \mathbf{0}, \tag{6.13}$$

where $\mathbf{M}$ and $\mathbf{K}$ are assembled mass and stiffness matrices for the domain Ω and $\mathbf{u}$ contains is a vector containing all of the degrees of freedom in Ω. In what follows, the domain Ω is defined as the union of 9 adjacent unit cells as depicted in Fig. 2.5. Then, Bloch wave analysis follows directly as decribed in Chapter 2.

The evaluation of the nonlinear force vector can be a computationally intensive task. The cost of this operation is here reduced through the symbolic evaluation of the integrals in Eq. (6.12) for each interpolation function N_i. The use of regular meshes with elements all of equal size leads to symbolic expressions for the elemental nonlinear forces that are identical for all elements. This further streamlines the nonlinear term evaluation, whose symbolic expression is saved as part of functions evaluated in terms of the elemental nodal displacements and the relevant constitutive parameters.

Nonlinear band structure calculations required repeated assembly and evaluation of $\mathbf{f}^{NL}$ for multiple wave vectors. Optimization codes that use band structure as part of an objective function may require evaluation of $\mathbf{f}^{NL}$ thousands of times. Further improvements are obtained by using compiled codes that utilize parallel assembly and efficient evaluation of $\mathbf{c}_1$. An efficient algorithm for evaluating the first Fourier coefficient $\mathbf{c}_1$ is described next. Figure 6.1 summarizes the nonlinear force vector assembly procedure and Fourier coefficient evaluation conducted as part of the nonlinear dispersion analysis described in Ch. 2.

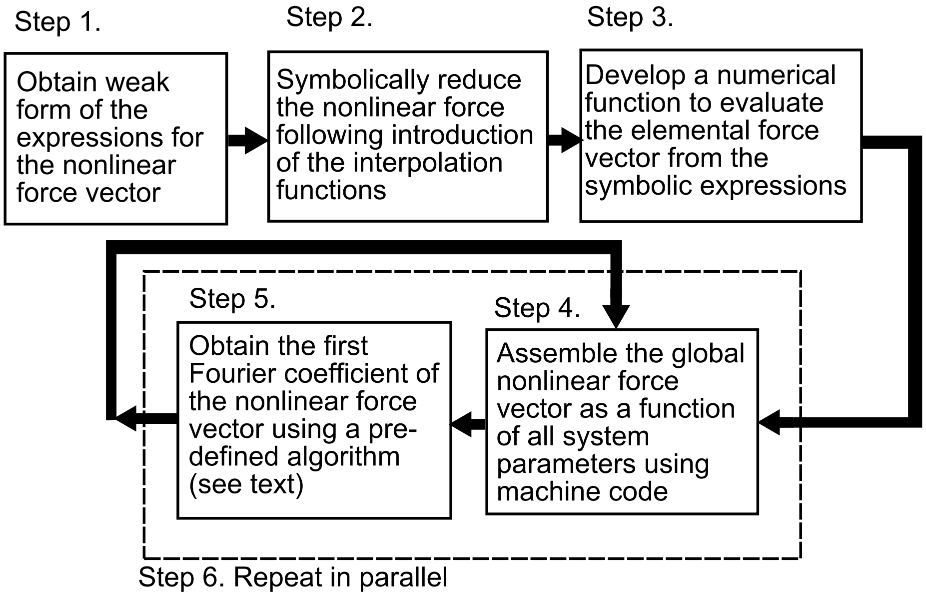

Figure 6.1: Efficient procedure for evaluating nonlinear dispersion band structures.

6.2.3 Efficient algorithm for calculation of Fourier coefficients

The nonlinear frequency correction requires the Fourier series expansion of $\mathbf{f}^{NL}$, and specifically the evaluation of the first coefficient $\mathbf{c}_1$. This is done through the numerical evaluation of the nonlinear force function at discrete times to ascertain the temporal behavior of each term in $\mathbf{f^{NL}}$. Previous work has evaluated the function at discrete time instants $\tau_i \in [0, 2\pi]$ and numerically computed the first Fourier coefficient using either numerical integration schemes or FFT algorithms (See Ch. 7 and Refs. [102, 111], for example). Both of these methods require fine temporal discretization over a single fundamental period to obtain accurate estimates for the $\mathbf{c}_1$ coefficient. Individual band structure computations do not suffer significantly from this method; however, optimization routines require optimized code. An improved evaluation method takes advantage of the polynomial nature of the constitutive law, and thus reduces the number of function evaluations to four.

Individual elements of the nonlinear force vector may generally be expressed in the form

$$\mathbf{f}_i^{NL}(\mathbf{u}(\tau)) = \sum_{l,m,n} \alpha_{lmn} u_l u_m u_n, \tag{6.14}$$

where each node u_i denotes the ith element of the displacement vector and is 2π periodic in dimensionless time τ. Thus, the temporal behavior of each term is known *a priori* to be of the form

$$\mathbf{f}^{\mathbf{NL}}(\tau) = \mathbf{A}_1 \cos(\tau) + \mathbf{A}_3 \cos(3\tau) + \mathbf{B}_1 \sin(\tau) + \mathbf{B}_3 \sin(3\tau) \tag{6.15}$$

as a result of trigonometric identities. This equation is linear in the four unknown amplitude vectors $\mathbf{A}_1, \mathbf{A}_3, \mathbf{B}_1, \mathbf{B}_3$. The first complex Fourier coefficient is determined from the expression

$$\mathbf{c}_1 = (\mathbf{A}_1 - \mathbf{i}\mathbf{B}_1)/2. \tag{6.16}$$

Thus, it remains only to compute the vectors $\mathbf{A}_1$ and $\mathbf{B}_1$. The unknown amplitude vectors are determined by evaluating the nonlinear force vector at four distinct times to obtain a consistent set of equations. Strategically chosen times $\tau_i = [0, \pi/2, \pi/3, \pi/6]$ reduce the complexity of the resulting expressions. The system of equations obtained using these τ_i is given by

$$\begin{bmatrix} \mathbf{I} & \mathbf{I} & \mathbf{0} & \mathbf{0} \\ \mathbf{0} & \mathbf{0} & \mathbf{I} & -\mathbf{I} \\ \cos(\pi/3)\mathbf{I} & -\mathbf{I} & \sin(\pi/3)\mathbf{I} & \mathbf{0} \\ \cos(\pi/6)\mathbf{I} & \mathbf{0} & \sin(\pi/6)\mathbf{I} & -\mathbf{I} \end{bmatrix} \begin{bmatrix} \mathbf{A}_1 \\ \mathbf{A}_3 \\ \mathbf{B}_1 \\ \mathbf{B}_3 \end{bmatrix} = \begin{bmatrix} \mathbf{f}^{\mathbf{NL}}(0) \\ \mathbf{f}^{\mathbf{NL}}(\pi/2) \\ \mathbf{f}^{\mathbf{NL}}(\pi/3) \\ \mathbf{f}^{\mathbf{NL}}(\pi/6) \end{bmatrix}, \tag{6.17}$$

where $\mathbf{I}$ denotes the $N \times N$ identity matrix and $\mathbf{0}$ denotes the $N \times N$ zero matrix, where N is the total number of degrees of freedom in the system.

The unique solution to this linear system of equations provides the desired $\mathbf{c}_1$ coefficient. The solution for $\mathbf{A}_1$ and $\mathbf{B}_1$ is

$$\mathbf{A}_1 = \mathbf{f}_a - \frac{1}{\sqrt{3}}\mathbf{f}_b, \quad \mathbf{B}_1 = \mathbf{f}_b - \frac{1}{\sqrt{3}}\mathbf{f}_a, \tag{6.18}$$

where the substitutions $\mathbf{f}_a = \mathbf{f}^{\mathbf{NL}}(0)+\mathbf{f}^{\mathbf{NL}}(\pi/3)$ and $\mathbf{f}_b = \mathbf{f}^{\mathbf{NL}}(\pi/2)+\mathbf{f}^{\mathbf{NL}}(\pi/6)$ have been made. This enhanced formulation dramatically increases the computation speed by reducing the number of $\mathbf{f}^{NL}$ evaluations to an absolute minimum of four.

6.2.4 Shift sensitivity analysis

Recall that the systems considered all contain cubic nonlinearities or exhibit one after a Taylor expansion. Recall also that $O(\varepsilon^0)$ Bloch wave solutions take the form $\mathbf{u}^{(0)} = A\boldsymbol{\phi}/2\exp(-\mathrm{i}\tau) + c.c.$. Since the nonlinear force term has been defined as the cubic contribution of a general nonlinear force function in Eq. (6.5d), it is possible to factor out A^3 from each element of $\mathbf{c}_1$ without loss of generality (see Eq. (6.14)). In doing so, the nonlinear dispersion corrections may be computed using the expression

$$\omega_{1,j} = K_\omega(\boldsymbol{\mu})A^2, \quad K_\omega \equiv \frac{\boldsymbol{\phi}_j^H \mathbf{c}_1}{\omega_{0,j}\boldsymbol{\phi}_j^H \mathbf{M}\boldsymbol{\phi}_j} \tag{6.19}$$

where we term K_ω is termed the *shift sensitivity*, and redefine $\mathbf{c}_1$ such that it is no longer parametrized by A. The shift sensitivity describes the quantitative and qualitative nature of the dispersion shifts for a given nonlinearity, independent of wave mode amplitude. Large K_ω are found for systems where large frequency shifts occur for relatively small amplitudes and are desirable for designing tunable systems which respond to signal gain. Softening nonlinearities shift the dispersion curves downward in frequency, implying $K_\omega < 0$, while hardening nonlinearities shift the dispersion curves upward, implying $K_\omega > 0$, for a given wave vector. Using Eq. (2.36) and the sensitivity K_ω, the updated dispersion relation is given by

$$\omega_j(\boldsymbol{\mu}) = \omega_{0,j}(\boldsymbol{\mu}) + \varepsilon A^2 K_\omega(\boldsymbol{\mu}) + O(\varepsilon^2). \tag{6.20}$$

Note that a group velocity calculation based on Eq. (6.20) yields a correction to the group velocity,

$$\mathbf{c}_g = \nabla_\mu \omega_{0,j} + \varepsilon A^2(\nabla_\mu K_\omega) + O(\varepsilon^2) = \mathbf{c}_g^{(0)} + \varepsilon \mathbf{c}_g^{(1)} + O(\varepsilon^2), \tag{6.21}$$

where ∇_μ denotes a gradient with respect to the components of the wave vector, $\mathbf{c}_g^{(0)}$ denotes the group velocity of the linear system, and $\mathbf{c}_g^{(1)} = A^2\nabla_\mu K_\omega$ denotes the group velocity correction.

6.3 Strain-induced dispersion shift in 1D layered systems

6.3.1 Model description

The bi-layer structure of Fig. 6.2 provides a straightforward context for exploring the manner in which topological changes can enhance advantageous behavior present in nonlinear band structures. In this example, material A includes a cubic nonlinearity in its stress-strain relationship, while material B includes only a linear term. The topology of this 1D system is defined by the length fraction a/d for a given unit cell length d. We consider, for material A, a hardening-type nonlinearity previously described, while material B is governed by a linear stress-strain constitutive relationship. Analytical solutions for the dispersion relation of a *linear* bi-layer system are widely available and can be expressed as [99, 100, 112],

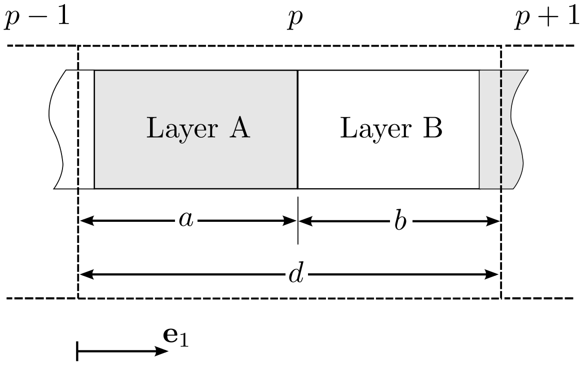

Figure 6.2: Unit cell p for a bi-layer system

$$\cos(\mu_1 d) = \cos\left(\frac{\omega a}{c_A}\right)\cos\left(\frac{\omega b}{c_B}\right) - \frac{1}{2}\left(\frac{Z_A}{Z_B} + \frac{Z_B}{Z_A}\right)\sin\left(\frac{\omega a}{c_A}\right)\sin\left(\frac{\omega b}{c_B}\right), \tag{6.22}$$

where $c_j = \sqrt{E_{1j}/\rho_j}$ denotes the phase speeds in a homogeneous material, and the *impedance* for a layer is given by $Z_j = \sqrt{E_{1j}\rho_j}$ with j being either A or B. Equation (6.22) indicates that band gaps arising in the linear layered system derive from an impedance mismatch caused by stiffness and density contrast at the material interface. The influence of stiffness contrast on the shift sensitivity parameter K_ω is considered next to identify configurations exhibiting optimized band gap width and frequency shifts.

6.3.2 Parametric analysis of dispersion shifts

Dispersion shifts for layered structures generally fall into two categories: individual dispersion branch shifts and band gap width shifts. Group velocity shifts are arguably an additional category; however, large dispersion branch shifts generally imply large group velocity shifts to some extent. Figure 6.3 illustrates the some effects that "small" and "large" shifts may have on dispersion. The middle figure, for example, illustrates that large acoustic branch shifts maintaining original band gap width may be possible. In contrast, large dispersion shifts to the acoustic branch combined with small optical branch shifts might result in band gap closure.

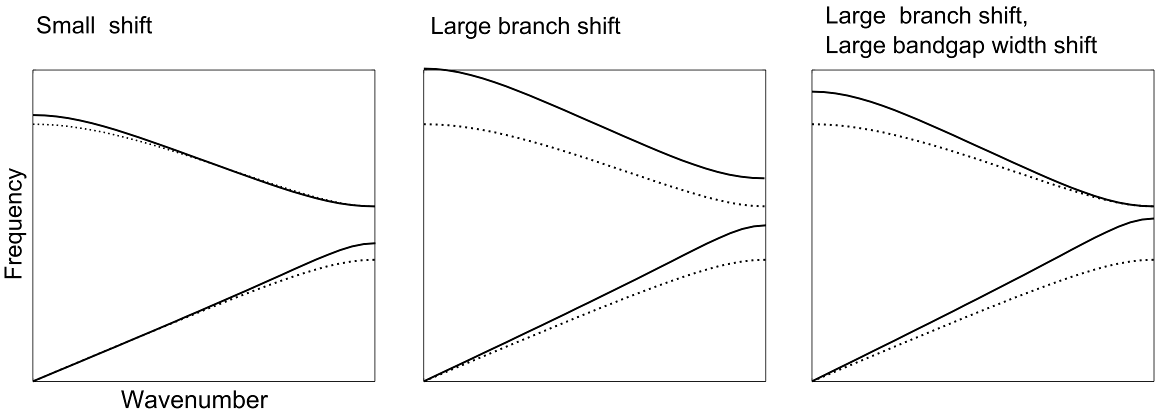

Figure 6.3: Optimizing 1D layered structures may achieve large shifts to individual dispersion branches (middle) and also to band gap widths (right). Dotted lines indicate a low-amplitude (linear) system, while solid lines indicate the nonlinearly shifted dispersion relation.

As an initial investigation into topology optimization of nonlinear layered systems, the length fraction a/d and linear stiffness ratio E_{1B}/E_{1A} are varied to determine their effects on dispersion. Consideration is given to metrics related to the first band gap. In particular, $\Delta\omega_1$ and $\Delta\omega_2$ denote the frequency shift for the first and second dispersion branches evaluated at the edge of the Brillouin zone ($\mu_1 = \pi$). The domain for the bi-layer rod is discretized into 200 linear Lagrange finite elements to obtain fine resolution for small layer fractions a/d. The system parameters used in Ch. 5 are chosen for comparison purposes, which also contains an account of the finite-element discretization procedure.

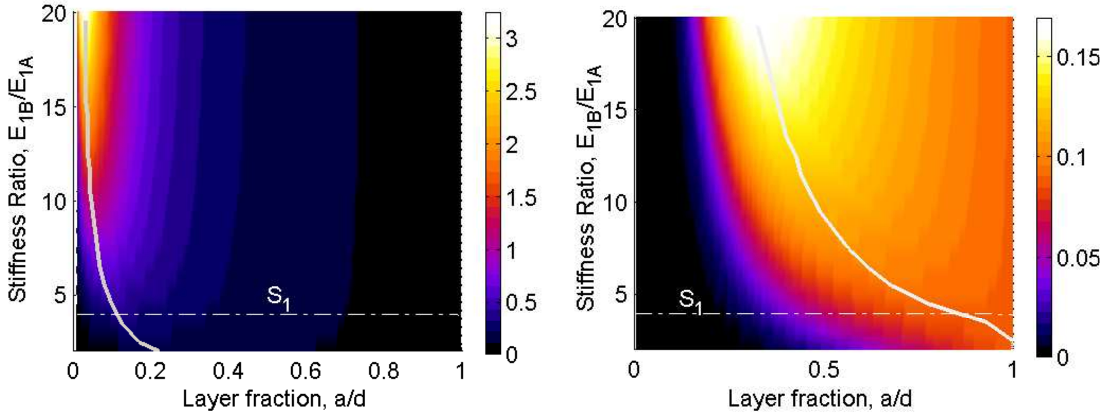

(a) First branch shift, $\Delta\omega_1(\pi)$ (b) Second branch shift, $\Delta\omega_2(\pi)$

Figure 6.4: Frequency shift maps evaluated at the edge of the Brillouin zone for a bi-layer unit cell ($\varepsilon = 0.1$). White lines indicate the locus of maximum shift for a given linear modulus or layer thickness.

Figure 6.4a depicts the computed frequency shift of the acoustic branch $\Delta\omega_1 \propto K_\omega(\pi)$. The maximum acoustic branch shift for a given material stiffness ratio, occurs in nearly all cases for nonlinear length fractions $a/d \ll 0.5$, the case considered in Ref. [62]. The white line indicating the locus of maximum frequency shift tends towards a length fraction of approximately 3% at high stiffness ratios. Figure 6.4b, on the other hand, reveals that maximum corrections to the second dispersion branch $\Delta\omega_2$ appear for larger length fractions $a/d \approx 0.35$. Therefore, the length fraction corresponding to a maximum first band gap width lies somewhere between the two optimum shift values for any given stiffness ratio. Figure 6.5 further details these results by considering a cross-section S_1 of the frequency shift maps taken at $E_{1B}/E_{1A} = 4$. Figure 6.5a depicts the frequency shifts to the first and second dispersion branches. The maximum shift to the acoustic branch occurs at a layer thickness of approximately 12% in this case.

The second dispersion branch, in contrast, does not exhibit a discernible optimum shift value. Instead, the correction $\Delta\omega_2$ increases towards an asymptote representing the shift expected for a continuous system ($a/d = 1.0$), reaching a slight maximum value near $a/d = 0.9$. A perturbation calculation based on a continuous, homogeneous system gives the

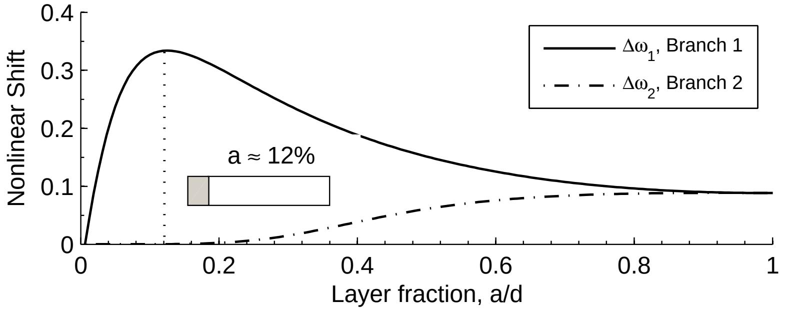

(a) Nonlinear branch shifts

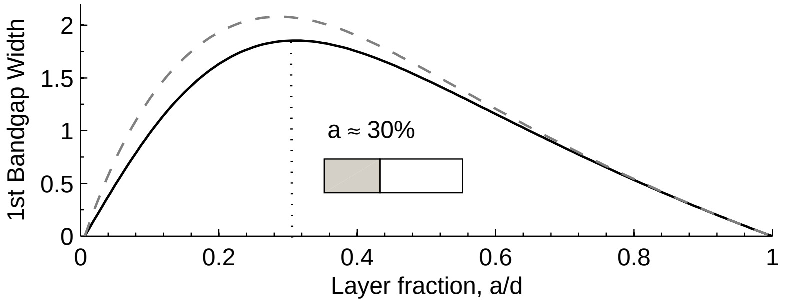

(b) First band gap width

Figure 6.5: Cross-sections of the frequency shift maps shown in Fig. 6.4a and 6.4b evaluated at $E_{1B}/E_{1A} = 4$. The gap width for low- and high-amplitude systems are shown in Fig. 6.5b with dashed and solid lines, respectively, to illustrate the effect of the nonlinearity on the band gap width at this cross-section.

value of this asymptote (details in Appendix C). Indeed, an examination of the frequency shift map in Fig. 6.4b shows that at stiffness ratios $E_{1B}/E_{1A} \lesssim 7$, a clear maxima is not discernible.

A relatively sharp transition between small and large frequency shifts as the length fraction increases is noted for the second dispersion branch that may be advantageous in nonlinear acoustic switches, diodes, and superprism crystals [76]. Figure 6.5b depicts how shifts to the first and second dispersion branches combine to vary the band gap width. The maximum gap width for a bi-layered system using these materials occurs at $a/d \approx 0.30$. These results indicate that, contrary to what might be expected, *less* nonlinear material (i.e., small a/d nonlinear layer fractions) corresponds to larger shifts for this example case, and highlights the importance of systematic topology optimization and design. We note that the combined effect of a large K_ω for the acoustic branch and a small K_ω for the optical branch (evaluated at the band edge) may result in a complete closure of the first band gap at large amplitudes for hardening nonlinearities, or a significant size increase for softening nonlinearities.

Figure 6.6 depicts the resulting dispersion diagram for a system with $a/d = 0.05$ and $E_{1B}/E_{1A} = 20$. Several important features on this nonlinear dispersion diagram may influence the design of nonlinear phononic crystals.

1. The band gap width of the nonlinear system decreases with amplitude due to a hardening nonlinearity. The change in band gap width is dominated by $\Delta\omega_1$ since $\Delta\omega_2$ is negligible (small K_ω). Operation at frequencies above $10\,\mathrm{rad\,s^{-1}}$, for low amplitudes, results in complete attenuation. A slight amplitude increase shifts the dispersion curve upward, allowing unattenuated wave propagation.

2. Frequency upshifts are greatest near the edge of the Brillouin zone where the group velocity is zero. Similar results have been demonstrated by the *photonic* crystal community for Kerr nonlinear electromagnetic materials [91, 76].

3. The group (and phase) velocity for wave numbers $\mu_1 < \pi$ are also significantly shifted; in fact, at greater amplitudes the material appears less dispersive because there exist a greater range of wave numbers with the same phase speed. This concept may be important in realizing soliton solutions and mitigating unwanted dispersion.

These features are explored for use in an amplitude-tunable filter next.

6.3.3 Application: Amplitude-tunable filter

A time-domain simulation elucidates how nonlinear layered systems behave as simple tunable filters. We consider a finite-element model of a bi-layered system composed of 80 elements per unit cell with material properties $\rho_A = \rho_B = 1$, $E_{1A} = 1$, $E_{1B} = 20$, and $\Gamma_x = 1$. A length fraction $a/d = 0.05$ achieves a large acoustic branch shift (see Fig. 6.4a). A harmonic stress $\sigma_{xx}(0,t) = \sigma_0 \cos(\omega t)$ at the left boundary excites Bloch wave propagation through the system. The right boundary is located sufficiently far from the excitation so that no reflections are produced.

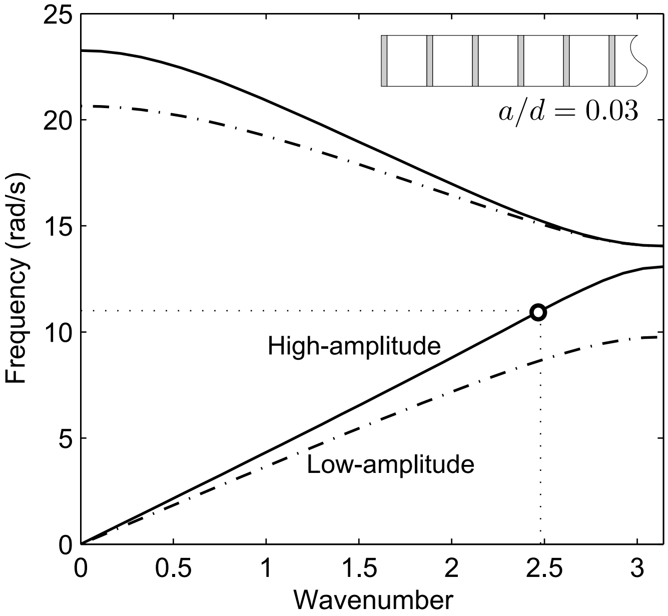

Figure 6.6: Dispersion diagram ($a/d = 0.05$ and $E_{1B}/E_{1A} = 20$) for the simulated system evaluated for low- and high-amplitude excitations. The marker (○) shows simulation results obtained via 2D-FFT of system transient response after a finite-element simulation.

Figure 6.6 depicts dispersion diagrams for low (dashed) and high (solid) amplitude excitations. The combination of amplitude (σ_0) and nonlinearity (Γ_x) considered yields a shift to the acoustic branch that is on the order of the first band gap width. Indeed, increasing the propagation amplitude would close this band gap entirely. This effect allows the first band gap to operate as an amplitude-dependent filter or switch that permits propagation at certain frequencies only for high amplitudes. The excitation frequency $\omega = 11.0\,\mathrm{rad\,s^{-1}}$ falls within the band gap for an essentially linear system (low-amplitude excitation); in contrast, $\omega = 11.0\,\mathrm{rad\,s^{-1}}$ falls well within the pass band for a weakly nonlinear system (high-amplitude). Two simulations are performed: the first at a low-amplitude excitation where the propagation is expected to decay exponentially, and a second at high-amplitude excitation where propagation is expected.

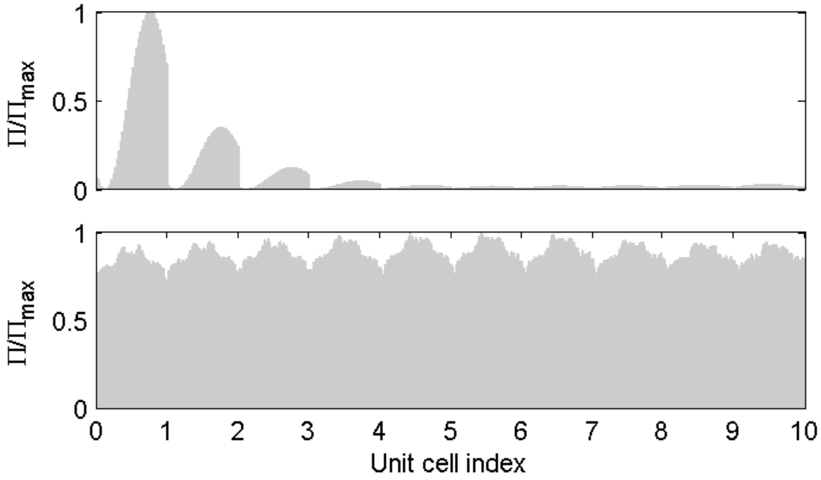

Figure 6.7: Normalized average power distributions for low- and high-amplitude excitations. Evanescent decay of power in space is observed, as expected, for the low-amplitude system.

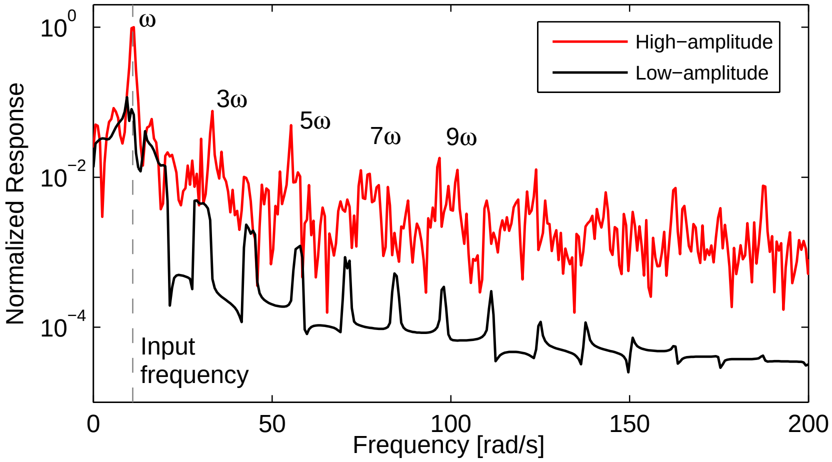

(a) Displacement FFT

Figure 6.8: Displacement signal frequency response in the 10th unit cell. The low amplitude system exhibits a response nearly two orders of magnitude less than the high-amplitude system. The frequency content of the low-amplitude response is distributed throughout the pass bands of the linear system. Super-harmonics of the high-amplitude response are dominant in the response.

A two-dimensional fast Fourier transform provides frequency-domain information from the simulation data that corresponds directly to the dispersion diagram, and facilitates a one-to-one comparison between the predicted dispersion relationship and the numerical simulation. The marker in Fig. 6.6 resulting from the 2D-FFT shows that the pair ω =

$11.0\,\mathrm{rad\,s^{-1}}, \mu_1 \approx 2.5$ dominates the signal content of the forced response simulation, in agreement with the theoretical dispersion relation.

Figure 6.7 further elucidates the qualitative disparity between the two simulations by considering the distribution of power Π throughout the domain (only the first 10 unit cells are shown). Power distributions are normalized to the highest power Π_{max} occurring to highlight the spatial distributions. The power distribution for the low-amplitude simulation (top) decays quickly in space, while for the high-amplitude excitation (bottom) power is evenly distributed through the system. Normalized fast Fourier transforms at the end of the 10th unit cell compare the two signals. Nearly all of the frequency content of the low-amplitude signal is due to wave transients with frequency content located within the first pass band (Fig. 6.6). In contrast, the high-amplitude signal contains a dominant frequency at $\omega = 11.0\,\mathrm{rad\,s^{-1}}$, as well as small third harmonic and sum-and-difference frequencies due to the cubic nonlinearity. Thus, the nonlinearity provides an amplitude-tunable filtering mechanism.

6.4 Analysis and optimization of 2D plane stress systems

The results of Sec. 6.3 demonstrate that multilayer materials exhibit optimum configurations with respect to shift sensitivity and band gap tunability. Next, we investigate optimal configurations of 2D phononic crystals constructed with a nonlinear matrix material. The arrangement of the nonlinear material is optimized in terms of band gap width and nonlinear shifts through both parametric analysis and topology optimization. The selected optimizer is a genetic algorithm that explores a design space defined by a unit cell Ω of the 2D periodic structure with fixed dimensions.

6.4.1 Model description

Figure 6.9 depicts the system under consideration. The material is of infinite extent and is constructed of a periodic arrangement of arbitrarily distributed materials *A* and *B*. Figure

6.9 arbitrarily depicts inclusions Ω_B inserted into a matrix of Ω_A; equally valid is a depiction of material A inclusions in a matrix of material B. Moreover, the distribution may not necessarily resemble a matrix/inclusion at all. The domain Ω is defined as the union of simply-connected domains $\Omega_A^{(i)}$ and $\Omega_B^{(i)}$ where the superscript (i) emphasizes that the system is not restrained to single inclusion type systems. The unit cell domain Ω is subdivided into a number of finite elements such that $\Omega = \bigcup_{(e)} \Omega^{(e)}$ as shown in Fig. 6.10. Each element comprises a sub-domain which takes on a binary value of 0 or 1 corresponding to material A (Ω_A, nonlinear) or material B (Ω_B, linear), respectively. Each sub-domain is considered a design variable, referenced by g_{ij} with $(i, j) = 1..48$ for a total of $2^{(48\times48)} = 2.8\text{e}+14$ potential design combinations.

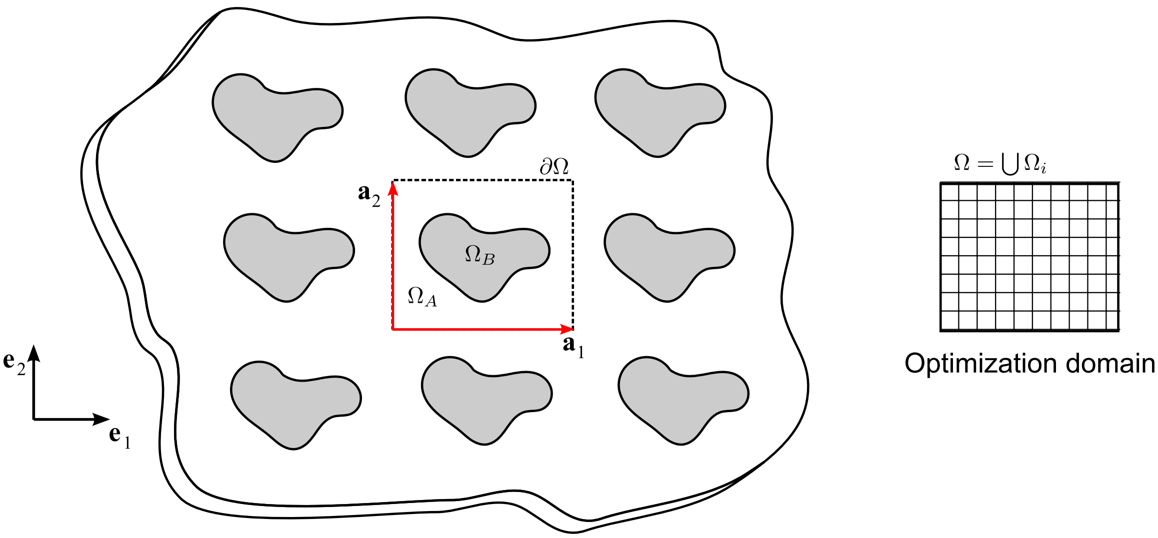

Figure 6.9: Schematic depiction of a periodic material constructed of two phases labeled A and B.

Application of a 1/8 symmetry constraint eliminates ambiguity in the design space due to translational-invariance. Moreover, 1/8 symmetry eliminates designs for which partial band gaps are preferentially larger in either the $\mathbf{e}_1$ or $\mathbf{e}_2$ directions [105, 106]. This reduces the design space from $2^{(48\times48)}$ to $2^{300} = 2\text{e}+9$. It is more convenient to index the domains in a linear fashion whereby g_{ij} is instead referenced with g_i, $i = 1..300$. The numbering scheme indexes elements from left to right, increasing from bottom to top as shown in Fig.

6.10.

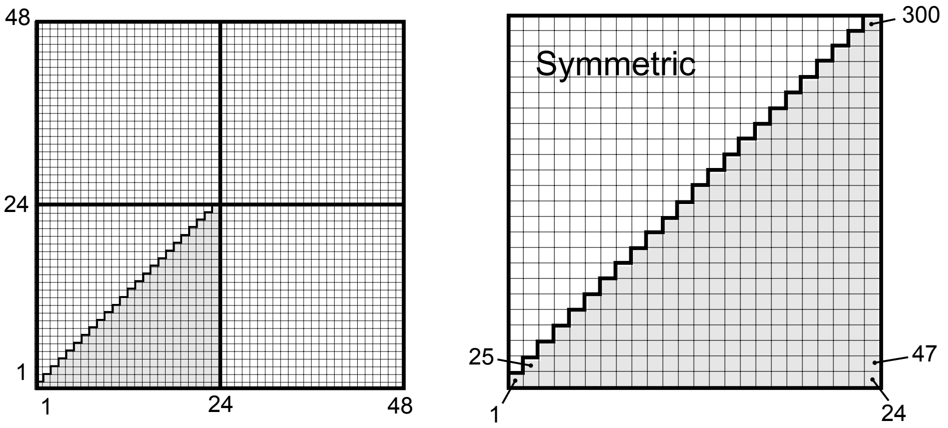

Figure 6.10: Structured unit cell mesh and numbering scheme for design variables g_{ij}

6.4.2 Analysis of strain-induced dispersion shifts

A specific subset of the possible designs informed by the results of Sec. 6.3 are considered next. Figure 6.4.2 depicts a prototypical unit cell (enclosed with dashed lines) with dimensions d_x and d_y describing the width and height. ΓXM symmetry calls for a square unit cell with $a = b$ and $d = d_x = d_y$ such that $\mathbf{a}_1 = \mathbf{a}_2$. White material represents a nonlinear matrix (Material A) within which stiffer inclusions (Material B, black) are embedded. The white sections are termed *nonlinear ligaments* because their purpose is to nonlinearly couple the motion of adjacent inclusions.

Recall that 1D layered systems exhibit sensitive tunability and large dispersion shifts when nonlinear material are

1. restricted to thin layers, and
2. compliant relative to inclusions.

These qualities eliminate some common phononic crystal structures, e.g. air/silicon, as potential design options. Indeed, nonlinear dispersion analysis of a similar two-dimensional

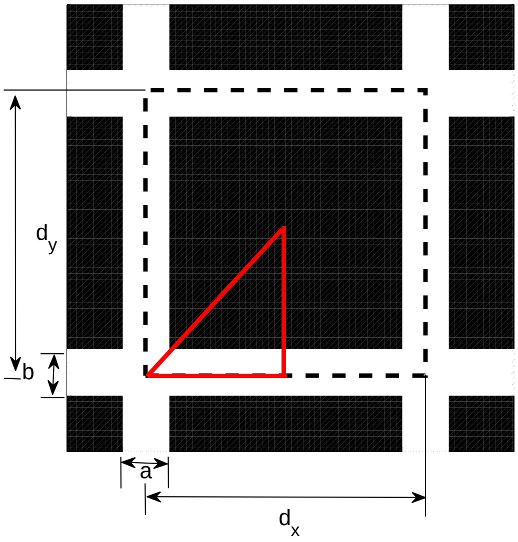

Figure 6.11: A specific subset of important unit cell designs are characterized by nonlinear ligament widths a and b. The subset considers unit cells with 1/8 symmetry as indicated by the red line.

structure confirms that the combination of thin, compliant[1] layers produces Bloch wave modes with localized high strain regions. An example unit cell is highlighted in Fig. 6.4.2. Figure 6.4.2 graphically depicts the dilitational strain field $\boldsymbol{\epsilon}(x, y) = \epsilon_{xx}\mathbf{e}_1 + \epsilon_{yy}\mathbf{e}_2$ produced in a unit cell for a Bloch wave mode on the ΓX portion of the acoustic dispersion surface with an approximate wavelength $3d$-$4d$. Strain-localizations enter the nonlinear force vector $\mathbf{f}^{NL}$ through a few large entries $\mathbf{f}_i^{NL}$ in the nonlinear force vector acting on nodes in the ligament, rather than the cumulative effect of many smaller contributions (as in a completely homogeneous material).

The specific relationship between ligament geometry and associated dispersion shifts is quite complex. The following analysis interrogates the effects of ligament width and stiffness contrast on group velocity and band gap width through systematic parameter variations. Table 2 contains the material properties used for the following analysis. Shear stiffness nonlinearities Γ_{xy} are assumed negligible.

---

[1] Compliance is described here as a property of linear systems, since for large strains a hardening material may not be compliant.

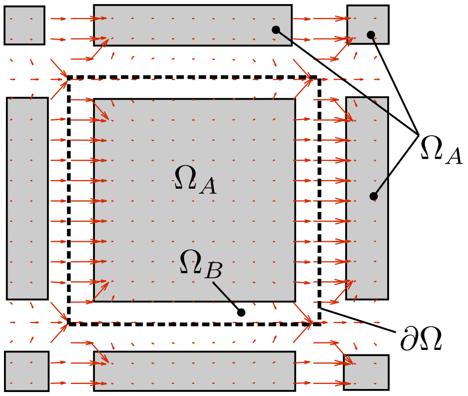

Figure 6.12: Small nonlinear ligaments result in high-strain areas localized in the nonlinear ligament sections. Dashed lines indicate boundaries of rigid inclusions. These high-strain Bloch wave modes are often found in the acoustic band.

Table 2: Material properties

	E_1	Γ_x	Γ_y	Γ_{xy}	ρ	ν	h
Material A	1.0	4.0	4.0	0	1.00	0.34	0.01
Material B	{5.0, 10.0, 20.0, 40.0}	0	0	0	1.00	0.34	0.01

The prototypical unit cell considered has dimensions of $d_x = d_y = 1.0$, thickness h, and is subdivided into 48x48=2304 linear Lagrange elements $\Omega^{(e)}$. Dispersion computations use a strain-normalization scheme with strain amplitude $e_0 = \max(\epsilon_{xx}, \epsilon_{yy}, \epsilon_{xy}) = 0.1$ as detailed in Sec. A. Nonlinear ligament thickness is increased from $a = 0$ (100% Material B) to $a = d$ (100% Material A) for various material stiffness contrasts.

Figure 6.13 and 6.14 depict the variation in group velocity and band gap width as a function of layer fraction a/d and material stiffness contrasts. Figures 6.13a and 6.13b display group velocity shifts evaluated on the acoustic dispersion surface at $\boldsymbol{\mu} = [\pi/6, 0]$. The transverse acoustic branch experiences no nonlinear shift because nonlinear shear moduli Γ_{xy} are zero. Low stiffness contrasts (curve A) result in a maximum group velocity shift for layer fractions of $a/d = 1$ (homogeneous nonlinear material), with a small local maximum appearing near $a/d = 0.25$. As the stiffness contrast increases (curves B–D), a global maximum appears where thin nonlinear ligaments ($a/d = 0.18$) produce larger $\mathbf{c}_g^{(1)}$ shifts than a purely homogeneous material. Increasing material contrasts tend to push the local maximum towards smaller layer fractions, as was seen in the bi-layer system.

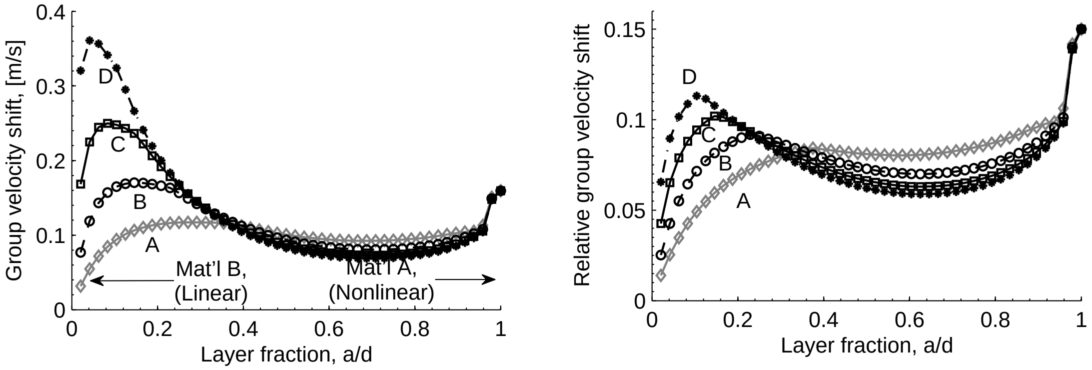

(a) Absolute group velocity shift

(b) Relative group velocity shift

Figure 6.13: (a) Absolute group velocity shift and (b) relative group velocity shifts for the longitudinal acoustic mode along the ΓX-direction. Curves A–D show results for material stiffness ratios E_{1B}/E_{1A} of 5 (A), 10 (B), 20 (C), and 40 (D).

We note that the linear group velocity $\mathbf{c}_g^{(0)}$ varies with topology because the physical system is changing. Thus, the group velocity shift $\mathbf{c}_g^{(1)}$ quantified relative to the linear group velocity provides another metric for defining optimal designs. Figure 6.13b depicts the relative group velocity shift defined by $c_{gr} = |\mathbf{c}_g^{(1)}|/|\mathbf{c}_g^{(0)}|$ such that $\mathbf{c}_g = \mathbf{c}_g^{(0)}(1 + c_{gr})$. All material combinations converge to a single value (0.15) as the layer fraction increases toward a homogeneous nonlinear material.

This result can be validated by considering Eq. (C.12) of Appendix C, repeated here with Γ_x for convenience with the substitution $\omega^{(0)} = c\mu$ for phase speed c.

$$\omega = c\mu\left(1 + \frac{3\Gamma_x}{8E_1}\epsilon_0^2\right). \tag{6.23}$$

As the homogeneous system exhibits no dispersion, the group velocity and phase velocity are identical such that $c_g^{(0)} = c$. Therefore, the relative group velocity is easily obtained from the group velocity $c_g = d\omega/d\mu$. This ratio is precisely

$$c_{gr}^{homog.} = \frac{3\Gamma_x}{8E_1}\epsilon_0^2. \tag{6.24}$$

The relative group velocity shift is $c_{gr}^{homog.} = 0.15$ when evaluated with the system parameters provided in Table 2 and $\epsilon_0 = 0.1$. Thus, the relative group velocity shift calculated using a discrete wave-based perturbation approach in two dimensions is validated by a perturbation analysis for the corresponding continuous system.

Figures 6.14a and 6.14b reveal that near-optimal configurations that achieve complete band gaps follow similar trends. Complete band gaps do not exist for $a/d > 0.5$. The first complete band gap is located between the 3rd and 4th dispersion branches. The width of the band gap is given as

$$\Delta\omega_i \equiv \min(\omega_{i+1}) - \max(\omega_i) = \quad \boldsymbol{\mu} \in \Gamma\mathrm{XM}, \tag{6.25}$$

while *band gap shifts* are defined as the difference between the linear and nonlinear band gap widths

$$\text{Band gap shift} \equiv |\Delta\omega_i^{(1)} - \Delta\omega_i^{(0)}|. \tag{6.26}$$

The hardening nonlinearity tends to shift the third branch more than the 4th branch for optimal configurations, resulting in a net decrease in band gap width. Similarly, a softening nonlinearity increases the band gap by down-shifting the 3rd dispersion branch. Black lines in figure 6.14a show results for a hardening nonlinearity, while the low-amplitude (linear) systems are shown with nearby gray lines for comparison.

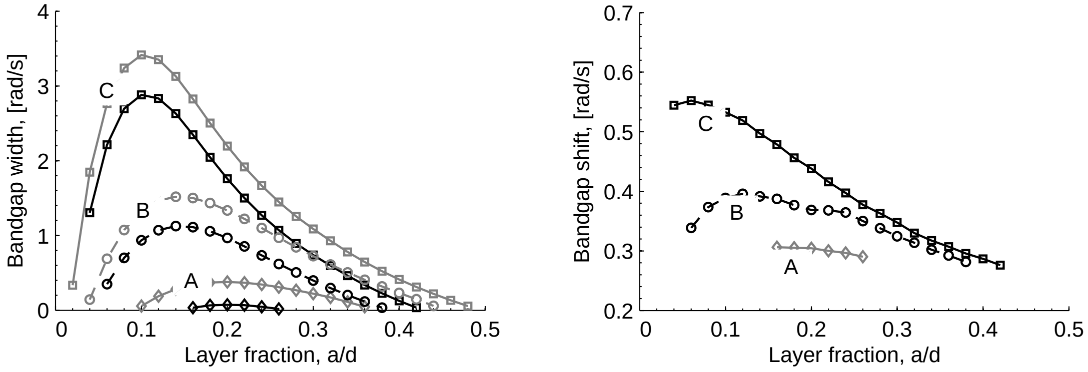

(a) Linear and nonlinear band gap width

(b) Nonlinear band gap shift

Figure 6.14: Complete band gap widths for material systems A–C are shown in 6.14a where black lines indicate the band gap width of the nonlinear system and nearby gray lines indicate the width of the corresponding linear system. The change in complete band gap width is shown in 6.14b, corresponding to the difference between nonlinear and linear band gaps.

Some material/geometry combinations may be effectively used to close the band gap at high amplitude. For instance, material system *A* corresponding to a geometry of $a/d = 0.16$ tends to exhibit a small band gap $\Delta\omega_3 \approx 0.3$ rad/s. For larger amplitudes, this band gap closes due to the frequency shift. The magnitude of this band gap shift is shown in Fig. 6.14b. Indeed, as the band gap *shift* is greater than the band gap *width*, the band gap closes. Both small layer fractions and high material contrasts tend to increase the band gap shift.

As in one-dimension, the maximum band gap width and maximum band gap shift for a given material system do not appear at the same layer fraction. However, both maxima appear for small layer fractions and thus this may be used to guide design of systems which are sensitive to Bloch wave amplitude. While the heuristic design utilized for parametric analysis produced simple configurations, the design space was restricted to those systems corresponding to the predefined geometry defined by the ligament width a. This constraint is removed in the following section whereby the selected optimizer assigns material properties to each of the elements in the considered domain.

6.4.3 Genetic algorithm optimization for tuning dispersion shifts

We seek to simultaneously optimize low-frequency band gap width and band gap shift (similar to Figs. 6.14). A genetic algorithm implementation offers a convenient and viable solution for strategically assigning material to each of the element domains within the 1/8 symmetry constraint $\Omega^{(e)}$ defined by $\mathbf{g} = \bigcup g_i$. Introduce a single aggregate objective function (fitness function) defined according to

$$F(\mathbf{g}) = \alpha_1 F_1(\mathbf{g}) + \alpha_2 F_2(\mathbf{g}), \tag{6.27}$$

where $F_1(\mathbf{g})$ is a metric on the band gap width and $F_2(\mathbf{g})$ is a metric on the band gap shift. The linear system band gap *width* appearing between branches 3 and 4 is calculated according to

$$F_1(\mathbf{g}) = \Delta\omega_3^{(0)}(\mu_1, \mu_2), \quad (\mu_1, \mu_2) \in \Gamma\text{XM}, \tag{6.28}$$

while the corresponding nonlinear band gap *shift* is obtained through the expression

$$F_2(\mathbf{g}) = \left|\Delta\omega_3(\mu_1,\mu_2) - \Delta\omega_3^{(0)}(\mu_1,\mu_2)\right|, \quad (\mu_1,\mu_2) \in \Gamma\text{XM}, \tag{6.29}$$

where the dispersion relation is evaluated along the first Brillouin zone contour ΓXM. The absolute value signs for $F_2(\mathbf{g})$ ensure that shifts which both open and close low-amplitude band gaps are equally awarded. Since almost any randomly generated design will not exhibit a band gap, the coefficients α_1 and α_2 are defined piecewise according to whether or not a band gap exists, similar to [106].

$$\begin{array}{lll} \alpha_1 = 10\text{e}4, & \alpha_2 = 10\text{e}3 & \text{if } F_1(\mathbf{g}) > 0 \text{ (band gap exists)} \\ \alpha_1 = 1, & \alpha_2 = 0 & \text{if } F_1(\mathbf{g}) \leq 0 \text{ (no band gap)} \end{array} . \tag{6.30}$$

This fitness function promotes individuals which exhibit large band gaps and, to a lesser extent, those which exhibit large band gap shifts. The piecewise jump in the α_1 function ensures that individuals exhibiting band gaps are always selected over those individuals which exhibit no band gap. Until a configuration exhibiting a band gap is reached, the band gap shift function F_2 has no meaning, and so α_2 is set to zero for configurations with no band gap. The optimization problem for simultaneously maximizing band gap width and shift is expressed as

$$\max_{\mathbf{g}} F(\mathbf{g}) \text{ subject to: } \mathbf{g} \in \tilde{\Omega}, \tag{6.31}$$

where $\tilde{\Omega}$ denotes the collection of sub-domains $\mathbf{g}$ within the $1/8$ symmetry constraint. *A priori* knowledge suggests choosing a high contrast stiffness ratio $E1_B/E1_A = 20$ for the analysis.

The algorithm begins by generating an initial population of 20 individuals. A uniform, random distribution of individual sequences (with all elements of **g** taking either 0, or 1) ensures that subsequent evolutionary iterations are not biased towards any particular design. Each individual of the population is evaluated according to the fitness function; individuals with greater fitness are selected to move on to the next generation (iteration), while those with lower fitness scores are discarded. New individuals enter into the population through both mutation and crossover. During mutation, small modifications (bit-flips from 0 to 1, or 1 to 0) to existing individuals are introduced through random selection. Crossover individuals spawn from combinations of two- or more parents. This implementation uses a single-point crossover scheme whereby two parents swap a randomly selected portion of their genes (sub-domains).

The genetic algorithm terminates when the change in objective function is less than 1e-6 (about 1500 iterations). Figure 6.15a depicts the final design surrounded by partial neighbor unit cells. The design consists of a square inclusion of rigid material surrounded by a thin nonlinear ligament of width $a/d = 0.125$. In contrast to the simple designs presented earlier, the optimized configurations contain rigid beams protruding from the corners of the unit cell. The appearance of these corner features may have been predicted, since previous (gradient-based) studies have shown that corner features tend to distinguish optimal designs from sub-optimal designs in linear band gap optimization problems [104]. The dispersion relation evaluated along the first Brillouin zone contour is shown in Fig.

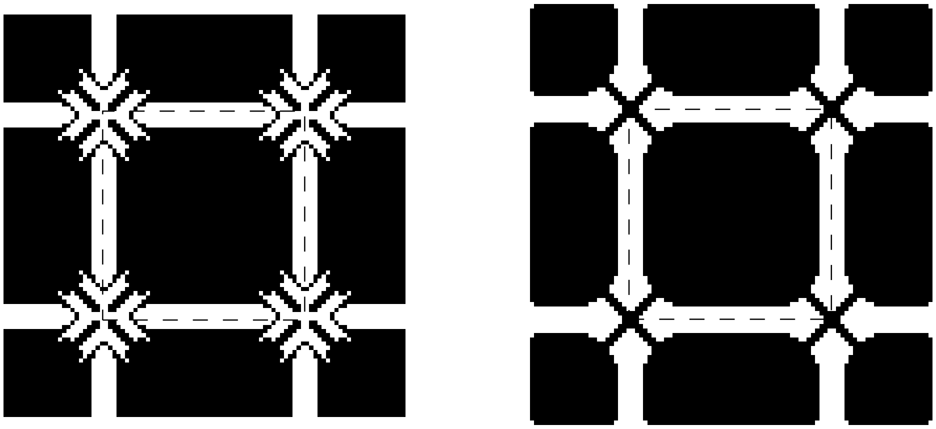

(a) Unit cell before processing

(b) Unit cell after processing

Figure 6.15: Final unit cell design (enclosed by dashed line) surrounded by partial neighboring cells. (a) Depicts the raw output from the genetic algorithm after 1500 iterations, while (b) depicts a processed version amenable to fabrication. White regions correspond to nonlinear material A, while black regions correspond to material B.

6.16. Points P_3 and P_4 bound the complete band gap of the nonlinear system with width $\Delta\omega_3 = 3.1906\,\mathrm{rad\,s^{-1}}$. The band gap shift ($0.43\,\mathrm{rad\,s^{-1}}$) results from nonlinear shifts at both of points P_3 and P_4. However, the branch shift may be roughly approximated by the difference between frequencies at P_2 and P_3.

Practical implementation of the optimal design may be effected through slight modification of the design produced by the genetic algorithm. Figure 6.15b depicts one such design whereby a majority image filter has been applied. The resulting design has a slightly smaller band gap width at $\Delta_3 = 3.0464\,\mathrm{rad\,s^{-1}}$, but a larger band gap shift ($0.44\,\mathrm{rad\,s^{-1}}$). The modified design retains longitudinal and transverse stiffness at the inclusion corners and exhibits no qualitative difference in dispersion band structure.

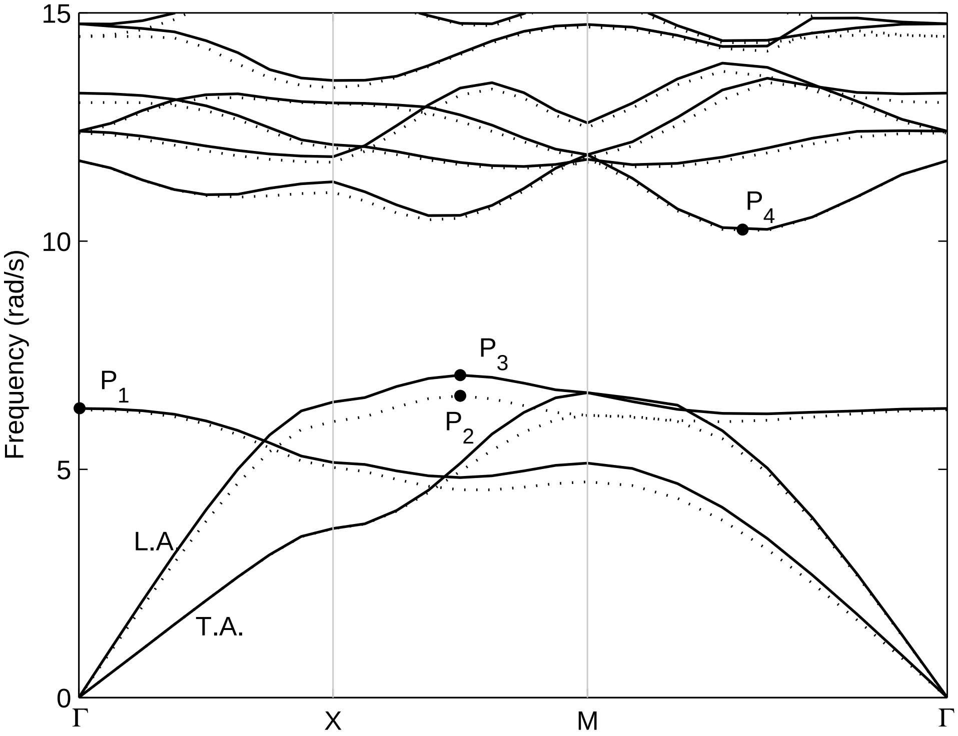

Figure 6.16: Dispersion diagram for optimized unit cell

6.4.4 Discussion

An understanding of wave modes which exhibit maximum shifts may be used to speed up computation times by reducing the number of wave vectors evaluations. Indeed, referencing Figs. 6.14a and 6.14b, one finds that the optimized unit cell has increased the band gap width at some expense of band gap shift. This is an expected outcome since the single aggregate objective function only distinguishes maximum function values based on the assigned weight coefficients α_1 and α_2.

An examination of the strain fields for Bloch wave modes at points P_1, P_3 and P_4 provides some intuition about where and why minimum and maximum shifts occur. The $O(\varepsilon^0)$ strain fields $\epsilon_{xx}(x, y)$, $\epsilon_{yy}(x, y)$, and $\epsilon_{xy}(x, y)$ evaluated at these points are shown in Fig. 6.17. Points P_1 and P_4 exhibit negligible shifts relative to the shift at point P_3. The ϵ_{xx} strain field at point P_3 is much stronger, relative to points P_1 and P_4, while the ϵ_{yy} components are approximately the same order of magnitude.

This localized tension and compression in the nonlinear ligaments is responsible for producing large stresses due to the Γ_x coefficient. This results in an effective stiffness increase, and therefore a shift in the dispersion curves. Similarly, points along the longitudinal acoustic branch, labeled L.A., receive shifts which produce effective group velocity variation. In contrast, points P_1 and P_4 exhibit greater shear strain ϵ_{xy} than the wave mode at P_3. As the nonlinear shear coefficient Γ_{xy} is zero, these modes exhibit no nonlinear shifts. In the same vein, those modes along the transverse acoustic branch (labeled T.A.) also exhibit no shift since they are in nearly pure shear. The reason for the rigid fingers protruding from the corner of the cell is less apparent; one possible explanation is that they may tend to compress/tension ligament material which would otherwise see less strain. An understanding of these Bloch wave mode features may assist in design strategies for nonlinear phononic systems and metamaterials.

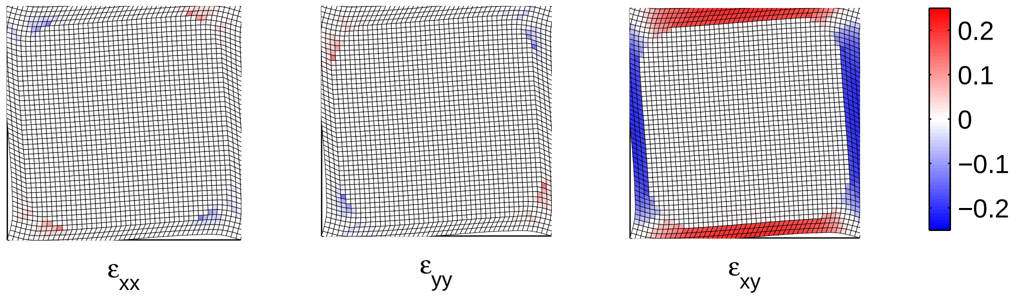

(a) Strain fields at P1

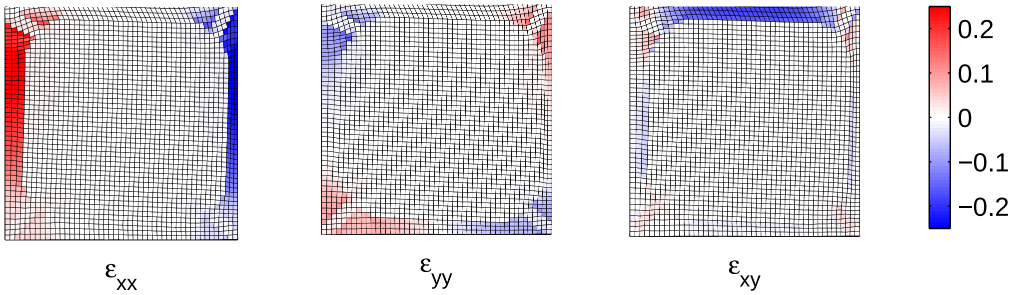

(b) Strain fields at P3 (and P2)

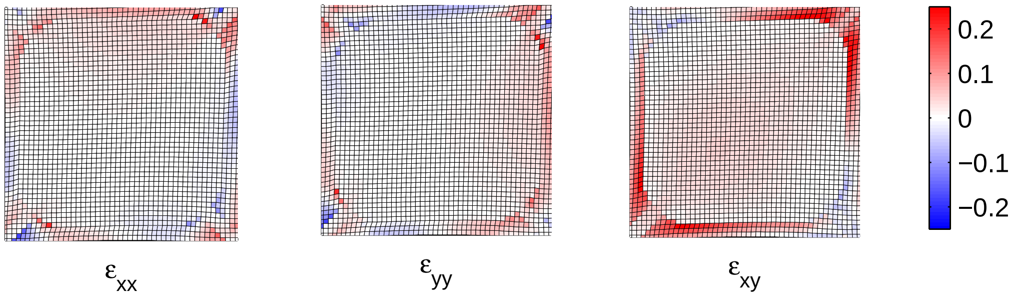

(c) Strain fields at P4

Figure 6.17: Mode shape deformation and strain at P1, P3 (P2), and P4.

6.5 Conclusion

Nonlinear systems such as those examined herein exhibit amplitude-dependent dispersion which introduces new design opportunities for tunable devices such as filters and waveguides. A frequency shift sensitivity K_ω quantifies the shift sensitivity for a particular configuration by isolating system-dependencies from amplitude. The nonlinear force vector presents the biggest technical hurdle because its functional time-dependence is required to obtain $\mathbf{c}_1$. However, techniques such as the one presented herein offer simple solutions to this problem.

We have shown that highly tunable nonlinear systems may be realized by arranging rigid inclusions in a compliant matrix of nonlinear material. In both 1D and 2D settings, arrangements with thin nonlinear layers resulted in highly sensitive group velocity and band gap width which may be practical in many applications (e.g., diodes, filters, and waveguides). A genetic algorithm topology optimization routine confirms that such designs are, indeed, optimal for achieving high sensitivity.

The genetic algorithm implemented herein tended toward a square inclusion with nominal dimensions $a/d = 0.125$ and small fingers protruding from the corners. A heuristic analysis of critical wave modes provides some insight into why some dispersion branch points result in large shifts, while others result in no shift. It is shown that high strain regions in the linear Bloch wave modes are evidence of such sensitivity, and may be used to enhance design strategies for nonlinear phononic crystals and metamaterial devices.

CHAPTER VII

DISPERSION ANALYSIS USING COMMERCIAL SOFTWARE

7.1 Overview

Wave propagation in continuous, periodic structures with weak nonlinearity is explored using the perturbation described in Ch. 2. Appropriate application of Bloch theory to a discrete and weakly nonlinear system results in an amplitude-dependent dispersion relationship. This chapter builds upon the perturbation framework by integrating commercial FEA software, thereby facilitating analysis of geometrically-complex continuous systems with weak nonlinearity. A scheme for evaluating the nonlinear force vector $\mathbf{f}^{NL}$ is particularly important in the process.

A periodic structure consists of a unit cell which repeats itself to form the entire structure. A number of interesting properties exhibited by periodic structures have been demonstrated analytically and experimentally [113, 114]. The dispersion relation relating frequency to the Bloch wave vector is of particular interest herein. An analysis of the dispersion relationship reveals pass bands, band gaps, phase velocities, and group velocities. Nonlinearity is known to modify the dispersion relationship in ways that can be useful in the design of materials or devices such as band gap-based diodes, switches, filters, and wave guides.

A nonlinear periodic structure can support a variety of wave solutions depending on the wave amplitude, magnitude, interaction of waves, and type of nonlinearity - for example solitary wave solutions and discrete breathers [38, 48, 115, 45, 116, 44, 117]. The existence of Bloch wave solutions for nonlinear, periodic materials and the effects of amplitude-dependent dispersion are considered. An understanding of amplitude-dependent dispersion enables tunable system design where propagation characteristics (directionality, intensity, etc.) vary with forcing amplitude. Two continuous nonlinear systems are investigated herein as examples of the perturbation procedure.

The first system considered is the one-dimensional multilayer rod governed by a material nonlinearity (the same type as in Ch. 5). This type of structure exhibits many of the interesting properties of periodic structures, such as dispersion and band gaps, while being sufficiently simple to analyze. The linear version of this system has received considerable attention in the past [97, 52]. Dispersion in the multilayer rod with a *nonlinear* constitutive stress-strain law was studied using an in-house FEA code and perturbation analysis in [62]. Results from this study are utilized in assessing the validity of output obtained from a commercial FEA package in calculating nonlinear dispersion relationships.

The second system considered is a two-dimensional membrane supported by periodically repeating supports. The supports provide a nonlinear restoring force to the membrane and thus influence the dispersion relationship. This particular system is partly motivated by the need to study the dynamic behavior of micro-machined ultrasonic capacitive transducers (CMUTs) [118]. CMUTs are essentially metallic membranes on flexible supports which vibrate due to alternating currents, and thus generate ultrasonic waves [119]. In the sensing mode, the pressure waves generate vibrations in the membrane which induces a measurable change in capacitance. These micro electro-mechanical systems are used in various applications such as low-frequency sonar applications [120] and photo-acoustic imaging [118]. In most cases, CMUT elements are arranged in 1D or 2D periodic array arrangements. For large membrane displacement, the dynamics of the CMUT element are nonlinear [121]. As a first approximation, the CMUT can be considered as a two dimensional nonlinear periodic structure with each element modeled as an elastic membrane supported by nonlinear springs. The reduced system is discretized and the nonlinear dispersion diagram is obtained using the perturbation procedure integrated with commercial FEA software.

This chapter is organized as follows: Sec. 7.2 describes the perturbation analysis and a method for integrating the analysis into a commercial FEA software package. Analyses for the multilayer rod and periodically-supported membrane appear in Sec. B.1 and 7.4, respectively. Results are presented and discussed to illustrate amplitude-dependent dispersion. Closing thoughts are presented in Sec. 7.5 along with suggestions for future research.

7.2 Theory and perturbation analysis integration

7.2.1 System model and dispersion analysis

The use of finite element discretization of continuous domains enables band gap analysis of structures with complex geometry. The developments that follow assume a periodic elastic structure whose dynamics are governed by Eq. (2.11) the conservation of momentum

$$\nabla \cdot \boldsymbol{\sigma} + \mathbf{f} = \rho_V \frac{\partial^2 \mathbf{u}}{\partial t^2}, \tag{7.1}$$

where $\boldsymbol{\sigma}$ denotes the elastic stress tensor, ρ_V is the material density, $\mathbf{u} = \mathbf{u}(\mathbf{r}, t)$ is the displacement field vector, and $\mathbf{f}$ denotes external body forces. The various approximations and simplified structural models described in Ch. 2 are equally applicable to this development. In particular, the rod and membrane structural model are used for examples in this chapter.

An elastic membrane supported by periodic elastic supports serves to illustrate the relevant components of a nonlinear dispersion analysis. This system, illustrated in Fig. 7.1, can be considered as a prototypical CMUT model. Weak nonlinearities may arise from the elastic support for large displacements. In this case, the equation of motion Eq (7.1) reduces to the simple membrane equation.

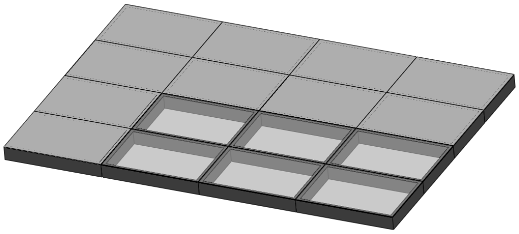

Figure 7.1: Depiction of a CMUT array. Pretensioned membranes are supported by elastic boundaries.

A nonlinear analysis of the *continuous* equations of motion is impractical in most situations; therefore, discretized equations of motion will be employed herein. Commercial finite-element software implementations offer a convenient and powerful interface to obtain mass and stiffness matrices for the discretized system, which are used in a subsequent perturbation approach. What typical commercial packages *do not* provide is a means for analyzing dispersion relations and extracting the nonlinear force vector.

Figure 7.2 outlines the typical procedure for evaluating approximate dispersion relationships for nonlinear systems. The governing PDE is first discretized. Then, after formally applying a perturbation procedure (Sec. 2.4.1), the linear Bloch wave modes and frequencies are obtained from the mass and stiffness matrices. The nonlinear force vector appearing in the first order equation is then calculated for each wave mode (Sec. 7.2.2) and used in the final calculation for the first-order accurate dispersion relationship.

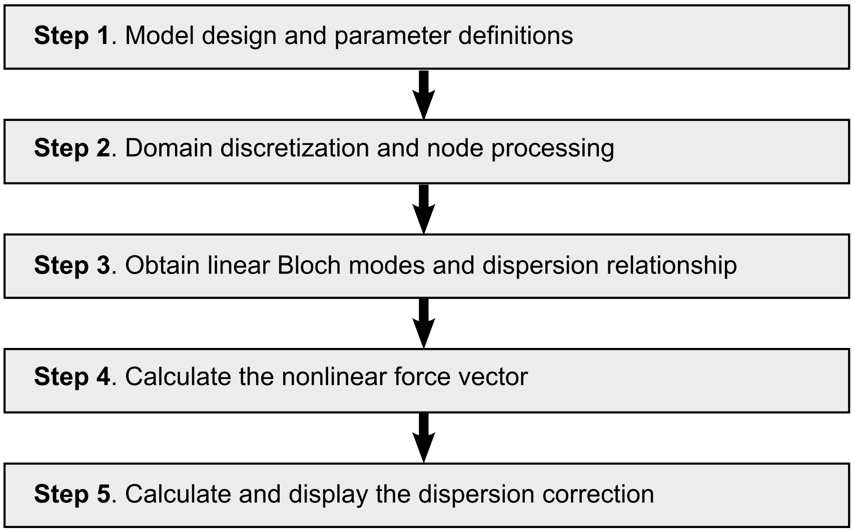

Figure 7.2: Basic procedure for calculating dispersion relationships in nonlinear systems

Finite-element software is a particularly useful aid in Steps 1, 2, and 4, while other computational software (e.g. MATLAB or custom C++) can handle the calculations for Steps 3 and 5. Many finite-element software can also be used in Step 3 to calculate the linear Bloch modes via frequency-domain analysis, but since the system matrices and Bloch wave modes are required for Step 5, it is useful to perform these calculations in the same software so that the results are close at hand.

Full details of the perturbation approach to be presented next, as applied to discrete systems are described in Ch. 2. The numerical implementation of the approach in full generality follows. We assume that the governing equations contain nonlinear terms and have been discretized such that the nonlinear system of equations may be expressed as Eq. (2.16), repeated here for convenience

$$\mathbf{M}\ddot{\mathbf{u}} + \mathbf{K}\mathbf{u} + \varepsilon\mathbf{f}^{NL}(\mathbf{u}) = \mathbf{f}^{int}. \tag{7.2}$$

The procedure for reducing the discrete equations of motion of the global system to those describing a single unit cell is straight forward when terms in the nonlinear force vector are known in closed-form. In this case, the first Fourier coefficient $\mathbf{c}_1$ can be analytically obtained and the dispersion corrections immediately follow. Simple systems such as the nonlinear diatomic spring-mass system admit tractable analytical expressions for $\mathbf{f}^{NL}$ and thus $\mathbf{c}_1$. However, for more complex systems such as those with inclusions, voids, nontrivial geometry, or complex nonlinearities, hand calculations for explicit expressions become impractical. Instead, numerical estimates of $\mathbf{c}_1$ can be obtained using commercial software so that the complex design space of periodic materials can be investigated. In what follows, the general procedure for determining $\mathbf{c}_1$ via commercial software implementation is described. The procedure is then applied to a practical and well-known example (the 1D multilayer system), and finally to a periodic membrane with nonlinear elastic supports.

7.2.2 Nonlinear force vector evaluation

The first Fourier coefficients $\mathbf{c}_1$ must be obtained from knowledge of the time dependence of $\mathbf{f}^{NL}(\mathbf{u})$. In an analytical setting, the functional time-dependence is explicit and the coefficients may be obtained exactly. When analytical solutions are not practical, numerical evaluation of the nonlinear force vector over a time range equal to one fundamental period yields an approximate time-domain signal from which $\mathbf{c}_1$ may be obtained. In presenting the procedure, we assume there are no constraints on the problem, the governing PDE is homogenous and contains no damping terms, and nonlinearity is only in the displacement field variable $\mathbf{u}$. Therefore, the boundary value problem consists only of the PDE and associated boundary conditions.

Finite element software routines typically form a residual vector $\mathbf{R}(\mathbf{u}, \ddot{\mathbf{u}})$ that can be decomposed into the equation system

$$\mathbf{R}(\mathbf{u}, \ddot{\mathbf{u}}) = \mathbf{M}\ddot{\mathbf{u}} + \mathbf{K}\mathbf{u} - \mathbf{f}^{L} - \mathbf{f}^{NL} = \mathbf{0}, \tag{7.3}$$

where each of the vectors $\mathbf{f}^{L}$ and $\mathbf{f}^{NL}$ are functions of $\mathbf{u}$. The load vector $\mathbf{f} = \mathbf{f}^{L} + \mathbf{f}^{NL}$ is comprised of those terms in $\mathbf{R}(\mathbf{u}, \ddot{\mathbf{u}})$ which are not part of the mass or stiffness matrix. These terms are typically only the applied external loads and any nonlinear terms that do not "fit" into the standard matrix form.

Obtaining the nonlinear force vector numerically requires calculation of $\mathbf{R}$ for specific displacement fields. Finite-element software packages can evaluate the residual vector numerically by linearizing the system about a prescribed solution vector $\mathbf{u}_0$. The linearization is done numerically with a first order Taylor series as

$$\mathbf{R}(\mathbf{u}, \ddot{\mathbf{u}}) \approx \mathbf{R}(\mathbf{u}_0, \ddot{\mathbf{u}}) + \nabla_{\mathbf{u}}\mathbf{R}(\mathbf{u}_0, \ddot{\mathbf{u}})^{\mathrm{T}}(\mathbf{u} - \mathbf{u}_0), \tag{7.4}$$

where $\nabla_{\mathbf{u}}$ represents a gradient with respect to each dependent variable in the displacement field vector $\mathbf{u}$ and the subscript (sys) is implied but removed for clarity.

The objective is to isolate the $\mathbf{f}^{NL}$ term in Eq. (7.3) at subsequent instances in time for a Bloch wave displacement fields $\mathbf{u}_0$. This is easily accomplished by setting the coefficients of linear operators in the boundary value problem to zero. Then, the evaluated load vector $\mathbf{f}(\mathbf{u}_0)$ contains only applied loads (which are zero in the homogeneous problem) and the nonlinear terms $\mathbf{f}^{NL}$. A simple example of this process is presented in Appendix B.1 for a single rod element subject to a nonlinear constitutive stress-strain law.

The first Fourier coefficient of $\mathbf{f}^{NL}$ is obtained by choosing the linearization point $\mathbf{u}_0$ as a Bloch wave mode $\boldsymbol{\phi}_j$. The residual vector is evaluated over a number of equally spaced times τ_i in the range $\tau \in [0, 2\pi]$. The information of how the nonlinear force vector varies over a single period is stored in a matrix of force vectors in the form

$$\mathbf{F}_j^{NL}(\tau) = \Big[\mathbf{f}^{NL}(\mathbf{u}_0(0)), \mathbf{f}^{NL}(\mathbf{u}_0(\tau_1)), \mathbf{f}^{NL}(\mathbf{u}_0(\tau_2)), \ldots, \mathbf{f}^{NL}(\mathbf{u}_0(2\pi))\Big]. \tag{7.5}$$

Each row in the force matrix $\mathbf{F}_j^{NL}(\tau)$ for the jth wave mode contains a time-series whose Fourier series yields the corresponding term in the coefficient vector $\mathbf{c}_{1,j}$. The coefficient vector for the jth mode is obtained via numerical integration of the Fourier integral

$$\mathbf{c}_{1,j} = \frac{1}{2\pi}\int_0^{2\pi} \mathbf{f}^{NL}(A, \boldsymbol{\phi}_j(\boldsymbol{\mu}), \tau)e^{-\mathrm{i}\tau}\mathrm{d}\tau$$

or via Fast Fourier Transform (FFT) routines. The resulting coefficient vector may be used to compute the nonlinear correction term ω_1 as in Eq. (2.36). The process is outlined for the 1D multilayered system in the following section.

7.3 Example 1: One-dimensional multilayer system

The linear 1D multilayer system is one of the simplest examples of a continuous periodic structure exhibiting dispersive wave propagation. Amplitude-dependence in the dispersion relationship may arise if, in addition to periodicity, one of the layers is governed by a nonlinear constitutive law. In this section, the basic process flow illustrated in Fig. 7.2 is applied to a specific example with discussion centered around the general technique and any difficulties that may arise. An implementation of the procedure using COMSOL as the commercial FEA package is detailed in Appendix B.2.

Step 1: Model design The first major task in evaluating the nonlinear dispersion relationship for the multilayer system is to develop a time-dependent elasticity model. The geometry of the model should consist of a single central unit cell surrounded by a single neighbor to each side as in Fig. 2.5. In one dimension, this means three complete unit cells should be drawn. The fact that internal forces on the neighbor unit cells are not included does not impact the model negatively, as only the equations governing the central unit cell are ultimately considered. This example considers a central unit cell composed of two layers, labeled *A* and *B*, that repeat periodically as shown in 7.3. Because we seek the dispersion relationship for free wave propagation, no external forces are applied and the governing PDE is homogeneous. The constitutive stress-strain relationship for the material in layer *A* contains a cubic nonlinearity such that

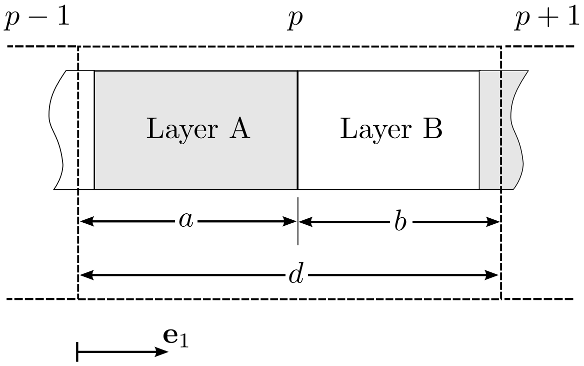

Figure 7.3: The *j*th unit cell in the multilayered system considered herein is composed of two repeating layers.

$$\sigma_{xx} = (E_{1,A} + \Gamma_A \epsilon_{xx}^2)\epsilon_{xx}, \tag{7.6}$$

where σ_{xx} is the stress as a function of strain ϵ_{xx}. The density of each layer is $\rho_A = \rho_B = 1\,\mathrm{kg\,m^{-1}}$ and the elastic moduli are $E_{1,A} = 1\,\mathrm{N\,m^{-2}}$ and $E_{1,B} = 4\,\mathrm{N\,m^{-2}}$, respectively. The nonlinear modulus for layer *A* is $\Gamma_A = 1\,\mathrm{N\,m^{-2}}$. The governing equations are given as

$$\frac{\partial^2 u}{\partial t^2} - \frac{\partial}{\partial x}\left[\left(1 + \left(\frac{\partial u}{\partial x}\right)^2\right)\frac{\partial u}{\partial x}\right] = 0, \quad 0 < x < a \tag{7.7}$$

$$\frac{\partial^2 u}{\partial t^2} - \frac{\partial}{\partial x}\left(4\frac{\partial u}{\partial x}\right) = 0, \quad a < x < b, \tag{7.8}$$

where the position coordinate x is measured from the left endpoint of a given unit cell. For this particular example, the boundary conditions should be homogeneous Neumann or Dirichlet conditions at the endpoints $x = 0$ and $x = d$ of the first and third unit cells, respectively, to eliminate pre-stressed states. However, homogeneous boundary conditions are not required, in general. The nonlinear membrane considered next, for example, may have a Neumann or Robin boundary condition on the interior or exterior boundaries to represent grounded linear and nonlinear supports.

Step 2. Discretize domain A primary motivation for integrating the formally developed perturbation procedure into a commercial FEA package is to automate discretization of continuous systems so that optimization routines and nonlinear system design processes can be effectively implemented. There is one constraining requirement: the meshes in each unit cell must be identical in order to apply the Bloch theorem to the discrete system properly. A unit cell of the multilayer system discretized into N elements is depicted in Fig. 7.4. As indicated by the node numbering in the figure, the left-most node $u_{1,p}$ in a unit cell is considered part of the pth unit cell, while the right-most node $u_{N,p+1}$ is considered part of the $(p+1)$th unit cell[1].

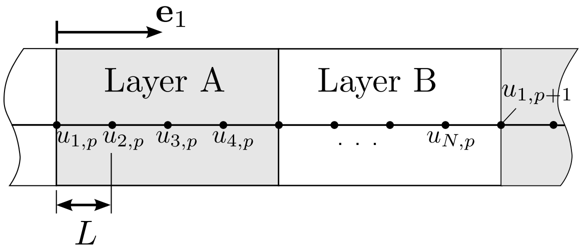

Figure 7.4: pth unit cell for a discretized multilayer system

Step 3: Obtain linear Bloch modes The most important step in obtaining the linear Bloch modes from the finite-element model is to identify nodes belonging to each unit cell. The nodal information is parsed to determine which unit cell each node belongs to. Once a unit cell (left, center, or right for a 1D case) has been identified for each node, the nodes must be sorted such that the nodes with identical local coordinates **r** (i.e., taken from a similar reference point within a unit cell) can be arranged into a vector

$$\mathbf{u} = [\mathbf{u}_{-1}, \mathbf{u}_0, \mathbf{u}_1]^{\mathrm{T}} \tag{7.9}$$

---

[1] This sequential numbering scheme is not required in general. However, appropriate pre-processing must identify boundary and interior nodes in any case.

as in Eq. (2.14), where $\mathbf{u}_{-1}, \mathbf{u}_0$, and $\mathbf{u}_1$ denote DOFs in the left, center, and right unit cells, respectively. This step is important so that the resulting mass and stiffness matrices may easily be combined in such a way that an infinite system is represented by the mass and wavenumber-reduced stiffness matrices (as in Eq. (2.25)).

Next, the global system matrices $\mathbf{M}$ and $\mathbf{K}$ must be obtained for the linear model (that is, with nonlinear coefficients set to zero). A two-step matrix-partitioning process yields the mass and stiffness matrices for the infinite system as illustrated in Fig. 7.5. Rectangular submatrices of $\mathbf{M}$ and $\mathbf{K}$ that correspond to DOFs within the central unit cell are extracted. These submatrices, in turn, can be partitioned into square matrices grouped by unit cell as described in Sec. 2.4.1. For the 1D system, this means three square matrices are formed for each of the three unit cells: $\mathbf{K}_{-1}$, $\mathbf{K}_0$, and $\mathbf{K}_1$ (and likewise for mass matrices). Application of the Bloch theorem to these matrices results in a familiar eigenvalue problem from which the linear Bloch wave modes may be obtained. For example, the stiffness matrix for the infinite system in this example is represented by:

$$\mathbf{K} = e^{-\mathrm{i}\mu d}\mathbf{K}_{-1} + \mathbf{K}_0 + e^{\mathrm{i}\mu d}\mathbf{K}_1. \tag{7.10}$$

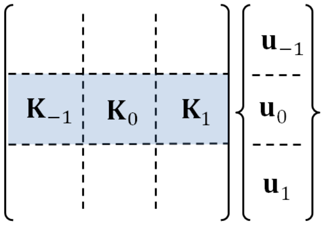

Figure 7.5: Illustrating how mass and stiffness sub-matrices are identified when the nodes are conveniently sorted in ascending order.

Step 4. Calculate nonlinear force vector Calculation of the nonlinear force vector follows directly from the procedure in Sec. 7.2.2. In order to evaluate the first Fourier coefficients $\mathbf{c}_{1,j}$ for use in Eq. (2.36), the nonlinear force vector $\mathbf{f}^{NL}(A, \boldsymbol{\phi}_j(\mu), \tau)$ must be evaluated for each desired wave number $\mu \in [0, \pi]$ and wave mode over equally spaced times $\tau_i \in [0, 2\pi]$.

The Bloch wave displacement field for the global system must be formed using Bloch's theorem and the linear Bloch wave modes. Then, the global nonlinear force vector corresponding to all three unit cells can be calculated. This vector is given by

$$\hat{\mathbf{u}}(\mu, \tau) = \left[\mathbf{u}_{-1}, \mathbf{u}_0, \mathbf{u}_1\right]^{\mathrm{T}} e^{\mathrm{i}\tau} = \frac{A}{2}\left[\boldsymbol{\phi}_j e^{\mathrm{i}\mu}, \boldsymbol{\phi}_j, \boldsymbol{\phi}_j e^{-\mathrm{i}\mu}\right]^{\mathrm{T}} e^{\mathrm{i}\tau}. \tag{7.11}$$

This vector should be passed as the linearization point $\mathbf{u}_0$ to the finite-element software of choice as described previously. The nonlinear force vector is obtained by setting all linear coefficients to zero so that the only remaining term in the residual vector is $\mathbf{f}^{NL}$. Repeated application of this procedure yields the nonlinear force matrix $\mathbf{F}_j^{NL}$ that may be numerically integrated for each Fourier coefficient $c_{1,j}$ for the jth wave mode.

Step 5. Calculate dispersion calculation The final step in the process is to combine the mass matrix, Bloch wave modes and frequencies, amplitude, and first Fourier coefficient vectors as in Eq. (2.36) to obtain the first-order dispersion corrections. This straightforward calculation is appended to the linear dispersion relationship $\omega_0 = \omega_0(\mu)$ to obtain the first-order accurate dispersion relationship $\omega(\mu)$. The weakly nonlinear dispersion relationship was calculated using an *in-house* finite-element code; details for the in-house finite-element code can be found in Ch. 5.

Figure 7.6 illustrates the results of this calculation using (i) in-house finite-element discretization and evaluation code (black line), and (ii) commercial finite-element software discretization and evaluation (square marker). Both formulations were run for three dispersion branches at 15 wavenumber points. At each wavenumber point, the nonlinear force vector was calculated at 8 equally spaced τ_i for a total of 3x15x8=360 calls to the nonlinear force assembly functions. The authors note that the level of temporal discretization depends on the nature of the nonlinearity; for cubic nonlinearity considered herein, eight points provide sufficient resolution. This statement is supported by results generated from an in-house

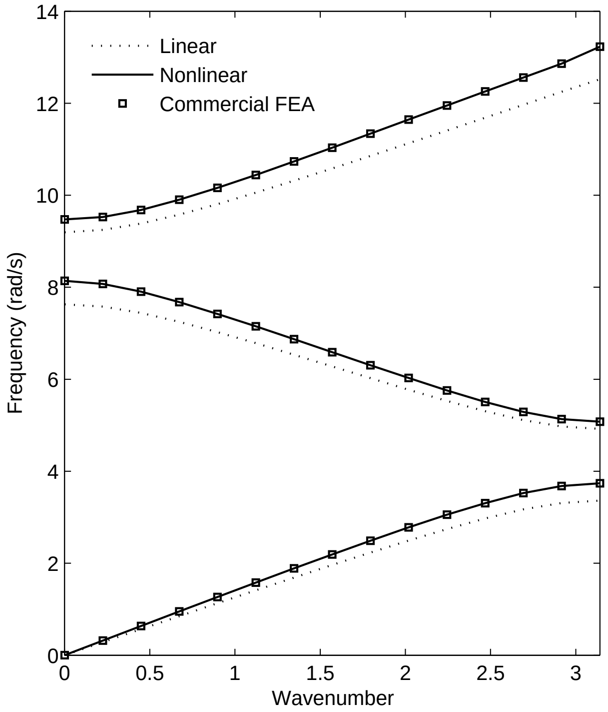

Figure 7.6: Linear (dotted) and nonlinear dispersion curves generated for the multilayer rod using in-house code (solid) and commercial FEA-assisted code (squares). The abscissa corresponds to a dimensionless Bloch wavenumber μ that has been nondimensionalized using the unit cell length d.

code that uses a much finer temporal discretization (256 points per fundamental period). Generally, however, the level of temporal discretization should be optimized to the specific nonlinearity being addressed. Both the in-house code and commercially-assisted code produce identical results. This result validation provides motivation to consider geometrically-complex systems where commercial finite-element routines are indispensable.

7.4 *Example 2: Membrane on periodic supports*

7.4.1 Model description

A membrane supported by a periodic arrangements of support springs illustrates the ability of the proposed analysis method to analyze complex meshes and geometry. Wave propagation through a periodically supported membrane also gives rise to more complex phenomena, such as frequency-dependent directionality, because wave propagation is not restricted to one dimension. Consider an elastic membrane under constant tension with the boundary of the element on a flexible support as shown in Fig. 7.7. The membrane is homogeneous, implying that the mass of the membrane per unit area (ρ_A) is constant. The tension per unit length caused by stretching the membrane is the same at all points and in all directions and is assumed to not change during the motion. Additionally, transverse deflection $w(x, y, t)$ of the membrane is small compared to the size of the membrane.

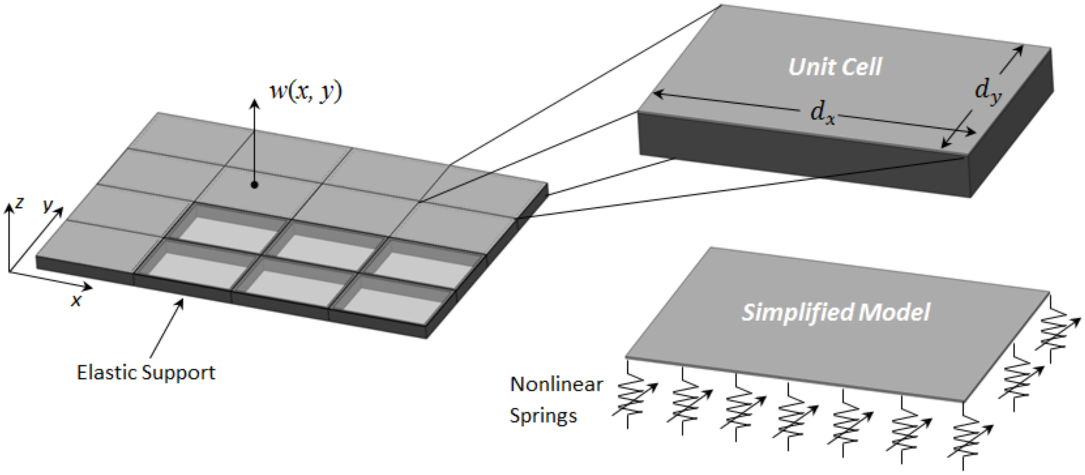

Figure 7.7: Periodically arrayed membrane elements under a constant tension and connected to ground through a flexible support

The equation of motion solved by commercial software packages for the membrane is

$$\ddot{w} = c^2 \nabla \cdot (\nabla w) + f_0, \tag{7.12}$$

where $w = w(x, y, t)$, $c = \sqrt{T_0/\rho}$, T_0 denotes the pretension per unit area, and f_0 is an applied force per unit area. The flexible support at the boundary of each unit cell can be modeled as an external force applied to the system on the boundaries of the membrane element [111], namely

$$f_0 = k_s u(x, y) + \varepsilon \Gamma_s u^3(x, y), \quad \forall (x, y) \in \partial\Omega, \tag{7.13}$$

where k_s denotes the equivalent linear stiffness, Γ_s denotes the equivalent cubic stiffness, $\partial\Omega$ denotes element boundaries, and ε denotes a small parameter ensuring weak nonlinearity.

Free wave propagation is investigated by considering the dynamics of a single unit cell from an infinite membrane. The open set of finite-difference equations are obtained by discretizing Eqs. (7.12) in conjunction with (7.13) over a set of 9 unit cells as shown in Fig. 2.5. The remainder of the problem formulation follows from Sec 2.4.1 from which the linear Bloch wave modes and nonlinear dispersion diagrams may be obtained. A comprehensive write-up of a manual finite-element discretization and analysis of the nonlinear elastically-supported membrane can be found in [111].

7.4.2 Linear system analysis and discretization

The nonlinear correction term ω_1 in Eq. (2.36) depends on the linear Bloch wave modes and frequencies. Therefore, a converged solution for the linear problem is paramount in the accurate determination of the weakly nonlinear dispersion relationship. The present section considers the flexible support stiffness to be governed by a linear force-displacement relationship such that $\Gamma_s = 0$. Figure 7.8 illustrates a discretization of the 9-cell membrane model using 56 elements per unit cell. It is imperative that the nodal points for each unit cell correspond to the same local coordinates so that displacements in neighboring unit cells are known through application of the Bloch theorem.

Convergence of the lowest two dispersion branches is typically the most important because a low-frequency band gap is always created by the flexible supports, while a second complete band gap may emerge between the first and second branches for some system

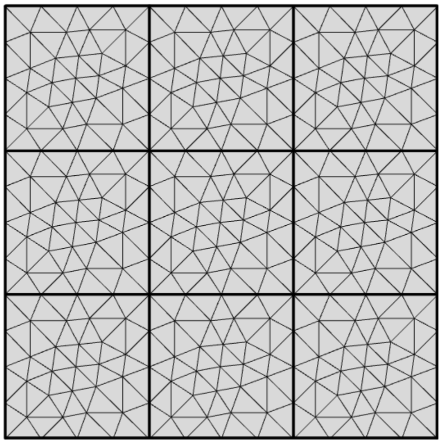

Figure 7.8: Meshing for a 9-cell assembly using 56 elements per unit cell. A critical aspect of this discretization is the existence of identical meshes for each unit cell. Moreover, edge mesh on adjacent unit cell sides are identical.

parameter choices. It was shown in [111] that, for a fixed geometry, the ratio of the linear support stiffness to the membrane pre-tension k_s/T_0 is a key parameter in the width and number of band gaps appearing in the dispersion diagram. The parameters used for the system considered next are $\rho_A = 1.0\,\mathrm{kg\,m^{-2}}$, $T_0 = 1.0\,\mathrm{N\,m^{-2}}$, $k_s = 2.0\,\mathrm{N\,m^{-3}}$, and side lengths $a = b = 1.0\,\mathrm{m}$.

The frequency corrections to the dispersion relationship of the nonlinear system provide an additional motivation for fine discretization levels. The order of the calculated weakly nonlinear corrections should not be of the same order as the error in the linear dispersion relationship. Figure 7.10 depicts the convergence of the first two dispersion branches as the number of elements per unit cell N_{el} increases. Approximately 170 triangular Lagrange elements per unit cell suffices to capture accurate low-frequency band gaps appearing between the first and second dispersion branches. At the critical location on the second branch ($\mu_1 = \pi$, $\mu_2 = 0$) that bounds any low-frequency band gaps which may appear, the dispersion branches for 170 elements per unit cell are within 0.5% of the values computed for 896 elements per unit cell; all other locations on the second branch are within 2.0. We choose 170 elements per unit cell to facilitate computations. However, higher-fidelity models should be used when appropriate.

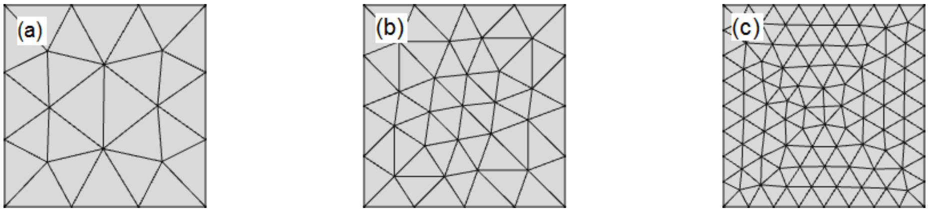

Figure 7.9: Discretization levels used in dispersion branch convergence study: (a) 26 elements per unit cell, (b) 56 elements per unit cell, and (c) 170 elements per unit cell.

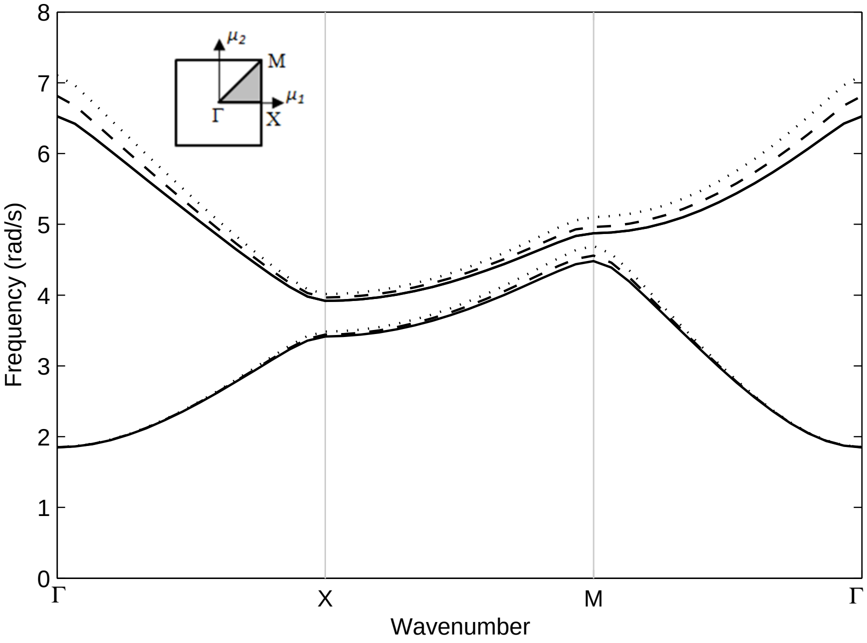

Figure 7.10: Convergence of the first two linear wave modes with increasing mesh density. The linear dispersion curves shown were calculated using 26 elements (dotted), 56 elements (dashed), and 170 elements (solid) per unit cell.

7.4.3 Nonlinear system analysis

Dispersion in the two-dimensional membrane on a nonlinear foundation is analyzed through band diagrams which are now amplitude-dependent. The considered system is the same as for the linear analysis, with the nonlinear stiffness parameter $\Gamma_s = -0.2\,\mathrm{N\,m^{-5}}$. The nonlinear dimensionless parameter ε quantifies the magnitude of the nonlinearity. Following [27], a characteristic length $L_0 = 1.0\,\mathrm{m}$ is chosen based on the unit cell dimensions so that the small parameter ε is identified as

$$\varepsilon \equiv \frac{\Gamma_s L_0^2}{k_s}.$$

Thus, for fixed unit cell dimensions, the ratio Γ_s/k_s determines the magnitude of the system nonlinearity. The system is considered to be weakly nonlinear when $|\varepsilon| \ll 1$. Time-domain simulations in previous work have indicated that the predicted nonlinear dispersion relationships may be reasonably valid up to $\varepsilon = 0.25$ [62, 36]. The nonlinear dispersion band diagram is obtained as detailed in Sec. 7.2.2. The band diagram is evaluated along the contour of the first Brillouin zone [4, 52]. The nonlinear correction to the dispersion relationship is sensitive to the Bloch wave mode, so a slight perturbation in the Brillouin contour was introduced to avoid situations where repeated frequencies (eigenvalues) occurred, such as when two dispersion branches converge.

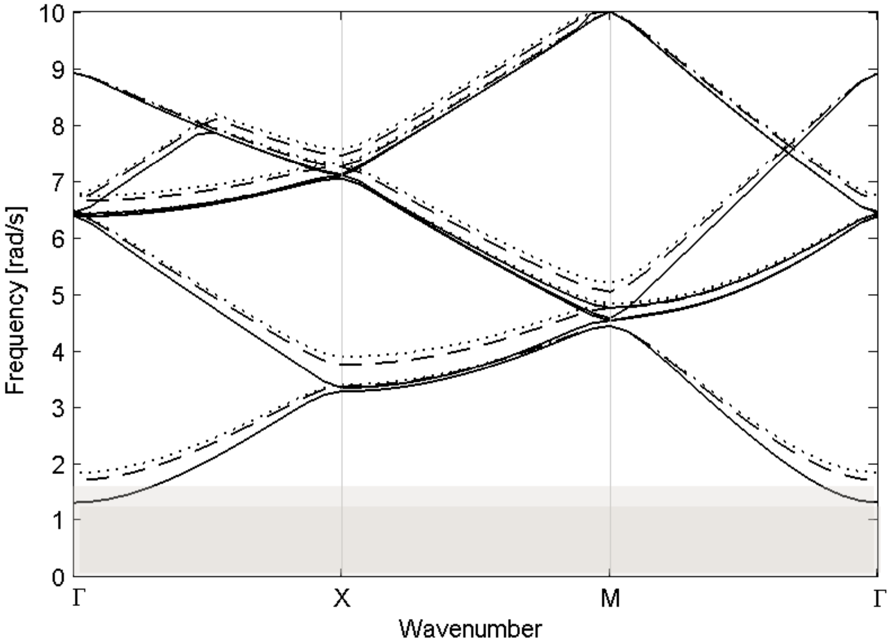

Figure 7.11: Band diagram of membrane system with $k_s/T_0 = 2.0\,\mathrm{m}^{-1}$ on nonlinear supports at two different amplitudes. The dotted black line indicates the membrane on linear supports. Nonlinear calculations are shown for amplitudes $A = 2.0$ (dashed) and $A = 4.0$ (solid). The low-frequency band gap is highlighted for each of the different amplitudes to illustrate the shift resulting from nonlinearity.

Figure 7.11 depicts results from the nonlinear calculation for several dispersion branches. The linear case is shown next to calculations at two different amplitudes for comparison. The system parameters are chosen such that $\varepsilon = \Gamma_s L_0^2/k_s = -0.1$. The case considered assumes a soft nonlinear foundation which generates a downward shift of the dispersion curves as the wave amplitude increases. This result is similar to that of the amplitude-dependent dispersion predicted in soft nonlinear spring-mass models [63]. Band gap shifts of this magnitude have been numerically verified in several previous publications [3, 63, 62, 36]. Of important note is the shift in the low-frequency band gap whose width is primarily governed by the elastic ground support. Due to the soft nonlinear foundation, the low-frequency band gap is decreased by an increase in amplitude. This implies, for example, that low-frequency wave propagation can be controlled with variation in wave amplitude.

The results for a higher k_s/T_0 ratio are presented in Fig. 7.12. The system parameters used are the same as before, except with $k_s = 10.0\,\mathrm{N\,m^{-3}}$ and $\Gamma_s = -1.0\,\mathrm{N\,m^{-5}}$ such that $k_s/T_0 = 10.0\,\mathrm{m^{-1}}$ and $\varepsilon = -0.1$ as before. The higher k_s/T_0 ratio results in the creation of a high-frequency band gap in the linear system between the first and second dispersion branches. The shift in the low-frequency band gap is less sensitive to the nonlinearity, whereas the high-frequency band gap exhibits a significant shift.

7.5 Conclusions

The amplitude-dependent dispersion relationship for continuous periodic systems with weak nonlinearities provides the opportunity to design tunable structures. A closed-form relationship describing a correction to the dispersion relationship was presented that is valid for 1D, 2D, and 3D periodic systems after appropriate discretization. A method for integrating the nonlinear dispersion analysis procedure with commercial finite-element software was also presented. Commercial FEA software facilitates meshing and numerical evaluation of the nonlinear force vector that is required to obtain nonlinear dispersion relationships. An

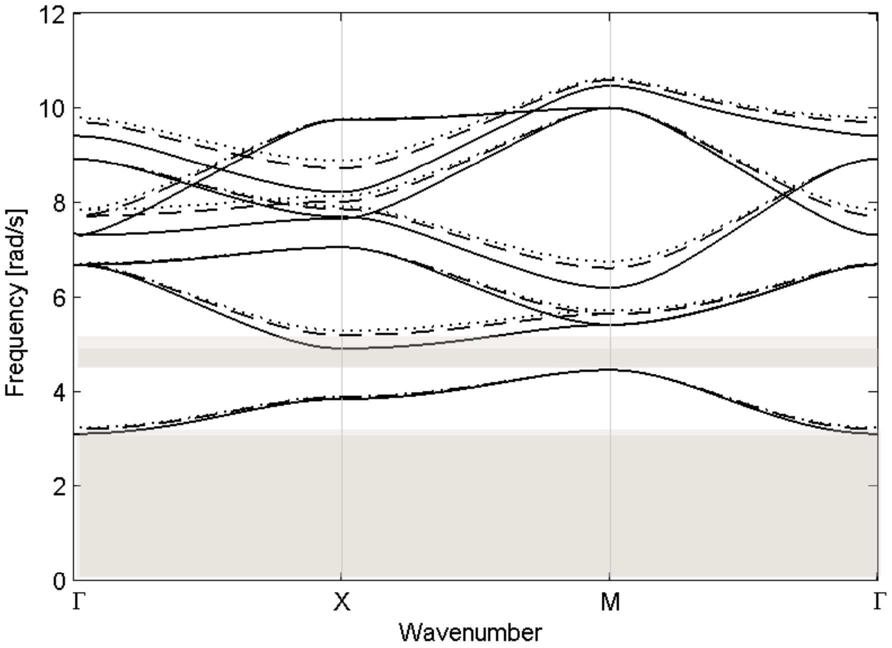

Figure 7.12: Band diagram of membrane system with $k_s/T_0 = 10.0\,\mathrm{m}^{-1}$ on nonlinear supports at two different amplitudes. The dotted black line indicates the membrane on linear supports. Nonlinear calculations are shown for amplitudes $A = 2.0$ (dashed) and $A = 4.0$ (solid). The low- and high-frequency band gaps are highlighted for each of the different amplitudes to illustrate the shift resulting from nonlinearity.

analysis of a multilayer system showed that the commercially integrated routine produced results identical to an explicit in-house FEA code that has been validated by time-domain simulations.

The analysis was extended to a structure composed of repeating membrane elements supported by a nonlinear foundation. A triangular mesh was utilized in anticipation of analyzing periodic structures with more complex geometry (such as voids or inclusions). The ability of the meshing software to produce identical meshes in each unit cell is necessary in order to apply the Bloch theorem. The dispersion behavior is observed to be affected by the ratio of support stiffness to membrane tension. With the nonlinear model and at low k_s/T_0 ratio, there exists a strong dependence of the low-frequency band gap on the wave amplitude. But as the ratio increases, the band diagram modifies in two ways; the first being the upward shift of the first mode depending on the support stiffness, and the second being the appearance of the band gap between the first and the second mode. For this case, i.e. high k_s/T_0 ratio, the first mode does not appear to have significant dependence on the amplitude but the band gap between the first and second mode appears to weaken with increase in wave amplitude.

The ability to successfully analyze nonlinear dispersion through an integrated commercial software environment enables exploration and optimization of geometrically-complex structures. Since unit cell topology affects the Bloch wave modes in a periodic structure (and thus the magnitude of the nonlinear correction), there may be optimal designs for periodic systems with weak nonlinearity. Investigation into topology design and optimization is presented in Ch. 6.

CHAPTER VIII

CONCLUDING REMARKS

8.1 Summary

The effect of finite-amplitude wave propagation in nonlinear periodic structures was analyzed within the framework of dispersion band structures. Nonlinearities in stand-alone nonlinear systems such as the classical Duffing oscillator are responsible for a variety dynamic effects not found in linear systems such as frequency conversion, harmonic generation, chaos, and amplitude-dependence. Engineered materials composed of periodically repeating nonlinear elements exhibit nonlinear amplitude-tunable wave propagation characteristics. Several analysis methods and techniques were presented as strategies for analyzing a variety of such systems.

Perturbation-based analysis methods applied to discretized unit cells lead to nonlinear dispersion relation corrections. These first-order corrected dispersion relations described amplitude-tunable qualities which are enhanced with nonlinearity such as pass and stop bands, group velocity, and wave beaming. A new multiple time scales perturbation analysis was presented which provides the additional generality needed for analyzing nonlinear wave interactions that result from multi-harmonic excitation.

Analysis of discrete-parameter atomic systems in one- and two-dimensions connected with cubically nonlinear spring elements demonstrated that the interaction of two waves results in different amplitude and frequency-dependent dispersion branches for each wave. This constrasts nonlinear dispersion relations derived from monochromatic excitation signals where only a single amplitude-dependent branch is present. A theoretical development utilizing multiple time scales results in a set of evolution equations which are validated by numerical simulation. For the specific case where the wavenumber and frequency ratios are *both* close to 1:3 as in the long wavelength limit, the evolution equations suggest that small amplitude- and frequency-modulations may be present. In the case of two-dimensional systems, it was shown that lattice anisotropy could be introduced by injecting a control plane wave. The resulting lattice anistropy can be used to control wave directionality for application in tunable-focus devices.

Experimental analysis of wave propagation in one-dimensional periodic systems revealed an intimate connection between duffing oscillators and nonlinear dispersion frequency shifts. This connection was analytically derived and experimentally demonstrated through measurement of resonant frequency shifts. Resonant frequencies of finite-sized systems surround a backbone curve which relates to dispersion frequency shifts.

The layered system was investigated as a first venture in applying the perturbation tools in continuous systems. A comparison with an existing analysis quasilinear transfer matrix analysis method suggested that the wave-based perturbation analysis methods presented herein capture Bloch wave mode details that may be ignored otherwise. Detailed finite-element time-domain simulations validated the predicted dispersion relation. It was discovered that thin, compliant layers of nonlinear material in one-dimensional systems resulted in sensitive dispersion shifts. Optimization of two-dimensional arrays was presented using plane-stress models discretized using bilinear Lagrange elements. Parametric analyses and a genetic algorithm implementation identified topologies that produce large increases in complete bandgap width or group velocity variation. Analysis of Bloch wavemodes which produce large nonlinear frequency shifts reveals that the largest contributions to the frequency shift are primarily produced from localized strains in compliant, nonlinear matrix material.

The dispersion analysis methods were integrated with commercial finite-element analysis software to expedite nonlinear analysis of geometrically-complex unit cells. A simple continuous multilayer system illustrates the principle aspects of the procedure. A periodic structure formed by membrane elements on nonlinear elastic supports was used to demonstrate the versatility of the procedure. Weakly nonlinear band diagrams are generated in which amplitude-dependent bandgaps and group velocities are identified. The nonlinear dispersion analysis procedure described, coupled with commercial FEA software, should facilitate the study of wave propagation in a wide-variety of geometrically-complex, nonlinear periodic structures.

8.2 Research Contributions

The research presented in this dissertation provides the following original contributions:

- A general multiple scales analysis method capable of assessing amplitude dependent dispersion variation from nonlinear wave interactions;
- Dynamic lattice anistropy introduction through nonlinear wave interactions, as applied to tunable-focus and steerable wave beam applications;
- Developed, compared, and contrasted two approaches for calculating intensity-dependent dispersion in one-dimensional nonlinear phononic crystals;
- Connected backbone curves in nonlinear resonant oscillator systems to dispersion relations in ideal periodic counterparts;
- Experimental validation of dispersion relation for a nonlinear periodic system;
- A general finite-element framework for analyzing Bloch wave propagation in continuous media with a nonlinear constitutive law;
- Identified conditions where frequency shifts are sensitive to amplitude changes, and a method for maximizing these effects; and,
- Efficient and general computational analysis tools for assessing nonlinear dispersion in complex continuous systems.

8.3 Recommendations for future work

Although the research presented here offers significant advancements in nonlinear dispersion analysis, there are a number of exciting opportunities available for further exploration. The tools and discussion presented have brought nonlinear dispersion analysis to the point of practical experiment design and implementation. Several fundamental theoretical investigations and possible designs are discussed next as potential options for future work.

8.3.1 Group velocity and group velocity dispersion analysis

Group velocity in nonlinear periodic systems exhibits amplitude-dependence. It is a natural and logical extension of amplitude-dependent dispersion relations, and has been analyzed successfully in this dissertation and in Ref. [50]. However, group velocity in the context of amplitude-dependent dispersion relations as applied to *frequency-localized pulses* is not well understood. Figure 8.1 depicts contrasts the idea of a frequency-domain amplitude distribution with the monochromatic signals previously considered. Pulses are most often described by a frequency-domain amplitude distribution (e.g. Gaussian). Thus, individual frequency components correspond to different amplitude-dependent dispersion curves. Furthermore, the interaction of various frequency components has additional consequences on dispersion as discussed in Chapters 3 and 3.2. The question remains: how does the group velocity of a pulse, with a specific frequency distribution, propagate? A Gaussian pulse may be a logical first step, and an interesting perspective may consider the energy content of the pulse, rather than a specific frequency-amplitude function.

8.3.2 Local resonance in unit cells

Local resonance refers to the inclusion of structural elements in a unit cell that associate with specific resonant frequencies. Local resonances have been connected to negative group velocity, and thus negative refraction in sonic materials [122]. Chapter 6 discussed how thin nonlinear ligaments can be incorporated into unit cell design to achieve sensitive

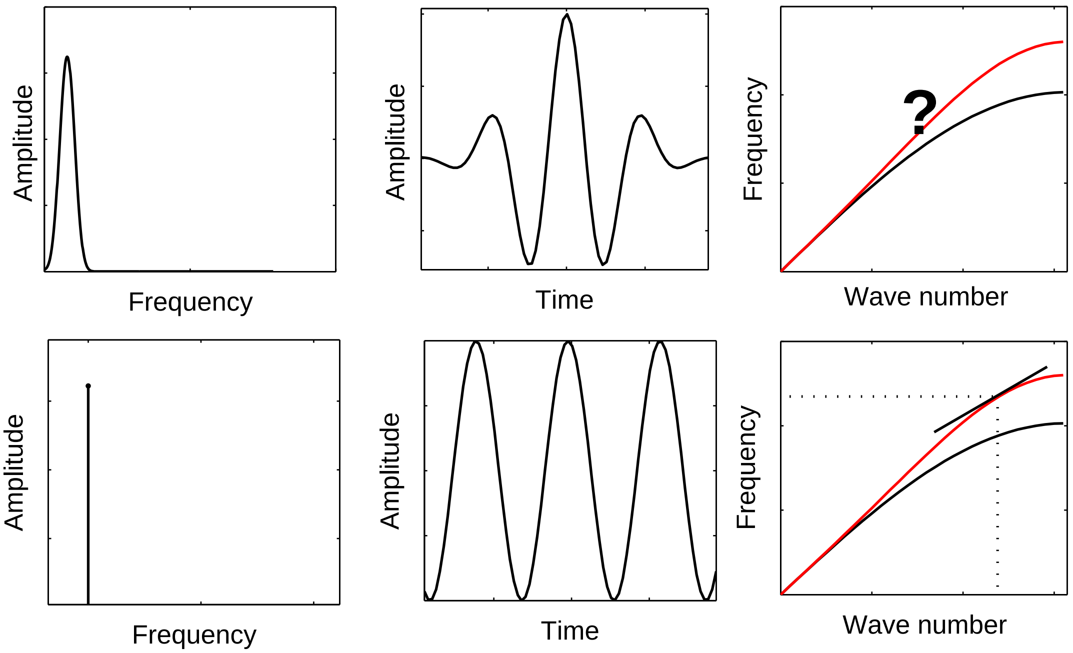

Figure 8.1: The *nonlinear* dispersion curve associated with frequency-domain amplitude distributions is not well understood for periodic systems (top figures). Dispersion curves for monochromatic signals (bottom figures), however, has been numerically validated as accurate.

nonlinear dispersion shifts. Thus, band gaps which appear at frequencies associated with local resonators should exhibit highly-sensitive dispersion shifts due to large displacements at resonance. Figure 8.2 depicts one possible configuration for a nonlinear locally-resonant unit cell. This configuration uses a symmetric and massive inclusion connected to a host material by a nonlinear ligament. However, variations on this simple configuration may introduce directionality by incorporating asymmetric inclusions and ligaments designs.

8.3.3 Experimental investigation of dispersion

Experimental observation of nonlinear dispersion should be a primary research area for future investigation. Nonlinear dispersion analysis results have been strongly confirmed by numerical simulation of physical systems. In addition, some preliminary work investigating dispersion experimentally was presented. Deeper investigations may be facilitated by designing nonlinear spring elements such as those considered in Ref. [30]. The design of

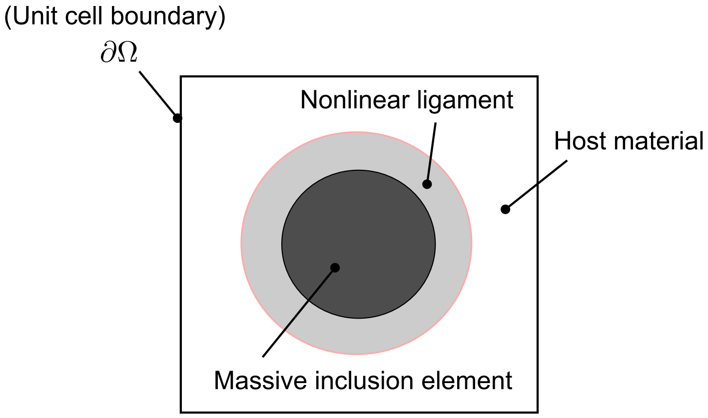

Figure 8.2: Schematic depiction of a locally-resonant unit cell which may exhibit negative refraction and highly-tunable dispersion

sensitive nonlinear elements should be at the forefront of future experimental analyses.

8.3.4 Transmission and reflection analysis

A fundamental study concerning the transmission and reflection behavior material interfaces of differing nonlinear phononic crystals should support future application designs. The investigation should explore the concept of amplitude-dependent impedance as it relates to transmission and reflection. If it is possible for amplitude-dependency to adjust the characteristic impedance of a material – then it may also be possible to design perfect transmission-interfaces at specific amplitudes, which may otherwise reflect portions (possibly significant) of the incident waves. A transmission/reflection study targeted at understanding amplitude-dependent impedances at junctions would provide a great deal of insight into design strategies for nonlinear phononic systems such as acoustic diodes and mirrors. An initial case study for a nonlinear diode is described in Sec. 8.3.5.

Transmission and reflection analysis for two-dimensional domains is a logical extension which should provide further understanding for designing two-dimensional devices such as those which utilize the superprism effect. Figure 8.3 depicts one conceptual design. Two nearly-identical phononic systems are coupled at an interface: the left infinite half-plane contains localized resonators while the right half-plane does not. One may expect

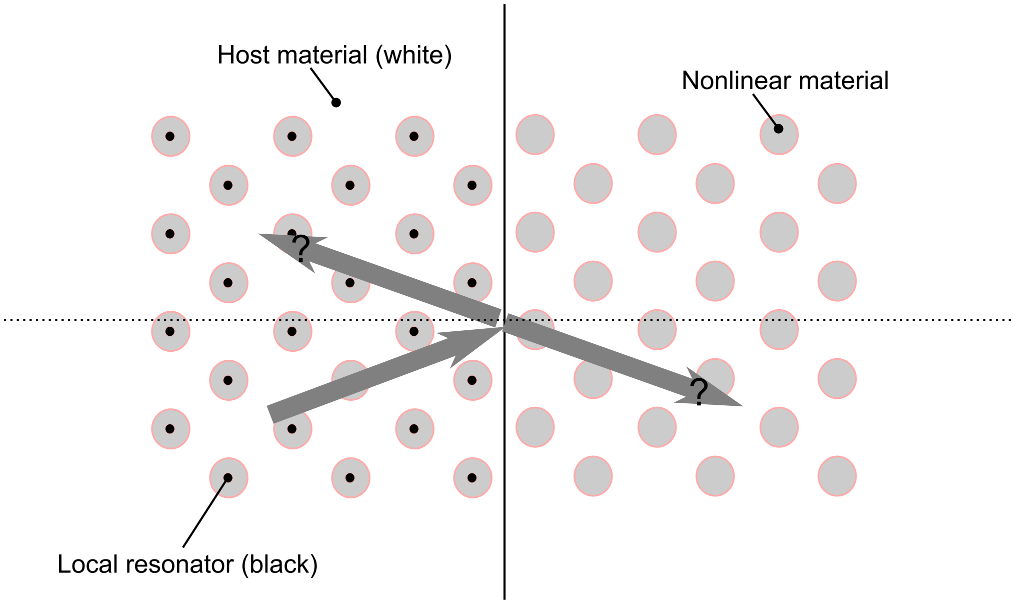

Figure 8.3: Transmission and reflection at the interface of two nonlinear phononic crystals is not well-understood. Appropriate design of nonlinear elements may lead to amplitude-tunable refraction angles and potentially high-amplitude activation of nonlinear refraction indices.

sensitive amplitude-dependent transmission and reflection at interfaces like these near the natural frequency of the local resonators. Such systems may naturally lend to frequency-demultiplexers, wave guiding, and imaging devices.

8.3.5 Transmission/reflection case study: nonlinear diode

One example of an application exploring transmission and reflection at an interface (junction) is a nonlinear diode. Figure 8.4 depicts one possible configuration that has been partially investigated. Diodes, by definition, must be asymmetrical in some sense to provide directional behavior. This nonlinear diode is formed by the union of nonlinear and linear transmission segments as well as an energy harvesting segment which extracts energy from the system. Each segment supports forward and backward propagating waves A^+ and A^-, with subscripts defining the relevant domain. The linear material is tuned to a critical cutoff frequency ($\omega_{co} = 2.15\,\mathrm{rad\,s^{-1}}$) as depicted in Fig. 8.5. The nonlinear material (colored red) exhibits hardening behavior such that the cutoff frequency increases with amplitude. At

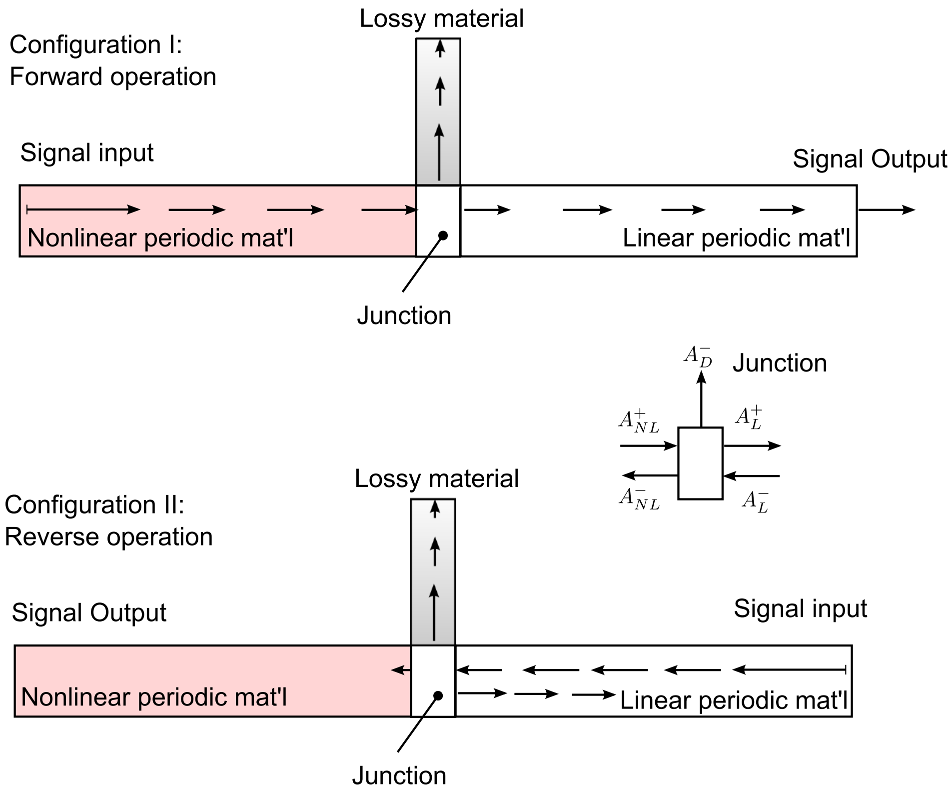

Figure 8.4: Schematic depiction of two operating modes for a wave-based diode. In Configuration I, the forward configuration, signals transmit from left to right for high enough amplitudes. In Configuration II, the reverse configuration, signal transmission is prevented by the existence of amplitude-dependent band gap behavior.

some critical amplitude $A = A_{crit}$, the cutoff frequency of the nonlinear segment aligns with ω_{co}.

In the forward operating mode, wave propagation at the critical frequency is prohibited until the critical amplitude $A_{crit} = 1.0$ is reached. At the junction, part of the wave transmits into a lossy-material (e.g. an energy harvester) while the remaining part partially propagates into the linear segment and may also reflect back into the nonlinear material. As the amplitude increases, the systems become more dissimilar and transmission is likely to be less efficient. In the reverse propagating mode, when a signal is transmitted from the linear segment, it is still partially transmitted into the lossy material. However, now a low amplitude signal enters the nonlinear segment and is immediately attenuated. The remaining portion reflects back into the linear segment.

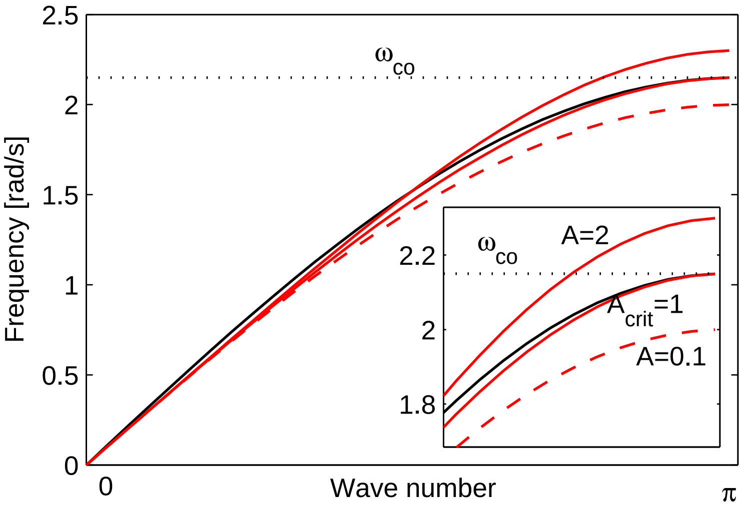

Figure 8.5: Dispersion diagram used for designing the nonlinear diode. Solid black lines indicate the dispersion relation for the linear segment, while red lines indicate dispersion of the nonlinear system at various amplitudes.

Figure 8.6 summarizes the results from several numerical simulations. In each simulation, wave propagation was stimulated by a time-harmonic displacement applied at either the left (forward mode) or right (reverse mode) side of the diode. The RMS amplitude of the time signal measured in each domain near the source, but several unit cells out in order to capture the effects of evanescent attenuation. The measured RMS amplitudes are normalized by the RMS amplitude of the input signal. Note that, as expected for the forward operating mode, negligible transmission is measured in any section until the critical amplitude $A_{crit} = 1.0$ is reached. Beyond this critical amplitude, forward propagation through the diode is permitted. In contrast, the reverse operating mode essentially prohibits propagation into the nonlinear section for all amplitudes $A < 2$. The reflected linear signal A_L^+ and partial absorption by the lossy material are responsible for decreasing the signal transmitted into the nonlinear segment. In this case, transmission amplitudes A_{NL}^- are such that the operation frequency lies in a bandgap. Beyond $A = 2$, the diode breaks down.

This device, and others utilizing the same principles should be explored both numerically and experimentally. However, before physical instantiations of devices can take place

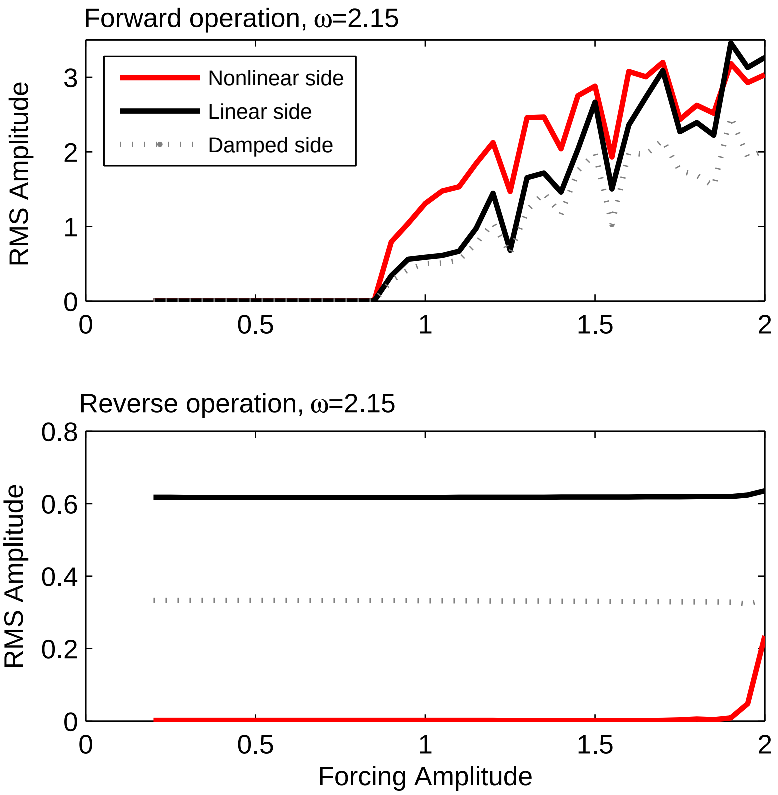

Figure 8.6: Numerical simulation results of a nonlinear band gap-based junction diode device. RMS responses are measured near the input and output of the system near after near steady-state conditions are achieved.

it is necessary to design nonlinear spring elements which can be practically implemented. Nevertheless, nonlinear system components composed of periodic materials may find a place in the future of nonlinear phononic crystals and metamaterials.

APPENDIX A

WAVE MODE NORMALIZATION

The frequency correction terms described by (2.36) and (2.67) capture frequency shifts due to displacement amplitude. The following focuses on monochromatic frequency corrections, but is equally applicable to the more general frequency content. Since Bloch wave modes are unique only up to a scalar multiple, one must choose a method for scaling the wave modes before evaluating ω_1. The displacement amplitude of the jth Bloch wave mode is given as

$$\max(\mathbf{u}^{(0)}) = \max(A\boldsymbol{\phi}_j), \tag{A.1}$$

where max(..) returns the maximum modulus of the imaginary components comprising an input vector. One normalization approach sets the maximum value of $\boldsymbol{\phi}_j(\boldsymbol{\mu})$ for all wave vectors to unity such that the overall amplitude of the Bloch wave mode is controlled by A [63, 3]. This approach is sufficient for dealing with lumped-parameter models where nonlinear restoring forces produced by spring elements depend only on the *displacement amplitude* and not on frequency or wavenumber. The same is not true for constitutive and geometric nonlinearities arising in continuous systems where spatial derivatives (due to strain or large deformation) will lead to frequency and/or wave number dependence in the nonlinear restoring forces.

We consider the simple homogeneous rod with a nonlinear constitutive law as an example. The stress-strain nonlinearities take the form $\sigma_{xx} = E_1 e_{xx} + \Gamma e_{xx}^3$, where σ_{xx} denotes stress, e_{xx} denotes strain, and the linear and nonlinear moduli are given by E_1 and Γ. This constitutive law may be rewritten as $\sigma_{xx} = \bar{E} e_{xx}$ where the stain-dependent elastic modulus is given by $\bar{E}(e_{xx}) = E_1(1 + \Gamma e_{xx}^2/E_1)$. The system is weakly nonlinear when $|\Gamma/E_1 e_{xx}^2| \ll 1$ or when e_{xx} is small. The material choice fixes the ratio Γ/E_1; thus, only the strain amplitude varies the stiffness contribution from the nonlinear term. As strain introduces wavenumber dependence into the nonlinear restoring forces for plane wave propagation, the magnitude of the nonlinearity increases with frequency[1].

A *strain normalization* scheme is appropriate in this situation to ensure predicted frequency shifts are within the weakly nonlinear regime. One may employ strain normalization by calculating the Bloch wave modes and then computing the maximum strain (e.g. numerically). Figure A.1 depicts two possible normalization schemes for the acoustic branch of a bilayer material discussed in later Chapters. The top subfigure depicts the Bloch wave mode amplitude $|\boldsymbol{\phi}_j|$ as a function of wavenumber while the bottom subfigure depicts corresponding amplitude-dependent dispersion relations. In the long wavelength limit, amplitude-normalization produces smaller shifts than a strain-normalization scheme; at higher frequencies it results in larger shifts. Each of these dispersion branches is valid in

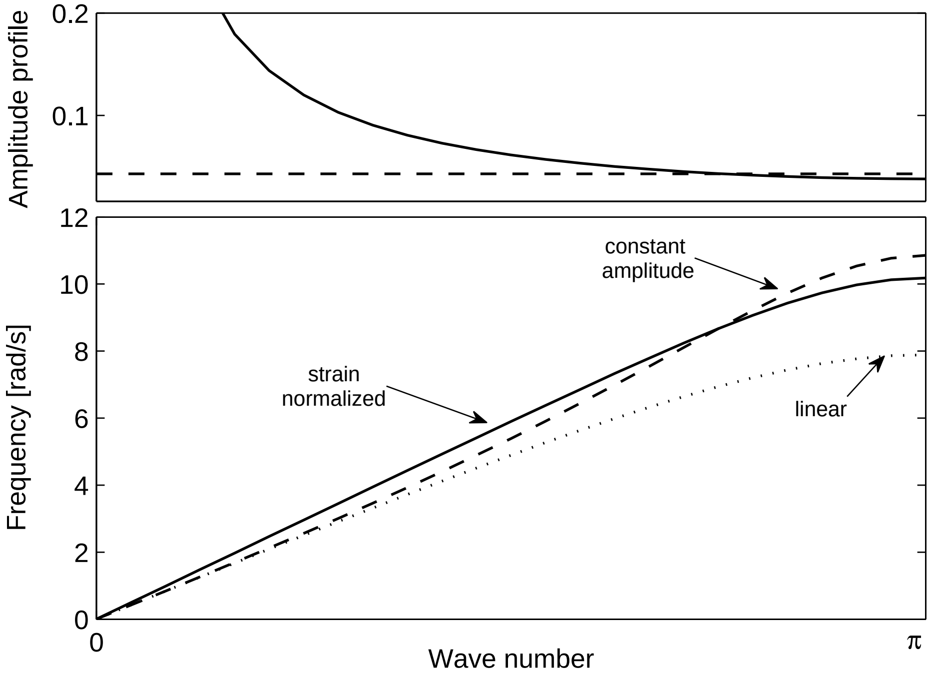

Figure A.1: Two possible methods for normalizing amplitude-dependent dispersion curves. The dotted black line indicates the dispersion relation for a low-strain (linear) system.

---

[1] Since frequency in a continuum is proportional to wavenumber according to $\omega = ck$

the sense that individual points convey correctly the wavenumber-frequency relationship as a function of wave amplitude, regardless of the normalization approach employed. A group velocity calculation based on NDA requires knowledge of multiple dispersion points because it expresses the propagation of a pulse that is localized in the frequency domain. The work presented herein utilizes a strain-normalization approach, unless noted otherwise, for presenting dispersion diagrams in continuous systems such that strains produced from all Bloch modes considered are consistent with a weak nonlinearity (small strains).

APPENDIX B

NONLINEAR DISPERSION ANALYSIS WITH FEA

B.1 Simple Example Using a Single Element in COMSOL

As a simple example, consider a rod *discretized using only a single linear Lagrange element*. We digress from periodic systems for a moment to study an elementary example that illustrates the majority of the process steps needed to obtain the nonlinear force vector. The homogenous PDE governing the system is

$$\frac{\partial}{\partial x}\left(\frac{\partial \sigma}{\partial x}\right) = \rho \frac{\partial^2 u}{\partial t^2} \tag{B.1}$$

where the constitutive law for stress σ may be a nonlinear function of the displacement u or its spatial derivatives. The weak formulation of Eq. (B.1) and subsequent discretization using shape functions $\psi_{1,2}$ leads to the residual vector

$$\mathbf{R} = \begin{bmatrix} \int_0^L (-\rho\psi_1\psi_2\ddot{u}_2 - \rho\psi_1^2\ddot{u}_1 - \sigma\psi_1') \,\mathrm{d}s \\ \int_0^L (-\rho\psi_2\psi_1\ddot{u}_1 - \rho\psi_2^2\ddot{u}_2 - \sigma\psi_2') \,\mathrm{d}s \end{bmatrix} = \begin{bmatrix} 0 \\ 0 \end{bmatrix}, \tag{B.2}$$

where a prime denotes a spatial derivative and a dot denotes a time derivative. The residual vector evaluated for linear Lagrange shape functions $\psi_1(x) = 1 - x/L$ and $\psi_2(x) = x/L$ and the nonlinear constitutive relationship $\sigma = E_1 u' + E_3 (u')^3$ is

$$\mathbf{R} = \begin{bmatrix} \frac{\rho L}{3}\ddot{u}_1 + \frac{1}{6}\ddot{u}_2 + \frac{E_1}{L}(u_1 - u_2) + \frac{E_3}{L^3}(u_1 - u_2)^3 \\ \frac{\rho L}{3}\ddot{u}_2 + \frac{1}{6}\ddot{u}_1 + \frac{E_1}{L}(u_2 - u_1) + \frac{E_3}{L^3}(u_2 - u_1)^3 \end{bmatrix} = \begin{bmatrix} 0 \\ 0 \end{bmatrix}. \tag{B.3}$$

It is clear that in this simple example the mass and stiffness are those typical of a rod element

$$\mathbf{M} = \rho L \begin{bmatrix} 1/2 & 0 \\ 0 & 1/2 \end{bmatrix} \quad \text{and} \quad \mathbf{K} = \frac{E_1}{L} \begin{bmatrix} 1 & -1 \\ -1 & 1 \end{bmatrix},$$

while the nonlinear components making up the load vector are

$$\mathbf{f}_{NL} = \left\{ \begin{array}{c} \frac{E_3}{L^3}(u_1 - u_2)^3 \\ \\ \frac{E_3}{L^3}(u_2 - u_1)^3 \end{array} \right\}.$$

A linearization of the residual vector about some displacement vector $\mathbf{u}_0$ would, in addition to the $\mathbf{f}^{NL}(\mathbf{u}_0)$ terms, include terms such as those arising from any pre-compression. Specifically, these terms are given by $\mathbf{K}(\mathbf{u}_0)\mathbf{u}_0$ The nonlinear force vector can be isolated in the residual vector by setting the coefficients ρ and E_1 of the linear differential operators to zero in the associated COMSOL model. The model can then be imported into MATLAB using the COMSOL function

```
model = mphload(<filename>).
```

The residual vector containing only the nonlinear forcing terms is obtained by prescribing a current solution vector and allowing COMSOL to evaluate the load vector. In COMSOL 4.2, the syntax inside MATLAB is as follows:

```
u0 = [u1, u2];
model.sol('sol1').setU(u0);
model.sol('sol1').setPVals(0);
model.sol('sol1').createSolution;


MA = mphmatrix(model, 'sol1', 'out', 'L', 'initmethod', 'sol');
```

The first command simply specifies the vector to evaluate for. The second command sets the nodal values of `'sol1'` to these values. The third command, `setPVals()` is required by COMSOL before `createSolution()` can be called. It sets the time vector at which solutions are stored for a time-dependent problem. The fourth command creates the solution object, while the last command outputs the load vector to a MATLAB structure that can be accessed as `MA.L`. A COMSOL model created with the parameters `L=1`, `E3=1` and linearization “point” `u0=[1,2]` returns the load vector `MA.L = [1, -1]`. Comparing this result with a direct computation using Eq. (B.3) shows that the residual vector returned by COMSOL contains only those terms previously denoted as $\mathbf{f}^{NL}$.

B.2 Bimaterial system FEA implementation

COMSOL is an ideal commercial FEA package to analyze nonlinear dispersion with. It provides direct access to the governing physical equations, mesh information, and residual vector. The information is easily manipulated with the aid of MATLAB through the optional LiveLink Software. A brief description of the commands used for a COMSOL 4.2 implementation are detailed here for reference.

The three unit cell model was created using the wave equation interface `waeq` along with a Time-Dependent study type. The model parameter $f = 0$ is chosen so that the governing PDE is homogenous. The nonlinear constitutive law for stress-strain is applied by setting the diffusion coefficient for Layer A to `E1+E3*ux^2`, where `E1=1.0` and `E3=1.0`. The final step in this process is to run the solver routine so that a default solution object `‘sol1’` is created. The saved model may then be directly imported into MATLAB for further processing.

The system matrices **M** and **K** describing the three unit cells may be obtained as detailed in as detailed in B.1. In order to obtain system matrices **M** and **K** describing the infinite system, mesh and node information must be processed so that appropriate partitions of **M** and **K** may be selected (see Sec. 5.4). The model object contains information regarding the nodes, coordinates, DOFs, solution, governing PDE, boundary conditions, and more. The COMSOL command `mphxmeshinfo()` provides the requisite information about nodal coordinates and degrees of freedom.

Once this information has been processed, linear Bloch wave modes $\boldsymbol{\phi}_j$ and frequencies ω_0 for the system may be obtained by solving the generalized eigenvalue problem for each wavenumber μ of interest. The nonlinear force vector for the infinite system can be calculated by eliminating the linear operators from the system and leaving only the nonlinear terms. Within MATLAB, the coefficients of the linear operators are set to zero programmatically by the commands:

```
model.physics('waeq').feature('weq1').set('c','ux^2');
model.physics('waeq').feature('weq2').set('c','0');
model.physics('waeq').feature('weq1').set('ea','0');
model.physics('waeq').feature('weq2').set('ea','0');
```

The first of these commands sets the “diffusion coefficient” of the first layer (the nonlinear layer) to only the nonlinear part `ux^2`. This eliminates the linear modulus from the problem. The second command sets the diffusion coefficient to zero because there is no nonlinearity here. The last two lines simply set the density for each material to zero; this is not strictly necessary since these terms should not appear in the load vector, but it is a good practice.

The discrete time-history of the nonlinear force vector $\mathbf{f}^{NL}$ is obtained by evaluating system load vector (as in B.1) over a full period of the displacement field $\mathbf{u}_0(\tau)$. The $O(\varepsilon^0)$ displacement field $\mathbf{u}_0$ is calculated for the three unit cells using the Bloch wave vector $\boldsymbol{\phi}_j$ and the Bloch theorem. This calculation is repeated for each desired wavenumber and frequency. The results for the multilayer rod of Sec. B.1 completed in approximately 20 minutes when each dispersion contour contained 16 equally spaced wavenumber points.

APPENDIX C

DISPERSION SHIFT FOR A HOMOGENEOUS ROD

The dispersion shift arising for a one-dimensional rod with a constitutive nonlinearity may be obtained through perturbation of the continuous PDE governing wave propagation

$$\frac{\partial \sigma}{\partial x} = \rho \frac{\partial^2 u}{\partial t^2}. \tag{C.1}$$

The constitutive law governing the strain displacement relationship is defined as

$$\sigma = E_1 \frac{\partial u}{\partial x} + E_3 \left(\frac{\partial u}{\partial x} \right)^3. \tag{C.2}$$

Substitution of Eq. (C.2) into Eq. (C.1) results a nonlinear wave equation. The small parameter ε is introduced through the relationship $E_3 = \varepsilon \hat{E}_3$ to enforce weak nonlinearity, where $\hat{E}_3$ is of the same order as the linear modulus E_1.

$$E_1(x) \frac{\partial^2 u(x,t)}{\partial x^2} + \varepsilon \hat{E}_3(x) \frac{\partial}{\partial x} \left(\frac{\partial u}{\partial x} \right)^3 = \rho(x) \frac{\partial^2 u(x,t)}{\partial t^2}. \tag{C.3}$$

Nondimensional time $\tau = \omega t$ and asymptotic expansions are introduced according to

$$\begin{aligned} \omega &= \omega^{(0)} + \varepsilon \omega^{(1)} + O(\varepsilon^2) \\ u &= u^{(0)} + \varepsilon u^{(1)} + O(\varepsilon^2). \end{aligned} \tag{C.4}$$

Substitution of the expansions Eq. (C.4) into the weakly nonlinear wave equation (C.3) produces a set of equations ordered by the small parameter ε

$$O(\varepsilon^0): \quad E_1 \frac{\partial^2 u^{(0)}}{\partial x^2} = \rho (\omega^{(0)})^2 \frac{\partial^2 u^{(0)}}{\partial \tau^2} \tag{C.5}$$

$$O(\varepsilon^0): \quad E_1 \frac{\partial^2 u^{(1)}}{\partial x^2} + 3\hat{E}_3 \left(\frac{\partial u^{(0)}}{\partial x} \right)^2 \frac{\partial^2 u^{(0)}}{\partial x^2} = \rho (\omega^{(0)})^2 \frac{\partial^2 u^{(1)}}{\partial \tau^2} + 2\rho \omega^{(0)} \omega^{(1)} \frac{\partial^2 u^{(0)}}{\partial \tau^2}. \tag{C.6}$$

The solution to the $O(\varepsilon^0)$ is well-known, and given by the plane wave

$$u^{(0)}(x,t) = \frac{A}{2} \exp \mathrm{i}(kx - \tau) + c.c = A \cos(kx - \tau). \tag{C.7}$$

where the wavenumber k is defined through the relationship $\omega^{(0)} = ck$, $c = \sqrt{E_1/\rho}$ denotes phase speed, and c.c. denotes complex conjugate terms. Subsequent substitution of $u^{(0)}(x,t)$ into the $O(\varepsilon)$ equation results in the equation

$$E_1 \frac{\partial^2 u^{(1)}}{\partial x^2} - \rho(\omega^{(0)})^2 \frac{\partial^2 u^{(1)}}{\partial \tau^2} = -2\omega^{(0)}\omega^{(1)}\rho A \cos(kx - \tau) + \frac{3}{4}\hat{E}_3 A^3 k^4 \cos(kx - \tau) + O(3kx - 3\tau), \tag{C.8}$$

where terms higher frequency terms are indicated by $O(3kx - 3\tau)$. The linear kernel of the $O(\varepsilon^1)$ equation is identical to the linear kernel of the $O(\varepsilon^{)}$ equation. Removing secular (those multiplying $\cos{(kx - \tau)}$) results in an equation which may be solved for a first-order frequency correction $\omega^{(1)}$

$$-2\omega^{(0)}\omega^{(1)}\rho A + \frac{3}{4}\hat{E}_3 A^3 k^4 = 0. \tag{C.9}$$

The solution for the first frequency correction is

$$\omega^{(1)} = \frac{3}{8}\frac{\hat{E}_3 A^2 k^4}{\rho\omega^{(0)}}. \tag{C.10}$$

The *strain* amplitude $e_0 = kA$ and the relationship $\omega^{(0)} = ck$ may be used to obtain alternate forms of the frequency correction, namely

$$\omega^{(1)} = \frac{3}{8}\frac{\hat{E}_3}{E_1} e_0^2 \omega^{(0)}. \tag{C.11}$$

Thus, the first-order corrected frequency is given by

$$\omega = \omega^{(0)} + \varepsilon\left(\frac{3}{8}\frac{\hat{E}_3}{E_1} e_0^2 \omega^{(0)}\right) = \omega^{(0)}\left(1 + \frac{3E_3}{8E_1} e_0^2\right). \tag{C.12}$$

This relationship is useful for validating results produced from nonlinear dispersion analysis routines.

REFERENCES

[1] R. H. Olsson and I. El-Kady, “Microfabricated phononic crystal devices and applications,” *Measurement Science and Technology*, vol. 20, p. 012002, Nov. 2009.

[2] S. Zhang, C. Xia, and N. Fang, “Broadband acoustic cloak for ultrasound waves,” *Physical Review Letters*, vol. 106, no. 2, p. 24301, 2011.

[3] R. K. Narisetti, M. J. Leamy, and M. Ruzzene, “A perturbation approach for predicting wave propagation in one-dimensional nonlinear periodic structures,” *ASME Journal of Vibration and Acoustics*, vol. 132, p. 031001, Jun. 2010.

[4] C. Kittel, *Introduction to solid state physics*. Wiley, New York, 5th ed. ed., 1976.

[5] D. G. Stavenga, B. D. Wilts, H. L. Leertouwer, and T. Hariyama, “Polarized iridescence of the multilayered elytra of the japanese jewel beetle, chrysochroa fulgidissima,” *Philosophical Transactions of the Royal Society B: Biological Sciences*, vol. 366, no. 1565, pp. 709–723, 2011.

[6] M. Ruzzene, “Vibration and sound radiation of sandwich beams with honeycomb truss core,” *Journal of sound and vibration*, vol. 277, no. 4, pp. 741–763, 2004.

[7] A. Spadoni, M. Ruzzene, S. Gonella, and F. Scarpa, “Phononic properties of hexagonal chiral lattices,” *Wave motion*, vol. 46, no. 7, pp. 435–450, 2009.

[8] F. Casadei and J. Rimoli, “Anisotropy-induced broadband stress wave steering in periodic lattices,” *International Journal of Solids and Structures*, 2013.

[9] C. Elachi, “Waves in active and passive periodic structures: A review,” *Proceedings of the IEEE*, vol. 64, no. 12, pp. 1666–1698, 1976.

[10] D. J. Mead, “Wave propagation and natural modes in periodic systems: I. Mono-coupled systems,” *Journal of Sound and Vibration*, vol. 40, pp. 1–18, May 1975.

[11] D. J. Mead, “Wave propagation in continuous periodic structures: Research contributions from southampton, 1964–1995,” *Journal of Sound and Vibration*, vol. 190, pp. 495–524, February 1996.

[12] N. Fang, H. Lee, C. Sun, and X. Zhang, “Sub–diffraction-limited optical imaging with a silver superlens,” *Science*, vol. 308, no. 5721, pp. 534–537, 2005.

[13] S. Yang, J. H. Page, Z. Liu, M. L. Cowan, C. T. Chan, and P. Sheng, “Focusing of sound in a 3d phononic crystal,” *Phys. Rev. Lett.*, vol. 93, p. 024301, Jul 2004.

[14] X. Guo, Z. Lin, J. Tu, B. Liang, J. Cheng, and D. Zhang, "Modeling and optimization of an acoustic diode based on micro-bubble nonlinearity," *The Journal of the Acoustical Society of America*, vol. 133, no. 2, pp. 1119–1125, 2013.

[15] M. Sigalas, M. Kushwaha, E. Economou, M. Kafesaki, I. Psarobas, and W. Steurer, "Classical vibrational modes in phononic lattices: theory and experiment," *Zeitschrift für Kristallographie*, vol. 220, no. 9-10, pp. 765–809, 2005.

[16] R. H. Olsson III, I. F. El-Kady, M. F. Su, M. R. Tuck, and J. G. Fleming, "Microfabricated vhf acoustic crystals and waveguides," *Sensors and Actuators A*, pp. 87–93, 2008.

[17] J. Page, A. Sukhovich, S. Yang, M. Cowan, F. van der Biest, A. Tourin, M. Fink, Z. Liu, C. Chan, and P. Sheng, "Phononic crystals," *Solid State Physics*, vol. 241, no. 15, pp. 3454–3462, 2004.

[18] K. Bertoldi and M. C. Boyce, "Mechanically triggered transformations of phononic band gap elastomeric structures.," *Physical Review B*, vol. 77, pp. 1–10, Feb. 2008.

[19] J.-H. Jang, C. K. U. Ullal, T. Gorishnyy, V. V. Tsukruk, and E. L. Thomas, "Mechanically tunable three-dimensional elastomeric network/air structures via interference lithography," *Nano Letters*, vol. 6, no. 4, pp. 740–743, 2006.

[20] B. Liang, B. Yuan, and J. Cheng, "Acoustic diode: rectification of acoustic energy flux in one-dimensional systems," *Phys. Rev. Lett.*, vol. 103, p. 104301, Sep 2009.

[21] O. Sigmund and J. S. Jensen, "Systematic design of phononic band-gap materials and structures by topology optimization," *Philosophical Transactions: Mathematical, Physical, and Engineering Sciences*, vol. 361, pp. 1001–1019, May 2003.

[22] Y. Yun, G. Miao, P. Zhang, K. Huang, and R. Wei, "Nonlinear acoustic wave propagating in one-dimensional layered system," *Physics Letters A*, vol. 343, no. 5, pp. 351 – 358, 2005.

[23] O. R. Asfar and A. H. Nayfeh, "The application of the method of multiple scales to wave propagation in periodic structures," *SIAM Review*, vol. 25, pp. 455–480, Oct 1983.

[24] G. Chakraborty and A. K. Mallik, "Dynamics of a weakly non-linear periodic chain," *International Journal of Nonlinear Mechanics*, vol. 36, no. 2, pp. 375 – 389, 2001.

[25] A. Marathe and A. Chatterjee, "Wave attenuation in nonlinear periodic structures using harmonic balance and multiple scales," *Journal of Sound and Vibration*, vol. 289, no. 4-5, pp. 871–888, 2006.

[26] V. Rothos and A. Vakakis, "Dynamic interactions of traveling waves propagating in a linear chain with a local essentially nonlinear attachment," *Wave Motion*, vol. 46, no. 3, pp. 174–188, 2009.

[27] Nayfeh and Mook, *Nonlinear Oscillations*. Wiley, New York, 1995.

[28] J. J. Rushchitsky and C. Cattani, “Evolution equations for plane cubically nonlinear elastic waves,” *International Applied Mechanics*, vol. 40, pp. 70–76, Jan. 2004.

[29] J. J. Rushchitsky and E. V. Saveleva, “On the interaction of cubically nonlinear transverse plane waves in an elastic material,” *International Applied Mechanics*, vol. 42, pp. 661–668, Jun. 2006.

[30] I. Kovacic and M. J. Brennan, *The Duffing equation: Nonlinear oscillators and their behaviour*. Wiley, 2011.

[31] W. O. Davis and A. P. Pisano, “Nonlinear mechanics of suspension beams for a micromachined gyroscope,” in *International conference on modeling and simulation of microsystems*, (Hilton oceanfront resort hotel), Mar. 2001.

[32] V. Kaajakari, T. Mattila, A. Oja, and H. Seppä, “Nonlinear limits for single-crystsal silicon microresonators,” *Journal of Microelectromechanical Systems*, vol. 13, Oct. 2004.

[33] V. Kaajakari, T. Mattila, A. Lipsanen, and A. Oja, “Nonlinear mechanical effects in silicon longitudinal mode beam resonators,” *Sensors and Actuators A: Physical*, vol. 120, pp. 64–70, Apr. 2005.

[34] A. Erturk and D. J. Inman, *Piezoelectric energy harvesting*. Wiley, 2011.

[35] N. Elvin and A. Erturk, *Advances in energy harvesting methods*. Springer, 2013.

[36] K. L. Manktelow, M. J. Leamy, and M. Ruzzene, “Multiple scales analysis of wave-wave interactions in a cubically nonlinear monoatomic chain,” *Nonlinear Dynamics*, vol. 63, pp. 193–203, 2011. 10.1007/s11071-010-9796-1.

[37] C. Daraio, V. F. Nesterenko, E. B. Herbold, and S. Jin, “Strongly nonlinear waves in a chain of teflon beads,” *Phys. Rev. E*, vol. 72, p. 016603, Jul 2005.

[38] C. Daraio, V. Nesterenko, E. Herbold, and S. Jin, “Tunability of solitary wave properties in one-dimensional strongly nonlinear phononic crystals,” *Phys. Rev. E*, vol. 73, p. 026610, Feb 2006.

[39] P. P. Banerjee, *Nonlinear optics: theory, numerical modeling and applications*. New York, NY: Marcel Dekker, Inc., 2004.

[40] S. D. Gupta, “Progress in optics,” in *Nonlinear Optics of Stratified Media* (E. Wolf, ed.), vol. 38, pp. 1 – 84, Elsevier, 1998.

[41] J. W. Haus, B. Y. Soon, M. Scalora, C. Sibilia, and I. V. Melnikov, “Coupled-mode equations for kerr media with periodically modulated linear and nonlinear coefficients,” *Journal of the Optical Society of America B*, vol. 19, p. 2282, Sep 2002.

[42] S. Inoue and Y. Aoyagi, “Design and fabrication of two-dimensional photonic crystals with predetermined nonlinear optical properties,” *Physical Review Letters*, vol. 94, no. 10, p. 103904, 2005.

[43] I. S. Maksymov, L. F. Marsal, and J. Pallarès, “Band structures in nonlinear photonic crystal slabs,” *Optical and Quantum Electronics*, vol. 37, no. 1, pp. 161–169, 2005.

[44] A. F. Vakakis and M. E. King, “Resonant oscillations of a weakly coupled, nonlinear layered system,” *Acta Mechanica*, vol. 128, pp. 59–80, 03 1998.

[45] A. F. Vakakis and M. E. King, “Nonlinear wave transmission in a monocoupled elastic periodic system,” *Journal of the Acoustical Society of America*, vol. 98, no. 3, pp. 1534–1546, 1995.

[46] E. B. Herbold, J. Kim, V. Nesterenko, S. Wang, and C. Daraio, “Tunable frequency band-gap and pulse propagation in a strongly nonlinear diatomic chain,” *Materials Science*, pp. 1–38, 2008.

[47] J. Yang, S. Dunatunga, and C. Daraio, “Amplitude-dependent attenuation of compressive waves in curved granular crystals constrained by elastic guides,” *Acta Mechanica*, pp. 1–14, 2012.

[48] S. Sen, J. Hong, J. Bang, E. Avalos, and R. Doney, “Solitary waves in the granular chain,” *Physics Reports*, vol. 462, no. 2, pp. 21 – 66, 2008.

[49] N. Boechler, C. Daraio, R. K. Narisetti, M. Ruzzene, and M. J. Leamy, “Analytical and experimental analysis of bandgaps in nonlinear one dimensional periodic structures,” in *IUTAM Symposium on Recent Advances of Acoustic Waves in Solids*, pp. 209–219, Springer, 2010.

[50] R. K. Narisetti, *Wave propagation in nonlinear periodic structures*. PhD thesis, Georgia Institute of Technology, 2010.

[51] V. Laude, R. Moiseyenko, S. Benchabane, and N. Declercq, “Bloch wave deafness and modal conversion at a phononic crystal boundary,” *AIP Advances*, vol. 1, no. 4, pp. 041402–041402, 2011.

[52] J. Joannopoulos, P. Villeneuve, and S. Fan, “Photonic crystals,” *Solid State Communications*, vol. 102, no. 2-3, pp. 165–173, 1997.

[53] K. Graff, *Wave motion in elastic solids*. Dover publications, 1991.

[54] W. Elmore and M. Heald, *Physics of waves*. Dover Publications, 1985.

[55] F. Farzbod and M. J. Leamy, “Analysis of bloch’s method and the propagation technique in periodic structures,” *Journal of vibration and acoustics*, vol. 133, no. 3, 2011.

[56] L. Kinsler, *Fundamentals of acoustics*. John Wiley & Sons Inc, 2000.

[57] J. D. Joannopoulos, S. G. Johnson, J. N. Winn, and R. D. Meade, *Photonic crystals: molding the flow of light*. Princeton University Press, 2 ed., 2008.

[58] W. C. Elmore and M. A. Heald, *Physics of waves*. New-York: Dover, 1985.

[59] A. H. Nayfeh and P. F. Pai, *Linear and Nonlinear Structural Mechanics*. Wiley, New York, 2004.

[60] T. J.R. Hughes, *The finite element method: linear static and dynamic finite element analysis*. Dover Publications New York, 2000.

[61] J. Reddy, *An introduction to the finite element method*, vol. 2. McGraw-Hill New York, 2nd ed., 1993.

[62] K. Manktelow, M. Leamy, and M. Ruzzene, "Intensity-dependent dispersion in nonlinear photonic and phononic crystals," *Wave Motion*, Accepted.

[63] R. K. Narisetti, M. Ruzzene, and M. J. Leamy, "A perturbation approach for analyzing dispersion and group velocities in two-dimensional nonlinear periodic lattices," *Journal of Vibration and Acoustics*, vol. 133, p. 061020, 2011.

[64] J. Simmonds and J. Mann, *A first look at perturbation theory*. Dover Publications, 1997.

[65] A. Nayfeh, *Perturbation methods*. Wiley-VCH, 2008.

[66] R. W. Boyd, *Nonlinear optics*. San Diego, CA: Academic Press, 1992.

[67] J. J. Rushchitsky, "Interaction of waves in solid mixtures," *Applied Mechanics Reviews*, vol. 52, no. 2, pp. 35–74, 1999.

[68] M. Peyrard and M. D. Kruskal, "Kink dynamics in the highly discrete sine-gordon system," *Physica D: Nonlinear Phenomena*, vol. 14, no. 1, pp. 88 – 102, 1984.

[69] A. H. Nayfeh and M. H. Rice, "On the propagation of disturbances in a semi-infinite one-dimensional lattice," *American Journal of Physics*, vol. 40, no. 3, pp. 469–470, 1972.

[70] A. Khelif, B. Djafari-Rouhani, J. Vasseur, and P. Deymier, "Transmission and dispersion relations of perfect and defect-containing waveguide structures in phononic band gap materials," *Physical Review B*, vol. 68, no. 2, p. 024302, 2003.

[71] F. Casadei, T. Delpero, A. Bergamini, P. Ermanni, and M. Ruzzene, "Piezoelectric resonator arrays for tunable acoustic waveguides and metamaterials," *Journal of Applied Physics*, vol. 112, no. 6, pp. 064902–064902, 2012.

[72] A. Askar, "Dispersion relation and wave solution for anharmonic lattices and korteweg de vries continua," *Proceedings of the Royal Society of London. A. Mathematical and Physical Sciences*, vol. 334, no. 1596, pp. 83–94, 1973.

[73] P. M. Morse and K. U. Ingard, *Theoretical acoustics.* McGraw Hill Book Co., 1987.

[74] R. Langley, N. Bardell, and H. Ruivo, "The response of two-dimensional periodic structures to harmonic point loading: a theoretical and experimental study of a beam grillage," *Journal of Sound and Vibration*, vol. 207, no. 4, pp. 521–535, 1997.

[75] M. Ruzzene, F. Scarpa, and F. Soranna, "Wave beaming effects in two-dimensional cellular structures," *Smart materials and structures*, vol. 12, no. 3, p. 363, 2003.

[76] N. Panoiu, M. Bahl, R. Osgood Jr, *et al.*, "Optically tunable superprism effect in nonlinear photonic crystals," *Optics letters*, vol. 28, no. 24, pp. 2503–2505, 2003.

[77] J. Kennedy, "High-intensity focused ultrasound in the treatment of solid tumours," *Nature Reviews Cancer*, vol. 5, no. 4, pp. 321–327, 2005.

[78] S. Parmley, T. Zobrist, T. Clough, A. Perez-Miller, M. Makela, and R. Yu, "Vibrational properties of a loaded string," *American Journal of Physics*, vol. 63, p. 547, 1995.

[79] S. Parmley, T. Zobrist, T. Clough, A. Perez-Miller, M. Makela, and R. Yu, "Phononic band structure in a mass chain," *Applied physics letters*, vol. 67, no. 6, pp. 777–779, 1995.

[80] V. Hopkins, L. Krysac, and J. Maynard, "Experimental studies of nonlinear continuous waves and pulses in disordered media showing anderson localization," *Physical Review B*, vol. 58, no. 17, p. 11377, 1998.

[81] J. Cabaret, V. Tournat, and P. Béquin, "Amplitude dependent phononic processes in a diatomic granular chain in the weakly nonlinear regime," *Physical Review E*, vol. 86, no. 4, p. 041305, 2012.

[82] N. Sugimoto, "Propagation of nonlinear acoustic waves in a tunnel with an array of helmholtz resonators," *Journal of Fluid Mechanics*, vol. 244, pp. 55–55, 1992.

[83] N. Sugimoto and T. Horioka, "Dispersion characteristics of sound waves in a tunnel with an array of helmholtz resonators," *The Journal of the Acoustical Society of America*, vol. 97, p. 1446, 1995.

[84] A. Elshurafa, K. Khirallah, H. Tawfik, A. Emira, A. Abdel Aziz, and S. Sedky, "Nonlinear dynamics of spring softening and hardening in folded-mems comb drive resonators," *Journal of Microelectromechanical Systems*, vol. 20, no. 4, pp. 943–958, 2011.

[85] R. Ansari, R. Gholami, and M. Darabi, "A nonlinear timoshenko beam formulation based on strain gradient theory," *Journal of Mechanics of Materials and Structures*, vol. 7, no. 2, pp. 195–211, 2012.

[86] C. Le, T. E. Bruns, and D. A. Tortorelli, "Material microstructure optimization for linear elastodynamic energy wave management," *Journal of the Mechanics and Physics of Solids*, vol. 60, no. 2, pp. 351 – 378, 2012.

[87] T. Meurer, J. Qu, and L. Jacobs, “Wave propagation in nonlinear and hysteretic media—-a numerical study,” *International Journal of Solids and Structures*, vol. 39, no. 21, pp. 5585–5614, 2002.

[88] S. R. Entezar, A. Namdar, Z. Eyni, and H. Tajalli, “Nonlinear surface waves in one-dimensional photonic crystals containing left-handed metamaterials,” *Phys. Rev. A*, vol. 78, p. 023816, Aug 2008.

[89] S. K. Adhikari, “Stabilization of a light bullet in a layered kerr medium with sign-changing nonlinearity,” *Phys. Rev. E*, vol. 70, p. 036608, Sep 2004.

[90] M. Scalora, J. Dowling, C. Bowden, and M. Bloemer, “Optical limiting and switching of ultrashort pulses in nonlinear photonic band gap materials,” *Physical Review Letters*, vol. 73, no. 10, pp. 1368–1371, 1994.

[91] M. Soljačić, S. Johnson, S. Fan, M. Ibanescu, E. Ippen, and J. D. Joannopoulos, “Photonic-crystal slow-light enhancement of nonlinear phase sensitivity,” *Journal of the Optical Society of America B*, vol. 19, no. 9, pp. 2052–2059, 2002.

[92] R. Joseph and A. Taflove, “FDTD Maxwell’s equations models for nonlinear electrodynamics and optics,” *Antennas and Propagation, IEEE Transactions*, vol. 45, no. 3, pp. 364–374, 2002.

[93] A. Huttunen and P. Törmä, “Band structures for nonlinear photonic crystals,” *Journal of Applied Physics*, vol. 91, p. 3988, 2002.

[94] I. Maksymov, L. Marsal, and J. Pallares, “Finite-difference time-domain analysis of band structures in one-dimensional Kerr-nonlinear photonic crystals,” *Optics Communications*, vol. 239, no. 1-3, pp. 213–222, 2004.

[95] R. K. Narisetti, M. Ruzzene, and M. J. Leamy, “Study of wave propagation in strongly nonlinear periodic lattices using a harmonic balance approach,” *Wave Motion*, vol. 49, no. 2, pp. 394 – 410, 2012.

[96] J. D. Joannopoulos, P. R. Villeneuve, and S. Fan, “Photonic crystals,” *Solid State Communications*, vol. 102, no. 2-3, pp. 165–173, 1997.

[97] M. I. Hussein, G. M. Hulbert, and R. A. Scott, “Dispersive elastodynamics of 1D banded materials and structures: analysis,” *Journal of Sound and Vibration*, vol. 289, no. 4-5, pp. 779 – 806, 2006.

[98] S. Sindhu and C. S. Menon, “Fourth order nonlinear elastic coefficients of hexagonal close packed lattice,” *Journal of Physics and Chemistry of Solids*, vol. 57, no. 9, pp. 1307 – 1309, 1996.

[99] D. S. Bethune, “Optical harmonic generation and mixing in multilayer media: analysis using optical transfer matrix techniques,” *J. Opt. Soc. Am. B*, vol. 6, pp. 910–916, May 1989.

[100] P. Luan and Z. Ye, "Acoustic wave propagation in a one-dimensional layered system," *Phys. Rev. E*, vol. 63, p. 066611, May 2001.

[101] F. Romeo and G. Rega, "Propagation properties of bi-coupled nonlinear oscillatory chains: analytical prediction and numerical validation," *International Journal of Bifurcation and Chaos*, vol. 18, no. 07, pp. 1983–1998, 2008.

[102] K. Manktelow, R. K. Narisetti, M. J. Leamy, and M. Ruzzene, "Finite-element based perturbation analysis of wave propagation in nonlinear periodic structures," *Mechanical Systems and Signal Processing*, pp. –, 2012.

[103] S. Halkjær, O. Sigmund, and J. S. Jensen, "Inverse design of phononic crystals by topology optimization," *Zeitschrift fur Kristallographie*, vol. 220, no. 9–10, pp. 895–905, 2005.

[104] J. S. Jensen, "Topology optimization problems for reflection and dissipation of elastic waves," *Journal of Sound and Vibration*, vol. 301, no. 12, pp. 319 – 340, 2007.

[105] O. Bilal, M. El-Beltagy, M. Rasmy, and M. Hussein, "The effect of symmetry on the optimal design of two-dimensional periodic materials," in *Informatics and Systems (INFOS), 2010 The 7th International Conference on*, pp. 1 –7, march 2010.

[106] O. R. Bilal and M. I. Hussein, "Optimization of phononic crystals for the simultaneous attenuation of out-of-plane and in-plane waves," *Proceedings of ASME 2011 IMECE*, pp. 1–4, November 11-17 2011.

[107] M. I. Hussein, G. M. Hulbert, and R. A. Scott, "Dispersive elastodynamics of 1d banded materials and structures: Design," *Journal of Sound and Vibration*, vol. 307, no. 35, pp. 865 – 893, 2007.

[108] H. Meng, J. Wen, H. Zhao, and X. Wen, "Optimization of locally resonant acoustic metamaterials on underwater sound absorption characteristics," *Journal of Sound and Vibration*, vol. 331, no. 20, pp. 4406 – 4416, 2012.

[109] R. A. Wildman and G. A. Gazonas, "Genetic programming-based phononic bandgap structure design," *Army Research Laboratory*, pp. 1 – 36, September 2011.

[110] M. J. Leamy and O. Gottlieb, "Internal resonances in whirling strings involving longitudinal dynamics and material non-linearities," *Journal of Sound and Vibration*, vol. 236, no. 4, pp. 683 – 703, 2000.

[111] R. K. Narisetti, M. Ruzzene, and M. J. Leamy, "Wave propagation in membrane-based nonlinear periodic structures," *Proceedings of ASME 2011 IDETC*, August 28-31 2011.

[112] M. Shen and W. Cao, "Acoustic bandgap formation in a periodic structure with multilayer unit cells," *Journal of Physics D: Applied Physics*, vol. 33, p. 1150, 2000.

[113] L. Brillouin, *Wave propagation in periodic structures*. Dover Publications Inc., New York, 1 ed., 1946.

[114] J. O. Vasseur, P. A. Deymier, G. Frantziskonis, G. Hong, B. Djafari-Rouhani, and L. Dobrzynski, "Experimental evidence for the existence of absolute acoustic band gaps in two-dimensional periodic composite media," *Journal of Physics: Condensed Matter*, vol. 10, no. 27, p. 6051, 1998.

[115] A. Vakakis, M. King, and A. Pearlstein, "Forced localization in a periodic chain of non-linear oscillators," *International Journal of Non-Linear Mechanics*, vol. 29, no. 3, pp. 429 – 447, 1994.

[116] A. Vakakis, "Non-linear normal modes (nnms) and their applications in vibration theory: An overview," *Mechanical Systems and Signal Processing*, vol. 11, no. 1, pp. 3 – 22, 1997.

[117] Y. Starosvetsky and A. F. Vakakis, "Traveling waves and localized modes in one-dimensional homogeneous granular chains with no precompression," *Phys. Rev. E*, vol. 82, p. 026603, Aug 2010.

[118] I. O. Wygant, X. K. Zhuang, P. Kuo, D. T. Yeh, O. Oralkan, and B. T. Khuri-Yakub, "Photoacoustic imaging using a two-dimensional cmut array," *IEEE Ultrasonic Symposium*, vol. 4, pp. 1921–1924, 2005.

[119] O. Oralkan, A. Ergun, J. Johnson, M. Karaman, U. Demirci, K. Kaviani, T. Lee, and B. Khuri-Yakub, "Capacitive micromachined ultrasonic transducers: next-generation arrays for acoustic imaging?," *IEEE Transactions on Ultrasonics, Ferroelectrics and Frequency Control*, vol. 49, pp. 1596–1610, November 2002.

[120] Y. Huang, A. Ergun, E. Haeggstrom, M. Badi, and B. Khuri-Yakub, "Fabricating capacitive micromachined ultrasonic transducers with wafer-bonding technology," *Journal of Microelectromechanical Systems*, vol. 12, pp. 128–137, April 2003.

[121] I. Wygant, M. Kupnik, and B. Khuri-Yakub, "Analytically calculating membrane displacement and the equivalent circuit model of a circular cmut cell," *IEEE Ultrasonics Symposium*, pp. 2111–2114, November 2008.

[122] Z. Liu, X. Zhang, Y. Mao, Y. Zhu, Z. Yang, C. Chan, and P. Sheng, "Locally resonant sonic materials," *Science*, vol. 289, no. 5485, pp. 1734–1736, 2000.